NELSON MANDELA UNIVERSITY

Design of metal ion-selective reagents for recovery of precious metals

by

Pulleng Moleko-Boyce

A thesis submitted for the degree of Doctor of Philosophy (Chemistry)

at

Nelson Mandela University

March 2019

Promoter: Prof Z.R. Tshentu

DECLARATION

I, Pulleng Moleko-Boyce (213509814), hereby declare that the thesis for Doctor of Philosophy in Chemistry to be awarded is my own work and that it has not previously been submitted for assessment or completion of any postgraduate qualification to another University or for another qualification.

Pulleng Moleko-Boyce

DEDICATION

This work is dedicated to:

Our Father God,

All my family members who have given me support through my journey;

Velile Wilson Moleko (Dad),

Nombeko Ethel Moleko (Mom),

Mputseng Moleko (Sister) and

Ncedile Boyce (Husband).

This work serves as a motivation to inspire youth to never be defined by their background or circumstances, but to use their background as a source of strength and as an inspiration to aspire to make a difference.

ABSTRACT

The study is divided into two sections; namely, (1) the design of rhodium(III) specific chelating ligands (tridentate *bis*-benzimidazole derivatives), and (2) the development of iridium(IV)-specific quaternary diammonium cations with electron donating and electron withdrawing groups. *Bis*-benzimidazole chelating ligands used were *bis*((1*H*-benzimidazol-2-yl)methyl)amine (NNN1), *bis*((1*H*-benzimidazol-2-yl)ethyl)amine (NNN2), *bis*((1*H*-benzimidazol-2-yl)methyl)sulfide (NSN1) and *bis*((1*H*-benzimidazol-2-yl)ethyl)sulfide (NSN2). Quaternary diammonium cations used were tetramethylbenzyl-1,10-diammonium chloride (QuatDMDAMeBnz), tetrabenzyl-1,10-diammonium chloride (QuatDMDABnz), tetratrifluoromethylbenzyl-1,10-diammonium chloride (QuatDMDACF3Bnz) and tetranitrobenzyl-1,10-diammonium chloride (QuatDMDANO2Bnz). For both studies, polyvinylbenzylchloride (PVBC) nanofibers were used as support material. The PVBC nanofibers which were functionalised with *bis*-benzimidazole derivatives and quaternary diammonium cations, respectively, were investigated for the selectivity for Rh(III) over Ir(III), Pt(II), Pd(II) and Ni(II), and for separation of Ir(IV) from Rh(III), respectively. The sorbent materials were characterised by FTIR, SEM, BET surface area, TGA, EDS and elemental analysis, and the results showed that the functionalization of the sorbent materials was successful.

The efficiency of *bis*-benzimidazole derivatives and quaternary diammonium cations, respectively, were investigated in a column study under dynamic flow adsorption conditions. The adsorption kinetics and isotherms were investigated under batch

conditions and fitted on pseudo-first-order and pseudo-second-order model, and Freundlich and Langmuir isotherm, respectively.

It was observed that the *bis*-benzimidazole derivatives showed uptake of $[RhCl_3(H_2O)_3]$, and the loading capacities were observed in the following order; NSN1 (181.06 mg/g) > NSN2 (148.55 mg/g) > NNN1 (131.88 mg/g) > NNN2 (75.87 mg/g). The *bis*-benzimidazole derivatives preference for metal ions was further investigated with a multi-element solution containing Rh(III), Ir(III), Pt(II), Pd(II) and Ni(II). The *bis*-benzimidazole derivatives showed the following order of loading capacity: NSN1 (47.28 mg/g) > NSN2 (23.89 mg/g) > NNN1 (17.47 mg/g) > NNN2 (14.91 mg/g) for Rh(III); NSN2 (10.64 mg/g) > NNN2 (6.84 mg/g) > NSN1 (5.74 mg/g) > NNN1 (5.02 mg/g) for Ir(III); NNN2 (33.96 mg/g) > NSN1 (30.95 mg/g) > NSN2 (19.95 mg/g) > NNN1 (14.92 mg/g) for Pt(II); NNN1 (47.94 mg/g) > NNN2 (28.90 mg/g) > NSN1 (16.22 mg/g) > NSN2 (15.83 mg/g) for Pd(II). *Bis*-benzimidazole derivatives showed no uptake of nickel(II) under these conditions. It was observed the ligand-selectivity order for Rh(III) was similar in both single-element and multi-element studies. This order showed that the *bis*-benzimidazoles containing a sulfur atom showed a high preference for rhodium(III) compared to Pt(II) which had a high preference for NNN2 as well as Pd(II) which had a high preference for NNN1. Ir(III) generally had a lower preference for the ligands presumably due to its higher kinetic inertness compared with Rh(III).

Column sorption of $[IrCl_6]^{2-}$ and $[RhCl_5(H_2O)]^{2-}$ on nanofibers functionalized with diammonium cations was carried out and the loading capacities of $[IrCl_6]^{2-}$ were obtained. $[RhCl_5(H_2O)]^{2-}$ was not adsorbed by the sorbent materials while $[IrCl_6]^{2-}$ was

loaded onto the column. The loading capacities of $[IrCl_6]^{2-}$ with the quaternary diammonium sorbent materials increased in the order of F-QuatDMDAMeBnz (60.29 mg/g) < F-QuatDMDABnz (67.61 mg/g) < F-QuatDMDACF3Bnz (107.59 mg/g) < F-QuatDMDANO2Bnz (140.47 mg/g). The loading capacity for Ir(IV) with quaternary diammonium cationic nanofibers increased with an increase in the electron-withdrawing nature of the quaternizing group. The charge delocalizing ability of the nitrobenzyl group resulted in the best interaction of the diammonium cation with $[IrCl_6]^{2-}$.

Batch equilibrium studies were carried out to assess the efficiency of *bis*-benzimidazole chelating derivatives as adsorbents using a multi-metal solution (Rh(III), Ir(III), Pt(II), Pd(II) and Ni(II)) in 0.5 M HCl. The efficiency of the quaternary diammonium cations was tested using a binary metal solution (Ir(IV) and Rh(III)) in 6 M HCl. The isothermal batch adsorption studies of a multi-metal solution with *bis*-benzimidazoles derivatives fitted the Langmuir isotherm model which confirmed monolayer adsorption onto a homogeneous surface. The Langmuir isotherm parameter (q_e (mg/g)), using functionalized nanofibers, showed the order of NNN2 (128.21 mg/g) > NSN1 (99.01 mg/g) > NSN2 (91.74 mg/g) > NNN1 (84.03 mg/g) for Pt(II); NNN1 (66.23 mg/g) > NNN2 (5.89 mg/g) > NSN1 (1.40 mg/g) > NSN2 (0.59 mg/g) for Pd(II); NSN2 (10.64 mg/g) > *NNN2* (6.84 mg/g) > NSN1 (5.74 mg/g) > NNN1 (5.02 mg/g) for Ir(III); NSN1 (140.85 mg/g) > NSN2 (109.89 mg/g) > NNN1 (104.17 mg/g) > NNN2 (91.74 mg/g) for Rh(III). The pseudo-first-order kinetics model was found to be the best fit to describe the adsorption kinetics of all metal ions onto all the

sorbent materials. K_1 (min^{-1}) value in pseudo-first-order kinetics showed the same order of adsorption as observed in the Langmuir isotherms.

The isothermal batch adsorption studies of $[IrCl_6]^{2-}$ and $[RhCl_5(H_2O)]^{2-}$ with quaternary diammonium cations fitted the Freundlich isotherm model and confirmed to be effective for multiple-layered adsorption onto a heterogeneous surface. The Freundlich isotherm parameter (k_f (mg/g)) using functionalized quaternary diammonium cationic nanofibers increased in the order of F-QuatDMDANO2Bnz (794.33 mg/g) > F-QuatDMDACF3Bnz (185.35 mg/g) > F-QuatDMDABnz (156.32 mg/g) > F-QuatDMDAMeBnz (112.46 mg/g) for Ir(IV) uptake. F-QuatDMDANO2Bnz resin showed the highest adsorption than that of F-QuatDMDAMeBnz, F-QuatDMDABnz and F-QuatDMDACF3Bnz and this order is similar to what was observed in column studies. The quaternary diammonium cations were shown to have the highest adsorption capacity for Ir(IV) compared with Rh(III). The adsorption of Rh(III) was also observed to increase in the order of F-QuatDMDANO2Bnz (177.83 mg/g) > F-QuatDMDACF3Bnz (40.37 mg/g) > F-QuatDMDABnz (36.98 mg/g) > F-QuatDMDAMeBnz (12.71 mg/g). The pseudo-second-order kinetic model was found to be the best fit to describe the adsorption kinetics of both metal ions onto all the sorbent materials. K_2 ($g.mg^{-1}min^{-1}$) value in pseudo-second-order kinetics showed the same order of adsorption as observed in the Freundlich isotherms. The adsorption studies showed adsorption takes place *via* chemisorption process.

This thesis presents PGMs and iridium-specific materials that could be applied in solutions of secondary PGMs sources containing rhodium, platinum and palladium

with *bis*-benzimidazoles as well as in feed solutions from ore processing with diammonium cations for iridium recovery.

KEYWORDS: tridentate *bis*-benzimidazoles, quaternary diammonium cations, polymer nanofibers, column studies, adsorption kinetics and isotherms.

ACKNOWLEDGEMENTS

First and foremost, I am deeply grateful to my Lord and Savior for the seed He has planted in me and the opportunities and daily directions He has given throughout my life.

An intense gratification to Prof Zenixole Tshentu (my supervisor) whom his contribution has raised the quality of this thesis. He has always supported and given me enthusiasm for science. He has patiently guided me, I am very grateful to his supervision and I owe him the greatest degree of appreciation.

I wish to express my deepest gratitude to Dr Sunday Ogunlaja for his invaluable guidance, the time and tremendous effort he offered to help to finish this thesis. It was a great honour to finish this work under his support.

I genuinely appreciate my lab mates (Dr Odame, Dr Ngororobanga, Tendai Dembaremba, Cyprian Moyo, Zola Hlongwe, Sinelizwe Joseph, Siphumelele Majodina, Zizipho Ngayeka and Sendi Gandidzwanwa) for their valuable scientific assistance and undoubted effort throughout this work.

I am grateful and appreciative of Ms Zikhona Majavu for her valuable assistance and undoubted effort towards the completion of this work.

I am thankful for technical assistance offered by Mr Schalekamp, Mrs Muller, Mr F. Olivier and Dr Hosten, and the entire support team from the Nelson Mandela University Department of Chemistry cannot be left unrecognized.

Special acknowledgement goes to the National Research Foundation (NRF) for funding, and the Nelson Mandela University Research Capacity Development office, and its dedicated and friendly staff for facilitating the finances.

The considerable educational foundation laid down by the Nelson Mandela University Department of Chemistry academic staff went a long way into the accomplishment of this work. I have innumerable appreciation for the Nelson Mandela University Department of Chemistry for providing the facilities used in this project.

The greatest appreciation goes to my family. They are the reason for my accomplishment to date. I thank them for great support and continuous care. I would like to recognize the undistinguished role played by my husband, Ncedile Boyce, who believed in me. His support encouraged me to survive the journey of undertaking a PhD study.

Table of contents

List of Figures

List of Tables

List of Schemes

List of Acronyms

B

BET: Barret-Emmett-Teller

BJH: Barret-Joyner-Halenda

D

DFT: Density functional theory

DMDA: Diaminodecane

E

EDS: Energy dispersive spectroscopic analysis

F

F: Fiber

Fac: Facial

H

HCl: Hydrochloric acid

HOMO: Highest occupied molecular orbital

I

Ir: Iridium

ICP-OES: Inductively coupled plasma - optical emission spectrometry

L

LUMO: Lowest unoccupied molecular orbital

L: Ligand

M

MeOH: Methanol

Mer: Meridional

M: Molar concentration

N

N: Nitrogen

NNN1: *bis*((1*H*-benzimidazol-2-yl)methyl)amine

NNN2: *bis*((1*H*-benzimidazol-2-yl)ethyl)amine

NSN1: *bis*((1*H*-benzimidazol-2-yl)methyl)sulfide

NSN2: *bis*((1*H*-benzimidazol-2-yl)methyl)sulfide

P

Pt: Platinum

Pd: Palladium

PGMs: Platinum group metals

PVBC: Polyvinylbenzylchloride

Q

QuatDMDANO2Bnz : Tetranitrobenzyl-1,10-diammonium chloride

QuatDMDAMeBnz: Tetramethylbenzyl-1,10-diammonium chloride

QuatDMDACF3Bnz: Tetratriflouromethylbenzyl-1,10-diammonium chloride

QuatDMDABnz: Tetrabenzyl-1,10-diammonium chloride

S

S: Sulfur

SEM: Scanning electron micrographs

T

TGA: Thermogravimetric analysis

Tu: Thiourea

Chapter 1: Introduction

1.1 Platinum group metals (PGMs)

South Africa is the world's largest producer of precious metals which include platinum group metals (PGMs). PGMs constitute platinum (Pt), palladium (Pd), ruthenium (Ru), osmium (Os), rhodium (Rh) and iridium (Ir). The PGMs occur together in nature alongside nickel, copper, and other base metals [1, 2]. In the world, 58% of PGMs production takes place in South Africa while Russia accounts for a further 26%, most of this is a co-product of nickel mining. Nearly all the rest comes from Zimbabwe, Canada and the USA (Figure 1.1) [3, 4].

Figure 1.1: Worlds production of PGMs shown by the country flag.

South Africa's PGMs producers have traditionally exploited three separate extensive layered reefs of the Bushveld Complex; the Merensky Reef, the Upper Group 2 (UG2) Chromitite Layer, and the Platreef [4]. PGMs are exceedingly rare and comprise less than 2% by weight of the earth's crust. Rhodium and iridium are exceedingly rare elements, comprising only 0.0001 and 0.001 ppm of the earth's crust respectively [5]. All the platinum group metals are generally associated with each other and rhodium and iridium, therefore, occur wherever the other platinum metals are found. However, the relative proportions of the individual metals are by no means constant and the more important sources of rhodium are the nickel-copper-sulfide ores found in South Africa and in Sudbury, Canada, which contain about 0. 1% Rh. Iridium is usually obtained from native osmiridium (Ir ~ 50%) or iridiosmium (Ir ~ 70%) found primarily in South Africa as well as Alaska [6, 7].

The Southern African deposits generally contain a higher proportion of platinum than palladium and rhodium. PGMs are either extracted from newly mined primary ore, or extracted from secondary sources, e.g., used, scrap, or by-product metals, compounds and mixtures. Johnson Matthey estimated primary supply in 2015 of the main PGMs, platinum, palladium and rhodium amounted to 13.31 million troy ounces (oz) [8]. This was augmented by a further 4.46 million troy oz of platinum, palladium, and rhodium recovered from the end of life consumer products automobile catalytic converters, jewellery scrap, and old electrical equipment [8]. Detailed supply by region is shown in Table 1.1.

Table 1.1: PGMs supply by region (1 Oz = 3,125x10^{-5} tons).

Location	**Pt (oz)**	**Pd (oz)**	**Rh (oz)**
South Africa	4,571	2,684	611
Russia	670	2,434	80
North America	318	864	23
Zimbabwe	401	320	35
Rest of the world	149	142	5
Total world supply	**6,109**	**6,444**	**754**

The PGMs represent a significant origin of revenue for South Africa. The economic development and consumption growth of PGMs are increasing. They are widely used in chemical industry, automobile industry and other high-tech fields due to their relatively high mechanical strength and good catalytic properties [9]. Nevertheless, the production of PGMs might decrease to an extent that the demand is not met due to its scarcity and high price. Natural resources for these metals are becoming more limited and their demand from industry is increasing and it is important to find effective separation processes to recover these metals from different sources [10]. The recovery of PGMs has become an increasingly important topic, both as a potential strategy for maintaining the supply of these metals and in terms of converting a previously disposable material into a valuable renewable resource.

1.2 Uses and properties of rhodium and iridium

Rhodium and iridium are used in the manufacturing industry. Rhodium is used as an alloying agent for hardening and improving the corrosion resistance of platinum and palladium. These alloys are used in furnace windings, bushings for glass fiber

production, thermocouple elements, electrodes for aircraft spark plugs, and laboratory crucibles [11]. A rhodium platinum alloy was formerly used in the Ostwald process, in the production of nitric acid. Rhodium-phosphine complexes have also been employed as catalysts for hydrogenation reactions [3]. Other rhodium uses includes electrical contacts, where it is valued for small electrical resistance, small and stable contact resistance, and great corrosion resistance. Rhodium plated by either electroplating or evaporation is extremely hard and useful for optical instruments. It is also used in filters in mammography systems for the characteristic X-rays it produces. Rhodium neutron detectors are used in combustion engineering nuclear reactors to measure neutron flux levels [12]. Rhodium, together with platinum and palladium, are mostly used as catalysts in the automotive industry. Due to increased environmental regulations, rhodium is used in catalytic converters in automobiles, to reduce noxious fume emissions to N_2. As the world becomes more environmentally aware and regulations regarding air pollution tighten, there will even be a greater demand for rhodium [13].

The primary application of iridium is in electronics, to make high-temperature resistant crucibles and in the manufacture of electrodes for long-life spark plugs. These plugs are expensive but have important military uses, particularly in helicopters. Iridium is also used to coat electrodes used in the chloro-alkali process, which involves the electrolysis of brine to chlorine and caustic soda [5]. Other main uses of iridium include its application as a hardening agent for platinum alloys and it forms an alloy with osmium that is used for tipping pens and compass bearings. Iridium is also used to make heavy-duty electrical contacts. Iridium was used in making the international

standard kilogram, which is an alloy of 90% platinum and 10% iridium. Also, radioactive isotopes of iridium are used in radiation therapy for the treatment of cancer, and its complexes are considered for chemotherapy [14]. More uses of PGMs are shown in Table 1.2 [3].

Rhodium is a silver-white metal. It has a melting point of 1,966°C and a boiling point of about 4,500°C. Its density is 12.41g.cm^{-3}. The rhodium special properties are its high electrical and heat conductivity [3]. Iridium is the most corrosion resistant metal known and is frequently employed as a hardening agent. It is also very heat resistant with a melting point as high as 2,443ºC and a boiling point of about 4,130°C. The density of iridium in 22.61g.cm^{-3} [15]. These Properties make these elements important for high temperature applications.

Table 1.2: Uses of PGMs in products for everyday use.

Product	**PGMs**	**Applications**
Automobiles	Pt, Pd and Rh Pt, Pd and Ir Pt Pt, Pd and Ru	Pollution control catalyst Spark plugs Engine control sensors, airbag initiators Electronics for engine management systems
Electronic equipment	Pt, Pd, Ru, and Ir	Connectors, printed circuits, resistors, capacitors, lasers
Computers	Pt and Ru	Thin layers in hard disks to increase memory storage capacity
Jewellery	Pt, Pd and Rh	Rings, chains, pendants, watch cases and straps
Glass and ceramic	Pt and Rh	Glass Fibre, display glass, optical glass, ceramic glass, tableware, decorative patterns and finishes
Medical and biomedical	Pt, Pd, Rh, Ru, Ir and Os	Antitumor drug, implants, treatments for heart disease, cancer screening
Chemical and petroleum	Pt, Pd, Rh, Ru and Ir	Plastics, polyester, pharmaceutical ingredients, high octane gasoline, fertilizers, explosive and silicones
Aircraft Engines	Pt	Turbine blades, spark plugs
Dental restorations	Pt, Pd, Ru, Ir	Dental inlays, crowns, bridges
Fuel cells	Pt, Ru	Electric vehicles, standby and auxiliary power, domestic power and heating

1.3 Chemistry of rhodium and iridium

The separation of rhodium and iridium from each other is complicated by the similarity in the chemistry of these metals ions, being 4d and 5d transition elements,

respectively. Hence, this results in a difficult separation process. Rhodium and iridium are commonly found in oxidation states (I) to (III) for rhodium and (I) to (IV) for iridium. Oxidation states (-I), (0), (V) and (VI) exist with suitable ligands for both metals. Rhodium(IV) does exist but is not common [16, 17]. Rh(I) and Ir(I) play an important role in catalytic reactions due to the ease of the two electron oxidation processes to Rh(III) and Ir(III). The metal(II) species readily disproportionate to the most stable oxidation states, (I) and (III) [16]. The most common state of rhodium, especially in aqueous media is Rh(III).

Rhodium and iridium are found to have a high covalent character in their bonding. They are known to form relatively inert complexes. Observing the transition metal group from cobalt to rhodium to iridium, there is an increase in the metals covalent character. This has been attributed to increased ligand field splitting and nephelauxetic effect where a large amount of d-electron delocalisation occurs from the metal ion to the ligand. The ligand field splitting increases down a group while the nephelauxetic parameter decreases. Both rhodium and iridium exhibit a tendency toward higher oxidation states. Very stable trivalent states of both rhodium and iridium commonly occur. These metals are primarily found in the form of spin-paired (d^6) octahedral complexes, rendering the trivalent state very stable for both 4d and 5d transition metals. Separation based on different oxidation states is considered, as iridium is known to occur in the quadrivalent oxidation state while the rhodium(IV) oxidation state is found to be very unstable.

$RhCl_6^{2-}$ + e^- ⇌ $RhCl_6^{3-}$ (1.2 V) (1)

$IrCl_6^{2-}$ + e^- ⇌ $IrCl_6^{3-}$ (0.87 V) (2)

Based on the redox potentials shown in equations 1 and 2, iridium(IV) chlorido species is more likely to occur than rhodium(IV) species. $RhCl_6^{3-}$ and $IrCl_6^{2-}$ exhibit different properties such as charge density and degree of aquation. Hence, this is encouraging for separation as they will require counter cations of different size and charge density. Comparison of the oxidation states shows the (+3) oxidation state of metal ion has t_{2g}^6 electronic configuration while (+4) oxidation state has a t_{2g}^5 electronic configuration. Ligand exchange is generally slow with these metal ions as they are both very covalent, particularly in the transition from 4d to 5d. Ligand exchange is thus not very straight forward unless an additional parameter can be introduced *via* the differences in the activity of the M(III) and M(IV) species.

The separation of iridium(IV) species, $IrCl_6^{2-}$, is suited for extraction *via* ion-pairing with suitable counter-cations in high [HCl]. Thus, differentiation of iridium(IV) species with rhodium(III) species *via* manipulation of the counter-cation. Differentiating between rhodium and iridium, at low [HCl], lies in the readiness of aquated rhodium(III) species to undergo complexation *via* ligand exchange with suitable ligands. Hence, separation is expected to be more ideal with rhodium(III) versus iridium(IV) due to the properties of these metals in their respective oxidation states.

HCl is involved in most processes in the refining the platinum group metals in industry, hence the iridium(IV) and rhodium(III) aqua chlorido species in HCl are of importance

to this study [17]. The aqueous chemistry of iridium is dominated by iridium(III) and (IV) species. As with rhodium, the chlorido species play a predominant function in the purification process. The similar chemical behaviour of rhodium and iridium in the same oxidation state is due to the similar ionic radii (Table 1.3). There is a small size difference between a 4d metal and the 5d metal of the same group due to the lanthanide contraction, which results in a smaller increase than expected with the size of the third transition series [18].

Table 1.3: Ionic radii of rhodium and iridium.

	Rh(III)	**Ir(III)**	**Rh(IV)**	**Ir(IV)**
Ionic radii (Å)	0.81	0.82	0.74	0.77

To understand the way in which two species affect each other in solution is through knowledge of each species. All oxidation-reduction mechanisms, aquation-anation equilibria, hydrolysis reactions, etc, must be considered so that these factors can be assessed for the combined system.

1.3.1 Rhodium and iridium speciation

It is important to establish which of the iridium(IV) and rhodium(III) chlorido complexes, could possibly be present at the specific HCl concentrations as shown in Table 1.4. Chlorido complexes containing coordinated water molecules will behave differently to their completely chloridated analogues in separation processes in which ion-exchange and coordination are involved. As shown in Figure 1.2, different rhodium(III) chlorido

complexes are formed upon the addition of water (aquation) or addition of chloride (anation) in the system [19].

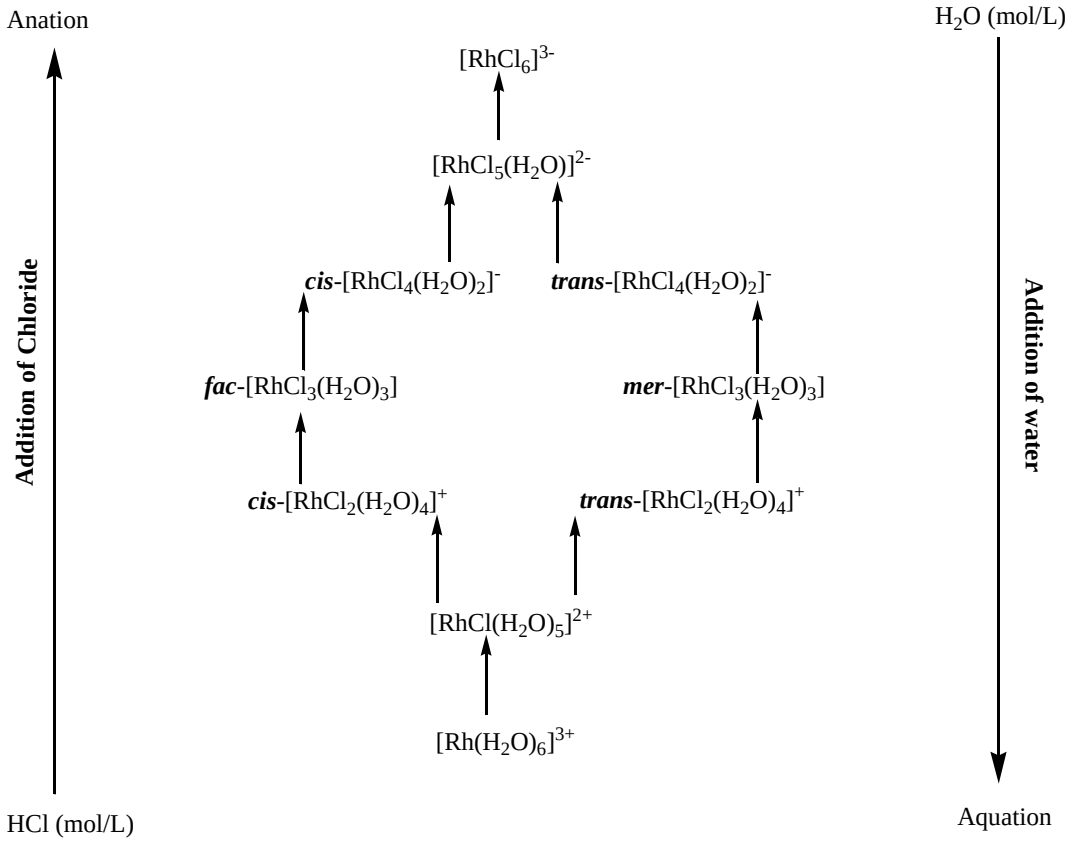

Figure 1.2: Rh(III) species present in HCl media.

Previous studies of rhodium and iridium at exact HCl concentration have shown contradiction as to the species formed at the specific [HCl] (Table 1.4). From these studies, it was observed that there was a clear indication that in HCl concentrations (from 0.5 M to 9 M) rhodium(III) and iridium(III)/(IV) appear to be in the form of higher chlorinated species as HCl concentration increases [20]. Hence, the stability of $IrCl_6^{2-}$ species is of great importance and the separation of rhodium and iridium can,

therefore, be based on the separation potential of $IrCl_6^{2-}$ from the rhodium(III) chlorido anionic species. The two rhodium(III) chlorido complexes present to a greater or lesser extent in a 3 M to 6 M HCl medium, is mostly $RhCl_5(H_2O)^{2-}$ and as the [HCl] concentration is increased, $RhCl_6^{3-}$ is also observed. Both these species are different to $IrCl_6^{2-}$ in terms of size, charge density and the ability to phase transfer [22, 23].

Table 1.4: Chlorido species of rhodium(III) and iridium(IV) metal ion solutions in different HCl concentrations.

HCl Concentration (M)	**Rhodium(III)**	**Iridium(III)**	**Iridium(IV)**
0.5	$RhCl_3(H_2O)_3$	$IrCl_3(H_2O)_3$	$[IrCl(H_2O)_5]^{2+}$ $[IrCl_2(H_2O)_4]^{+}$
1	$RhCl_3(H_2O)_3$ $RhCl_4(H_2O)_2^-$	$IrCl_3(H_2O)_3$ $IrCl_4(H_2O)_2^-$	$[IrCl(H_2O)_5]^{2+}$ $[IrCl_2(H_2O)_4]^{+}$
1.4	$RhCl_3(H_2O)_3$ $RhCl_4(H_2O)_2^-$	$IrCl_4(H_2O)_2^-$ $IrCl_5(H_2O)^{2-}$	$[IrCl(H_2O)_5]^{2+}$ $[IrCl_2(H_2O)_4]^{+}$ $IrCl_5(H_2O)^-$
2	$RhCl_4(H_2O)_2^-$ $RhCl_5(H_2O)^{2-}$	$IrCl_5(H_2O)^{2-}$	$IrCl_5(H_2O)^-$ $IrCl_6^{2-}$
3	$RhCl_5(H_2O)^{2-}$ $RhCl_6^{3-}$	$IrCl_5(H_2O)^{2-}$	$IrCl_5(H_2O)^-$ $IrCl_6^{2-}$
4	$RhCl_4(H_2O)_2^-$ $RhCl_5(H_2O)^{2-}$ $RhCl_6^{3-}$	$IrCl_5(H_2O)^-$ $IrCl_6^{3-}$	$IrCl_5(H_2O)^-$ $IrCl_6^{2-}$
5	$RhCl_4(H_2O)_2^-$ $RhCl_5(H_2O)^{2-}$ $RhCl_6^{3-}$	$IrCl_5(H_2O)^-$ $IrCl_6^{3-}$	$IrCl_5(H_2O)^-$ $IrCl_6^{2-}$
6	$RhCl_5(H_2O)^{2-}$ $RhCl_6^{3-}$	$IrCl_5(H_2O)^-$ $IrCl_6^{3-}$	$IrCl_6^{2-}$
7	$RhCl_5(H_2O)^{2-}$ $RhCl_6^{3-}$	$IrCl_5(H_2O)^-$ $IrCl_6^{3-}$	$IrCl_6^{2-}$
8	$RhCl_6^{3-}$	$IrCl_5(H_2O)^-$ $IrCl_6^{3-}$	$IrCl_6^{2-}$
9	$RhCl_6^{3-}$	$IrCl_6^{3-}$	$IrCl_6^{2-}$

1.3.2 Electronic spectroscopic character of chlorido complexes

The molar extinction values of chlorido complexes of rhodium(III) and iridium(III) are in the order of 100 as shown in Table 1.5. Due to their nephelauxetic character, the molar extinction coefficients are higher than that of 3d metals, which vary between 10 and 50. Most of the chlorido complexes of rhodium and iridium have low symmetry resulting in a slightly higher molar extinction value. Tetravalent iridium complexes have much higher molar extinction values of more than 1000 (Table 1.6). The advantage of this is that analytical determination of the specific iridium(IV) species can be done spectrophotometrically, but also has disadvantage of obscure the lower molar extinction spectra of the trivalent rhodium and iridium complexes [22].

1.3.2.1 Rhodium(III) chlorido species

The rhodium-HCl system is less complicated than the iridium-HCl system as the existence of rhodium(IV) species need not be considered. Rhodium(I) is an oxidation state which requires pi-back donating ligands [23]. Rhodium(III) is, thus, the only oxidation state of importance in HCl solution. Parameters such as the chloride concentration, acidity and the aquation-anation processes all need to be considered. In contrast with iridium(IV), species like $\mathrm{Rh(H_2O)_6^{3+}}$, $\mathrm{RhCl(H_2O)_5^{2+}}$ and $\mathrm{RhCl_2(H_2O)_4^{2+}}$ have been isolated with difficulty. However, chloride anation of these centres occurs readily. Anionic complexes of rhodium(III) have been found to be more labile than neutral and cationic complexes so the aquation-anation equilibria will play an important role in any absorbance changes of the spectra [22].

To qualitatively identify the rhodium(III) species in solution *via* Uv-Vis spectrophotometry, the difference spectra require to be characterized. Table 1.6 shows the absorbance maxima of various rhodium(III) aqua chlorido species [23, 25].

Table 1.5: Absorbance maxima and molar extinction coefficients of rhodium(III) aqua chlorido species. Isomers are noted in brackets.

Complex	**Wavelength (nm)**	**ε_M ($M^{-1}.cm^{-1}$)**
$RhCl_6^{3-}$	411	93.8
	518	111.5
$RhCl_5(H_2O)^{2-}$	402	73.4
	507	72.8
$RhCl_4(H_2O)^{2-}$	385	54.1
	488	72.0
$RhCl_3(H_2O)_3$	376 (*mer*)	93.5
	474 (*mer*)	68.3
	370 (*fac*)	71.6
	471 (*fac*)	77.1
$RhCl_2(H_2O)_4^{2+}$	349	49.5
	450	64.9
$RhCl(H_2O)_5^{2+}$	335	50.0
	426	50.4
$Rh(H_2O)_6^{3+}$	311	67.4
	396	62.0

1.3.2.2 Iridium(III)/(IV) chlorido species

The identification and investigation of specific equilibria of iridium(III)/(IV) species are very difficult since there are so many side reactions. Parameters such as pH, chloride concentration and temperature, all influence the iridium(IV) aqua chlorido complexes [25]. The effect of these parameters is discussed in terms of the various equilibria that exist in HCl system. However, the absorption spectra of the individual iridium(IV) chlorido species have been determined [27, 28]. To identify the various species, absorbance maxima and molar extinction coefficients are listed in Table 1.6. According to Table 1.6, as the aquation of $IrCl_6^{2-}$ occurs, the molar extinction coefficients decrease.

Table 1.6: Absorbance maxima and molar extinction coefficients of iridium(IV) chlorido aqua species. Isomers are noted in brackets.

Complex	**Wavelength (nm)**	**ε_M ($M^{-1}.cm^{-1}$)**
$IrCl_6^{2-}$	488	4060
$IrCl_5(H_2O)^-$	450	3320
$IrCl_4(H_2O)_2$	350 (*trans*)	1090
	445 (*trans*)	2900
	535 (*trans*)	1310
	445 (*cis*)	2790
	535 (*cis*)	1290
$IrCl_3(H_2O)_3^+$	375	1700
	510	1400
	375	1900
	512	1750

The higher molar extinction values (ε_M) of the iridium(IV) metal ion species, provides a means of detection in the presence of rhodium(III). This is ideal for mixtures of iridium(IV) and rhodium(III), allowing for detection and analysis of both metal ion species [27].

1.4 Separation of iridium and rhodium

The binary systems such as Pd-Pt, Rh-Ir, and Ru-Os are the common pairs of platinum group metals which exhibit some challenges in their separation. There are numerous other combinations which have been investigated. These separations use the selective oxidation, electrostatic effects and kinetic effects. The separation of rhodium and iridium from each other is one of the most difficult and problematic aspects of PGMs processing [20]. The chemical similarity between these two metal ions and the extremely inert nature of rhodium and iridium complexes creates a most challenging problem in their separation. The complexity of the solution chemistry of the PGMs has contributed to the challenges of the production of methods for their separation [22, 23].

Understanding the probability of complexes in solution, their kinetic and thermodynamic stability properties is key. There are two ways to follow the separation of rhodium and iridium. The first route is through the inner-sphere coordination of the ligand to the metal species and the second route *via* ion-pair formation of anionic chlorido species with cations. Solvent extraction (SX) and ion-exchange (IX) methods are the most commonly used separation methods to achieve high purity metals.

1.4.1 Solvent extraction (SX)

SX has been extensively utilized for the separation of the Ir and Rh [24, 25]. The challenge with this extraction procedure is the slow reaction of the chlorido complexes. The separation of binary or multi-elements of PGMs, using solvent extraction as a method of separation, use the differences in the kinetic behaviour for the formation of extractable species and the strength of the electrostatic interaction of the chlorido complexes formed with liquid ion-exchangers [30].

The charge of the complex and its character contribute towards hydration and has been useful for the separation of Ir and Rh [26, 27]. The inertness of the chlorido complexes of iridium(IV) and rhodium(III) towards aquation plays a vital role in their extraction from acidic solution by an anion-exchange mechanism with cations such as ammonium and quaternary ammonium salts, and other nitrogen-containing exchangers [31–37]. However, because both metal ions are highly extractable as chlorido complexes their separation is difficult [22, 23, 37, 38, 27, 29, 31–36].

The Ir(IV) chlorido complex ($IrCl_6^{2-}$) is highly extractable in the organic solvents [26–32, 39], while the Ir(III) form is much less extractable, owing to the increase in the charge on the complex [29, 31, 33, 36]. The chlorido complex of Rh(III) is poorly extracted, and the reason is due to the charge and the charge labile character of the complex toward aquation [24, 25, 29, 32, 34, 35, 39]. Several extractants have been used and exhibit differences in behaviour of the chlorido complexes of binary mixtures of the metal ions using different types of organic solvents [31, 39, 40]. The differences in the formation rate of the extractable anionic, neutral, or cationic species of the binary

mixtures of Rh and Ir with numerous complexing or chelating agents have been exploited for their separation from aqueous solution. The relatively labile character of rhodium compared to iridium in the formation of the extractable anionic [41–43] or neutral [44–48] complexes play an important role in their separation [48, 53]. This commonly involves converting rhodium into the extractable form while maintaining iridium in the unextractable chloride form or vice versa [49–51].

Solvent extraction is known to have disadvantages that include; (i) a need for a multi-stage extraction to achieve complete recovery, (ii) lower ability for enrichment, and (iii) the difficulty in phase separation (iv) Fire risks and disposal of organic solvents. Generally, the volume ratio between the organic phase and the aqueous phase cannot be very large to prevent solvent loss. This result in high production costs that are due to solute losses from handling and storage of the organic solvent. From an industrial perspective, the equipment associated with solvent extraction can be rather complex, difficult to control, and may run into problems with reagent losses or disengagement of phases.

1.4.2 Ion exchange

Numerous cationic and anionic ion-exchange methods have been produced for the separation of iridium from rhodium. This method is based on the separation of the metal ion species due to different affinities for the functional group on the resin [33, 34, 40, 52]. Ion exchange resins, on the other hand, are known for their high capacity and selectivity for platinum group metal ions. Ion exchange resins are polymer ion

exchangers with a variety of functional groups, which present a broad scope of application both in hydrometallurgy and analytical chemistry [53, 54].

The design of support materials, especially anion exchange solid phase materials, to improve the loading capacity and separation factors for the PGMs remains an interesting area of research. Ion exchange is a preferred technology due to the high separation efficiency, high loading capability and simplicity of operation [55, 56]. Ion exchange, however, has its own disadvantages, for example, the slow kinetics of metal ion or complex anion uptake. This drawback can be overcome by increasing the availability of the functional groups within the support material [62]. Types of ion exchange resins which can be used are cation, anion or amphoteric exchange resins depending on the form of the targeted metal ion. Anion exchange resins are classified into two categories; weak base and strong base anion exchangers [63]. Weak base anion exchangers are classified as primary, secondary and tertiary amines while strong base anion exchangers are classified as quaternary amines. Previous investigations have explored the use of quaternary diammonium centres as anion exchange sites. Anion exchangers with ammonium or quaternary ammonium functionalities are known to interact with anionic chlorido complexes of the PGMs [64].

1.4.3 Separating agents used for separating rhodium and iridium

Despite the difficulties in the separation of rhodium and iridium, a variety of separating agents have been reported in the literature. Several quaternary ammonium separating agents have been used to separate iridium from rhodium as shown in Figure 1.3 [60,

61]. Ammonium cations include; ammonium (1), methylammonium (2), dimethylammonium (3), trimethylammonium (4), tetramethylammonium (5) and tetraethylammonium (6). The diammonium cations include; ethane-1,2-diammonium (1), butane-1,4-diammonium (2), hexane-1,6-diammonium (3), tetramethylethyenediammonium (4), ethane-1,2-trimethylenediammonium (5), and ethane-1,2-dimethylethyldiammonium (6) [40, 62].

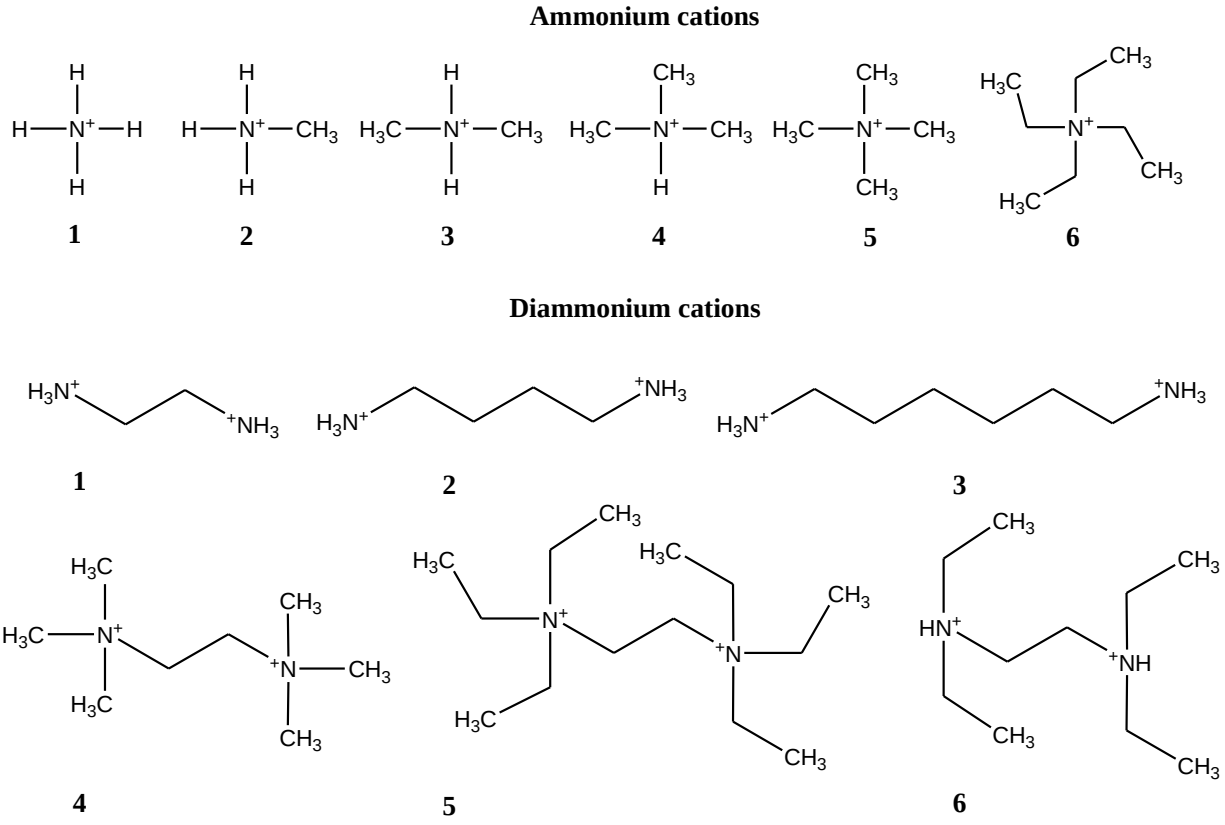

Figure 1.3: Chemical structures of ammonium and diammonium cations.

The aliphatic and aromatic N-donor ligands, O-donor ligands and S-donor ligands have been extensively used in the separation of rhodium from iridium as separating agents, and a few are shown in Figure 1.4 [22, 25, 70–79, 26–28, 44, 57, 67–69].

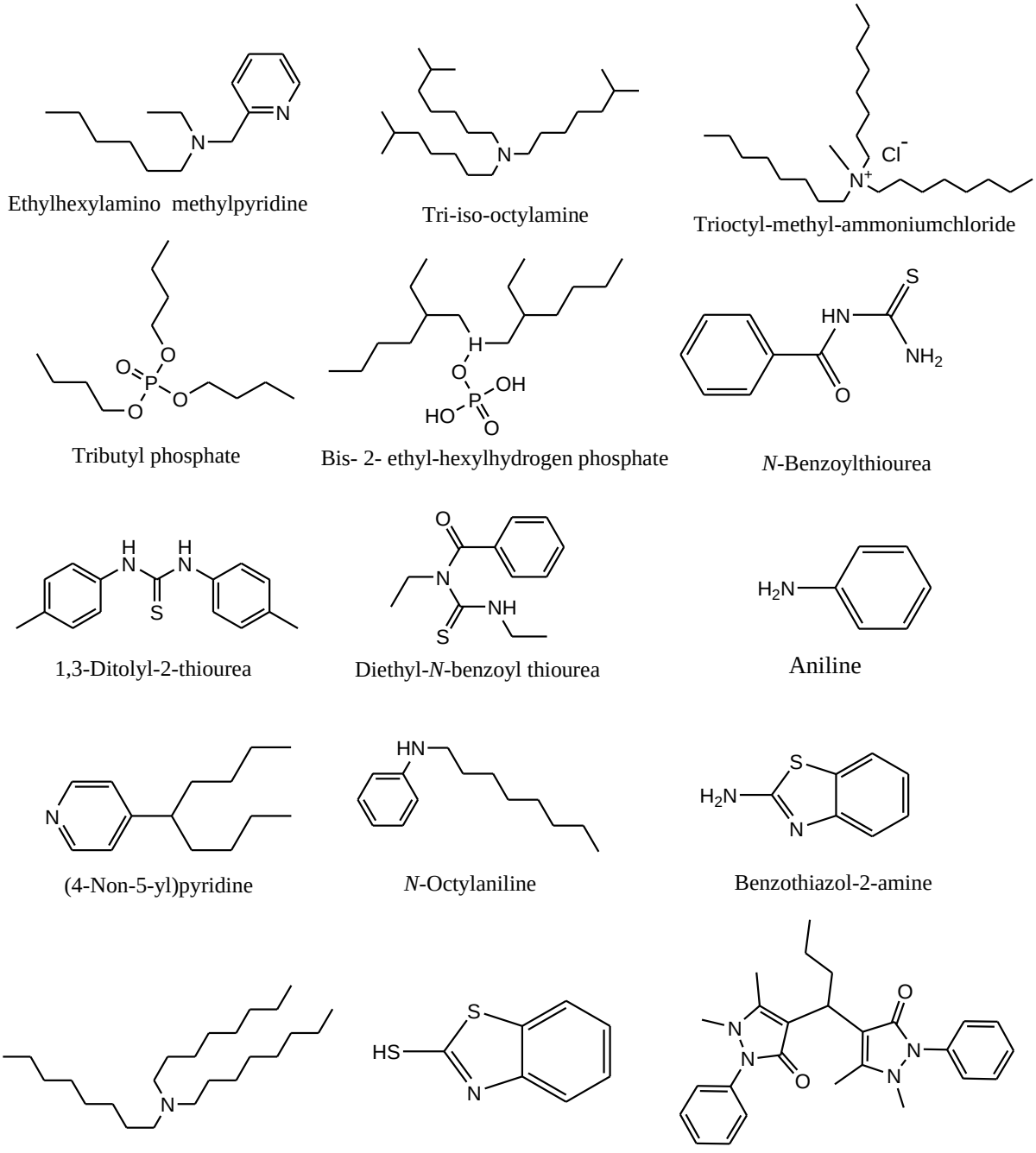

Figure 1.4: Chemical structures of separating agents of rhodium from iridium.

1.5 Coordinating ligands and Ion-pairing cations

1.5.1 Coordinating ligands

Rhodium selective ligands study in this research will involve the use of benzimidazoles (Figure 1.5). The development of benzimidazole-based ligands has also led to the synthesis of metal complexes with applications in the field of coordination chemistry. The assembly of two benzimidazole units is necessary for the preparation of chelating compounds with at least two or three nitrogen donors. The specific case of benzimidazoles assembled around a central nitrogen atom offers an additional reactive site at the secondary amine. This can be exploited for the incorporation of different functional groups to obtain novel *bis*(benzimidazoles) with modified metal selectivity, as well as for generating a series of new chelating ligands for transition-metal chemistry.

Benzimidazole compound is one of the most frequently encountered ligands in transition metals complexes [63, 64]. Benzimidazole contains a benzene ring fused to an imidazole ring. The two nitrogens present in the imidazole ring are different from one another in their nature and makes the properties of the ring system diverse in character. The hydrogen attached to the nitrogen (N1) is in tautomerism with the other nitrogen (N3) [3, 11, 12, 16, 63]. Due to this tautomerism, certain benzimidazole derivatives, which seem at first as isomers, are tautomers [16]. The capacity for coordinating metals is due to the presence of the N3 atom known as the pyridinic nitrogen, whose lone pair of electrons are donated to the corresponding metal. The

N1 atom, known as the “pyrrole nitrogen” of the benzimidazole moiety, has the lone pair of electrons of N1 involved in the aromatic sextet of the π-electrons of the rings [69]. The N3 atom remains the principal electron-donor in the formation of metal complexes and involved in the chelation process (metal-chelate ring) for multidentate ligands.

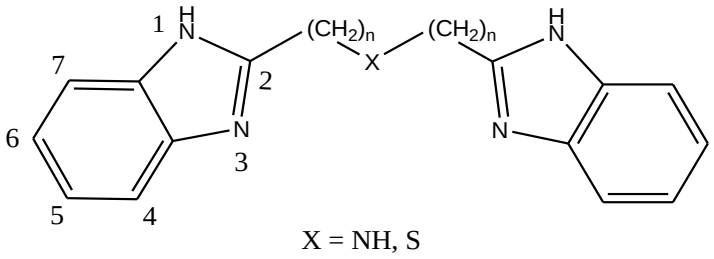

Figure 1.5: Benzimidazole derivatives used in this study.

1.5.1.1 Chelate effect and ring size

The chelate effect or chelation is one of the most important ligand effects in transition metal coordination chemistry. It has been shown that chelate ligands form stable complexes with metal ions. In chelate ligands, 5-membered ring compounds are well known to be more stable than 4- and 6-membered ring compounds [81, 82]. In the chelate compounds, central metals are generally coordinated with two or more coordinating donor atoms as shown in Figure 1.5. There are two types of intramolecular coordination compounds, σ-coordination compounds (coordination is with donor atoms such as O, N, S, P) and π-coordination compounds (coordination groups such as cyclopentadienyl, alkenyl, allyl, alkynyl, dienyl, aryl, etc) [83–87]. The stability of the complex of a metal ion with a bidentate or polydentate ligand is

significantly greater than the complex of the same ion with monodentate ligands of comparable donor ability. For bidentate or polydentate ligands, the stability becomes higher because the probability of cutting at two or more points at the same time is higher than a single bond (statistical effect) [81, 88]. Hence, the 5-membered ring of two bidentate ligands is more stable than a single 5-membered ring. The entropy effect ($\Delta G = \Delta H - T\Delta S$) is the stabilizing factor in the chelate effect.

The interior angle within the chelate ring has shown to play a significant role in forming stable complexes and the angle of interaction is known as the bite angle (angle occupied by the chelate ligand). The interior angles of a regular 4-, 5- and 6-membered rings are 90^o, 108^o and 120^o, respectively (Figure 1.6). The 4-membered ring experiences much more ring strain. The structure of a carbon-carbon single bond is a tetrahedral structure, and its bond angle is 109.28^o. Therefore, if all of the elements of a ring are carbon, the equilateral 5-membered ring easily forms an almost planar stable structure without strain because the bond angles of the tetrahedral structure are almost the same as the interior angles of the equilateral pentagon (5-membered ring) [89–92]. Hence, 5-membered chelate rings are considered more stable. Formation of 5-membered chelate rings are prefered for metal ions with ionic radii greater than 1 [93–99]. Small metal ions ($r < 1$) that form complexes with a chelating ligand result in less stable complexes than large metal ions which tend to form more stable 5-membered ring complexes [94], [99]. Depending on the ligand used to form a 5-membered chelate ring, the ionic radius of approximately 1.0 Å tend to form long M-L

bond distances. Metal ions with smaller ionic radii tend to form shorter M-L bond distances with 6-membered ring chelate ligands [100].

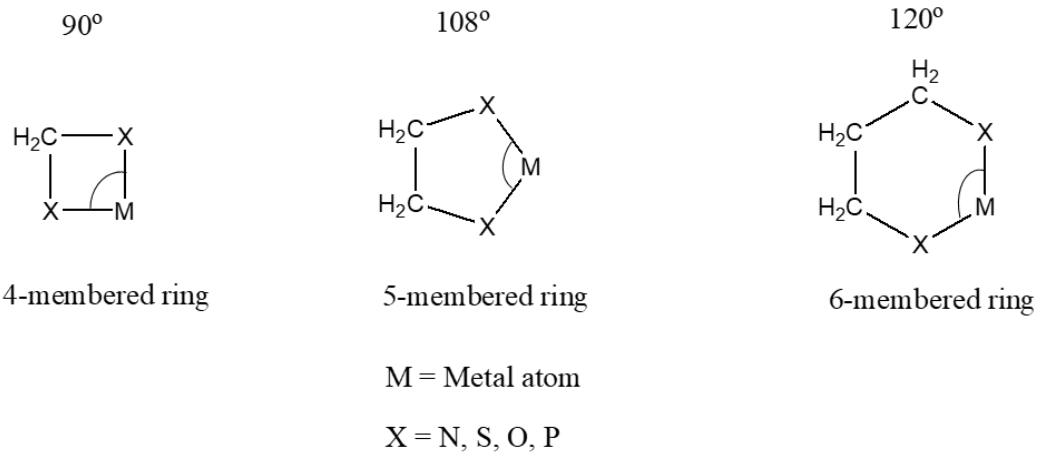

Figure 1.6: Comparison of a 5-membered ring with 4- and 6-membered ring chelates.

1.5.2 Ion-pairing cations

There has been some indication, in the chemistry of ion pairing, that cations have an affinity for anions of a similar charge although this is not the only important parameter in determining the mutual affinity, as solubility also plays a role. There are other aspects which relate to the differences in behaviour of cationic species. It must be remembered that a great number of anionic metal complexes have two or three negative charges. It is, therefore, necessary to take note of the charge differences between the cations and anions to consider the behaviour of cations as separating agents. It has been shown that the dications (Cat^{2+}) are more effective as separating agents for $IrCl_6^{2-}$. Another aspect that was explored is two cationic (Cat^{+}) centres that are spaced apart [101–103]. This study will exploit the derivatives of Cat^{2+} (Figure 1.7).

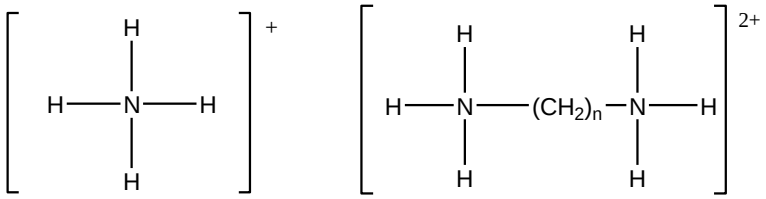

Figure 1.7: Chemical structures of (A) mono-cation (Cat^{+}) and (B) dication (Cat^{2+}).

The application of quaternary ammonium cations has been investigated [102, 103]. This type of cation has been extensively studied and used in industry in the form of extractants and polystyrene resins but does not afford high selectivity in the separation of iridium from rhodium. This was observed in the case where the duration of contact is extended for the treatment of large quantities of metal solutions in industry [104, 105]. It can be stated that the improvement of the separation of rhodium(III) and iridium(IV), can only be achieved by examining how the extraction of the following species, $RhCl_5(H_2O)^{2-}$, $RhCl_6^{2-}$ and $Rh_2Cl_9^{3-}$can be minimised, while at the same time maximising the extraction of $IrCl_6^{2-}$ [19, 106].

1.6 Polymer functional materials

1.6.1 Separation using functional materials

Selective extraction of metal ions on a solid material is gaining attention due to their simplicity, rapidity and ability to provide a high loading capacity [107]. The characteristic of high metal loading capacity and a high rate of metal extraction makes them economical for dilute solutions and a large volume of liquids [108]. The recovery

of the metal ion and the ability to reuse the adsorbent are very important aspects for the successful application of this process.

Chelating resins contain chelating agents (ligands) that have been fused on the solid material by the process known as functionalization. Ion-pairing resins are ion exchangers in which ion-pairing agents (cations or anions) have been fused on the solid material [109]. In this study, *bis*-benzimidazole derivatives will be used as chelating agents and quaternary diammonium cations will be used as ion exchange agents, where these will complex and specifically select a metal ion *via* coordination and ion pairing, respectively. Coordination and ion exchange offer advantages such as high selectivity since the affinity for a specific metal ion depends mainly on the chelating group or ion-pairing group. Kinetics on the solid material in a chelating resin or ion exchange resin are considered to be slow and controlled either by a particle diffusion mechanism or by a second-order chemical reaction [110]. Binding of chelating agents and ion exchange agents with polymer-supported reagents experiences no loss of extractants to the aqueous phase since the ligands or cations are covalently bonded to an insoluble polymer. The aqueous phase (metal solution) can flow through the polymer in a column while the chelating or ion exchange resin removes the metal through complex formation *via* coordination or ion pairing [111, 112]. After the polymer is loaded and washed, the metal is stripped by the passage of a suitable solution through the polymer support to produce a solution containing the extracted metal, and the resin is regenerated. The ability of a polymer resin to be regenerated after recovering the metal ions is considered an important factor for

application in a continuous process [113]. There are different solid materials that have been used such as polystyrene beads, silica and nanofibers shown in Figure 1.8.

Figure 1.8: Different types of solid support materials SEM images; (A) polystyrene beads, (B) silica and (C) nanofibers.

1.6.1.1 Silica

Silica-based (poly)amine ion exchangers have been used to extract PGMs [114]. Recently there has been increasing attention to using silica gel due to its excellent thermal and mechanical stability, unique large surface area and well-modified surface properties. Generally, it is difficult for organic functional groups to bond to silica gel directly because of the relative inertness of the original surface of the silica gel. However, bonding of organic functional groups to the silica gel surface can be achieved after surface activation and modification by functional silanes. As an amorphous inorganic polymer, silica gel is composed of internal siloxane groups (Si–O–Si) with a large number of silanol groups (Si–OH) distributed on the surface [115].

1.6.1.2 Polystyrene beads/ microspheres

Polystyrene beads are generally crosslinked using divinylbenzene to provide stable beads as well as to define some of the characteristics of the materials such as pore size and particle density [116]. Polystyrene resins can either be synthesized using modified monomeric units to include functional groups during the polymerization, or the modifications can be made post-polymerization. These functional groups provide the metal binding sites which provide both capacity and selectivity for the species targeted for separation. The functional or extracting groups on the material have strong effect on the geometry which these materials can interact with the species of interest, resulting in disputes in the coordination environments present. This effect results in significant changes in the geometry at the binding sites and can result in changes in the specificity of functional groups for different species [117].

1.6.1.3 Nanofibers

The use of polymer nanofibers has not been exploited for the separation of PGMs except by Tshentu's group recently [118]. Nanofiber-based sorbent materials offer superior properties at a sub-micron/nanoscale level since they possess a large surface area per mass and high porosity [119]. The ease of surface functionalization is an additional advantage of the nanofiber technology, and this property may play a role in overcoming the limitation of the slow kinetics of uptake of metal species. The smaller diameter of fibers is the main parameter that is sought after in the nanofiber fabrication process in order to give the desirable attributes of the fiber mats. Lately, there has

been a growing interest in sorbents based on nanofibers due to their attractive features. As described in the literature, polymer nanofibers obtained from electrospinning show excellent heavy-metal ions and organic pollutants removal ability from water [119–121]. Polyvinyl benzyl chloride (PVBC) is an important polymer that has been widely applied. PVBC nanofibers will be employed in this study with various quaternary diammonium cations and *bis*-benzimidazole derivatives to specifically target $IrCl_6^{2-}$ and $RhCl_2(H_2O)_3$ species, respectively. Applications of electrospun nanofibers are numerous with lots of potential owing to the simplicity and flexibility of their fabrication. Nanofibers have been used to reinforce composite materials, membranes and smart clothes, as supports for enzymes and catalysts, and as solid phase extraction materials [123]. Separation of metal ions by sorption with electrospun nanofibers as adsorbents is a new technology. This is majorly due to the large surface area to volume ratio they offer as sorbent materials with increased sites for adsorbate interaction.

1.6.2 Production of nanofibers

Fibers may be produced by a variety of methods such as; drawing template synthesis, deposition on a substrate, thermally induced phase separation and electrospinning [123, 124]. Nanofibers can be produced through the electrospinning process and it can be carried out *via* the following processes, interfacial polymerization, coaxial electrospinning, emulsion electrospinning and melt electrospinning (Figure 1.9) [126]. The electrospinning technique allows the fabrication of extremely fine, low nanometre (nm) fibers. Electrospinning is a technique that provides a simple and adaptable

method for making ultra-thin fibers [127]. Electrospinning depends on repulsive electrostatic forces to draw a viscous-elastic solution into nanofibers [128].

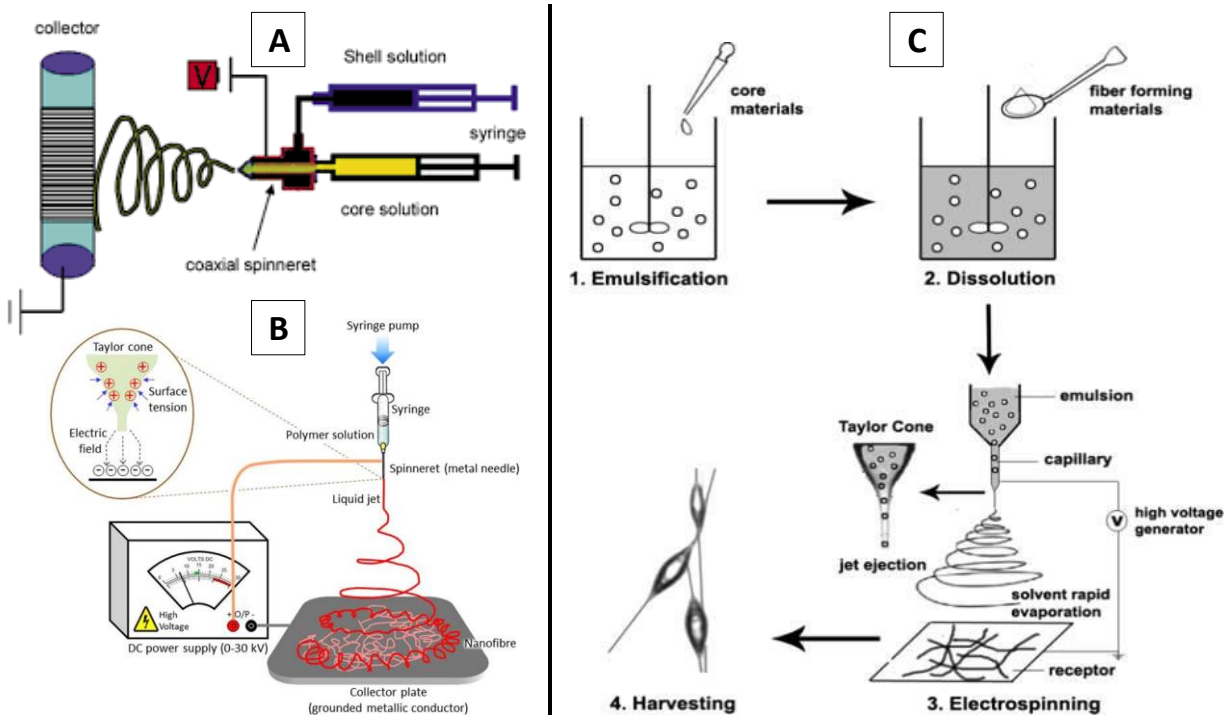

Figure 1.9: Different types of electrospinning; (A) Coaxial electrospinning, (B) Interfacial electrospinning and (C) Emulsion electrospinning.

Electrospun nanofibers exhibit a range of unique features and properties that distinguish the nanofibers from nanostructures fabricated using other techniques. The electrospun nanofiber is highly charged after it has been ejected from the nozzle, making it possible to control its path electrostatically by applying an external electric field. The properties of electrospun nanofibers include; extremely long length, thus making it easy for fibers to be assembled into a three-dimensional non-woven mat. When compared with fibers fabricated using a conventional spinning process,

electrospun fibers are much thinner in diameter and thus possess a higher surface-to-volume ratio. The pores in an electrospun nanofibers non-woven mat are relatively large and all the pores are fully interconnected making the entire surface fully accessible to chemical species. An outstanding benefit of electrospinning in the fabrication of sorbent materials is that it is easy to control the orientation of the nanofibers since the arrangement of the fibers play a significant role in their performance as sorbents [129].

1.6.2.1 Electrospinning and parameters

Electrospinning is made up of three major components namely; a high-voltage power supply, a spinneret (a metallic needle that delivers the polymer solution), and a collector (a grounded fiber collector) as shown in Figure 1.10. A direct current (DC) supply is usually used for electrospinning, though an alternating (AC) current is also feasible [129, 130]. The spinneret is usually connected to a syringe which contains the polymer solution connected to a pump. The polymer solution is fed through the spinneret at a constant rate using a syringe pump. A high voltage is applied to the needle tip usually in the range between 10 to 30 kV. As the polymer solution drops from the nozzle of the spinneret, it becomes highly electrified and the induced charges are evenly distributed over the surface, thus the drop experiences two major types of electrostatic forces; the electrostatic repulsion between the surface charges and the coulombic force exerted by the external electric field. The liquid drop having been distorted appears in the form of Taylor cone. As the applied voltage increases beyond this point, the liquid jet is continuously elongated, and the solvent is evaporated while

its diameter is greatly reduced from hundreds of micrometres to as small as tens of nanometres. As the jet travels towards the collector, the tensile force brought about by the surface charge repulsion produces a bending motion while the polymer chains within the jet are stretched and oriented [132].

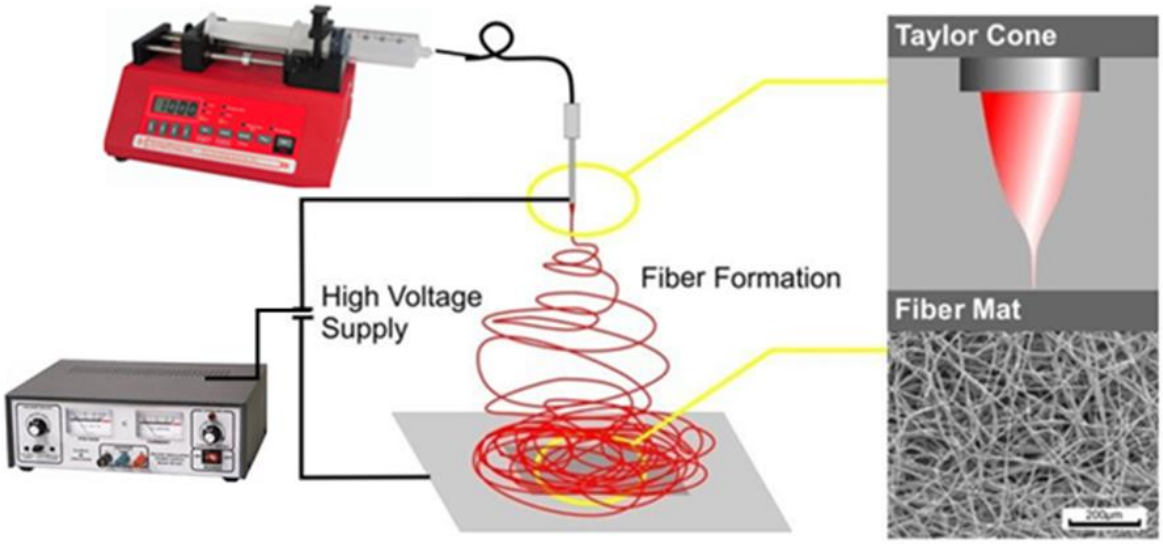

Figure 1.10: Schematic illustration of the basic set-up for electrospinning.

The process parameters require optimizations that include applied voltage, the polymer solution feed rate, and the tip-to-collector distance as shown in Table 1.7 [118, 132]. This becomes necessary because the applied voltage drives the electrospinning process, and therefore provides the charges necessary to overcome surface tension and subsequently produce the polymer jet. The polymer solution flow rate, on the other hand, dictates the speed at which the polymer solution is delivered to the needle tip. It is known that too high flow rate may result in deposition of wet fibers. The flow rate has a definite effect on the resultant fiber diameters. When the tip-to-collector distance

is increased it correspondingly increases the flight time of the polymer jet. This provides time for solvent evaporation as well as time for the stretching of the jet. The net result is typically a decrease in diameter of the fibers with an increase in tip-to-collector distance [133, 134].

Several parameters are known to influence the formation of stable fibers in electrospinning and these are classified as; (A) solution properties (viscosity, conductivity, surface tension, polymer molecular weight, dipole moment, and dielectric constant), (B) controlled variables (distance between the needle tip and collector, voltage and flow-rate) and (C) ambient parameters (temperature and humidity). The detailed information on parameters is shown in Table 1.7.

Table 1.7: Electrospinning parameters.

Parameters	**Effect on nanofiber structure**
Voltage	Voltage variation has been the most controlled parameter during electrospinning. A proper voltage produces a Taylor cone which gives rise to bead-free fibers. A Taylor cone refers to the cone observed in electrospinning processes from which a jet of charged particles originates. When a Taylor cone is formed, the force of the electric field has overcome the surface tension of the solution [123].
Distance (between needle tip and collector)	Varying the distance between the needle tip and grounded collector has resulted in nanofibers having different diameters and morphology. The minimum distance required in obtaining smooth fibers is said to be a function of the fiber drying time and the volatility of the solvent. The shape and design of a collector do affect fiber morphology as porous fiber structures are obtained when a porous collector is employed [135, 136].
Flow rate	Varying polymer electrospinning flow rate also affects the fiber size and morphology. Low flow-rates yield nanofibers with smaller diameters and this may be due to the longer time it takes for the travelling charged polymer to reach the collector. The long jet travelling time allows the polymer solvent to evaporate, thus producing dry fibers. High flow-rates produced beaded nanofibers which do not dry upon reaching the collector due to short polymer jet travelling time [138].
Viscosity, polymer concertation and polymer molecular weight	Low polymer solution concentrations result in low viscosity of solutions and tend to form beaded nanofibers when electrospun. Increasing the polymer solution concentration reduces the formation of beaded fibers. Fiber diameters increase with increasing concentration/viscosity. Varying the concentration of polymer solution affects polymer fiber morphology, however, at a very high polymer solution concentration, charged solutions dry out at the tip of the needle hence preventing electrospinning [123]. Polymer molecular weight also determines the morphology of fibers, most polymers with low molecular weight result in beaded fibers [135, 136].
Solution conductivity	Increasing polymer solution conductivity can produce more uniform nanofibers with fewer beads. A simple approach to increasing polymer solution conductivity is the use of alcohols as dissolution solvents [123].
Ambient parameters	Ambient conditions such as a change in temperature and humidity during the polymer electrospinning process do affect nanofibers morphology and diameter [123]. Reneker *et al.* 1999 electrospun polymer solutions under vacuum and the fibers produced under this condition gave rise to large diameters [139].

1.7 Significance of the study

PGMs are known to be the most expensive, rare, and highly in demand. PGMs play a significant role in the environment and human health. They also play a vital role in the removal of air pollutants such as toxic gases from the vehicle's engine upon combustion, namely, carbon monoxide, nitro-oxides, hydrocarbons and sulfur oxides. However, finding these metals from the mining industry is becoming more and more difficult as the supply is decreasing, whereas their demand is increasing. South Africa is the largest supplier of PGMs in the world, hence, it is very important to find an effective way to recover PGMs in highest purity to provide a platform for South Africa to sustainably produce these metals. Therefore, efficient extraction and separation procedures for iridium and rhodium are essential for the recovery of these metals with high purity. Hence, the research seeks to improve the selectivity, extraction, separation and higher loading capacity of iridium and rhodium.

The thesis focuses on quaternized diammonium derivatives with electron donating and electron withdrawing groups hosted on nanofibers for the selectivity of iridium(IV) *via* ion exchange. These diammonium derivatives are employed to improve the loading capacity and for better separation for iridium. *Bis*-benzimidazole derivatives hosted on nanofibers were prepared for recovery of rhodium(III) *via* the inner sphere coordination mechanism. Both studies follow a combined theoretical and experimental approach.

1.8 Aims and objectives

The aim of this project is divided into two parts:

(1) To design the rhodium(III) specific ligands based on *bis*-benzimidazole derivatives.

(2) To develop the iridium(IV)-specific quaternary diammonium cations by incorporating electron donating and electron withdrawing groups.

To achieve the abovementioned aims, the following research objectives were outlined:

1.8.1 Rhodium(III) study

(i) To fabricate a chelating material (nanofibers) functionalized with *bis*-benzimidazoles derivatives namely; *bis*((1*H*-benzimidazol-2-yl)methyl)amine (NNN1), *bis*((1*H*-benzimidazol-2-yl)ethyl)amine (NNN2), *bis*((1*H*-benzimidazol-2-yl)methyl)sulfide (NSN1), *bis*((1*H*-benzimidazol-2-yl)ethyl)sulfide (NSN2).

(ii) The designed materials are directed towards achieving a higher loading capacity and better separation of rhodium from a mixture of PGMs, i.e. for maximum uptake of $RhCl_3(H_2O)_3$ species and poor uptake of Ir(III), Pd(II), Pt(II) and Ni(II) species in a column experiment.

(iii) To study the adsorption kinetics of $RhCl_3(H_2O)_3$ on the functional materials through batch experiments. The kinetics was described using pseudo-first-order and pseudo-second-order models. The adsorption mode was also investigated by Langmuir and Freundlich isotherms.

(iv) To study the underlying chemistry using computational methods (DFT) to investigate the complexation between *mer* and *fac* isomers of $[RhCl_3(H_2O)]_3$ and the *bis*-benzimidazoles ligands.

1.8.2 Iridium(IV) study

(i) By fabricating anion exchange material (nanofibers) functionalised with 1,10-diaminodecane (DMDA) and quaternized with electron donating groups (benzyl (F-QuatDMDABnz) and methylbenzyl (F-QuatDMDAMeBnz) and electron withdrawing groups (nitrobenzyl (F-QuatDMDANO2Bnz) and triflouromethylbenzyl (F-QuatDMDACF3Bnz)).

(ii) The effect of the electron donating and withdrawing was investigated. The designed materials are directed towards improving the loading capacities and for better separation of iridium from rhodium, i.e. for maximum uptake of $[IrCl_6]^{2-}$ and poor uptake of $[RhCl_5(H_2O)]^{2-}$ in a column experiment.

(iii) To study the adsorption kinetics of $[RhCl_5(H_2O)]^{2-}$and $[IrCl_6]^{2-}$ on the functional materials through batch experiments. The kinetics was described using pseudo first order and pseudo-second-order models. The adsorption mode was also investigated by Langmuir and Freundlich isotherms.

(iv) To study the underlying chemistry in the separation chemistry using computational methods (DFT) to investigate the interaction of the cations and the anionic chlorido species of rhodium(III) and iridium(IV) (anion-cation interactions).

1.9 Thesis outline

This section provides a short summary of what is covered in each chapter in accomplishing the aims and objectives of the study. This study is aimed at the design of reagents that are specific in recovering iridium(IV) *via* ion exchange and rhodium(III) *via* inner sphere coordination.

Chapter 1 contains the introduction that covers the research background and literature review which gives an understanding of the study based on the iridium and rhodium chemistry. Separation techniques and extractants employed in the recovery of iridium and rhodium are discussed. In addition, it introduces the use of functional support material (nanofibers) for the selectivity of iridium and rhodium. The main problem that captivated the undertaking of this research is discussed. The aims and objectives to be carried out to address the problems are also listed.

Chapter 2 contains the materials, experimental techniques and methods section in the form of general reagents used, and list of the instrumentation and general experimental procedures. For this study the following instruments were utilized in the study, namely FT-IR SPECTROSCOPY, NMR (nuclear magnetic resonance) spectrometer, thermogravimetric analyser (TGA), scanning electron microscope (SEM), X-ray diffractometer (XRD), Brunauer-Emmett-Teller (BET) surface area analyser, and inductively coupled plasma-optical emission spectrophotometer (ICP-OES).

Chapter 3 focuses on the separation of rhodium(III) over other PGMs using nanofibers functionalized with *bis*-benzimidazole derivatives as chelating ligands.

Chapter 4 focuses on the selectivity of iridium(IV) over rhodium(III) by improving the loading capacity using nanofibers functionalized with diammonium cations that are quaternized with electron donating and electron withdrawing benzyl groups. These cationic extractants are expected to function *via* ion exchange.

Chapter 5 contains the conclusions, recommendations and future works of the study.

Chapter 2: Materials, experimental methods and techniques

2.1 General reagents

The chemicals used for this study are presented in Table 2.1 and were used as received.

Table 2.1: Specialized chemicals employed in this study.

Chemical name	Purity (%)	Supplier
1,10-Diaminodecane	97	Sigma-Aldrich
Benzyl bromide	98	Sigma-Aldrich
3-Triflouromethylchloride	97	Sigma-Aldrich
4-Nitrobenzylchloride	99	Sigma-Aldrich
4-Methylbenzylchloride	98	Sigma-Aldrich
2,6-Lutidine	98	Sigma-Aldrich
Iridium(III) chloride hydrate	98	Sigma-Aldrich
Rhodium(III) chloride hydrate	98	Sigma-Aldrich
Platinum(IV) chloride	96	Sigma-Aldrich
Palladium(II) chloride	99	Sigma-Aldrich
Nickel(II) chloride	98	Merck
Hydrochloric acid	32	Sigma-Aldrich
Sodium hydroxide	98	Merck
Chloroform	99	Merck
Ethanol	99	Merck
4-Vinylbenzylchloride	90	Sigma-Aldrich
Dimethylformamide	99	Merck
Tetrahydrofuran	99	Merck
Ferric chloride	99	Merck
Sodium metabisulfite	98	Merck
2,2'-Iminodiacetic acid	98	Sigma-Aldrich
3,3'-Iminodipropionitrile	97	Sigma-Aldrich
2,2'-Thiodipropionic acid	97	Riedel-De Haen AG Seelze-Hannover
3,3'- Thiodipropionic acid	98	Fluka

2.2 ICP-OES standards

Calibrations for metal ions was done from a multi-element standard solution (platinum, palladium, iridium and rhodium) that was prepared from 100 ppm of respective metal solutions: 10 ppm in 10% HCl and 1% HNO_3 from Perkin Elmer. Nickel 10 ppm standard solution (in the multi-element standards) was prepared from 1000 ppm standard solution in 0.5 M HNO_3 from Merck. Calibration was performed using six standards typically; 0.1 mg/L, 0.5 mg/L, 1 mg/L, 2 mg/L, 3 mg/L and 4 mg/L. The standards were prepared by appropriate dilution of the 10 mg/L stock solution.

2.3 Instrumentation and general experimental procedures

2.3.1 FT-IR spectroscopy

The infrared spectra were recorded on a Perkin Elmer 2000 FT-IR Spectrometer using KBr discs or as neat compounds on a Perkin Elmer 100 ATR-IR (4000-650 cm^{-1}).

2.3.2 NMR spectroscopy

The structures of all ligands were determined by ^{1}H NMR spectroscopy on a Bruker AMX 400 MHz NMR spectrometer and reported relative to tetramethylsilane (TMS) δ 0.00.

2.3.3 UV-Vis spectrophotometer

Speciation analysis of iridium(IV) and rhodium(III) chlorido species were conducted on a Perkin Elmer UV-Vis spectrophotometer Lamba 12 series with 1 cm quartz cells,

respectively. Scans were conducted over 200-800 nm wavelength range, using a 2.0 nm slit width at medium speed. The reference or blank was prepared using the relevant HCl concentration.

Absorption in the ultraviolet and visible regions results in molecules undergoing electronic transitions. The absorbance is measured, and the concentration of the analyte is related to the signal by the Beer-Lambert law. The Beer-Lambert equation is expressed as follows:

$$A = \varepsilon bc$$

where A, ε, b and c are the absorption, molar absorptivity (a constant which is characteristic of the absorbing species at a specific wavelength), the path length of the sample and the concentration, respectively. The absorption is therefore directly proportional to concentration for a given set of instrumental conditions [140].

2.3.4 Inductively coupled plasma – Optical emission spectroscopy

The iridium, rhodium, platinum, palladium and nickel containing samples were determined using a Perkin Elmer (Avio 200) Inductively Coupled Plasma (ICP) spectrometer equipped with an Optical Emission Spectrometer (OES) as the detector. The following wavelengths were chosen for iridium detection (224.268 nm), rhodium (343.489 nm), platinum (299.797 nm), palladium (340.458 nm) and nickel (341.476 nm). These wavelengths were the most sensitive and had minimal interferences. Three runs were performed at each wavelength. Additional operating parameters have been listed in Table 2.2. All solutions were filtered through 0.45 µM Millipore® filters

to prevent nebulizer blockages. 20 µl of column study sample and 50 µl batch study samples solutions were then diluted with Millipore water to 10 mL and 15 ml respectively, filtered with 0.45 µM filters and analysed using ICP-OES. Prior to the iridium, rhodium, platinum, palladium and nickel analysis, standard samples of known iridium, rhodium, platinum, palladium and nickel concentrations were run as calibration.

Table 2.2: ICP-OES method and operating parameters.

Parameter	**Setting**
Plasma Ar gas flow rate	8 $L.min^{-1}$
Auxiliary Ar gas flow rate	0.2 $L.min^{-1}$
Nebulizer Ar gas flow rate	0.7 $L.min^{-1}$
Sampling depth	8.5 mm
Pump rate	100 rpm
N_2 addition flow rate	1.0 $L.min^{-1}$
Cooled spraying chamber temperature	4°C
Selected wavelengths: Iridium Rhodium Platinum Palladium Nickel	 224.268 nm 343.489 nm 299.797 nm 340.458 nm 341.476 nm
Sample flush time	30 s
Points per peak	3
Time scan acquisition	50 ms/point
RF power	1500 Watts

2.3.5 Elemental analysis

To gain an understanding of the chemical composition of the synthesized compounds and sorbent materials, elemental analysis was performed to reveal the percentage of

C, H, and N using a Vario Elementary ELIII Microcube CHNS analyser. Calibration of the instrument was done with the use of the following standards in a linear curve adjustment within the total working range.

Standard 1: Sulfanamide; C, 41.81; H, 4.65; N, 16.25 and S; 18.62%

Standard 2: Acetanilide; C, 71.09; H, 0.67; N, 10.36 and O; 12.0%

The basic principle of quantitative CHNOS analysis is high-temperature combustion of organic and many inorganic solid or liquid samples. The gaseous combustion products are purified, separated into their various components and analysed with a suitable detector such as thermal conductivity detector (TCD), an optional infrared detector (IR) for sulfur, etc [141].

2.3.6 Thermogravimetric analysis

Thermogravimetric analysis was performed using a Perkin-Elmer TGA 7 thermogravimetric analyser (TGA). Typically, the samples were heated at a rate of 10 °C.min^{-1} under a constant stream of nitrogen gas. The temperature range differed depending on the sample used. The samples were contained in platinum pans. The onset of decomposition or mass loss (T_{onset}) was determined from the normal TG-curve.

2.3.7 Scanning electron microscopy (SEM) and X-ray energy dispersive spectroscopy (EDS)

Samples were prepared for scanning electron microscopy (SEM) by coating them in gold using a Balzers' Spluttering device. The samples were imaged using a TESCAN Vega TS 5136LM typically operated at 20 kV at a working distance of 20 mm. Elemental analysis of samples using energy dispersive spectroscopy (EDS) was determined by using the same procedure as described for SEM analysis, except that no sample surface coating was needed. Before images were taken; the nanofibers were coated with gold to prevent surface charging and to protect the surface material from thermal damage by the electron beam.

2.3.8 Brunauer-Emmett-Teller (BET) surface area analysis

Adsorption/desorption isotherms were measured using a Micromeritics TriStar II 3020 3.02, Surface Area and Porosity Analyzer. Prior to each measurement, samples were degassed for a minimum of one week to ensure complete removal of adsorbed impurities. Degassing was performed at 70°C for all nanofibers. Approximately 0.2 g of sample was used, and an equilibration interval of 30 seconds was allowed during the run. The surface area (BET), total pore volume and pore size distribution (BJH method) were calculated from the BET isotherms.

2.3.9 X-ray crystallography

X-ray diffraction studies were performed at 200 K using a Bruker Kappa Apex II diffractometer with a monochromated Mo Kα radiation (λ = 0.71073 Å). The crystal

structures were solved by direct methods using SHELXTL.157 All non-hydrogen atoms were refined anisotropically. Carbon-bound hydrogens were placed in calculated positions and refined as riding atoms with bond lengths 0.95 (aromatic CH), 0.99 (CH_2), and 0.98 (CH_3) Å and with $U_{iso}(H) = 1.2$ (1.5 for methyl) U_{eq} (C). Hydrogens bonded to nitrogen were located on a Fourier map and allowed to refine freely. Hydrogens on the water were restrained to an O–H bond length of 0.84 Å and H–O–H angle of 110°. Diagrams and publication material were generated using SHELXTL, and ORTEP-3 [142].

2.3.10 Lab Shaker

The Labcon microprocessor controlled orbital platform shaker model SPO-MP 15 was used for contacting the metal ions and the sorbents.

2.3.11 Melting point

The melting points of the quaternary diammonium chloride salts were determined with the Stuart Measuring Point SMP30 from Lasec.

2.3.12 Column

A custom-made glass column with the following dimensions was used for the column (dynamic) studies; 10 cm length, the internal diameter of 3.5 mm and a tip diameter of 1 mm.

2.4 Adsorption equilibrium studies

The adsorption isotherm was studied under batch conditions. These provide information which indicates how the metal ions interact with the sorbent, i.e. how the ions distribute between the liquid phase and solid phase when the adsorption process reaches an equilibrium state. Langmuir and Freundlich's isotherms were used to describe the equilibrium characteristics of adsorption.

2.4.1 Adsorption dynamics for $[IrCl_6]^{2-}$ and $[RhCl_5(H_2O)]^{2-}$

The amount of adsorption at equilibrium (q_e, mg/g) of the complex species was calculated using equation 2.1, and metal ion uptake was calculated using equation 2.2 [143].

$$q_e = \frac{(C_0 - C_e) \times V}{W} \qquad (2.1)$$

where C_o is the initial metal concentration (mg/mL), C_e is the equilibrium metal concentration (mg/mL), V being the volume of the metal solution (mL) and W is the mass of the sorbent (g).

$$\text{Adsorption } (\%) = \frac{C_0 - C_e}{C_0} \times 100 \qquad (2.2)$$

2.4.2 Langmuir isotherm

The Langmuir adsorption model assumes that the maximum adsorption corresponds to a saturated monolayer of metal ions on the sorbent surface. Thus, adsorption occurs

uniformly on the active sites of the sorbent and once metal ions occupy the sites, no further adsorption will take place at the site [144–148]. The linear form of Langmuir isotherm is express as in equation 2.3.

$$\frac{C_e}{Q_e} = \frac{C_e}{Q_o} + \frac{1}{bQ_o} \qquad (2.3)$$

Thus, Q_e is the amount of metal ions loading capacity per unit weight of sorbent (mg/g) and C_e is the equilibrium concentration of metal ion in solution (mg/L). The Langmuir constant Q_0 signifies the adsorption capacity (mg/g) and b is related to the energy of the adsorption (L/mg). A plot of $\frac{C_e}{q_e}$ versus C_e yields a straight line with slope $\frac{1}{Q_0}$ and intercept$\frac{1}{Q_0 b}$. The Langmuir isotherm can be expressed in terms of dimensionless constant separation factor (R_L), which is given by equation (2.4) [149].

$$R_L = \frac{1}{1 + bC_o} \qquad (2.4)$$

R_L, indicates the isotherm slope according to the following assumption characteristics R_L > 1 is unfavourable, R_L = 1 is linear adsorption, 0 < R_L < 1 is favourable. C_0 is the concentration of each metal solution and b is the Langmuir constant [145–148].

2.4.3 Freundlich isotherm

The well-known Freundlich isotherm used for adsorption is a special case for heterogeneous surface energy in which the energy term in the Langmuir equation

varies as a function of surface coverage strictly due to the variation of the sorption. The Freundlich equation is given in equation 2.5.

$$\text{Log}\, q_e = \log\, k_f + \frac{1}{n} \log\, C_e \qquad (2.5)$$

Thus, k_f can be defined as the distribution coefficient and represents the quantity of metal ion adsorbed onto the sorbent at equilibrium. The slope $\frac{1}{n}$, ranging between 0 and 1, is a measure of adsorption intensity or surface heterogeneity, becoming more heterogeneous as its value gets closer to zero. K_f and $\frac{1}{n}$ can be determined from a linear plot of log q_e versus log C_e. The magnitude of the exponent $\frac{1}{n}$ gives an indication of the favourability of adsorption. C_e and q_e are equilibrium concentration and adsorption capacity at equilibrium stage [145, 146].

2.5 Adsorption kinetics studies

The kinetics of the adsorption process was studied by carrying out a set of adsorption experiments at constant temperature and monitoring the amount adsorbed with time. Two simplified kinetic models, i.e. pseudo-first-order and pseudo-second-order, were used to investigate the adsorption mechanisms using equations 2.3, 2.4 and 2.5, respectively.

2.5.1 Pseudo 1st order kinetics

The Lagergren rate equation, which is the first-rate equation developed for sorption in a liquid/solid system. The pseudo-first-order equation is represented by equation 2.6.

$$\log\ (q_e - q_t) = \log q_e - \frac{k_1}{2.303}\ t \qquad (2.6)$$

Thus, q_e and q_t are the amount of metal ions adsorbed on the sorbent at equilibrium and at time t, respectively (mg/g). The slope of the plot of log $q_e - q_t$ versus t (min) was used to determine the pseudo-first-order rate constant k_1 (h^{-1}) [149–151].

2.5.2 Pseudo 2nd order kinetics

The pseudo-second-order model can be represented as in equation 2.7.

$$\frac{t}{q_t} = \frac{1}{k_2 q_e^2} + \frac{1}{q_e} t \qquad (2.7)$$

Thus, k_2 (g/mg.min) is the rate constant of pseudo-second-order adsorption, If the pseudo-second-order is applicable, the plot $\frac{t}{q_t}$ versus t shows a linear relationship. q_e and k_2 can be determined from the slope and intercept of the plot [150, 151].

2.6 Computational studies

All the calculations were carried out using Gaussian 09 (revision E.01) [152–154]. The molecular interaction between metal complexes and various compounds were investigated using density functional theory (DFT). These were optimized using the

Becke's Three-Parameter Hybrid Functional using the Lee-Yang-Parr correlation functional theory (B3LYP) [155–158] and the SDD basis set, which was chosen considering the relativistic effect into account, which is especially important when dealing with a system containing transition metals. DFT/B3LYP is highly recommended for the understanding of thermodynamics data, chemical and selectivity parameters known as the electronic structure identifiers. These are parameters used to identify the structure and these are derived from molecular modelling calculations such as HOMO energy (EHOMO), LUMO energy (ELUMO), electron affinity (*I*), ionization potential (*A*). hardness (η), softness (σ) and electronegativity (χ). According to Koopman's theorem [157], the ionization energy (*I*) and the electron affinity (*A*) can be obtained as the negative values of the highest occupied molecular orbital energy (E_{HOMO}) and lowest unoccupied molecular orbital energy (E_{LUMO}), respectively.

$$I = -E_{HOMO} \quad (2.8)$$

$$A = -E_{LUMO} \quad (2.9)$$

Based on the finite difference approximation of Pearson and Parr [158], approximate values the chemical potential, electronegativity [159], and chemical hardness [160] structural identifiers can be calculated *via* the following equations:

$$\chi = -\mu = \frac{I+A}{2} \quad (2.10)$$

$$\eta = \frac{I-A}{2} \quad (2.11)$$

The softness, which is the inverse of the hardness, measures the polarization of the electron cloud of a chemical species [161], and is obtained as follows:

$$\sigma = \frac{1}{\eta} \qquad (2.12)$$

The thermodynamic parameter, Gibbs free energy of formation ((ΔG_F), was calculated in (Kcal/mol)). DFT molecular modelling was used to calculate the energy minima for various adducts formed between various compounds and metal complexes. Gibbs free energy of formation was calculated as shown in equation 2.13. Gibbs free energy is useful to characterise the complexation process and to derive trends of preferred interactions. Gibbs free energy of formation of a substance is the difference between the free energy of the products and the free energies of the reactants in their thermodynamically most stable states. When ΔG^o is negative the reaction is possibly favourable or spontaneous [162].

$$\Delta G^o_F = \Sigma \Delta G^o_P - \Sigma \Delta G^o_{M+L} \qquad (2.13)$$

Where F is for complex formation, P for product (complex), M+L for metal (anion) and ligand (or cation).

Chapter 3: Extraction of PGMs using tridentate *bis*-benzimidazole-based ligands hosted on polymer nanofibers

3.1 Introduction

There is an increasing demand for platinum group metals (PGMs), such as palladium, platinum, rhodium and iridium. This has been observed because of their wide range of industrial applications, e.g. as catalysts in organic processes, value-added components in metal alloys and vehicle catalytic converter systems, in chemical, pharmaceutical, petroleum, electronic industries and jewellery making. These applications of PGMs have increased the demand for these metals, whereas the natural resources are limited [162–164]. Hence, the gap between the demand and supply from natural sources must be replaced by the recycling of spent materials, especially spent vehicle catalytic converters. Metals that might be present in catalytic converters are Ru, Os, Se, Cu, Fe, Ni, Ce, Zr, La, Pb, Al and alkaline-earths [18, 165, 166]. These metals are known to improve stabilization of catalytic converters hence their presence cannot be avoided in the leach solutions of catalytic converters [165–168]. However, spent catalytic converters contain mostly Rh, Pt and Pd. The automobile industry consumes significant quantities of PGMs (Pd, Pt and Rh), and approximately about 34% of total platinum, 55% of total palladium, and 95% of total rhodium demand are used to produce automotive catalytic converters [8, 10, 169, 170].

Processes of separation and purification of PGMs are difficult and complicated due to their chemical properties and formation of many chemical species in chloride media.

Palladium and platinum have very similar chemical properties as so rhodium and iridium, hence these metals pairs are difficult to separate [171–173]. This thesis deals with extraction of rhodium from a mixture of platinum, palladium, iridium and nickel. Nickel metal ion was included in this study to observe the behaviour of the *bis*-benzimidazole derivatives in presence of a platinum group metals ions (Pt(II), Pd(II), Ir(III) and Rh(III)) and a base metal ion (Ni(II)). Nickel(II) metal ion is found to be one of the base metals that stabilizes the spent catalytic converter. Nickel was chosen as a metal ion that will be used to access the affinity of the *bis*-benzimidazole ligands to base metals in comparison to PGMs. Hence, the study focuses mainly on five metal ions (Pt(II), Pd(II), Ir(III), Rh(III) and Ni(II)) in dilute hydrochloric acid medium.

Palladium and platinum are members of the 4d and 5d transition metals series, respectively. The two metals have a high covalent character in their bonding and have kinetic stability of their complexes. Palladium and platinum are known to be soft metals compared to rhodium and iridium. Pt and Pd prefer soft donor ligands as opposed to hard donor ligands, i.e. σ donor ligands like aliphatic amines and ammonia but have a greater preference for π acceptor ligands like sulfur, arsenic and phosphorous donors. The divalent metal complexes are spin paired square planar d^8 systems, while tetravalent ions are spin-paired octahedral d^6 systems [171–176]. Rhodium and iridium commonly occur as very stable trivalent states. These metals are primarily found in the form of spin-paired (d^6), kinetically inert octahedral complexes, rendering the trivalent state very stable for both 4d and 5d transition metals, respectively. This study mainly focuses on the following metal ion oxidation states; Pt(II), Pd(II), Ir(III), Rh(III) and Ni(II). The separation of rhodium from platinum, palladium, and iridium will have

to be based on subtle metal ion differences. The major factor would be the kinetics and thermodynamics of the substitution reaction at the metal centres.

In this study, the application of tridentate *bis*-benzimidazole ligands containing nitrogen (N) and/or sulphur (S) atoms have been explored. Application of tridentate *bis*-benzimidazole ligands has not been extensively explored as separating agents for PGMs. Nevertheless, aromatic nitrogenous ligands have a relative preference for metals that relate to σ and π bonding and are known to be highly reactive compounds [176]. The separation behaviour of chelating *bis*-benzimidazole derivatives has been studied herein (Figure 3.1). The differences in the activities of the ligands can be accounted for by the effect of N and S donor atoms and the effect of five or six-membered ring chelates. The rhodium(III) extraction over iridium(III), palladium(II), platinum(II) and nickel(III) using *bis*-benzimidazole ligands (Figure 3.1): *bis*((1*H*-benzimidazol-2-yl)methyl)amine (NNN1), *bis*((1*H*-benzimidazol-2-yl)ethyl)amine (NNN2), *bis*((1*H*-benzimidazol-2-yl)methyl)sulfide (NSN1), *bis*((1*H*-benzimidazol-2-yl)ethyl)sulfide (NSN2) hosted on nanofibers, in 0.5 M HCl media, was investigated.

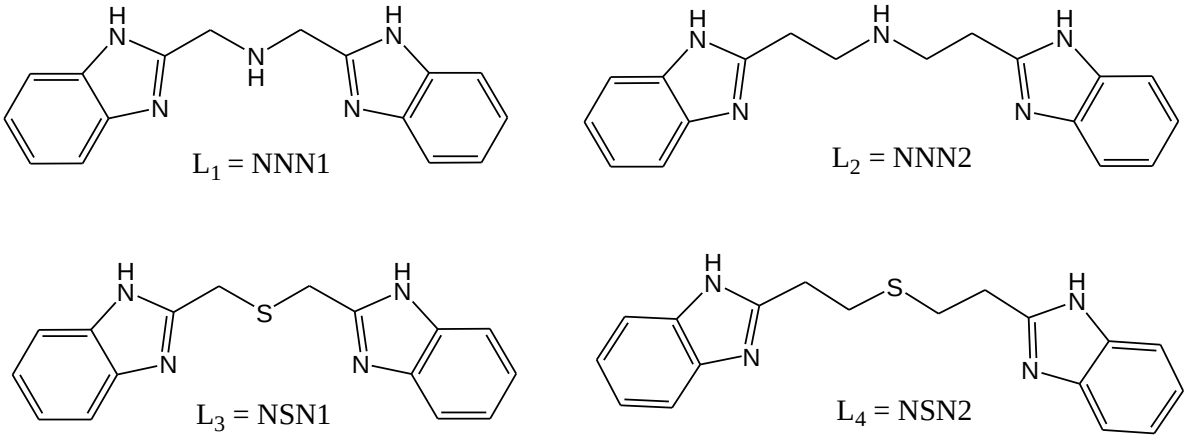

Figure 3.1: Chemical structures of tridentate *bis*-benzimidazole derivatives.

3.2 Experimental

3.2.1 Preparation of *bis*-benzimidazole derivatives

The synthesis of L_1 - L_4 was carried out using the starting materials as shown in Scheme 3.1 [181–183]. A mixture of 2,2'-iminodiacetic acid (5.0 g, 0.0376 mol) (for L_1) or 3,3'-iminodipropionitrile (5.0 g, 0.0406 mol) (for L_2) or 2,2'-thiodipropionic (5.0 g, 0.0333 mol) (for L_3) or 3,3'-thiodipropionic acid (5.0 g, 0.0284 mol) (for L_4) and *o*-phenylenediamine (10.0 g, 0.0930 mol) was added in 4 M aqueous HCl (250 mL). The resulting solution was refluxed for 24 hrs, followed by cooling the solution in ice. As the solution was cooled, a precipitate formed and was filtered. The precipitates were identified as dihydrochlorides ($L{\cdot}2HCl$) for L_3 and L_4 or trihydrochlorides ($L{\cdot}3HCl$) for L_1 and L_2. The free base ligands were obtained by treatment of the hydrochloride ligands with excess aqueous ammonia. A precipitate was obtained, filtered and dissolved in ethanol and decolourized with charcoal. The solution was filtered and concentrated to obtain a final product: light brown (L_1 and L_3), pale purple (L_2) and white (L_4).

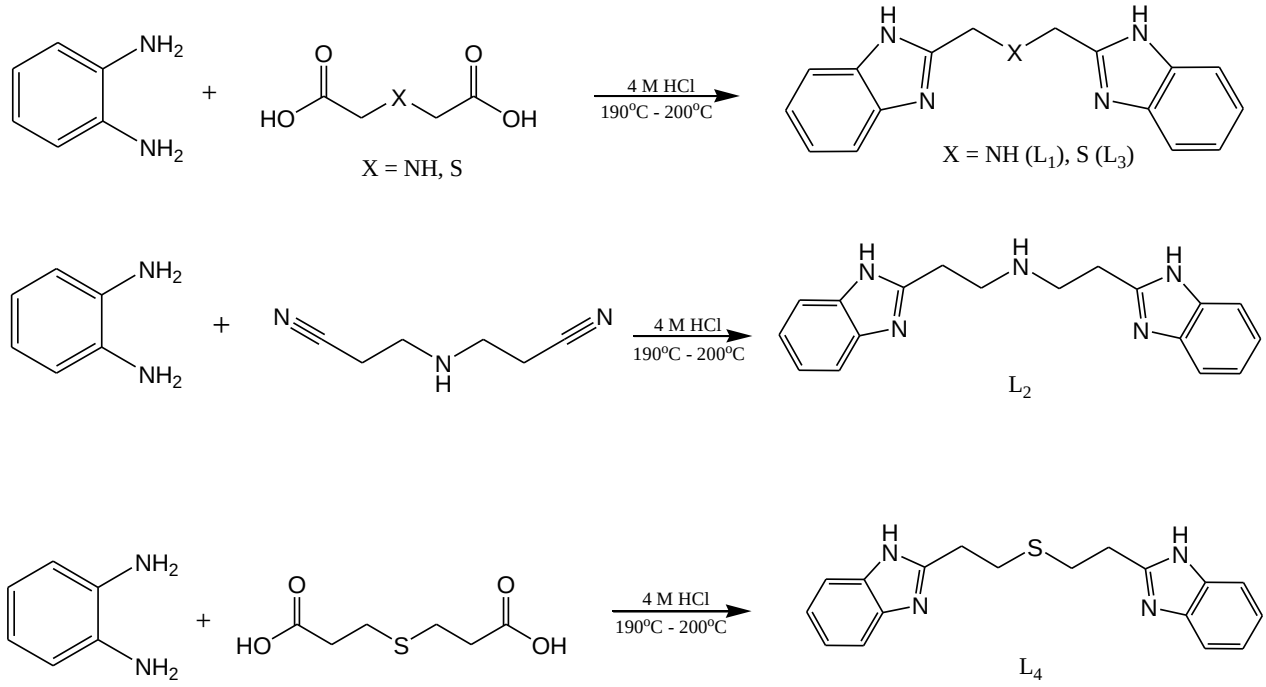

Scheme 3.1: Synthesis of *bis*-benzimidazole derivatives. L_1 = NNN1, L_2 = NNN2, L_3 = NSN1 and L_4 = NSN2.

3.2.2 Fabrication of nanofibers

3.2.2.1 Preparation polyvinylbenzylchloride (PVBC)

4-Vinylbenzylchloride (5.0 mL) and azobisisobutyronitrile (AIBN) (0.04 g) as the initiator (Scheme 3.2) were stirred at room temperature to form a homogeneous mixture. The mixture was heated under argon at 70°C overnight with no stirring. The solid polymer obtained was washed several times with THF, precipitated with methanol, filtered and air dried [140, 183].

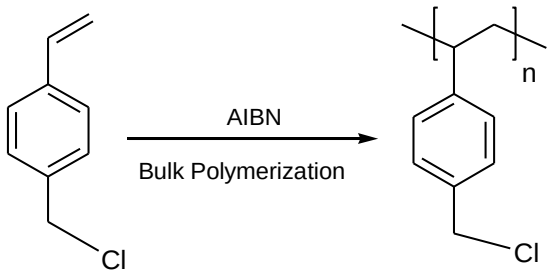

Scheme 3. 2: Scheme for the polymerisation of 4-vinylbenzylchloride.

3.2.2.2 Electrospinning

A 40% solution (wt/v%) of the poly(vinylbenzylchloride) was prepared in a DMF:THF (1:1) solvent mixture. The polymer solution was stirred for 1 hour at room temperature to ensure complete dissolution and then loaded into a 20 mL syringe with an internal needle diameter of 1 mm. The syringe was loaded onto a programmable syringe pump model No. NE-1010 (new era pump system). The applied electrical voltage, working distance (the distance between the needle tip and the collection plate) and flow rate were respectively fixed at 25 kV, 15 cm and 0.3 mL/h. Dry nanofibers were accumulated on the surface of an aluminium foil and collected as a fibrous web.

3.2.2.3 Functionalization of nanofibers

The PVBC nanofibers were functionalized with NNN1, NNN2, NSN1 and NSN2, respectively, using methanol as a solvent while being shaken for 7 days at 120 rpm on a shaker. The functionalization step was carried out as described by Okewole *et al*. (2013) (Scheme 3.3) [180]. The fibers were then collected, washed with ethanol and dried in air. The nitrogen content (%) was determined by microanalysis.

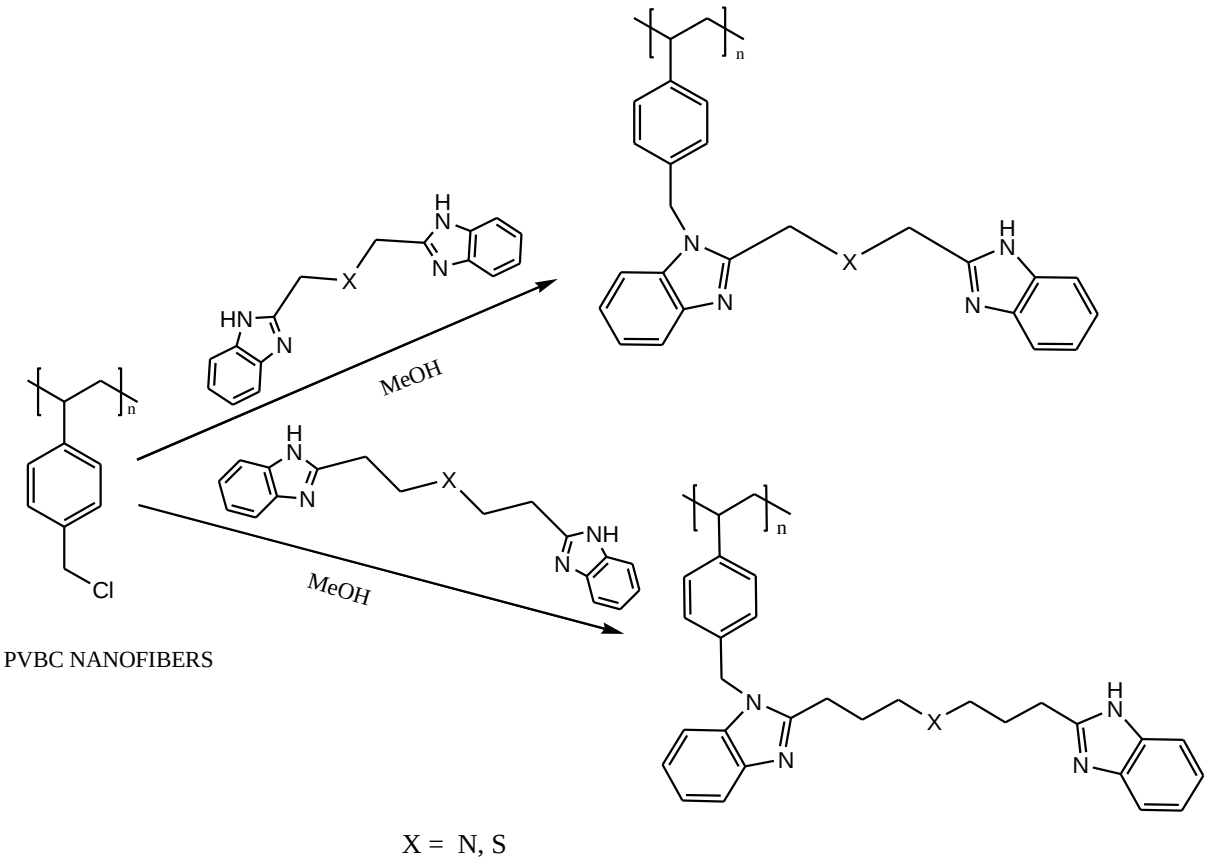

Scheme 3.3: A generalization of the functionalization of PVBC nanofibers with *bis*-benzimidazole derivatives (NNN1, NNN2, NSN1 and NSN2) to form PVB-L.

3.2.3 Preparation of metal stock solutions

3.2.3.1 Rhodium solution

The rhodium starting material was obtained as black solid rhodium(III) chloride salt ($RhCl_3$). 0.47 g of the salt was weighed and 50 mL of 0.5 M HCl was added. The solution was heated to reflux for an hour at 70°C and a dark red solution was obtained [181].

3.2.3.2 Multi-element solution

A mixture of Rh(III), Ir(III), Pt(II), Pd(II) and Ni(II) multi-element solution, was prepared by making concentrations of Rh (0.02 M), and 0.01 M for Ir, Pt, Pd and Ni respectively in 50 ml of 0.5 M HCl. The mixture was heated to reflux at 70°C for an hour and a light red solution was obtained.

3.2.4 Column study

3.2.4.1 Single element study

0.1 g of nanofiber was packed into a custom-made glass column. A small amount of glass-wool was placed at both ends to retain the sorbent in the column. MilliQ water (5 mL) and 0.5 M HCl (5 mL) were successively passed through the packed column for conditioning the sorbent materials. 2 mL of the rhodium solution was loaded onto the column. The solution was then allowed to flow using a previously optimized flow rate of 0.5 ml/hr [149, 151]. 5 mL of 0.5 M HCl was used to wash off the un-adsorbed metal complex. 0.5 M (5 mL) solution of aqueous sodium perchlorate in 5 M HCl solution was used to release ion-paired complexes, followed by stripping/elution step with 10 mL of 3% thiourea in 5 M HCl solution. The 0.5 mL fractions were collected throughout the process and finally diluted for ICP-OES analysis.

3.2.4.2 Multi-element study

2 mL of a multi-metal solution (Rh, Ir, Pt, Pd and Ni) was loaded onto a conditioned column as mentioned in Section 3.3.4.1. Thereafter, the un-adsorbed metal complex species were washed off the column using 0.5 M HCl, followed by a wash with 0.5 M

sodium perchlorate solution and then stripping/elution with 10 mL 3% thiourea in 5 M HCl. The 0.5 mL fractions were collected, diluted appropriately and analysed for the metal content by ICP-OES.

3.2.5 Adsorption studies

3.2.5.1 Adsorption kinetics

The binding kinetics were carried out in the range of 1-30 minutes of equilibration. A 0.1 g of fibers were weighed and added into a beaker, and 10 mL of 0.5 M HCl solution was added. The mixture was shaken in a mechanical shaker for 1 minute up to 10 minutes and thereafter 20, 30 minutes to condition the material. 2 mL of multi-metal solution was added (0.02 M Rh and 0.01 M (Ir, Pd, Pt and Ni)), and the mixture was placed on a rotary shaker at an agitation speed of 120 rpm. 50 µl of aliquots were sampled at fixed time intervals from 1 minute to 30 minutes, diluted appropriately, filtered through a 0.45 µm pore size filter and analyzed by ICP-OES. Two simplified kinetic models, i.e. pseudo-first-order and pseudo-second-order, were tested to investigate the adsorption kinetics.

3.2.5.2 Adsorption isotherms

The studies were carried out at 25˚C using 0.1 g of nanofiber with shaking in a beaker for 5 minutes using the concentration range of 200 to 2000 ppm for Rh, Ir, Pd, Pt and Ni. An adsorption isothermal study was carried out on two well-known isotherms, namely, Langmuir and Freundlich adsorption isotherm, represented by equations in Chapter 2 (Section 2.4).

3.2.6 Computational modelling

DFT calculation protocols are presented in Chapter 2, Section 2.6.

3.3 Results and Discussion

3.3.1 DFT calculations

Theoretical investigations utilizing density functional theory (DFT) has been carried out in this study to explore the structural behaviour of *bis*-benzimidazole derivatives (NNN1, NNN2, NSN1 and NSN2) with respect to their effectiveness in selectivity for rhodium through coordination chemistry. The rhodium species of interest are *mer*-[$RhCl_3(H_2O)_3$] and *fac*-[$RhCl_3(H_2O)_3$] in 0.5 M HCl. The chemical properties and behaviour of *bis*-benzimidazoles were investigated before and after interaction with rhodium species using a hybrid method B3LYP and SDD basis set. The calculated results of the molecular structures were mainly based on the thermodynamic data and chemical parameters such as highest occupied molecular orbital energy (HOMO (E_H)) and lowest unoccupied molecular orbital energy (LUMO (E_L)), band gap energy (HOMO-LUMO (E_G)), hardness (η), softness (σ) and electronegativity (χ). The energies of HOMO, LUMO, HOMO-LUMO gap energies were converted from a.u to eV using the conversion factor of 27.2114.

3.3.1.1 HOMO and LUMO

For the metal ion species, *mer*-[$RhCl_3(H_2O)_3$] and *fac*-[$RhCl_3(H_2O)_3$], the HOMO positions originated around the metal ions and chlorides while the LUMO positions originated around the metal ions, chlorides and oxygens on the waters (Figure 3.2).

The ligands (L) indicated that the HOMO positions originated around one benzimidazole for NNN1, for NNN2 around one benzimidazole, methylene and amine, and for NSN1 and NSN2 it originated around the entire ligand (Figure 3.3). The LUMO positions on the ligands originated around one benzimidazole for NNN1 and NNN2, for NSN1 around the entire ligand and for NSN2 it originated around one benzimidazole, methylene and sulfur. This clearly showed that the interactions with *bis*-benzimidazole ligands and metal ion species are possible.

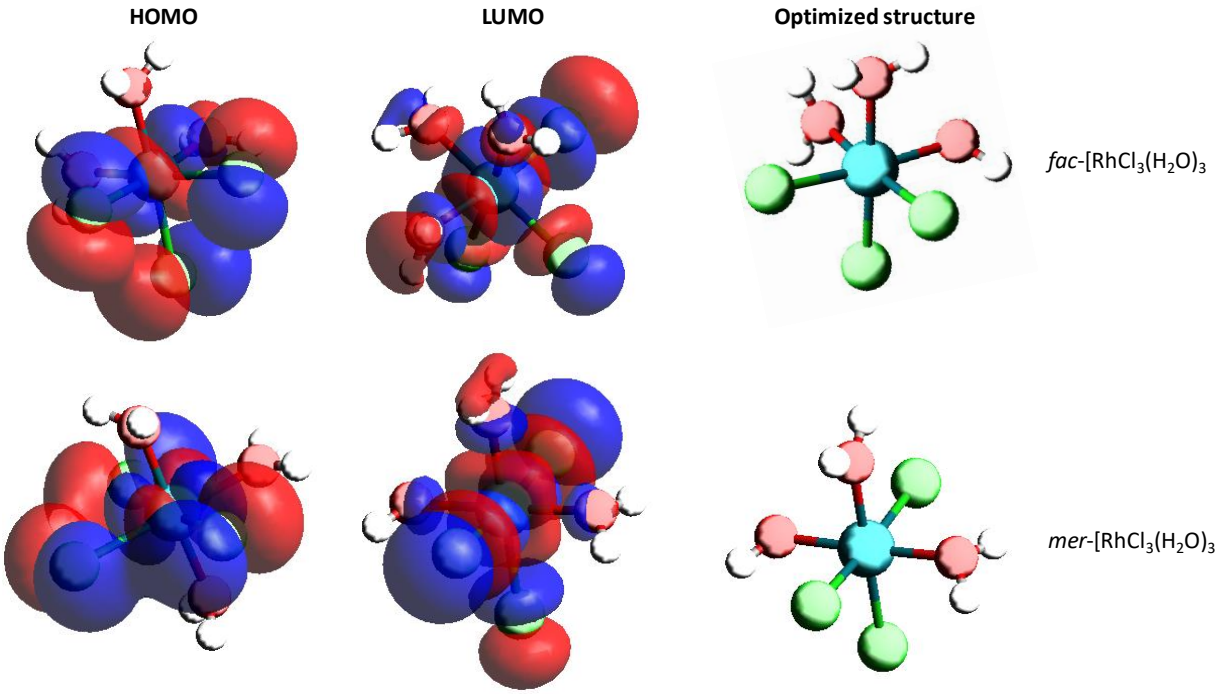

Figure 3.2: HOMO-LUMO of *fac*-[$RhCl_3(H_2O)_3$] and *mer*-[$RhCl_3(H_2O)_3$].

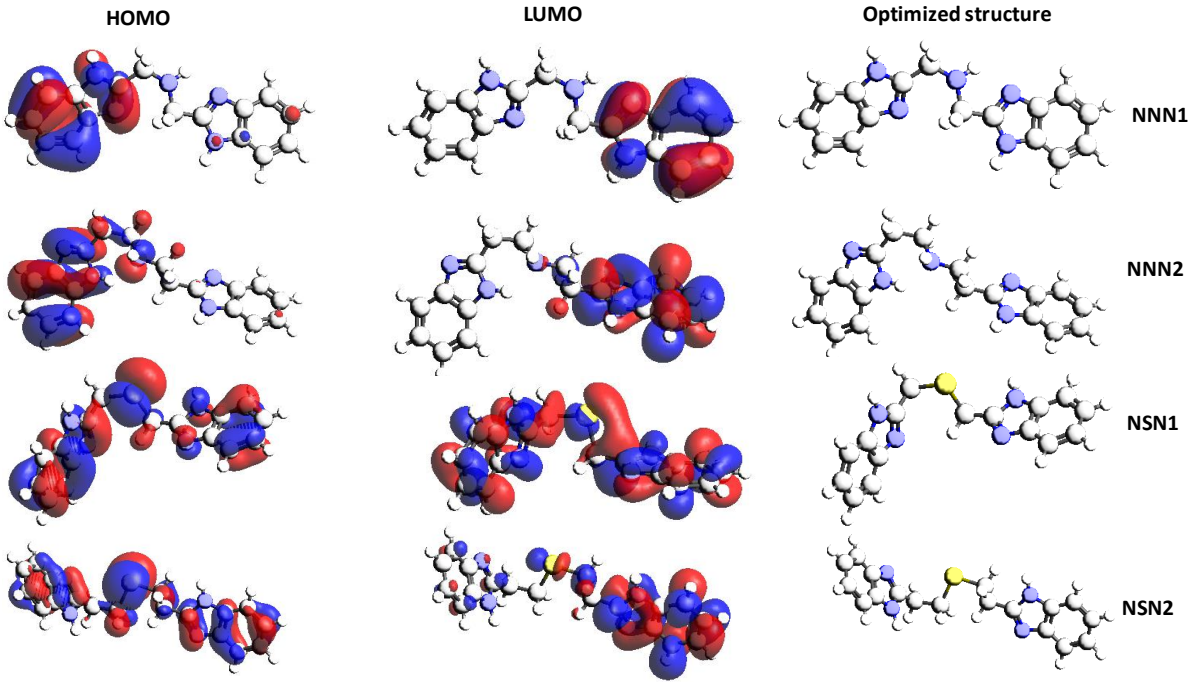

Figure 3.3: HOMO-LUMO of *bis*-benzimidazole derivatives (NNN1, NNN2, NSN1 and NSN2).

Adducts formed between NNN1, NNN2, NSN1 and NSN2 and metal ion species indicated that the HOMO positions originated around the ligands (benzimidazole) while the LUMO centres on the metal ions (Figures 3.4 and 3.5). This clearly showed that the interaction between the benzimidazole ligands and metal ions is possible through coordination. The mode of interactions between benzimidazole ligands with metal ion species was observed to be similar.

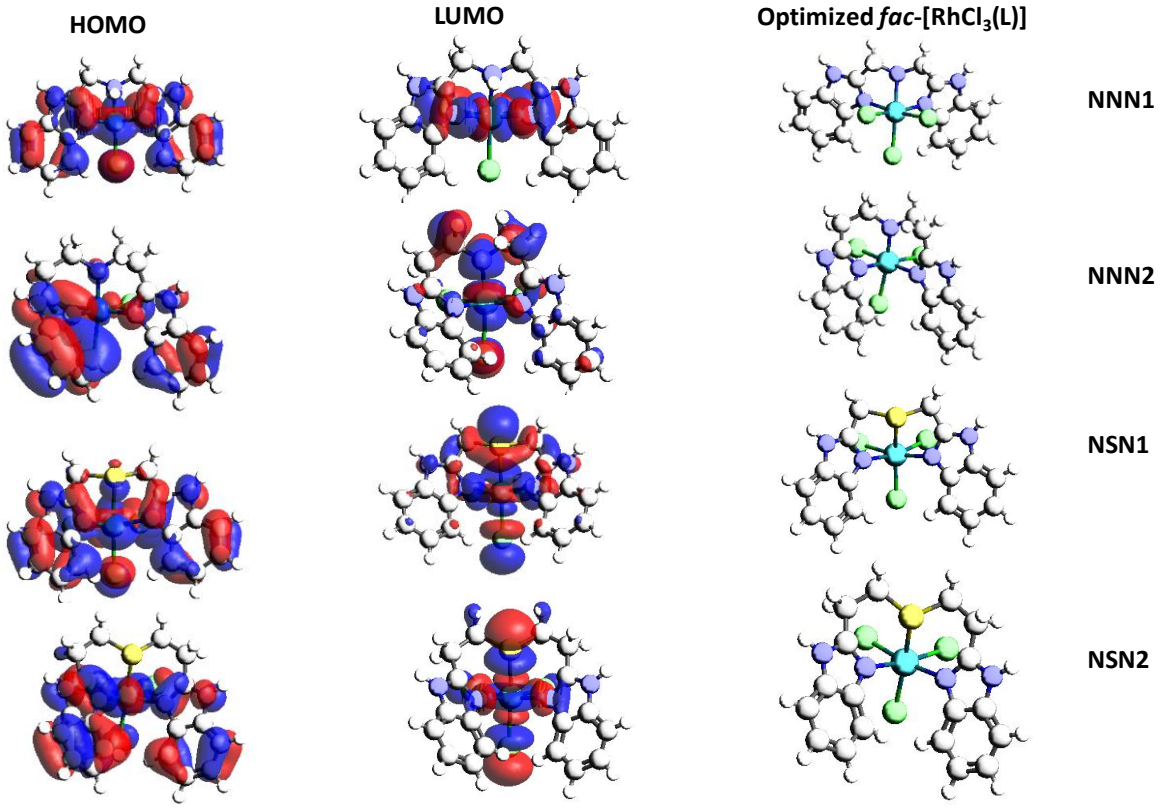

Figure 3.4: HOMO-LUMO of *fac*-[$RhCl_3(H_2O)_3$] complexes with *bis*-benzimidazole derivatives (NNN1, NNN2, NSN1 and NSN2).

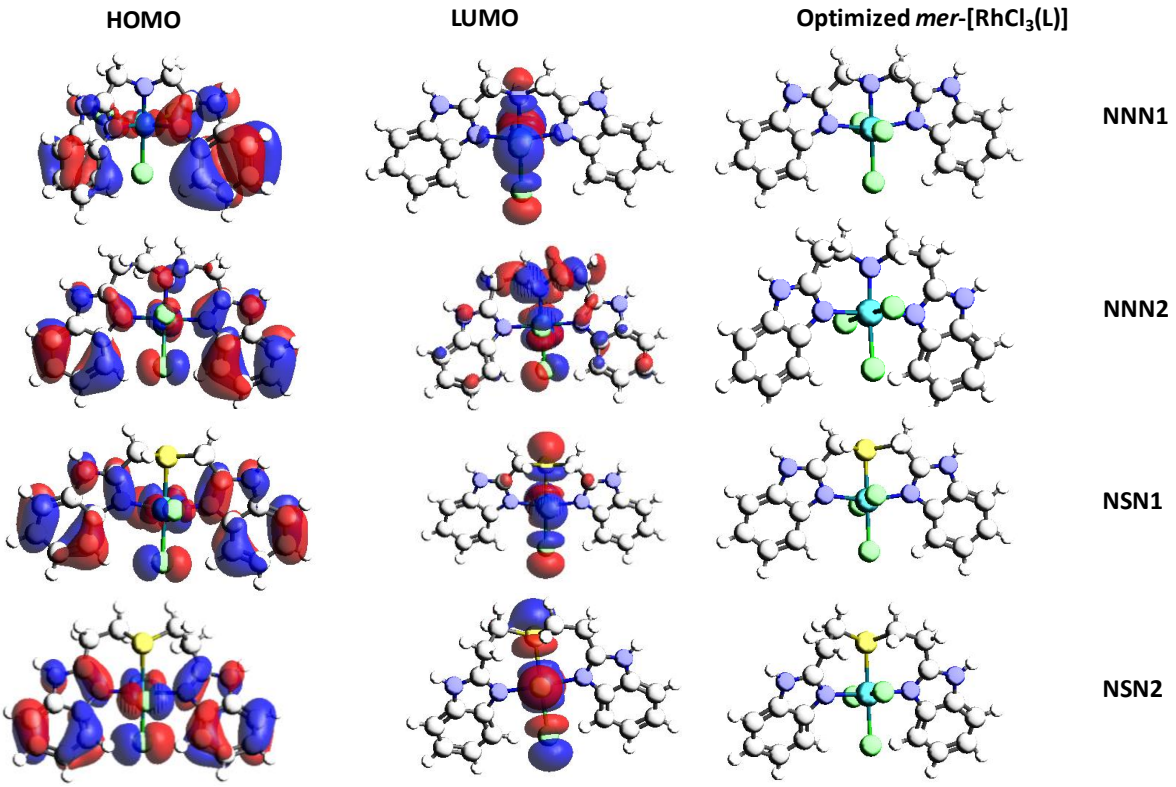

Figure 3.5: HOMO-LUMO of *mer*-[$RhCl_3(H_2O)_3$] complexes with *bis*-benzimidazole derivatives (NNN1, NNN2, NSN1 and NSN2).

The energy gap is an important parameter to define the reactivity of the ligand towards the metal ion. As the energy gap decreases, the reactivity of the ligand increases leading to better ligand efficiency. A hard ligand has a large energy gap and a soft molecule has a small energy gap [28]. The *bis*-benzimidazole ligands resulted in a decrease in the HOMO-LUMO energy gap in the following order; NSN2 > NSN1 > NNN2 > NNN1 (Table 3.1). The sequence of reactivity of the ligands concludes NNN2 is the more reactive and NSN2 is the least reactive. The metal ion species *mer*-[$RhCl_3(H_2O)_3$] is shown to have a slightly lower energy gap compared to *fac*-[$RhCl_3(H_2O)_3$], indicating that the *mer* geometry might be the preferred for coordination with *bis*-benzimidazole ligands.

Molecular interactions between the *bis*-benzimidazole ligands with *mer*-[$RhCl_3(H_2O)_3$] and *fac*-[$RhCl_3(H_2O)_3$] resulted in a decrease in HOMO-LUMO energy gap when compared to the HOMO-LUMO gap of the benzimidazole ligands, thus further indicating that interactions would form a more stable adduct. *fac*-[$RhCl_3$(NNN1)] and *fac*-[$RhCl_3$(NNN2)] showed to be the least stable adduct compared to *fac*-[$RhCl_3$(NSN1)] and *fac*-[$RhCl_3$(NSN2)] which seems to form more stable complexes. The sequence of forming the more stable *fac* complexes is as follows; *fac*-[$RhCl_3$(NSN2)] > *fac*-[$RhCl_3$(NSN1)] > *fac*-[$RhCl_3$(NNN1)] > *fac*-[$RhCl_3$(NNN2)]. The sequence of forming the more stable *mer* complexes is as follows; *mer*-[$RhCl_3$(NSN2)] > *mer*-[$RhCl_3$(NSN1)] > *mer*-[$RhCl_3$(NNN2)] > *mer*-[$RhCl_3$(NNN1)]. Comparing the most stable *fac* and *mer* complexes the order is as follows; *fac*-[$RhCl_3$(NSN2)] > *fac*-[$RhCl_3$(NSN1)] > *mer*-[$RhCl_3$(NSN2)] > *mer*-[$RhCl_3$(NSN1)]. This indicates the NSN2 and NSN1 ligands are the most preferred ligands to form stable complexes (to displace the three aqua ligands). The *fac*-[$RhCl_3$(NSN2)] complex has shown to be the most stable compared to *fac*-[$RhCl_3$(NSN1)], *mer*-[$RhCl_3$(NSN2)], *mer*-[$RhCl_3$(NSN1)] complexes (Table 3.1). However, this does not suggest that the *mer* isomer might be the most preferred for interaction with the tridentate ligands.

Table 3.1: Chemical parameters, HOMO (E_H), LUMO (E_L), Band gap energies (E_G), Hardness (η), Softness (σ) and electronegativity(χ).

	E_H (eV)	E_L (eV)	E_G (eV)	η	σ	χ
Ligand (L)						
NNN1	-6.631	-2.811	3.820	1.910	0.524	4.721
NNN2	-6.463	-4.088	2.375	1.188	0.842	5.276
NSN1	-6.439	-1.300	5.139	2.570	0.389	3.870
NSN2	-6.283	-0.910	5.373	2.687	0.372	3.597
Metal ion species						
***fac*-[$RhCl_3(H_2O)_3$]**	-7.240	-3.126	4.114	2.057	0.486	5.183
***mer*-[$RhCl_3(H_2O)_3$]**	-7.173	-3.126	4.047	2.024	0.494	5.150
***fac*-[$RhCl_3$(L)]**						
***fac*-[$RhCl_3$(NNN1)]**	-6.569	-2.441	4.128	2.064	0.484	4.505
***fac*-[$RhCl_3$(NNN2)]**	-6.562	-2.277	4.285	2.143	0.467	4.420
***fac*-[$RhCl_3$(NSN1)]**	-6.736	-4.118	2.618	1.309	0.764	5.427
***fac*-[$RhCl_3$(NSN2)]**	-6.487	-3.948	2.539	1.270	0.788	5.218
***mer*-[$RhCl_3$(L)]**						
***mer*-[$RhCl_3$(NNN1)]**	-6.532	-2.590	3.942	1.971	0.507	4.561
***mer*-[$RhCl_3$(NNN2)]**	-6.305	-2.557	3.748	1.874	0.534	4.431
***mer*-[$RhCl_3$(NSN1)]**	-6.570	-2.926	3.644	1.822	0.549	4.748
***mer*-[$RhCl_3$(NSN2)]**	-6.351	-2.838	3.513	1.757	0.569	4.595

3.3.1.2 Chemical hardness and softness

HOMO and LUMO energies were used to predict the interaction or coordinating centres of the ligands. For the simplest transfer of electrons, interaction should be better for molecules with the highest softness (σ) according to Koopman's theorem

[182]. Electronegativity (χ), hardness (η), and softness (σ) have proved to be very useful properties in chemical reactivity theory. When two systems, metal ion and ligand, are brought together, electrons will flow from lower χ (ligand) to higher χ (metal ion) until the chemical potentials become equal [153, 183, 184]. Absolute hardness and softness are important properties to measure molecular stability and reactivity. The chemical hardness fundamentally signifies the resistance towards the deformation or polarization of the electron cloud of the atoms, ions, or ligands under a small perturbation of chemical reaction [153, 185].

Table 3.1 shows that NNN2 ligand has the highest value of softness and small energy gap value, where the simplest transfer of electrons and interaction should occur compared to the ligands that have the lowest value of softness. The ligands sequence of softness is as follows NNN2 > NNN1 > NSN1> NSN2. The softness for the metal ion species showed that *mer*-[$RhCl_3(H_2O)_3$] is softer than *fac*-[$RhCl_3(H_2O)_3$]. Normally, the ligand with the least value of absolute hardness (hence, the highest value of absolute softness) is expected to have the highest ligand efficiency. This means NNN2 should have the highest ligand efficiency.

According to the complexation theory (Table 3.1), the *fac*-[$RhCl_3$(L)] complexes showed the softness values in the following order; *fac*-[$RhCl_3$(NSN2)] > *fac*-[$RhCl_3$(NSN1)] > *fac*-[$RhCl_3$(NNN1)] > *fac*-[$RhCl_3$(NNN2)]. *mer*-[$RhCl_3$(L)] complexes showed the softness values in the following order; *mer*-[$RhCl_3$(NSN2)] > *mer*-[$RhCl_3$(NSN1)] > *mer*-[$RhCl_3$(NNN2)] > *mer*-[$RhCl_3$(NNN1)]. *fac*-[$RhCl_3$(NSN2)] followed by *fac*-[$RhCl_3$(NSN1)] are the complexes that show the highest softness value, indicating these are the most stable complexes and that is in agreement with

the energy gap order for the complexes. Therefore, the *fac* geometry forms most stable complexes with NSN2 and NSN1 due to the presence of the sulfur donor atom compared to the nitrogen at the centre of the *bis*-benzimidazole ligands. This shows that upon complexation, the ligands (NSN1 and NSN2) are more preferred by the rhodium(III) ion, and this result is also in agreement with the experimental findings in the column study (single-element and multi-element study in Section 3.3.6).

3.3.1.3 Electronegativity

The electronegativity (χ), indicates the tendency of a molecule to attract electrons (or electron density) towards itself. Species with large electronegativity can be considered as stronger electron acceptors [154]. As displayed in Table 3.1, electron-accepting ability increases as follows; NNN2 > NNN1 > NSN1 > NSN2. It has been observed that NNN1 and NNN2 are more electronegative, whereas NSN1 and NSN2 are less electronegative. This was also confirmed by the electrostatic potential (ESP) in Figure 3.6. For NNN1 and NNN2, the nitrogens are more electron rich whereas the sulfurs are less electron rich.

The electronegativity of the *fac*-[$RhCl_3(L)_3$] complexes was observed in the following order; *fac*-[$RhCl_3$(NSN1)] > *fac*-[$RhCl_3$(NSN2)] > *fac*-[$RhCl_3$(NNN1)] > *fac*-[$RhCl_3$(NNN2)], while *mer*-[$RhCl_3$(NSN1)] > *mer*-[$RhCl_3$(NSN2)] > *mer*-[$RhCl_3$(NNN1)] > *mer*-[$RhCl_3$(NNN2)]. This sequence is in agreement with the experimental findings in a column study (single-element and multi-element in Section 3.3.6). According to the electronegativity theory, NSN1 is the most preferred ligand to form stable complexes with *mer* and *fac* geometries.

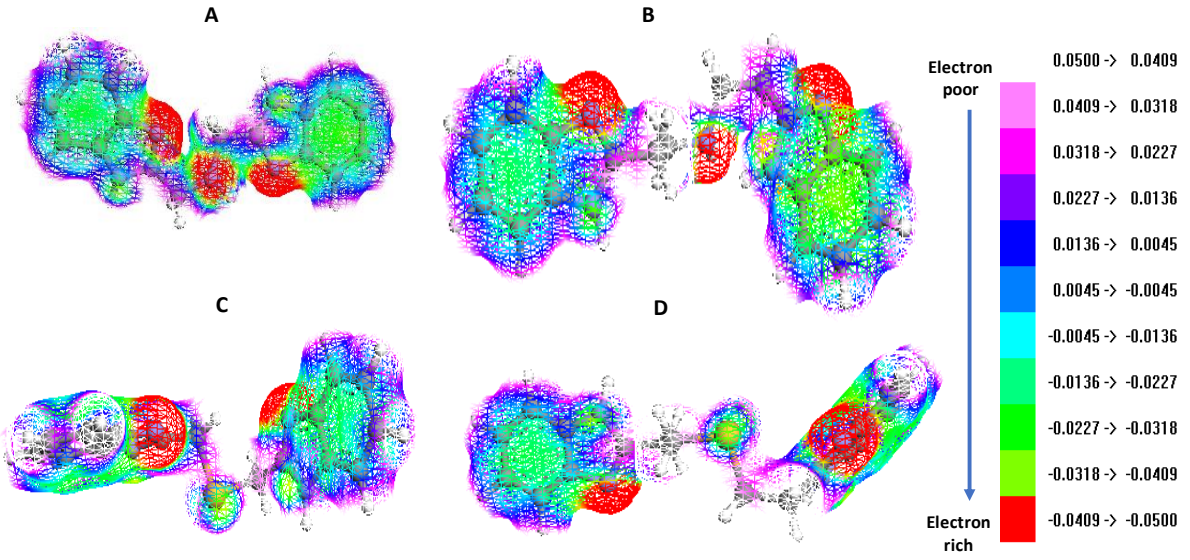

Figure 3.6: Electrostatic potential **(**ESP) of tridentate *bis*-benzimidazole ligands; (A) NNN1, (B) NNN2, (C) NSN1 and (D) NSN2.

3.3.1.4 Thermodynamic data

The frequency calculations made during the optimization process also include the results of the thermochemical analysis of the system. Standard thermodynamic functions are selected for thermochemical analysis such as Gibbs free energies (ΔΔG), enthalpy (ΔΔH) and entropy (ΔΔS) resulting from adduct formation are presented in Table 3.2. A decrease in the Gibbs free energy of the system ($\Delta G_b < 0$) confirmed that the complexation process is spontaneous or favoured. A decrease in the randomness of the interacting molecules gives rise to negative entropies ($\Delta S_b < 0$) and vice versa. Negative enthalpy (ΔH_b) value resulting from the interaction of ligands with metals contributed to an exothermic process. The optimized structures of the metal ions (*mer*-[$RhCl_3(H_2O)_3$] and *fac*-[$RhCl_3(H_2O)_3$)], ligands (NNN1, NNN2, NSN1 and NSN2) and complexes (*fac*-[$RhCl_3$(NNN1)], *fac*-[$RhCl_3$(NNN2)], *fac*-

[$RhCl_3$(NSN1)], *fac*-[$RhCl_3$(NSN2)], *mer*-[$RhCl_3$(NNN1)], *mer*-[$RhCl_3$(NNN2)], *mer*-[$RhCl_3$(NSN1)] and *mer*-[$RhCl_3$(NSN2)]) are shown in Figures 3.2-3.5.

Table 3.2: DFT molecular modelling thermodynamic data (ΔΔH, ΔΔG and ΔΔS) on the formation of an adduct between metal ions (mer-$RhCl_3(H_2O)_3$) and fac-$RhCl_3(H_2O)_3$) and ligands (NNN1, NNN2, NSN1 and NSN2).

Ligands	**ΔΔG (kcal.mol^{-1})**	**ΔΔH (kcal.mol^{-1})**	**ΔΔS (kcal.mol^{-1})**
mer-[$RhCl_3$(NNN1)]	510.221	483.725	483.725
mer-[$RhCl_3$(NNN2)]	744.870	716.189	716.782
mer-[$RhCl_3$(NSN1)]	-21.713	-49.991	-49.398
mer-[$RhCl_3$(NSN2)]	-26.155	-56.082	-55.488
fac-[$RhCl_3$(NNN1)]	162.516	-9.787	-9.195
fac-[$RhCl_3$(NNN2)]	746.010	714.962	715.555
fac-[$RhCl_3$(NSN1)]	-13.466	-40.490	-40.490
fac-[$RhCl_3$(NSN2)]	-5.542	-35.001	-34.408

The thermodynamic data (Table 3.2) showed that the interaction between *mer*-[$RhCl_3(H_2O)_3$] with NSN1 and NSN2 and *fac*-[$RhCl_3(H_2O)_3$] with NSN1 and NSN2 were shown to be the most favourable and exothermic in nature where the *mer*-[$RhCl_3$(L)] complex geometry was preferred. The order of favourability between the metal ions and *bis*-benzimidazole ligands is as follows; *mer*-[$RhCl_3$(NSN2)] > *mer*-[$RhCl_3$(NSN1)] > *mer*-[$RhCl_3$(NNN1)] > *mer*-[$RhCl_3$(NNN2)] while *fac*-[$RhCl_3$(NSN1)] > *fac*-[$RhCl_3$(NSN2)] > *fac*-[$RhCl_3$(NNN1)] > *fac*-[$RhCl_3$(NNN2)]. The *mer* geometry is more favoured with NSN1 and NSN2, while the *fac* geometry is the less favoured for the

same ligands. The interaction between *mer*-[$RhCl_3(H_2O)_3$] with NNN1 and NNN2 as well as *fac*-[$RhCl_3(H_2O)_3$] with NNN1 and NNN2 were endothermic in nature. In the experimental results, based on the single-element (Rh) and multi-element (Rh, Ir, Pt, Pd and Ni) column study (Section 3.3.10), the order of favourability towards Rh(III) agreed with the thermodynamic data, where NSN1 > NSN2 > NNN2 > NNN1 order was observed for both column studies, specifically for Rh(III) extraction. Since the order of extraction of Rh(III) with *bis*-benzimidazole ligands from the column studies is in agreement with the theoretical thermodynamic values, this shows that the *fac*-[$RhCl_3$(L)] complexes are possibly the dominating species in the separation studies. In terms of ring size formed with *fac*-[$RhCl_3(H_2O)_3$], the five-membered ring chelation is preferred with *fac*-[$RhCl_3$(NSN1)] followed by six-membered ring chelation with *fac*-[$RhCl_3$(NSN2)] (Figure 3.7). The *mer*-[$RhCl_3$(L)] complex showed that the six-membered ring chelation is preferred as in *mer*-[$RhCl_3$(NSN2)], followed by five-membered ring chelation with *mer*-[$RhCl_3$(NSN1)]. Figure 3.7 shows an example of five-membered ring chelation and six-membered ring chelation with *fac*-[$RhCl_3$(NSN1)] and *fac*-[$RhCl_3$(NSN2)], respectively.

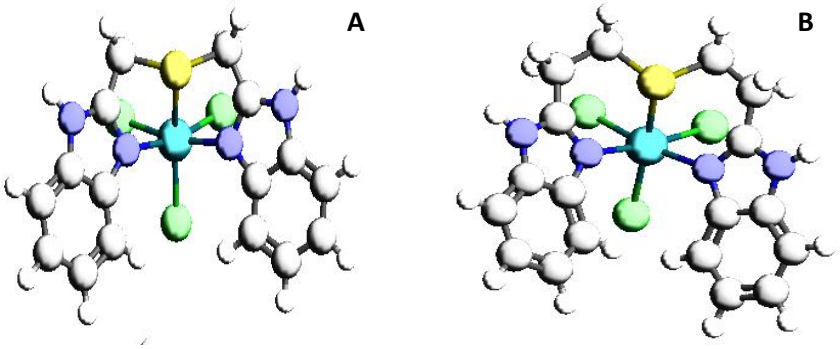

Figure 3.7: (A) *fac*-[$RhCl_3$(NSN1)] sharing five-membered ring chelation, and (**B**) *fac*-[$RhCl_3$(NSN2)] showing six-membered ring chelation.

3.3.2 Synthesis and characterisation of *bis*-benzimidazole derivatives

The tridentate ligands, namely *bis*((1*H*-benzimidazol-2-yl)methyl)amine (NNN1), *bis*((1*H*-benzimidazol-2-yl)ethyl)amine (NNN2), *bis*((1*H*-benzimidazol-2-yl)methyl)sulfide (NSN1), *bis*((1*H*-benzimidazol-2-yl)ethyl)sulfide (NSN2) were synthesized by condensation/cyclization between 2,2'-iminodiacetic acid, 3,3'-iminodiorpionitrile, 2,2'-thiodiacetic acid, 3,3'-thiodipropionic acid, respectively, and *o*-phenylenediamine [186]. The mechanism for the cyclization reaction in the formation of *bis*-benzimidazoles in NNN1, NNN2, NSN1 and NSN2 goes by the acid catalysed the initial formation of diamides followed by ring closure and elimination of water molecules. The reactions were therefore conducted at elevated temperature (190°C) and in acid medium. The purity of the ligands was confirmed by elemental analyses and ^{1}H NMR characterization (Figures 3.8 to 3.11). The formation of the *bis*-benzimidazole was confirmed by the appearance of the peaks between the region 7.11 to 7.83 ppm in the ^{1}H NMR spectra of the compounds which signified the presence of *bis*-benzimidazole and region between 2.98 to 4.41 ppm that confirmed the presence of methylene groups. The purity of the ligands was further assured by the agreement of the elemental micro-analysis results to the theoretical values.

3.3.2.1 *Bis*((1*H*-benzimidazol-2-yl)methyl)amine (NNN1)

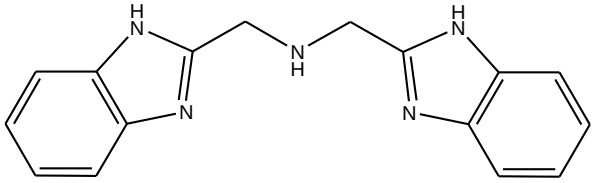

Yield = 73%. Anal. Calcd for $C_{16}H_{15}N_5$ (%): C, 69.29; H, 5.45; N, 25.25. Found: C, 69.09; H, 5.32; N, 24.99. ^{1}H NMR (400 MHz, DMSO) δ (ppm): 7.83 (4H, s, CH), 7.54 (4H, s, CH), 4.51 (4H, m, CH_2). IR (v_{max}/cm^{-1}): 3208 v(N-H), 3049 v(sec N-H), 1592 v(C=N).

3.3.2.2 *Bis*((1*H*-benzimidazol-2-yl)ethyl)amine (NNN2)

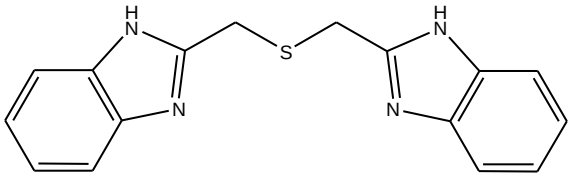

Yield = 70 %. Anal. Calcd for $C_{16}H_{19}N_5$ (%): C, 70.80; H, 6.27; N, 22.93. Found: C, 69.99; H, 6.08; N, 22.84. ^{1}H NMR (400 MHz, DMSO) δ (ppm): 7.43 (4H, s, CH), 7.11 (4H, s, CH), 3.05 (4H, m, CH_2), 2.98 (4H, m, CH_2). IR (v_{max}/cm^{-1}): 3216 v(N-H), 3124 v(sec N-H), 1586 v(C=N).

3.3.2.3 *Bis*((1*H*-benzimidazol-2-yl)methyl)sulfide (NSN1)

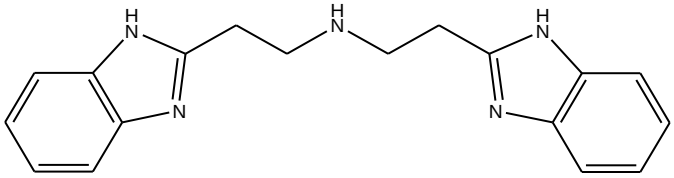

Yield = 75%. Anal. Calcd for $C_{16}H_{14}N_4S$ (%): C, 65.28; H, 4.79; N, 19.03; S, 10.89. Found: C, 64.96; H, 4.58; N, 18.89; S, 10.67. ^{1}H NMR (400 MHz, DMSO) δ (ppm): 7.53 (4H, s, CH), 7.18 (4H, s, CH), 4.04 (4H, m, CH_2). IR (v_{max}/cm^{-1}): 3377 v(N–H), 1534 v(C=N), 1128 v(C-S-C).

3.3.2.4 *Bis*((1*H*-benzimidazol-2-yl)ethyl)sulfide (NSN2)

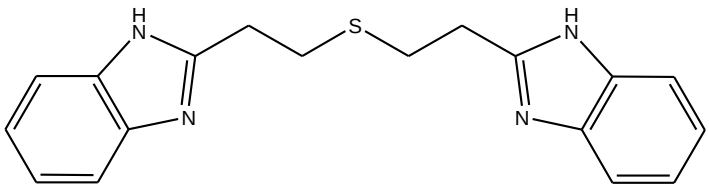

Yield = 73%. Anal. Calcd for $C_{16}H_{18}N_4S$ (%): C, 67.05; H, 5.63; N, 17.38; S, 9.94. Found: C, 67.00; H, 5.58; N, 17.14; S, 9.60. ^{1}H NMR (400 MHz, DMSO) δ (ppm): 7.49 (4H, s, CH), 7.26 (4H, s, CH), 3.13 (4H, m, CH_2), 3.03 (4H, m, CH_2). IR (v_{max}/cm^{-1}): 3386 v(N–H), 1547 v(C=N), 1139 v(C-S-C).

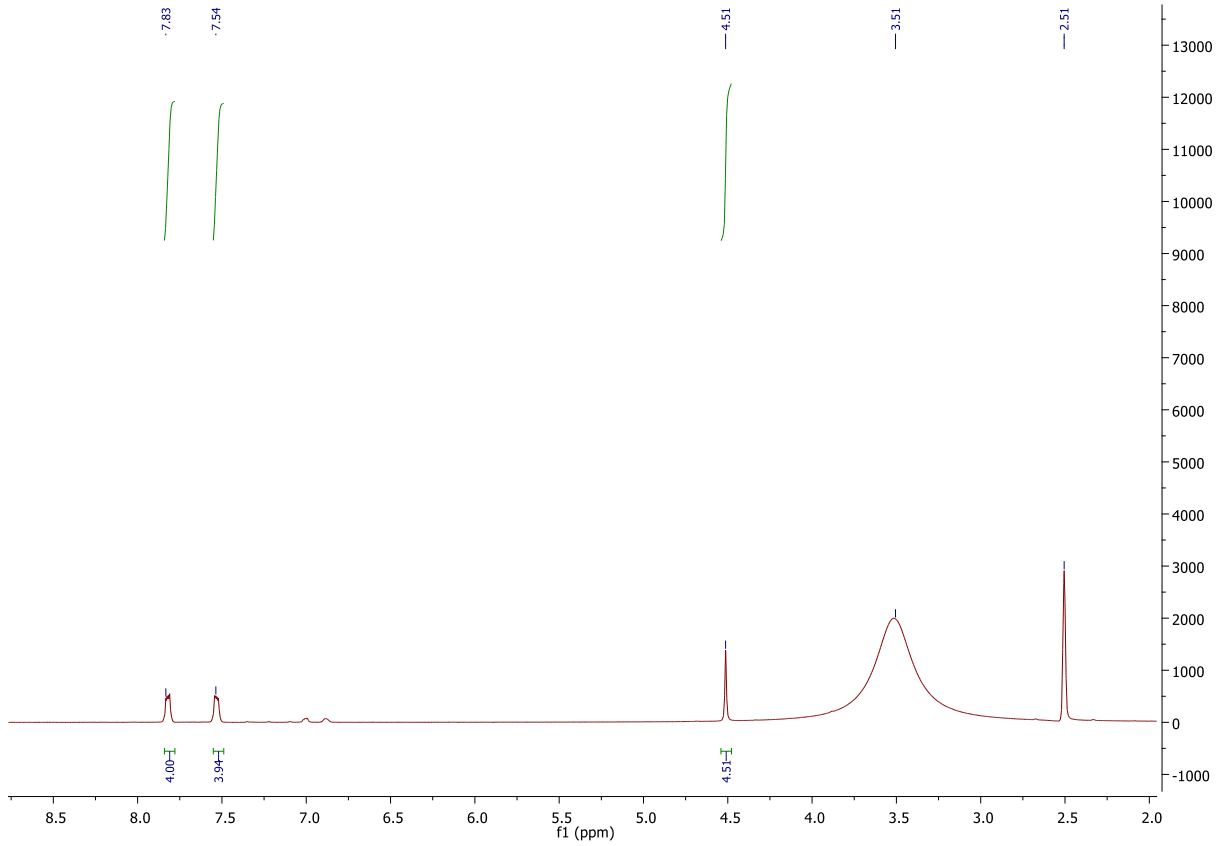

Figure 3.8: The ^{1}H NMR spectrum of bis((1*H*-benzimidazol-2-yl)methyl)amine (NNN1). The solvent peaks appeared at 2.5 ppm (DMSO) and at 3.5 ppm (H_2O).

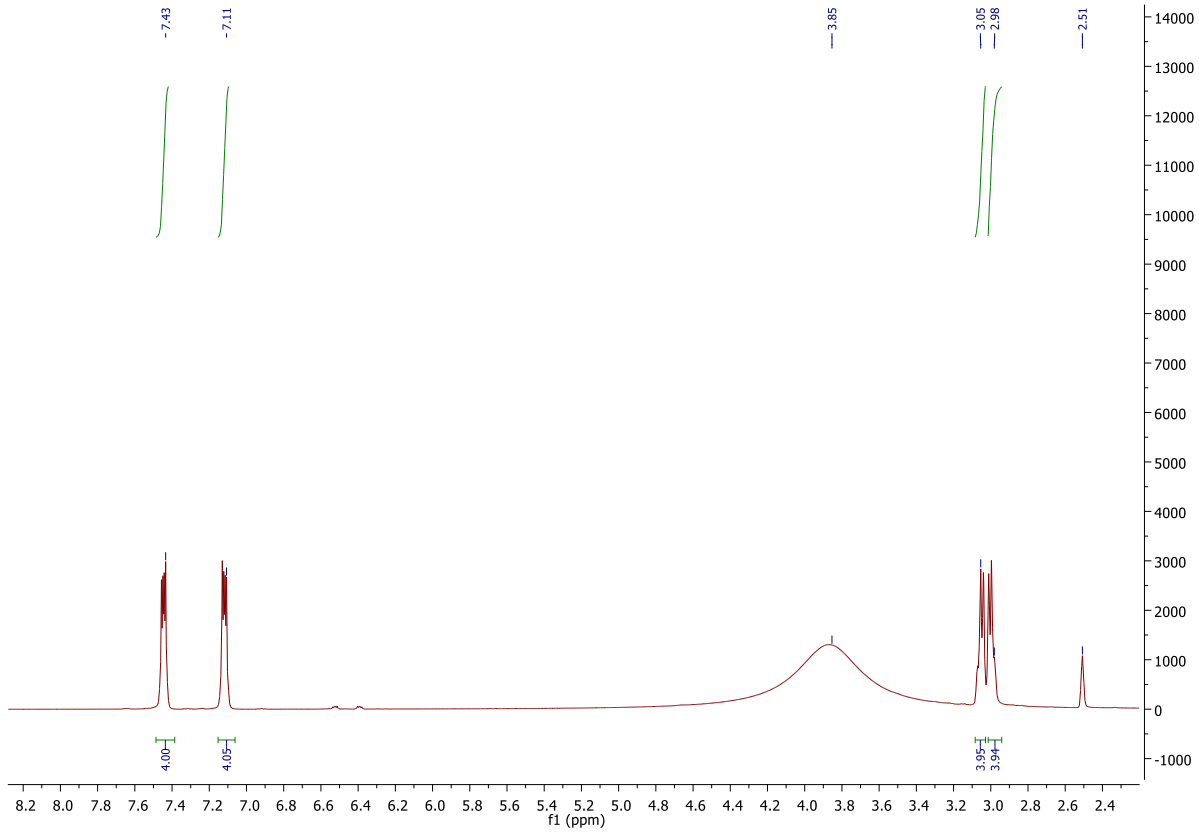

Figure 3.9: The ^{1}H NMR spectrum of bis((1*H*-benzimidazol-2-yl)ethyl)amine (NNN2). The solvent peaks appeared at 2.5 ppm (DMSO) and at 3.7-4.0 ppm (H_2O).

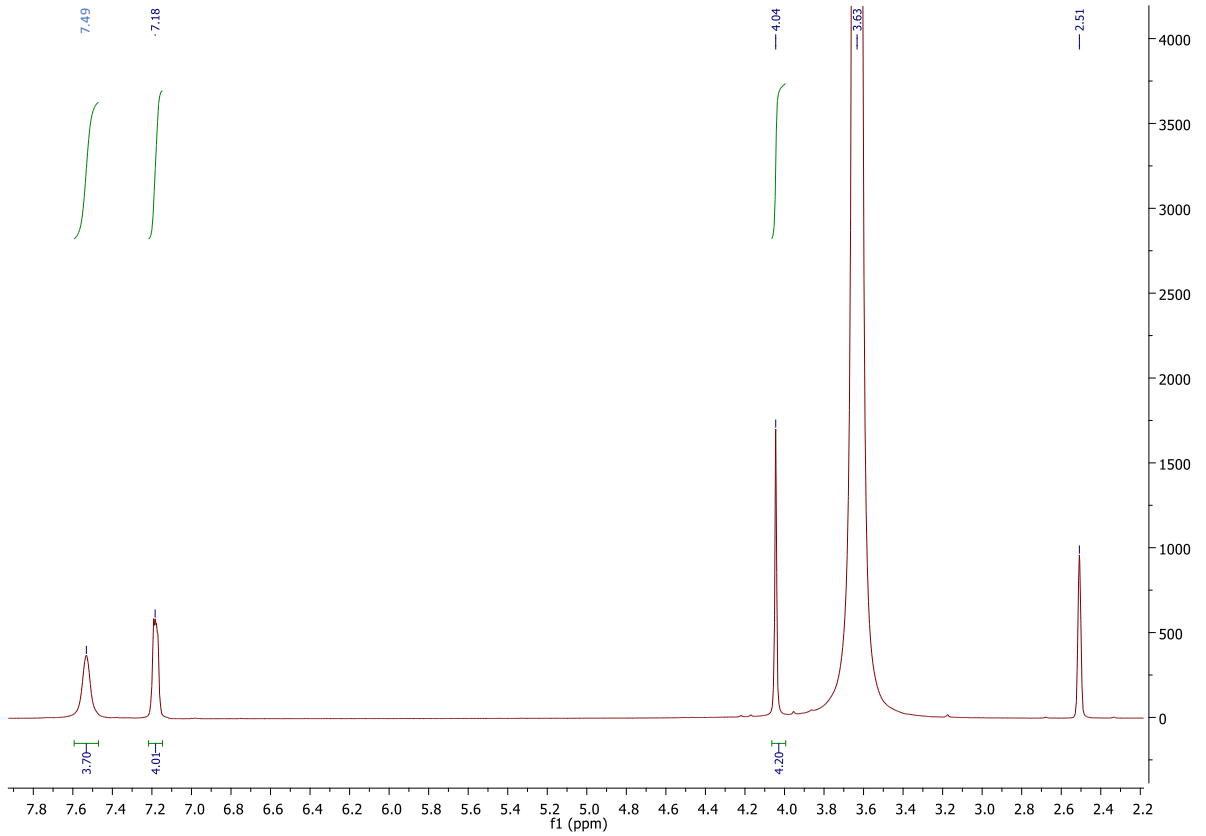

Figure 3.10: The ^{1}H NMR spectrum of bis((1*H*-benzimidazol-2-yl)methyl)sulfide (NSN1). The solvent peaks appeared at 2.5 ppm (DMSO) and at 3.7-3.8 ppm (H_2O).

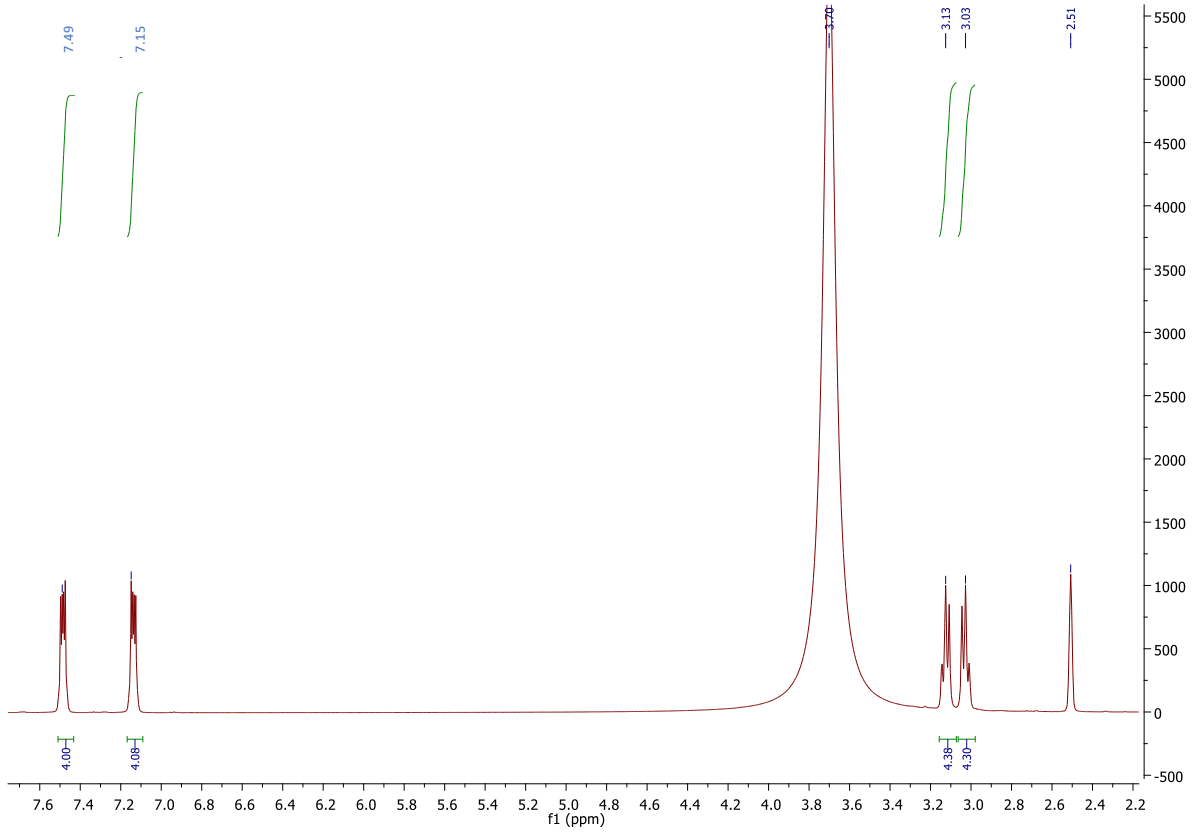

Figure 3.11: The ^{1}H NMR spectrum of bis((1*H*-benzimidazol-2-yl)ethyl)sulfide (NSN2). The solvent peaks appeared at 2.5 ppm (DMSO) and at 3.5-3.9 ppm (H_2O).

3.3.3 Crystal structures

3.3.3.1 *Bis*-benzimidazole ligands crystal structures

The ORTEP diagrams of the protonated ligands, $[H_3NNN1]Cl_3$, $[H_2NSN1]Cl_2$ and $[H_3NNN2]Cl_3$, are shown in Figures 3.12-3.14. Selected crystallographic data is presented in Table 3.3, and selected bond lengths and angles in Table 3.4. The average bond lengths and angles for NNN1, NSN1 and NNN2 are in agreement with those of similar *bis*(benzimidazolyl)-substituted compounds, which are 1.30-1.40 Å and 104°-129° [187].

(a) Crystal structure of $[H_3NNN1]Cl_3$

The compound is a trihydrochloride salt of bis((1*H*-benzimidazol-2-yl)methyl)amine (NNN1) The symmetric unit contains two methyl benzimidazoles connected to NH. The charge on the NNN1 unit is due to the protonation of the nitrogen atoms (N(5), N(2) and N(3)) (Figure 3.12). The C-N bond lengths in the imidazole ring are in the range 1.324(18)-1.373(17) Å and these are shorter than the single bond length of 1.560(2) Å and longer than the typical C=N distance of 1.280 Å, indicating partial double bond character. The bond angle on the imidazole ring, N_1-C_1-N_2, is 109.25° (12). The NNN1 unit is disordered around C_3-N_6-C_4. The crystal structure data confirmed that a triply protonated NNN1 ligand was formed in acid medium.

(b) Crystal structure of $[H_2NSN1]Cl_2$

The compound is a dihydrochloride salt of bis((1*H*-benzimidazol-2-yl)methyl)sulfide (NSN1) The symmetric unit contains two methyl benzimidazoles connected to S. The charge on the NSN1 unit is due to the protonation of the nitrogen atoms (N(2) and N(3)) (Figure 3.13). The C-N bond lengths in the imidazole ring are in the range 1.327(18)-1.333(18) Å, and these are shorter than the single bond length of 1.488(2) Å and longer than the typical C=N distance of 1.280 Å, indicating partial double bond character. The bond angle on the imidazole ring, N_1-C_1-N_2, is 109.46° (12). The crystal structure data confirmed that a doubly protonated NSN1 ligand was formed in acid medium, with the sulfur atom free.

(c) Crystal structure of $[H_3NNN2]Cl_3$

The compound is a trihydrochloride salt of bis((1*H*-benzimidazol-2-yl)ethyl)amine (NNN2) The charge on the NNN2 unit is due to the protonation of the nitrogen atoms (N(4), N(1) and N(3)) (Figure 3.14). The C-N bond lengths in the imidazole ring are in the range 1.294(13)-1.364(11) Å, and these are shorter than the single bond length of 1.480(13) Å and longer than the typical C=N distance of 1.280 Å, indicating partial double bond character. The bond angle on the imidazole ring, N_1-C_1-N_2, is 109.50° (8). The crystal structure data confirmed that a triply protonated NNN2 ligand was formed in acid medium.

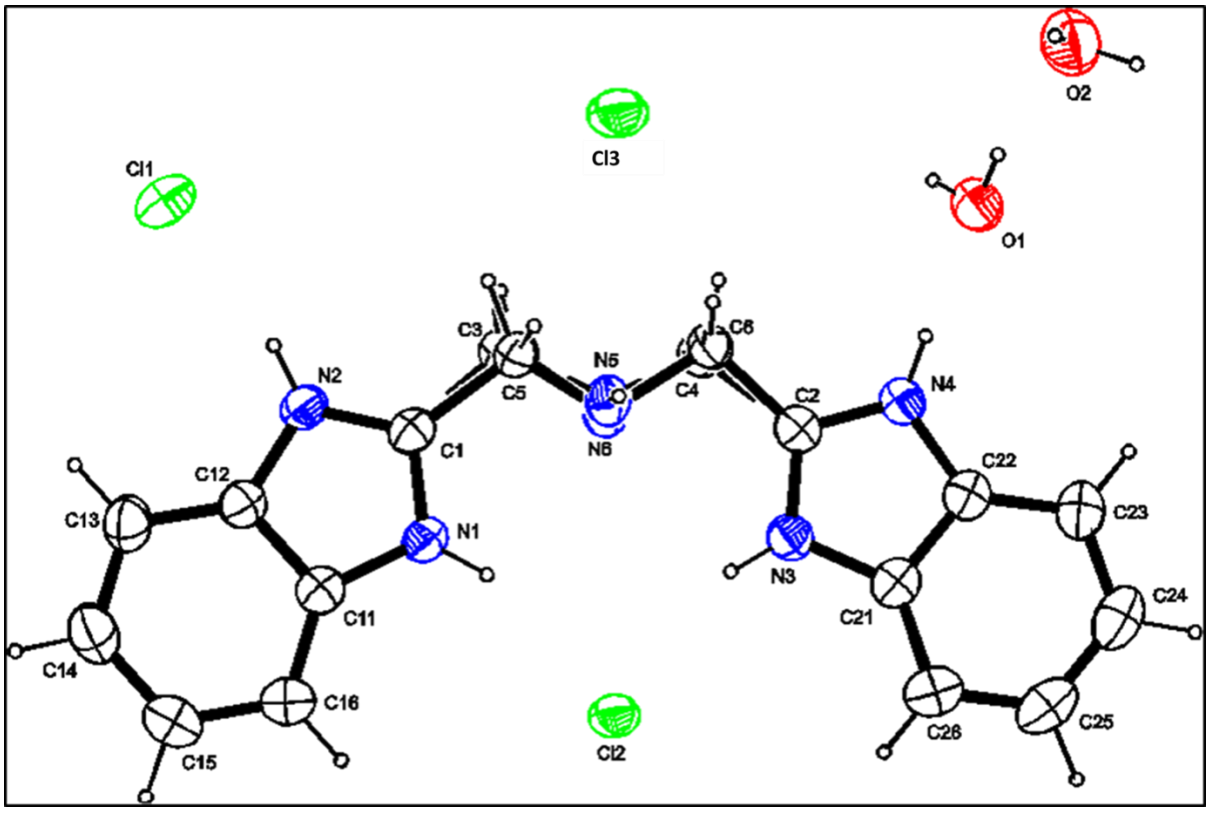

Figure 3.12: ORTEP diagram of $[H_3NNN1]Cl_3{\cdot}2H_2O$ showing the atom-labelling scheme.

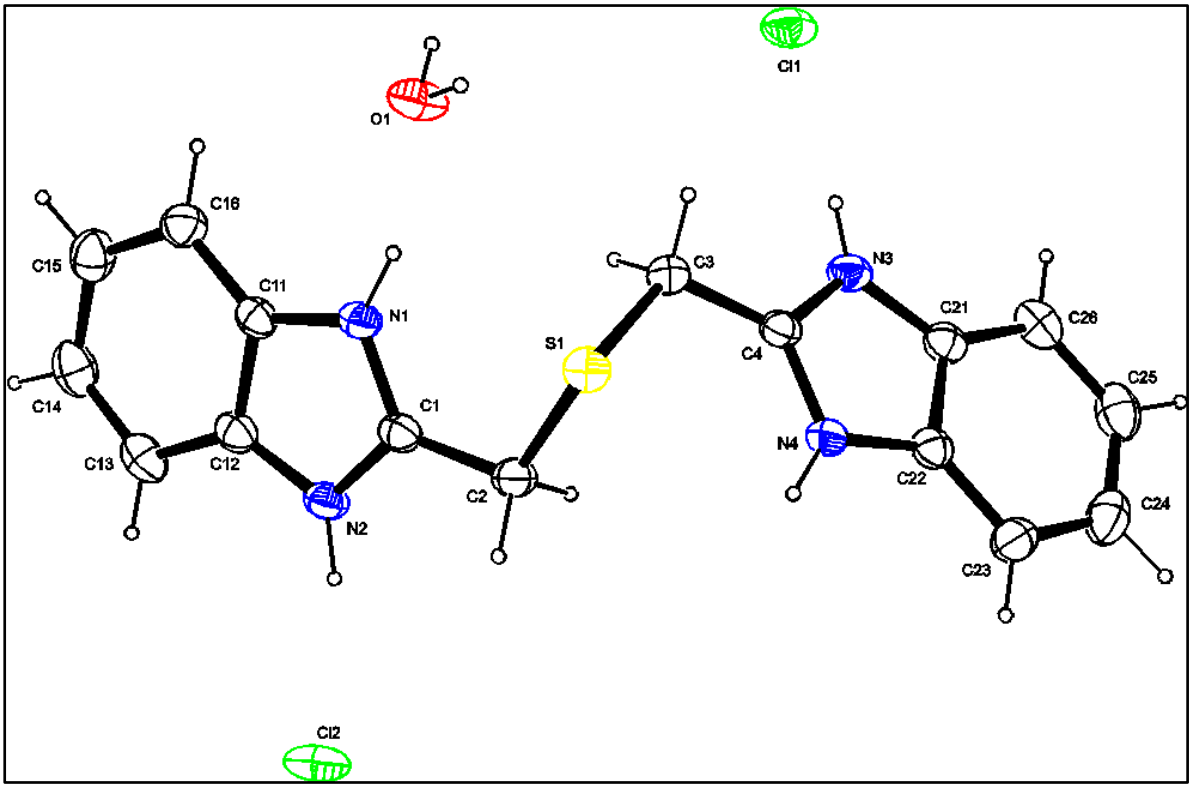

Figure 3.13: ORTEP diagram $[H_2NSN1]Cl_2 \cdot H_2O$ showing the atom-labelling scheme.

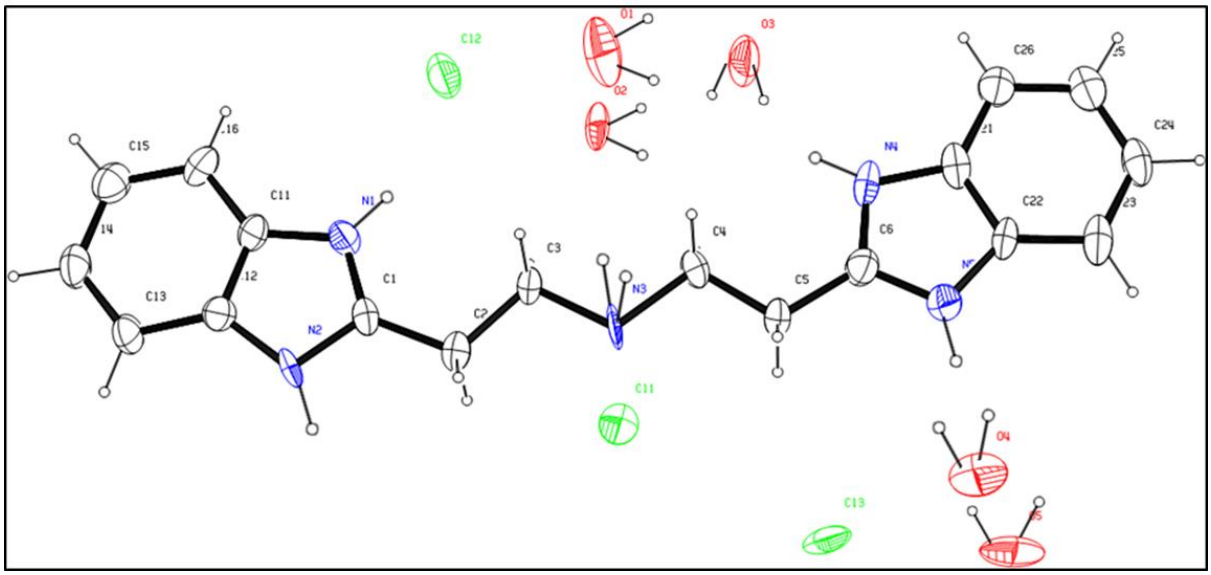

Figure 3.14: ORTEP diagram of $[H_3NNN2]Cl_3 \cdot 5H_2O$ showing the atom-labelling scheme.

Table 3.3: Selected crystallographic data for $[H_3NNN1]Cl_3$, $[H_2NSN1]Cl_2$ and $[H_3NNN2]Cl_3$.

Compound	$[H_3NNN1]Cl_3$	$[H_2NSN1]Cl_2$	$[H_3NNN2]Cl_3$
Chemical formula	$C_{16}H_{17}N_5$,3(Cl), 2(H_2O)	$C_{16}H_{16}N_4S$, 2(Cl), H_2O	C_{18} H_{19} N_5, 3(Cl), 5(H_2O)
Formula weight	386.28	385.30	453.26
Crystal colour	Light brown	Yellow	Light brown
Crystal system	monoclinic	monoclinic	triclinic
Space group	*P*-21/c	*P*21/c	*P*-1
Temperature (K)	200	200	200
Crystal size (mm^{-3})	0.09 x 0.010 x 0.55	0.07 x 0.29 x 0.71	0.07 x 0.16 x 0.50
α (Å)	7.1328(3)	14.6760(7)	6.6522(12)
b (Å)	15.0799(6)	5.0581(3)	11.235(2)
c (Å)	17.6613(7)	24.3201(13)	16.663(3)
α (˚)	90	90	85.848(13)
β (˚)	93.601(2)	98.156	89.689(9)
ɣ (˚)	17.6613(7)	90	74.660(8)
V (Å)	1835(13)	1787.09(17)	1197.7(4)
Z	4	4	2
D_{calc} (g cm^3)	1.353	1.432	1.257
μ/mm^{-1}	0.362	0.491	0.306
F (000)	808	800	466
Theta min-max (˚)	1.8, 28.3	1.4, 28.3	1.2, 27.2
S	1.02	1.03	2.25
Tot.uniq.data, r(int)	35492, 4726, 0.024	24934, 4441, 0.024	18062, 5184, 0.059
Observed data [I>2.0σ(I)]	3838	3637	3513
R	0.0326	0.0299	0.2130
R_w	0.0892	0.0758	0.5664

Table 3.4: Selected bond distances (Å) and angles (°) for $[H_3NNN1]Cl_3$, $[H_2NSN1]Cl_2$ and $[H_3NNN2]Cl_3$.

$[H_3NNN1]Cl_3$		$[H_2NSN1]Cl_2$		$[H_3NNN2]Cl_3$	
Bond distances (Å)					
N1-C1	1.3334(17)	S1-C2	1.8021(15)	N1-C1	1.294(13)
N2-C1	1.3270(17)	S1-C3	1.8057(14)	N2-C1	1.364(11)
N5-C4	1.4540(8)	N1-C1	1.3321(18)	C1-C2	1.480(13)
N2-C3	1.3734(17)	N2-C1	1.3271(18)	C2-C3	1.487(13)
N4-C2	1.3239(18)	N3-C4	1.3328(18)	N3-C3	1.451(12)
C1-C5	1.5600(2)	N4-C4	1.3331(18)	N3-C4	1.504(12)
C2-C6	1.4700(3)	C1-C2	1.4880(2)	C4-C5	1.462(13)
N6-C5	1.3900(2)	C3-C4	1.4860(2)	C5-C6	1.504(13)
-	-	-	-	N4-C6	1.322(13)
-	-	-	-	N5-C6	1.347(12)
Bond angles (°)					
N1-C1-N2	109.25(12)	C2-S1-C3	102.04(7)	C3-N3-C4	106.5(8)
N3-C2-N4	109.38(11)	N1-C1-N2	109.46(12)	C4-C5-C6	115.4(8)
N6-C5-C1	110.30(14)	N3-C4-N4	109.04(12)	C1-C2-C3	115.4(8)
N5-C4-C2	109.00(5)	S1-C3-C4	113.69(10)	N2-C1-N1	109.5(8)
C5-N6-C6	111.10(16)	S1-C2-C1	114.72(11)	N4-C6-N5	110.6(8)

3.3.4 Fabrication and characterization of nanofibers

PVBC was used as a host polymer, and it was synthesized and electrospun in order to generate nanofibers. Typical morphology of nanofibers structure was obtained by adjusting the solvent type, concentration of the polymer, distance between needle tip to a collector, flow rate and the applied voltage [140, 151]. In this experiment, the flow rate used was 0.2 mL/min, the tip-to-collector distance was 15 cm while the applied

voltage was 20 kV. A solvent mixture of DMF:THF (1:1) was used to prepare a 40 wt/v% solution to produced uniform nanofibers. The diameter range was 93-108 nm. The scanning electron micrographs (SEM) of electrospun PVBC nanofibers are presented in Figure 3.16(a). Other characterization techniques were also used to characterize the nanofibers.

3.3.4.1 FT-IR spectroscopy

The infrared spectra of the *bis*-benzimidazole ligands (NNN1, NNN2, NSN1 and NSN2), unfunctionalized nanofibers and functionalized nanofibers were confirmed by FTIR. FTIR spectra of PVBC, before and after functionalization with *bis*-benzimidazoles, are shown in Figures 3.15 (a & b). In all spectra, an adsorption band between 3205-3218 cm^{-1} was present revealing the stretching vibration of the v(N-H) and the band at 1593-1598 cm^{-1} for the v(C=N) stretching confirmed the presence of the *bis*-benzimidazole. Unfunctionalized nanofibers showed a strong peak at 673 cm^{-1} due to the ν(C-Cl) and a strong peak at 1262 cm^{-1} which can be assigned to the (CH_2-Cl) bending. These peaks disappeared or got reduced after functionalization. The most striking peak (v(C=N)), between 1588-1598 cm^{-1}, confirmed the presence of *bis*-benzimidazole ligands. This indicates that all sorbent material contained ligands after functionalization.

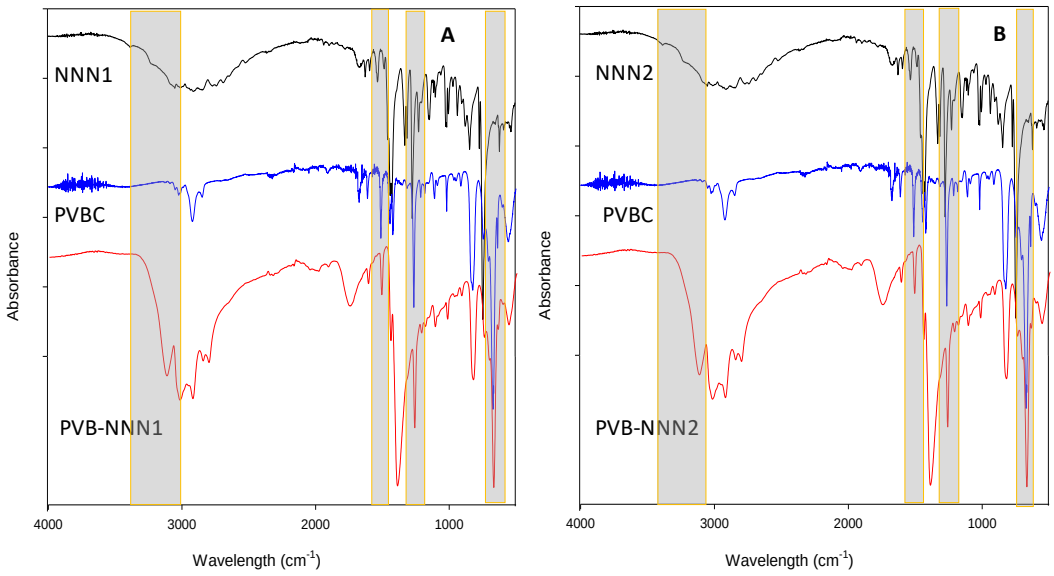

Figure 3. 15(a): FTIR spectra for the ligand (black), unfunctionalized PVBC nanofibers (blue) and functionalized PVBC nanofibers (red). (A) NNN1 and (B) NNN2.

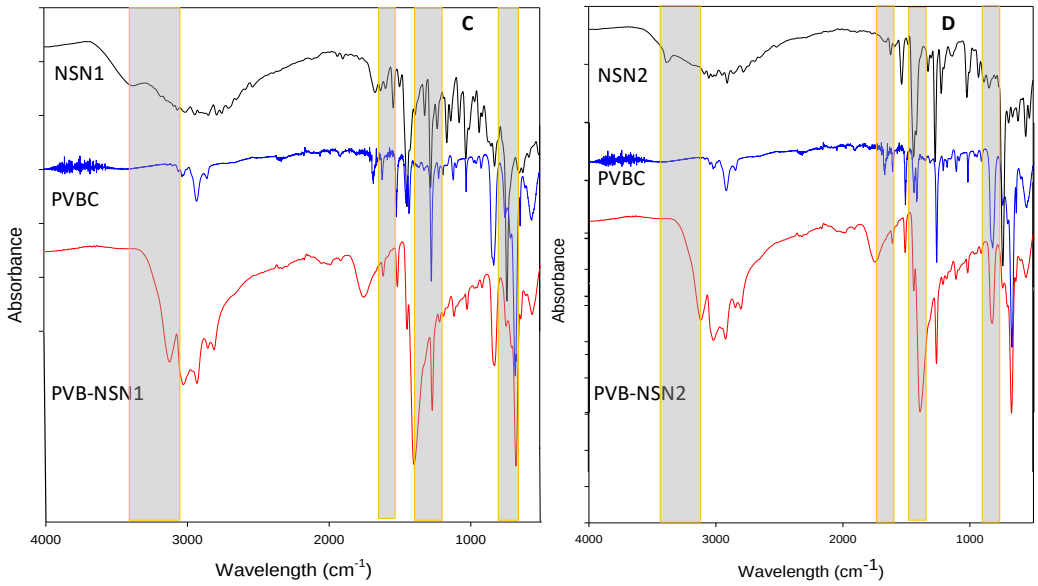

Figure 3.15(b): FTIR spectra for ligand (black), unfunctionalized PVBC nanofibers (blue) and functionalized PVBC nanofibers (red). (C) NSN1 and (D) NSN2.

3.3.4.2 Microanalysis of nanofibers

The unfunctionalized PVBC nanofibers and functionalized PVBC nanofibers, with *bis*-benzimidazole derivatives (NNN1, NNN2, NSN1 and NSN2), were analysed to confirm the composition of the nanofibers, and results are presented in Table 3.5. Functionalization of PVBC nanofiber was confirmed by the presence of nitrogen (%) for NNN1 and NNN2, and the presence of nitrogen (%) and sulfur (%) for NSN1 and NSN2. It is not clear how the functionalization on the amine was achieved, i.e. whether on one or both amines (Scheme 3.3). The monomer-to-ligand ratios confirmed that not all the chloride groups were displaced by amine of the ligand (as has been noticed on the IR spectra).

Table 3.5: The microanalyses data (%) for the nanofibers (before and after functionalization with NNN1, NNN2, NSN1 and NSN2).

Sorbent materials*	**C (%)**	**H (%)**	**N (%)**	**S (%)**	**C:N**	**Monomer:L**
PVBC	72.86	5.41	-	-	-	-
PVB-NNN1	76.72	5.85	17.13	-	6.39:1.22	5:1
PVB-NNN2	77.29	6.39	16.02	-	6.44:1.14	5:1
PVB-NSN1	73.63	5.37	13.13	7.46	6.14:0.94	6:1
PVB-NSN2	74.37	5.93	12.31	7.01	6.20:0.88	6:1

3.3.4.3 SEM images of nanofibers

The morphology of the unfunctionalized and functionalized nanofibers were observed using a scanning electron microscope (SEM) and the images are shown in Figure 3.16. The nanofibers showed no morphological changes or damage after the

functionalization step. There were some changes in the diameter of the nanofibers after the functionalizing with different ligands. The nanofiber sizes of the unfunctionalized ranges from 93-108 nm, while the size increased upon functionalization with NNN1, NNN2, NSN1, NSN2 to the ranges from 110-132, 138-161, 121-152 and 142-168 nm, respectively. These nanofibers diameters seem to be influenced by the size of the *bis*-benzimidazole derivatives, the larger the ligand the bigger the diameter.

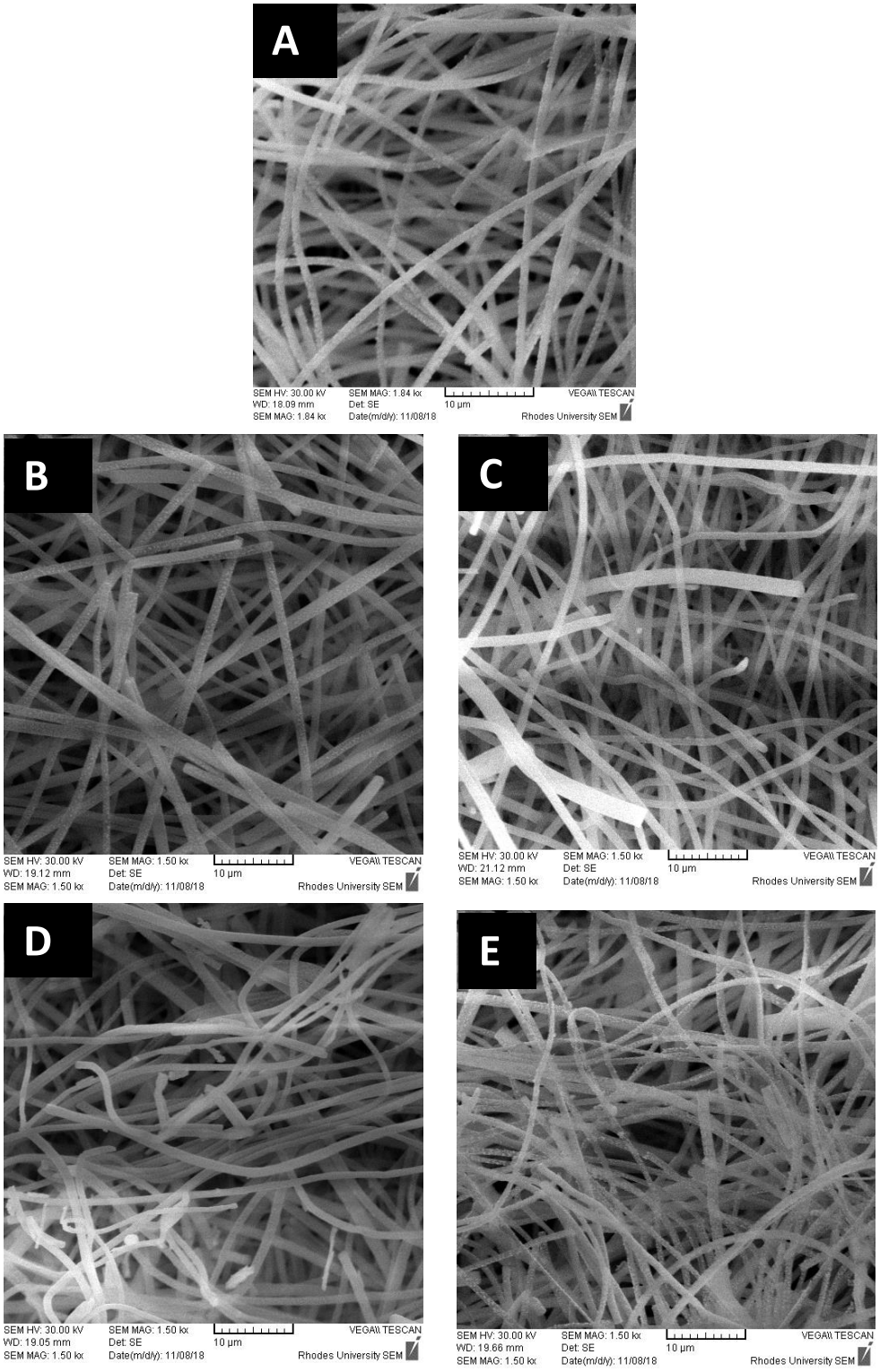

Figure 3.16: SEM images of nanofibers; (A) Unfunctionalized PVBC nanofibers, PVBC nanofibers functionalized with (B) NNN1, (C) NNN2, (D) NSN1 and (E) NSN2.

3.3.4.4 Energy dispersive spectroscopic analysis

Chemical characterization of nanofibers before and after functionalization with NNN1, NNN2, NSN1, NSN2 were investigated with energy dispersive spectroscopic analysis (EDS). The peaks showing the elements present on the sorbent materials are presented in Figure 3.17. The unfunctionalized PVBC nanofibers revealed C and Cl atoms which are expected for the nanofiber material. The functionalization of the nanofiber material with the ligands NNN1, NNN2, NSN1 and NSN2 were confirmed by the presence of N and S peaks in the spectra. Chloride peaks were also observed and are due to the unfunctionalized parts of the PVBC nanofiber.

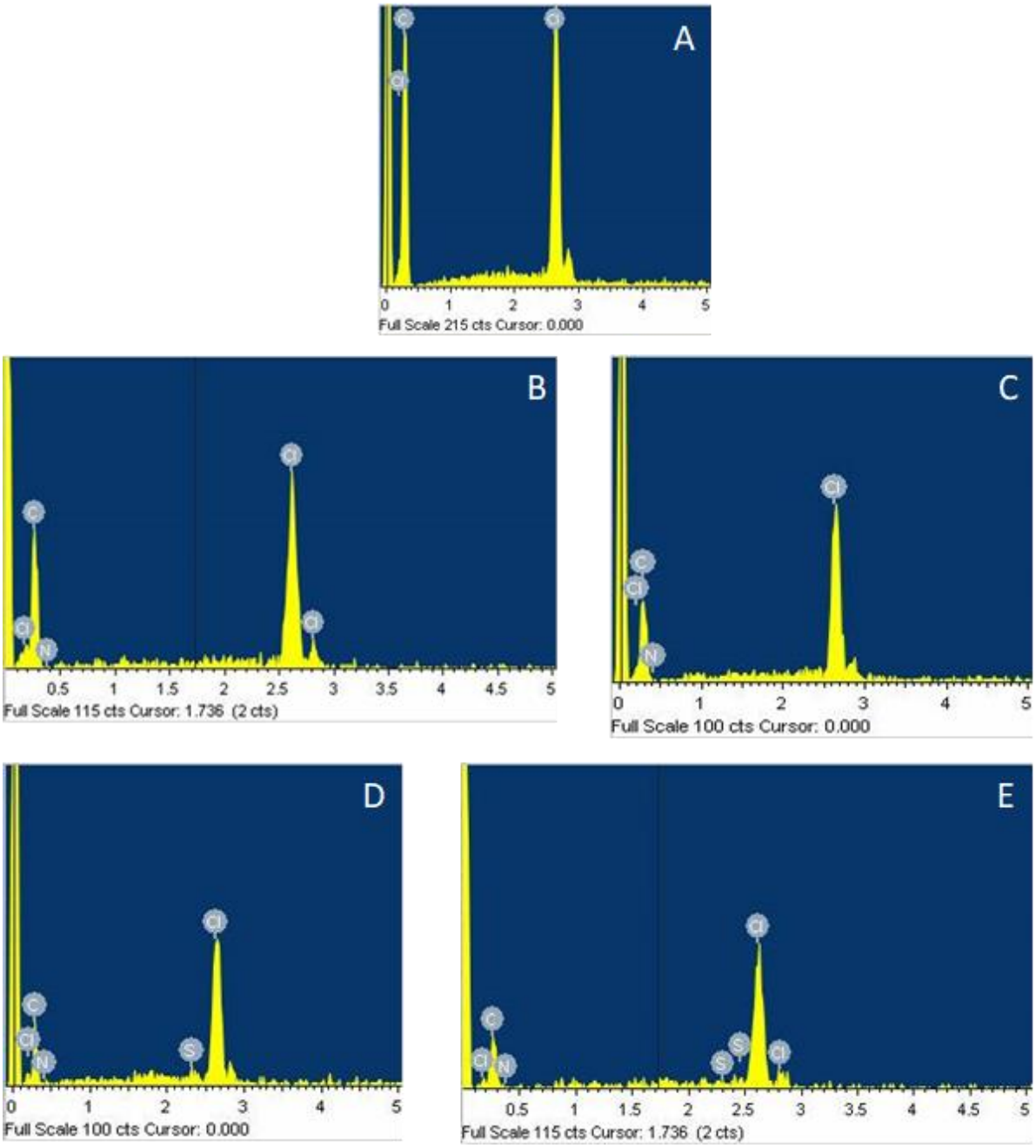

Figure 3.17: EDS images of PVBC nanofiber functionalized with; (A) PVBC, (B) NNN1, (C) NNN2, (D) NSN1 and (E) NSN2.

3.3.4.5 BET surface area of nanofibers

A Barrett–Emmett–Teller (BET) model was used to calculate the specific surface area and a Barrett–Joyner–Halenda (BJH) model was used to calculate the pore volume distribution and the average pore size Å of (A) PVBC nanofibers, (B) NNN1 nanofibers, (C) NNN2 nanofibers, (D) NSN1 nanofibers and (E) NSN2 nanofibers. The nitrogen adsorption-desorption isotherms of unfunctionalized nanofibers (PVBC) and functionalized nanofibers (PVB-NNN1, PVB-NNN2, PVBC-NSN1 AND PVBC-NSN2) are shown in Figure 3.18. Specific pore sizes and surface areas of unfunctionalized nanofibers (PVBC) and functionalized nanofibers are shown in Table 3.6.

The cavities created in unfunctionalized nanofiber (PVBC) and functionalized nanofibers (PVB-NNN1, PVB-NNN2, PVBC-NSN1 AND PVBC-NSN2) showed well defined pore openings with pore diameters of 51.33 Å (5.13 nm), 51.84 Å (5.18 nm), 52.81 Å (5.28 nm), 51.96 Å (5.20 nm) and 52.70 Å (5.27 nm), respectively, and fall in the upper end of the mesopore region (2 nm < pore diameter < 50 nm) [186–188]. Functionalized nanofibers exhibited a higher surface area than the unfunctionalized nanofibers which was unexpected. The changes in surface area from NNN1 to NSN2 was attributed to the presence of a hysteresis loop in the adsorption-desorption isotherms of the functionalized nanofibers (Figure 3.18). Hysteresis effects similar to type III were observed (Figure 3.18). PVB-NNN1 and PVB-NNN2 were observed to have type-2(b) hysteresis loop. Type-2 hysteresis loops are given by more complex pore structures in which network effects are important. The very steep desorption branch, which is a characteristic feature of hysteresis type-2(b), is associated with pore blocking [192, 194], But the size distribution of neck widths is now much larger. PVB-

NSN1 and PVB-NSN2 were observed to follow type-1 hysteresis loop that is found in materials which exhibit a narrow range of uniform mesopores [195–199].

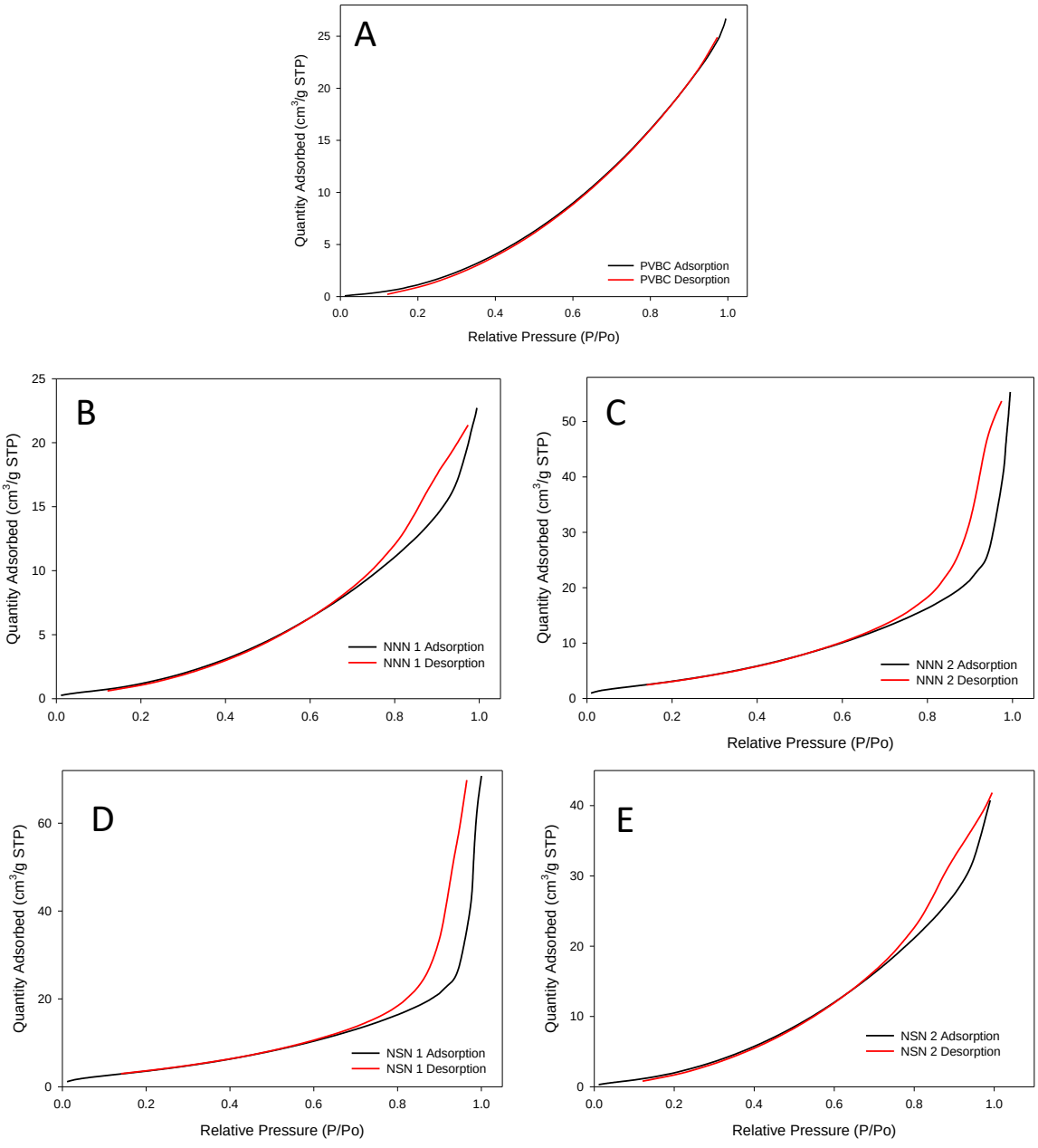

Figure 3.18: N_2 adsorption isotherms for unfunctionalized and functionalized nanofibers (with *bis*-benzimidazoles derivatives), (A) unfunctionalized PVBC nanofiber, (B) NNN1, (C) NNN2, (D) NSN1 and (E) NSN2.

Table 3.6: BET surface area of functionalized nanofibers with *bis*-benzimidazoles.

Nanofibers	BET surface area (m^2/g)	Pore Size (Å) (Adsorption)	Pore Size (Å) (Desorption)
PVBC	7.54	51.33	51.52
PVB-NNN1	9.08	51.84	56.63
PVB-NNN2	14.08	52.81	64.97
PBV-NSN1	10.57	51.96	57.27
PVB-NSN2	23.12	52.70	61.27

3.3.4.6 Thermogravimetric analysis (TGA) of nanofibers

Thermogravimetric analysis of functionalized nanofibers with NNN1, NNN2, NSN1 and NSN2 was conducted under a nitrogen atmosphere (Figure 3.19). Samples were heated from room temperature to 600°C at a heating rate of 10°C/min. The TGA curves for the functionalized nanofibers showed an initial weight loss of ~ 5% which occurred up to 100°C and was attributed to the intramolecular solvents. The TGA curves of functionalized nanofibers all gave similar decomposition patterns with a distinct three step degradation process observed at around 200ºC-300°C, 300-400°C and between 400-450°C. The first weight loss was assigned to the decomposition of the functionalized ligands which occurred at a temperature of about 200-300°C, hence, confirming the functionalized nanofiber's thermal stability, where a sharp endothermic process was observed especially for NNN1. The second weight loss resulted in a breakdown of the polymer nanofiber backbone between 300-400°C, where a small broad endothermic process was observed for NNN2, NSN1 and NSN2. The collapse of the polymer was observed from 400-450°C and thereafter residual amount has been

completely decomposed by continuous heating until the end of the measurement at 600°C where carbon will remain.

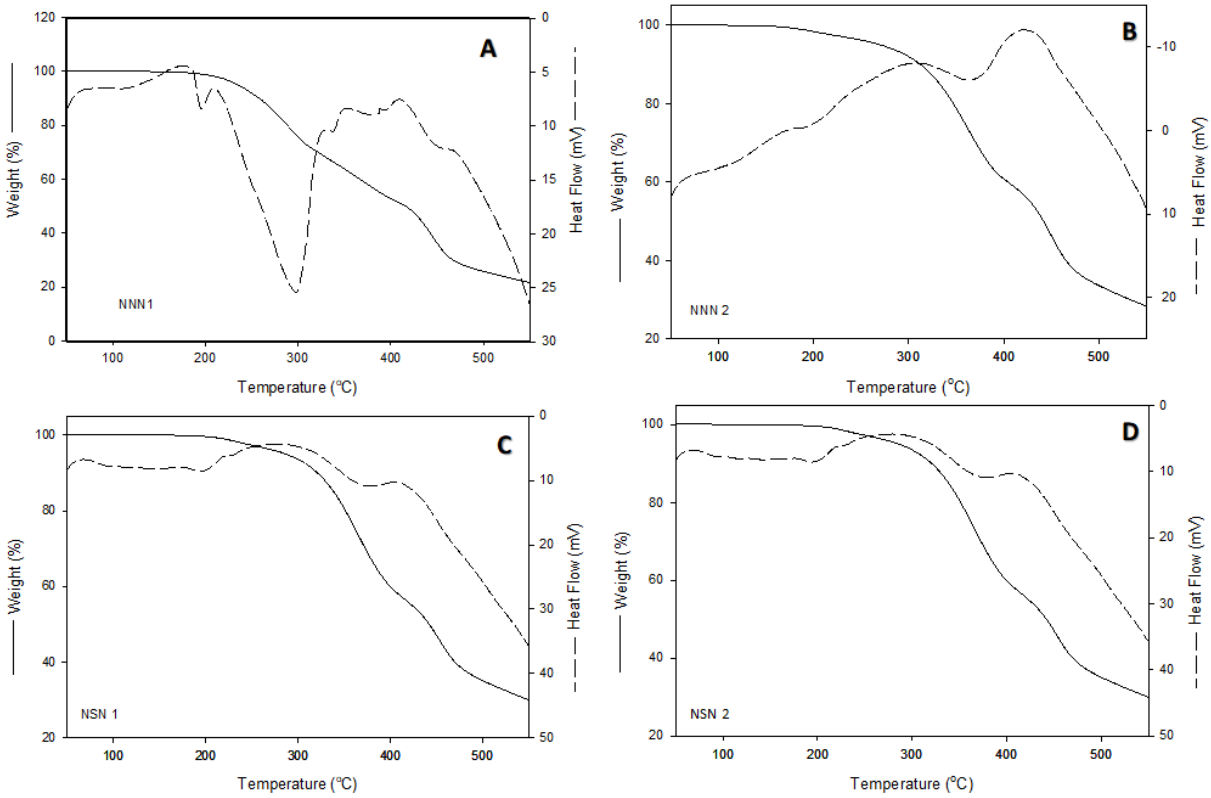

Figure 3.19: TGA diagrams for PVBC nanofibers functionalized with *bis*-benzimidazole derivatives; (A) NNN1, (B) NNN2, (C) NSN1 and (D) NSN2.

3.3.5 UV-VIS spectroscopic characterization of the metal solutions

3.3.5.1 Rhodium(III) metal ion stock solution

The synthesis of the metal ion chlorido species was carried out as outlined in the literature [196]. The rhodium complex species were confirmed spectroscopically. A peak corresponding to $RhCl_3(H_2O)_3$ was found at 485 nm using a UV-Vis Spectrophotometer (Figure 3.20).

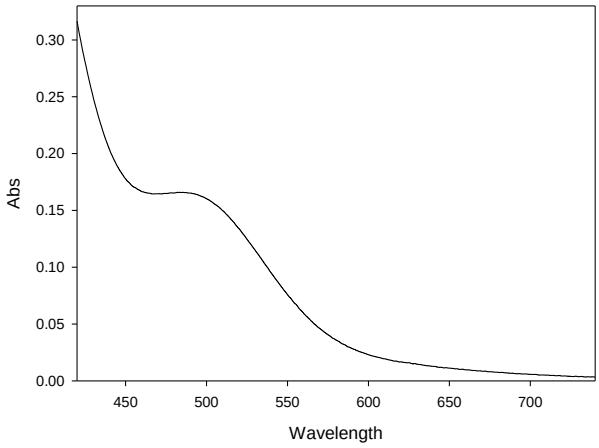

Figure 3.20: UV-Vis spectrum of $RhCl_3(H_2O)_3$ in 0.5 M HCl.

3.3.5.2 Mixed metal solutions

The synthesis of the chlorido species was carried out as outlined in section 3.3.4.2. A mixture of the precious metal ions (Pt(II), Pd(II), Ir(III) and Rh(III)) and base metal ion (Ni (II)) complex species was confirmed spectroscopically. A peak at 480 nm was observed using a UV-Vis Spectrophotometer (Figure 3.21).

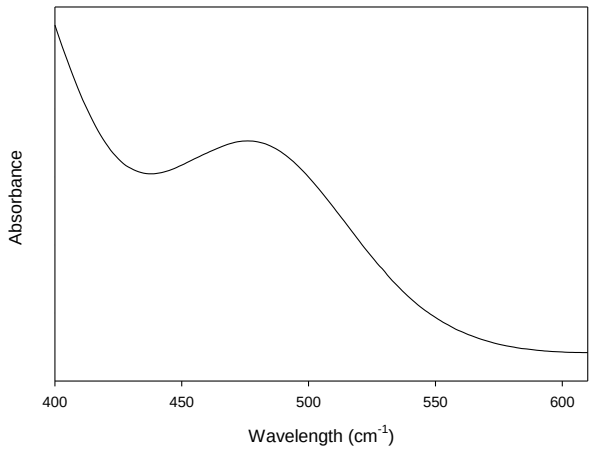

Figure 3.21: A UV-Vis spectrum of a multi-element solution containing 0.02 M Rh(III), and 0.01 M Pt(II), Pd(II), Ir(III) and Ni(II) respectively, in 0.5 M HCl.

3.3.6 Column studies and materials analysis

3.3.6.1 Single element column elution profile

The performance of the sorbents with regards to Rh(III) selectivity was studied under dynamic flow adsorption conditions. The adsorption/elution profiles of the sorbent materials are presented in Figure 4.22. The single element elution profile study was carried out to essentially understand the reactivity of *bis*-benzimidazole derivatives (ligands) hosted on nanofibers towards the rhodium(III) chlorido complex $RhCl_3(H_2O)_3$ in 0.5 M HCl medium. The column study was carried out using *bis*-benzimidazole derivatives (NNN1, NNN2, NSN1 and NSN2) hosted on nanofibers as shown in Figure 3.22. On the single element column study elution profile, it was observed the *bis*-benzimidazole derivatives show uptake of $RhCl_3(H_2O)_3$. However, the coordinated Rh(III) was observed in fractions 20-40 after stripping and elution with thiourea in HCl. The order of rhodium(III) affinity of the *bis*-benzimidazole ligands was observed as follows (from higher to lower ligand affinity); NSN1 > NSN2 > NNN2 > NNN1 as shown in Figures 3.22 and 3.23. Rhodium(III) loading capacity on the sorbents were in the following order; NSN1 (181.06 mg/g) > NSN2 (148.55 mg/g)> NNN2 (131.88 mg/g) > NNN1 (75.87 mg/g) (Figure 3.23). The rhodium that was adsorbed on the sorbent material was quantitatively eluted using 3% w/v thiourea in 5 M HCl at room temperature. A crystal structure of rhodium(II) complexed with five thiourea molecules and one chloride is shown in Figure 3.24, where it seems rhodium(III) was reduced to rhodium(II) by thiourea. Thiourea can also act as a reducing agent [197]. Rhodium(III) loading capacity on the sorbents were in the following order; NSN1 (181.06 mg/g) > NSN2 (148.55 mg/g)> NNN2 (131.88 mg/g) > NNN1 (75.87 mg/g) (Figure 3.23).

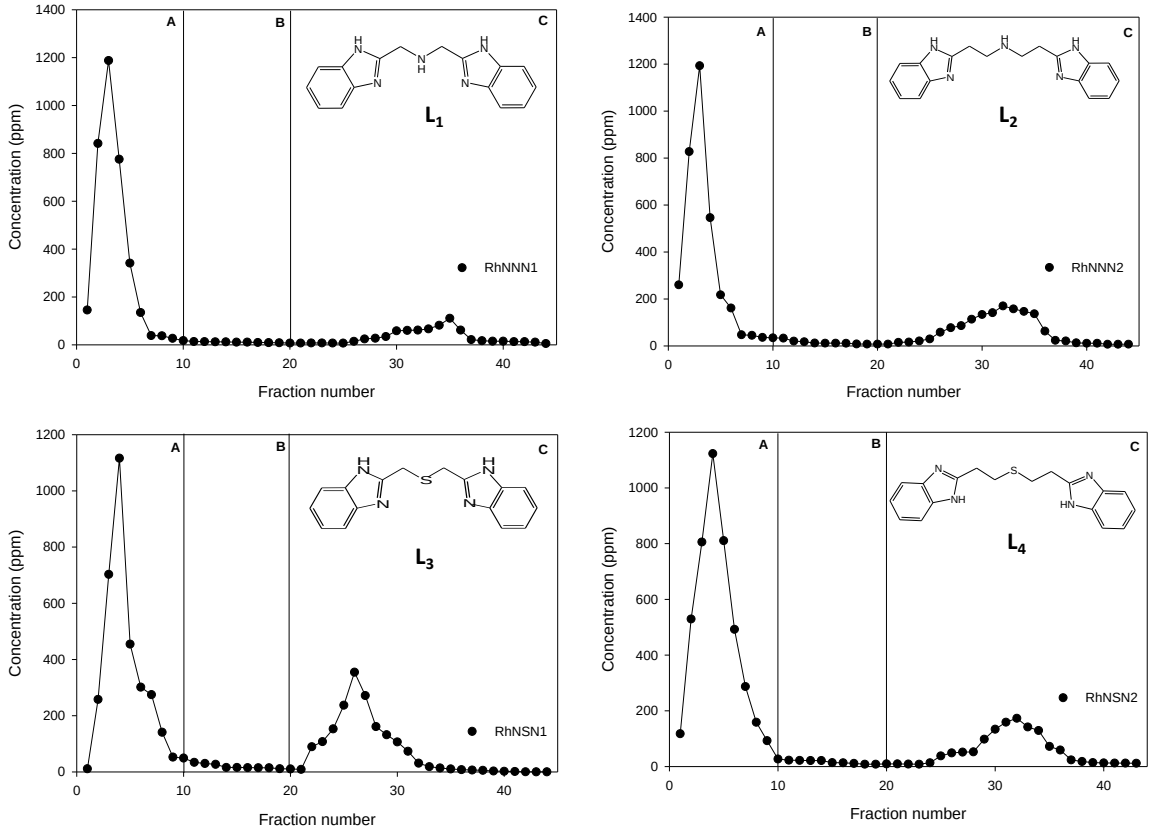

Figure 3.22: Single element column elution profile of Rh(III) in 0.5 M HCl for (L_1) NNN1, (L_2) NNN2, (L_3) NSN1 and (L_4) NSN2 in 0.1 g of nanofiber, 2 ml of 0.5 M $RhCl_3(H_2O)_3$ loaded, where (A) is the washing step with 5 ml of 0.5 M HCl, (B) is the removal of ion-paired complex step with 5 ml of 0.5 M sodium perchlorate in 5 M HCl, and (C) is the stripping and elution step with 10 ml of 3% thiourea in 5 M HCl.

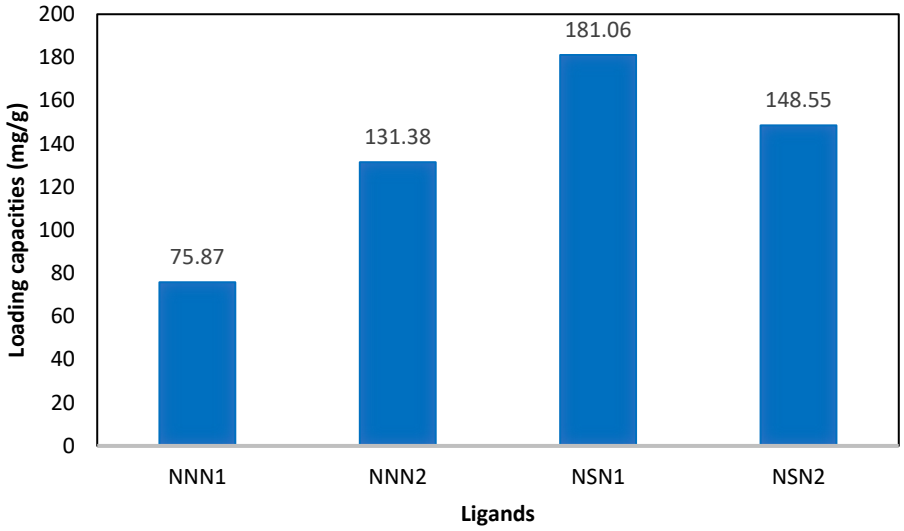

Figure 3.23: Loading capacities of Rh(III) in 0.5 M HCl using nanofibers functionalized with *bis*-benzimidazole derivatives (NNN1, NNN2, NSN1 and NSN2).

3.3.6.1.1 Rhodium(II) complex formed with thiourea

$[RhCl(tu)_5]Cl$ complex was obtained after eluting with 3% w/v of thiourea in 5 M HCl, thiourea also acted as a reducing agent [197]. The geometry of the complex is suggested to be distorted octahedral (Figure 3.24) and was isolated in a triclinic crystal system and P-1 space group. Selected crystal data and bond angles and lengths are shown in Tables 3.7-3.8. The triclinic crystal system is described by vectors of unequal length, as in the orthorhombic system. In addition, the angles between these vectors must all be different. The counter ion to the $[RhCl(tu)_5]Cl_2$ complex is a chloride. The crystal data gives an indication of how Rh(III) ions are complexed occurs during column study stripping/elution step, thereby facilitating the selective removal of the rhodium metal ions.

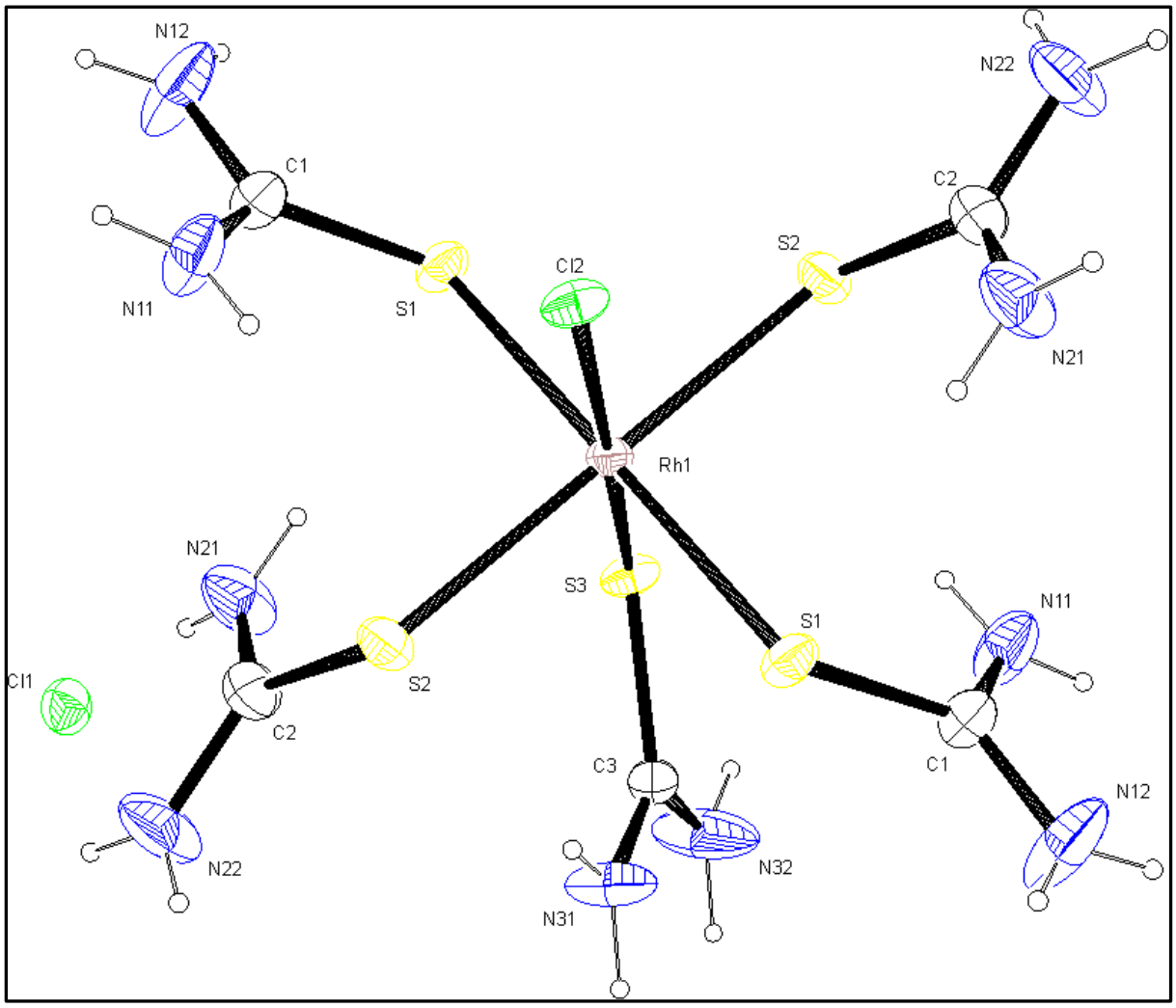

Figure 3.24: ORTEP diagram of $[RhCl(tu)_5]Cl$ showing the atom-labelling scheme.

Table 3.7: Selected crystallographic data for $[RhCl(tu)_5]Cl$.

Compound	**$[RhCl(tu)_5]Cl$**
Chemical formula	$C_5H_{20}ClN_{10}RhS_5$, 2(Cl)
Formula weight	589.87
Crystal colour	Orange
Crystal system	triclinic
Space group	P-1
Temperature (K)	200
Crystal size (mm^{-3})	0.05 x 0.25 x 0.38
α (Å)	6.7346(4)
b (Å)	8.3196(4)
c (Å)	10.3753(4)
α (˚)	83.132(2)
β (˚)	81.739(1)
ɣ (˚)	76.023(2)
V (Å)	556.07(5)
Z	1
D_{calc} ($g\ cm^3$)	1.762
μ/mm^{-1}	1.610
F (000)	296
Theta min-max (˚)	2.0, 28.3
S	1.15
Tot.uniq.data, r(int)	24533, 2756, 0.020
Observed data [I>2.0σ(I)]	2628
R	0.0169
R_w	0.0419

Table 3.8: Selected bond distances (Å) and angles (°) for [RhCl(tu)$_5$]Cl.

[RhCl(Th)$_5$]Cl	
Bond distances (Å)	
Rh1-Cl2	2.358(14)
Rh1-S1	2.3827(4)
Rh1-S2	2.3915(4)
Rh1-S3	2.377(14)
Rh1-S1_a	2.3827(4)
Rh1-S2_a	2.3915(4)
Bond angles (°)	
Cl2-Rh1-S1	87.6(3)
Cl-Rh1-S2	93.7(4)
Cl2-Rh1-S3	4.5(5)
Cl2-Rh1-Cl2_a	180.00
Cl2-Rh1-S1_a	92.4(3)
Cl2-Rh1-S2_a	86.3(4)
S1-Rh1-S2	97.48(1)
S1-Rh1-S3	83.2(3)
Cl2_a-Rh1-S1	92.4(3)
S1-Rh1-S1_a	180.00
S1-Rh1-S2_a	82.52(1)
S2-Rh1-S3	94.9(4)

3.3.6.1.2 Scanning electron microscope (SEM) analysis of the used sorbent material

The morphology of the used sorbent materials NSN1 and NSN2 were observed using a scanning electron microscope (SEM) and the images are shown in Figure 3.25. The morphology of the used functionalized nanofibers after elution with 3% w/v thiourea were observed. The nanofibers showed no morphological changes or damage after the column study. The SEM images do not show any significant changes in the size or shape of the sorbent materials, indicating possible reusability of the sorbent materials with minimum loss in functionality.

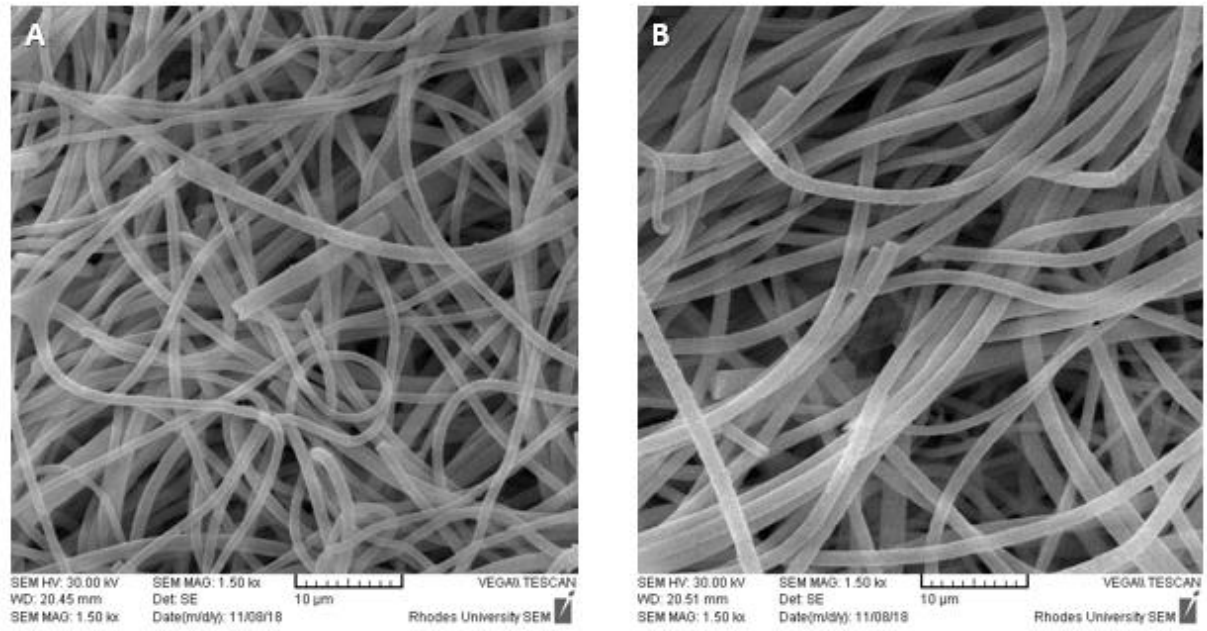

Figure 3.25: SEM images of used nanofibers after a column study based on a single element (Rh); (A) NSN1 and (B) NSN2.

3.3.6.1.3 Energy dispersive spectroscopy (EDS) analysis of used sorbent material

The recovery of rhodium ions from the sorbent materials was investigated by the EDS analysis of materials (Figure 3.26) after elution with 3% w/v thiourea. The presence of the S and N peaks in the spectra of the NSN1 and NSN2 sorbent materials confirmed the retention of the ligands on the materials after use. The spectra suggest that the stripping agent was effective in removing the adsorbed Rh on the NSN1 and NSN2 sorbent materials as trace amounts of adsorbed Rh were observed on the spectrum based on the peak at 3.3 eV. There seem to be big peaks for Rh which are not representative of traces of metals quantities, and the only explanation is that they are riding on the big sulfur and chloride peaks.

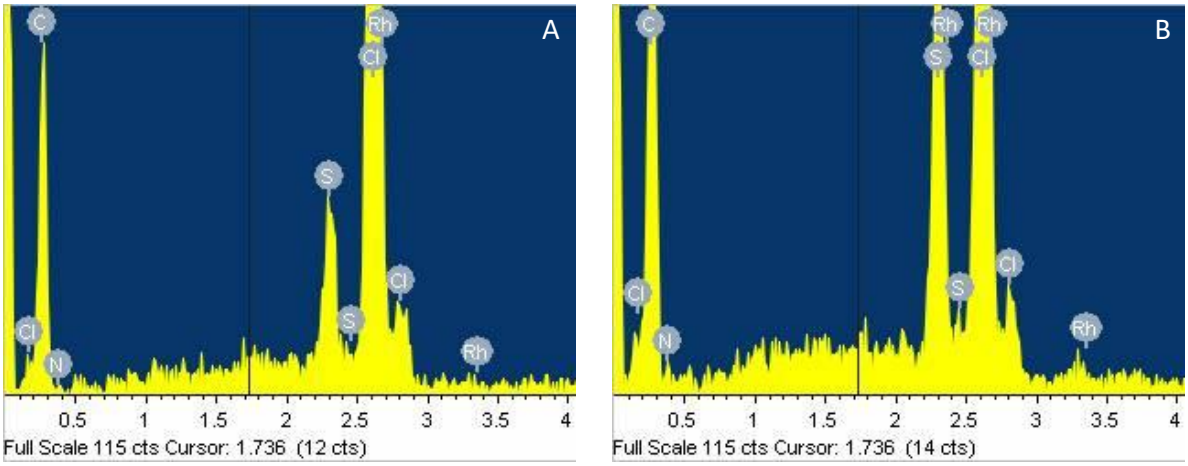

Figure 3.26: EDS spectra of single element (Rh) sorbent materials after 3% w/v thiourea (a) NSN1, (b) NSN2.

3.3.6.2 Multi-element column elution profile

The performance of the sorbents with regards to Rh(III) selectivity over Pd(II), Pt(IV), Ir(III) and Ni(II) was studied under dynamic flow adsorption conditions. The adsorption/elution profiles of the sorbent materials are presented in Figures 3.27-3.30. The column study was carried out using *bis*-benzimidazole derivatives (NNN1, NNN2, NSN1 and NSN2) hosted on nanofibers, loaded with a multi-element solution containing 0.02 M Rh(III) and 0.01 M (Pt(II), Pd(II), Ir(III) and Ni(II). The column was washed with 0.5 M HCl to remove unabsorbed ions, followed by perchlorate and then stripping/ elution with thiourea solution in HCl as described before.

The multi-element column elution profile for NNN1, NNN2, NSN1 and NSN2 resins showed uptake of Rh, Pt, Pd and Ir, and no uptake of nickel was detected by ICP. All the nickel was washed out at the washing step. Rh, Pt, Pd and Ir were stripped/eluted using 3% w/v thiourea in 5 M HCl at room temperature. The order of preference of the ligands for the metals is summarized below. NNN1 resin showed preference for the PGMs in the order of Pd(II) (0.45 mmol/g) > Rh(III) (0.17 mmol/g) > Pt(II) (0.08 mmol/g) > Ir(III) (0.03 mmol/g). NNN2 resin showed preference for the PGMs in the order of Pd(II) (0.27 mmol/g) > Pt(II) (0.17 mmol/g) > Rh(III) (0.14 mmol/g) > Ir(III) (0.04 mmol/g). NSN1 resin showed preference for the PGMs in the order of Rh(III) (0.46 mmol/g) > Pt(II) (0.16 mmol/g) > Pd(II) (0.15 mmol/g) > Ir(III) (0.03 mmol/g). NSN2 resin also showed preference for the PGMs in the order of; Rh(III) (0.19 mmol/g) > Pd(II) (0.15 mmol/g) > Pt(II) (0.12 mmol/g) > Ir(III) (0.06 mmol/g). NSN1 had a higher loading capacity for rhodium(III) uptake than NSN2. All loading capacities are shown in Figure 3.31.

The order of preference of the metals for the ligands is summarized below. Pt(II): NNN2 (33.96 mg/g) > NSN1 (30.95 mg/g) > NSN2 (23.89 mg/g) > NNN1(14.92 mg/g). Pd(II): NNN1 (47.94 mg/g) > NNN2 (28.90 mg/g) > NSN1 (16.22 mg/g) > NSN2 (0.27 mg/g). Ir(III): NSN2 (10.64 mg/g) > NNN2 (6.84 mg/g) > NSN1 (5.74 mg/g) > NNN1 (5.02 mg/g). Rh(III): NSN1 (47.28 mg/g) > NSN2 (19.95 mg/g) > NNN1 (17.47 mg/g) > NNN2 (14.91 mg/g). The experimental studies compared well with theoretical studies in that NSN1 is the most preferred with Rh(III) in the *fac* geometry. This shows the preferred coordination with Rh(III) is the five-membered chelate ring.

Pt(II) and Pd(II) prefer ligands such as NNN2 and NNN1, respectively. These ligands have a higher σ donor character than NSN1 and NSN2 hence have a stronger interaction with Pt(II) and Pd(II). The divalent metals are proposed to possibly form spin paired square planar complexes with NNN1 and NNN2. Rh(III) and Ir(III) prefer ligands containing N and S donor atoms such as NSN1 and NSN2. These ligands have π acceptor character. Rhodium and iridium are very stable at their trivalent states as these metals are known to form kinetically inert octahedral complexes [198–200]. Due to different oxidation states between platinum(II) and palladium(II), rhodium(III) and iridium(III), the kinetics and the thermodynamics of substitution will be different for the metal ions with the ligands. But this study is beyond the scope of this thesis.

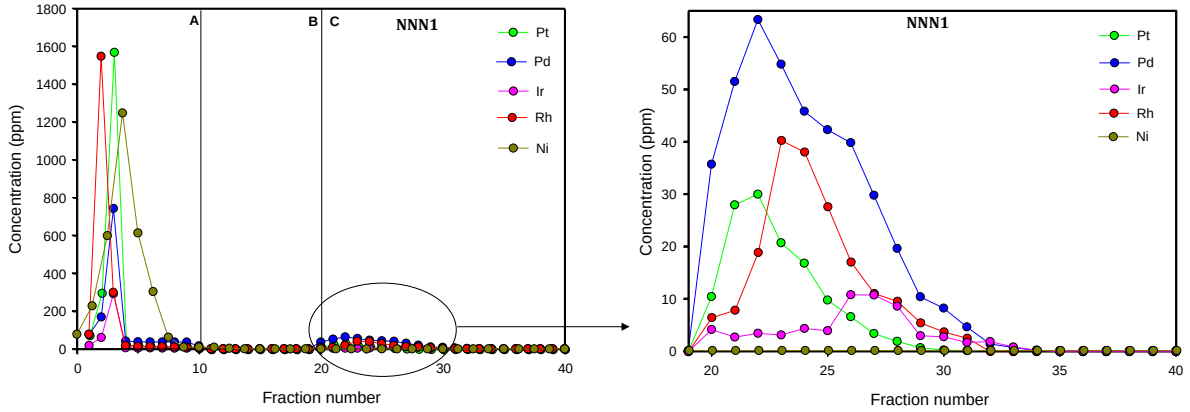

Figure 3.27: (1) Multi-element column elution profile of 0.02 M Rh(III), 0.01 M (Pt(IV), Pd(II), Ir(III) and Ni(II), respectively, in 0.5 M HCl for NNN1 on 0.1 g of nanofiber, 2 ml of 0.5 M $RhCl_3(H_2O)_3$ loaded, where (A) is the washing step with 5 ml of 0.5 M HCl, (B) is the removal of ion-paired complex step with 5 ml of 0.5 M sodium perchlorate in 5 M HCl, and (C) is the stripping and elution step with 10 ml of 3% thiourea in 5 M HCl. **(2)** Expanded elution step with 10 ml of 3% thiourea in 5 M HCl.

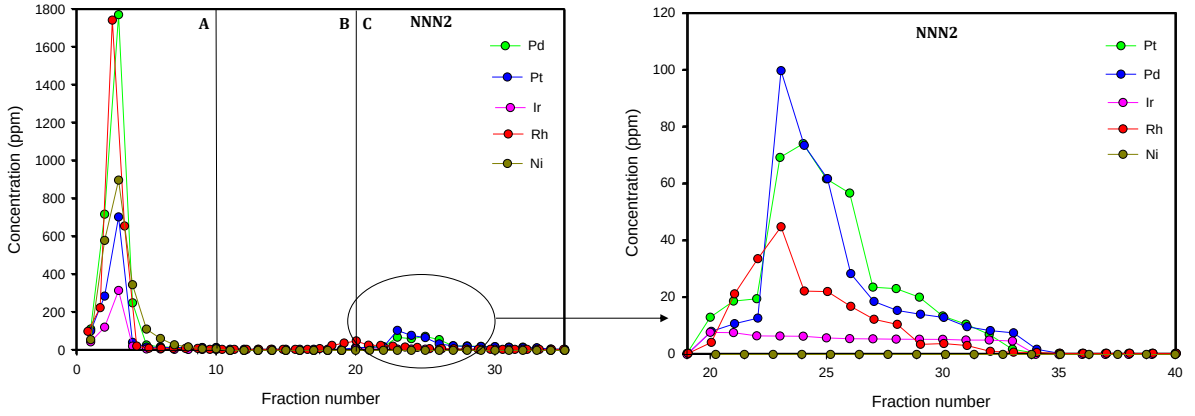

Figure 3. 28: (1) Multi-element column elution profile of 0.02 M Rh(III), 0.01 M (Pt(IV), Pd(II), Ir(III) and Ni(II), respectively, in 0.5 M HCl for NNN2 on 0.1 g of nanofiber, 2 ml of 0.5 M $RhCl_3(H_2O)_3$ loaded, where (A) is the washing step with 5 ml of 0.5 M HCl, (B) is the removal of ion-paired complex step with 5 ml of 0.5 M sodium perchlorate in 5 M HCl, and (C) is the stripping and elution step with 10 ml of 3% thiourea in 5 M HCl. **(2)** Expanded elution step with 10 ml of 3% thiourea in 5 M HCl.

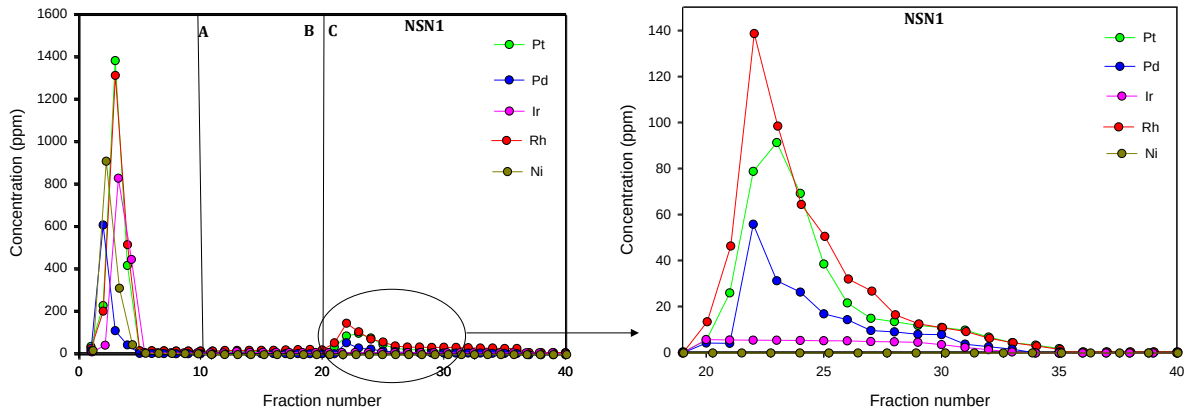

Figure 3.29: (1) Multi-element column elution profile of 0.02 M Rh(III), 0.01 M (Pt(IV), Pd(II), Ir(III) and Ni(II), respectively, in 0.5 M HCl for NSN1 on 0.1 g of nanofiber, 2 ml of 0.5 M $RhCl_3(H_2O)_3$ loaded, where (A) is the washing step with 5 ml of 0.5 M HCl, (B) is the removal of ion-paired complex step with 5 ml of 0.5 M sodium perchlorate in 5 M HCl, and (C) is the stripping and elution step with 10 ml of 3% thiourea in 5 M HCl. **(2)** Expanded elution step with 10 ml of 3% thiourea in 5 M HCl.

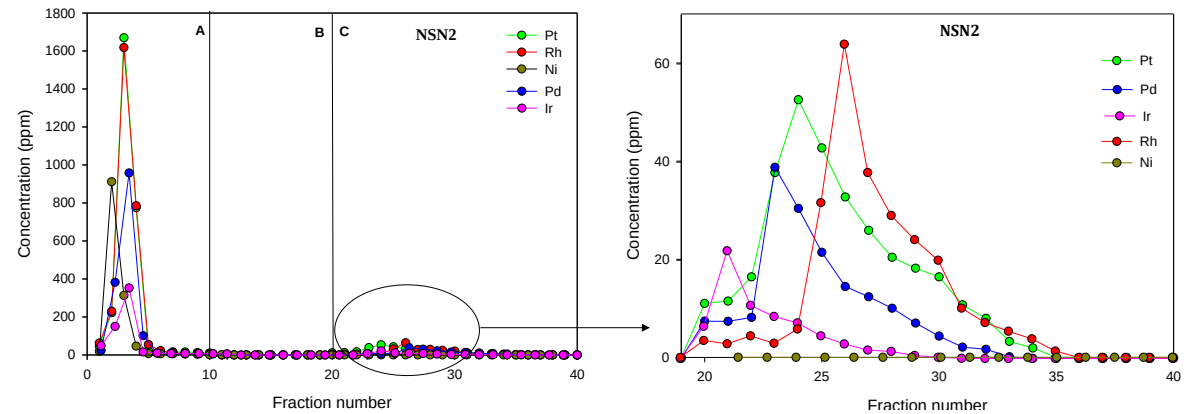

Figure 3.30: (1) Multi-element column elution profile of 0.02 M Rh(III), 0.01 M (Pt(IV), Pd(II), Ir(III) and Ni(II), respectively, in 0.5 M HCl for NSN2 on 0.1 g of nanofiber, 2 ml of 0.5 M $RhCl_3(H_2O)_3$ loaded, where (A) is the washing step with 5 ml of 0.5 M HCl, (B) is the removal of ion-paired complex step with 5 ml of 0.5 M sodium perchlorate in 5 M HCl, and (C) is the stripping and elution step with 10 ml of 3% thiourea in 5 M HCl. **(2)** Expanded elution step with 10 ml of 3% thiourea in 5 M HCl.

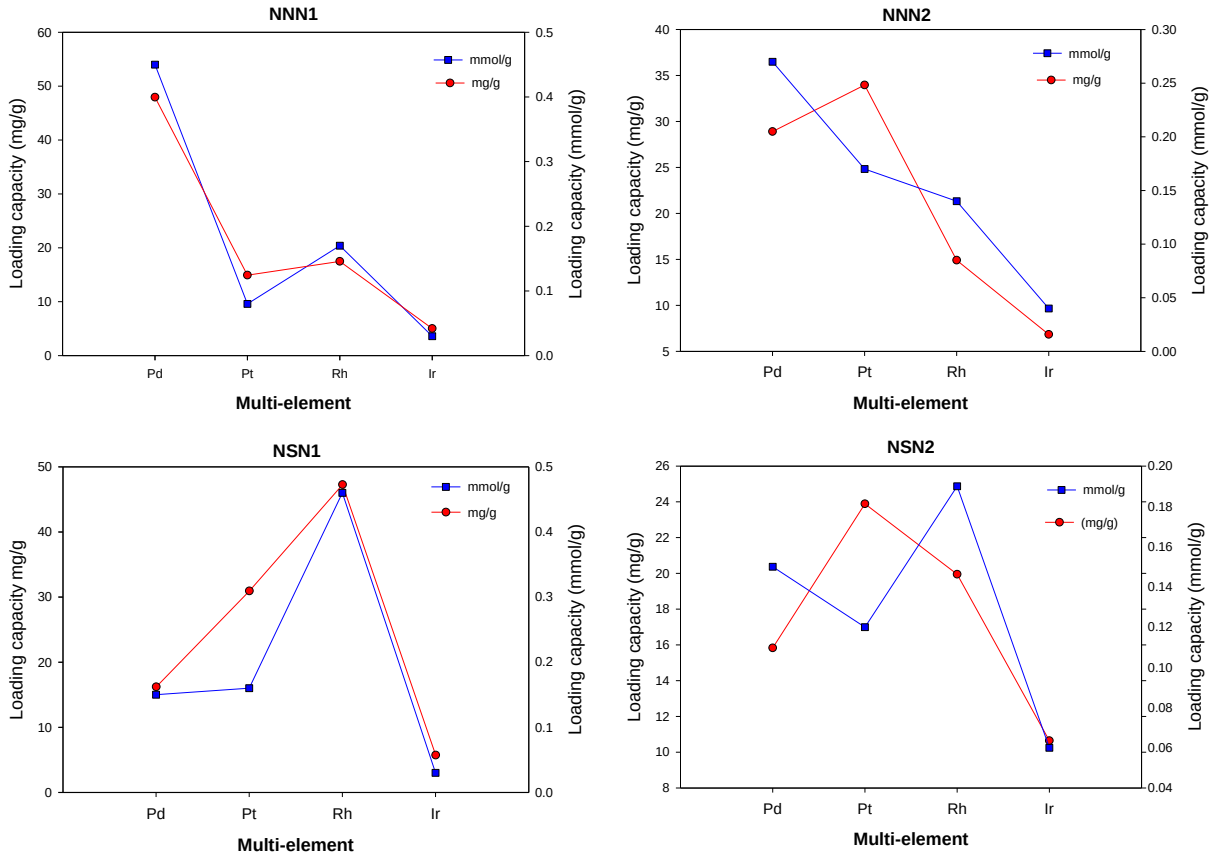

Figure 3.31: Loading capacities of multi-element (Rh, Pt, Pd and Ir) in 0.5 M HCl extracted using *bis*-benzimidazole derivatives (NNN1, NNN2, NSN1 and NSN2) hosted on nanofibers.

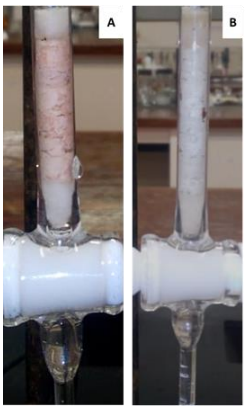

Figure 3.32: NNN2 nanofibers used for multi-element column study; (A) before and (B) after the stripping/elution step with 3% thiourea in 5 M HCl.

The functionalized nanofibers had a light red colour at the stripping/elution step after a multi-element solution was loaded onto the column (Figure 3.32). This confirmed the adsorption of metals on the NNN2 nanofibers. The resin was further eluted with 3 % w/v thiourea in 5 M HCl, and a yellow a solution was observed as the column was being eluted, 0.5 ml fractions were collected and analysed by ICP-OES. It was observed that all the functionalized nanofibers were changing colour from the light red colour to a white resin and this confirmed the removal of metals that were adsorbed on the column. This was also confirmed by EDS after eluting with 3 % w/v thiourea in 5 M HCl.

3.3.6.2.1 Scanning electron microscope (SEM) analysis of the used sorbent material

The morphology of the used sorbent materials, functionalized with NNN1 and NSN2, were observed using a scanning electron microscope (SEM) and the images are shown in Figure 3.33. The morphology of the used functionalized nanofibers after eluting with 3% w/v thiourea was imaged. The nanofibers showed no morphological changes but only slight patches of foreign material for NSN2 fibers (B). The SEM images do not show any significant changes in the size or shape of the sorbent materials, indicating possible reusability of the sorbent materials with minimum loss in functionality.

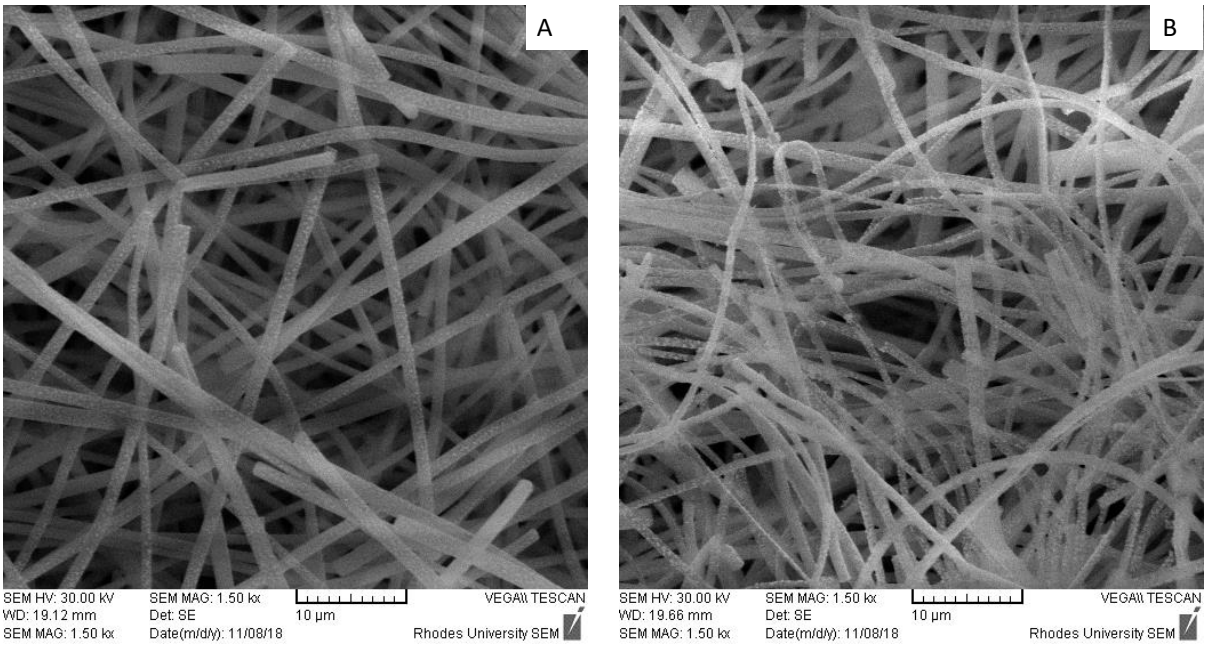

Figure 3.33: SEM images of used nanofibers for multi-metal studies (Rh, Pt, Pd, Ir and Ni) after stripping/elution with 3% w/v thiourea; (A) NNN1 and (B) NSN2.

3.3.6.2.2 Energy dispersive spectroscopy (EDS) analysis of used sorbent material

The recovery of metal ions from the sorbent materials was investigated by EDS analysis of materials (Figure 3.34) after elution with 3% w/v thiourea. The presence of the N and S peaks in the spectra of the NNN1 and NSN2 sorbent materials confirmed the retention of the ligands on the materials after use. The spectra suggested that the stripping agent was effective in removing the adsorbed Rh, Ir, Pd and Pt on the NNN1 and NSN2 sorbent materials and that there were traces amounts of adsorbed Rh, Pd and Pt. There seem to be big peaks for Rh, Pd and Pt which are not representative of traces metals quantities, and the only explanation is that they are riding on the big sulfur and chloride peaks.

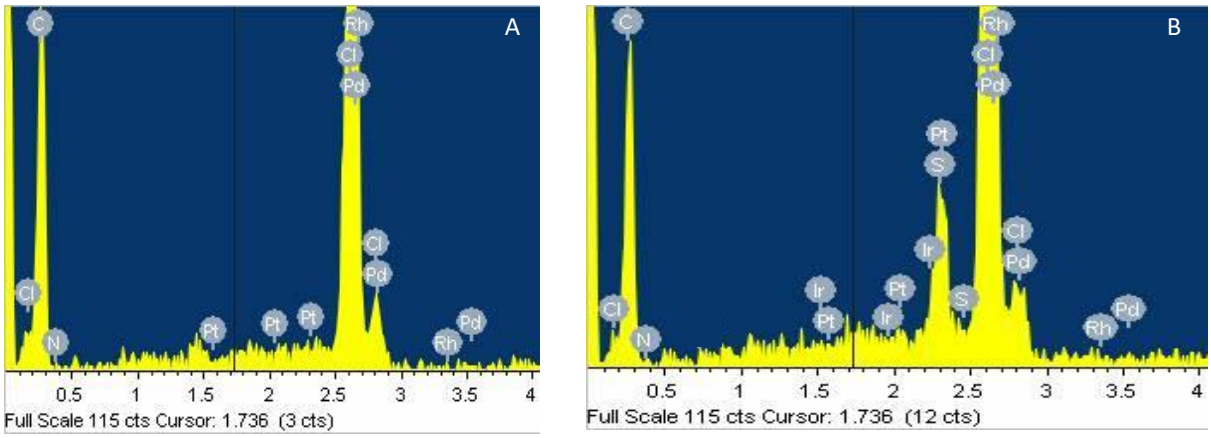

Figure 3.34: EDS spectra of sorbent material used for multi-metal studies (Rh, Pt, Pd, Ir and Ni) after 3% w/v thiourea (a) NNN1, (b) NSN2.

3.3.7 Adsorption studies

Adsorption studies of *bis*-benzimidazole ligands were performed by a batch process for a better understanding of the adsorption kinetics and isotherms. In the adsorption studies, the effect of time on the adsorption of Pt(II), Pd(II), Ir(III), Rh(III) and Ni(II), using *bis*-benzimidazoles derivatives (NNN1, NNN2, NSN1 and NSN2) hosted on nanofibers, were studied (Figures 3.35-3.42). *Bis*-benzimidazoles functionalized nanofibers show that the adsorption of metal ions was initially fast due to the availability of active sites on the surface of the sorbents. Adsorption equilibrium was reached within 6-7 minutes and the adsorption rate slowed as surface saturation was reached. Figures 3.35-3.38 show the adsorbed fraction of metal ions as the function of time. Figures 3.39-3.42 show the percentage of adsorption as the function of time.

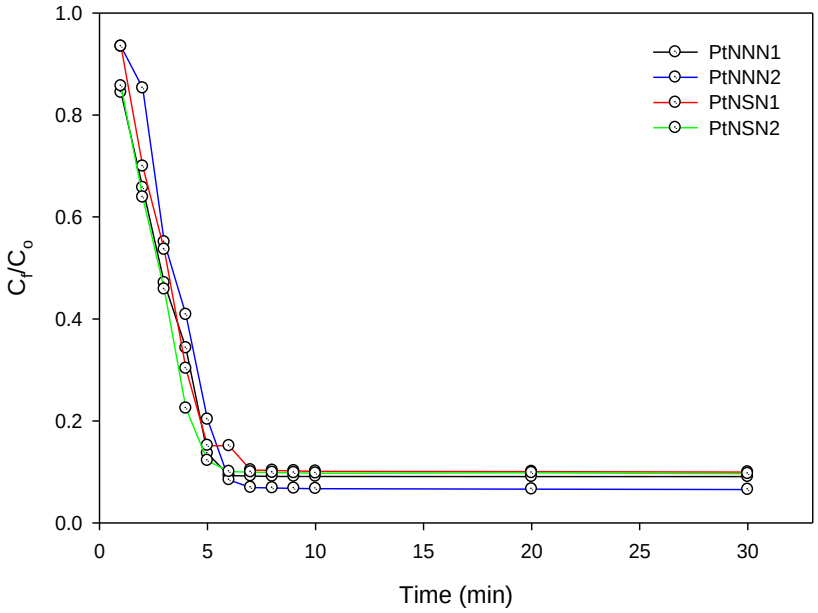

Figure 3. 35: Adsorbed fraction of platinum(II) in presence of *bis*-benzimidazole derivatives hosted on nanofibers.

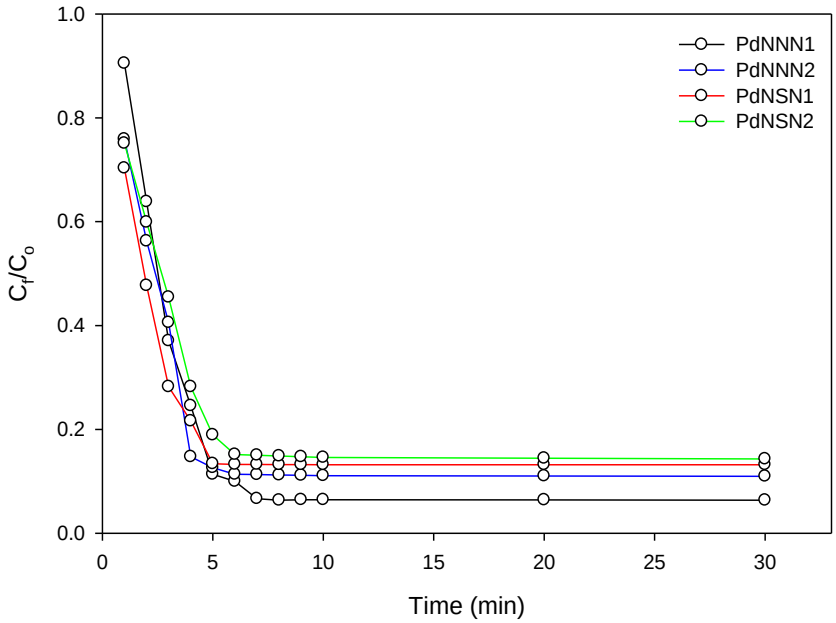

Figure 3.36: Adsorbed fraction of palladium(II) in presence of *bis*-benzimidazole derivatives hosted on nanofibers.

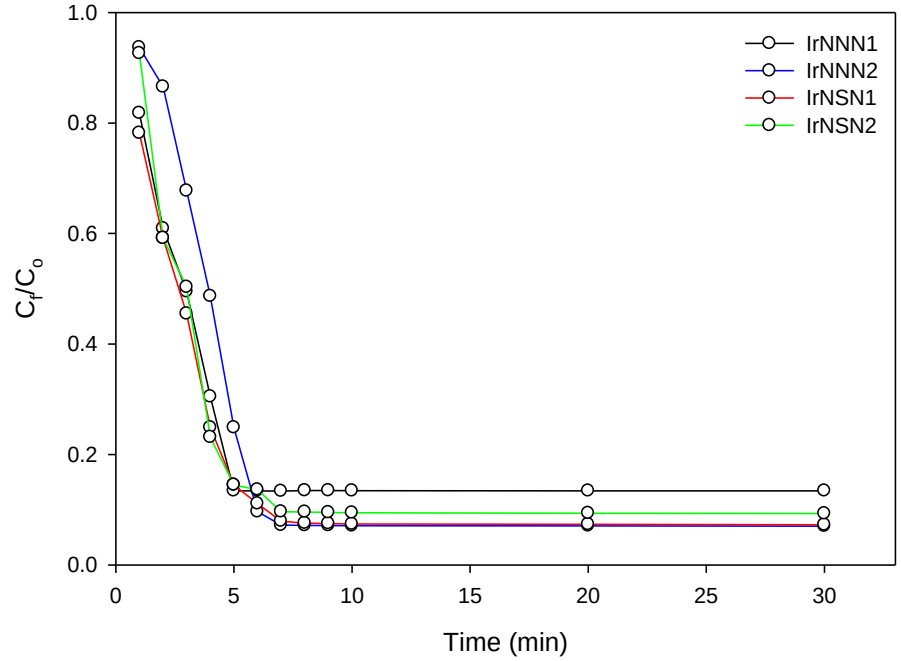

Figure 3.37: Adsorbed fraction of iridium(III) in presence of *bis*-benzimidazole derivatives hosted on nanofibers.

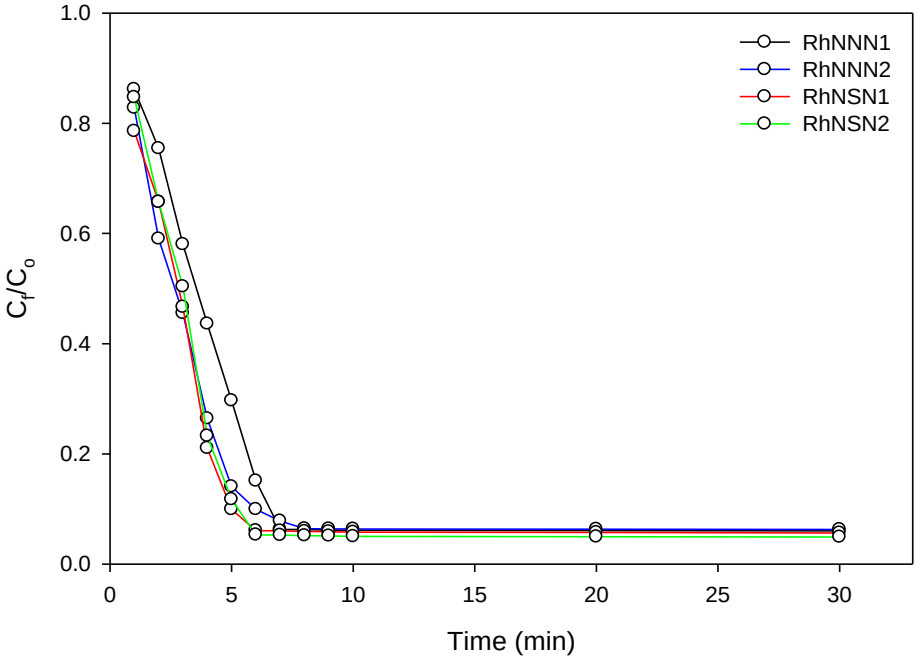

Figure 3.38: Adsorbed fraction of rhodium(III) in presence of *bis*-benzimidazole derivatives hosted on nanofibers.

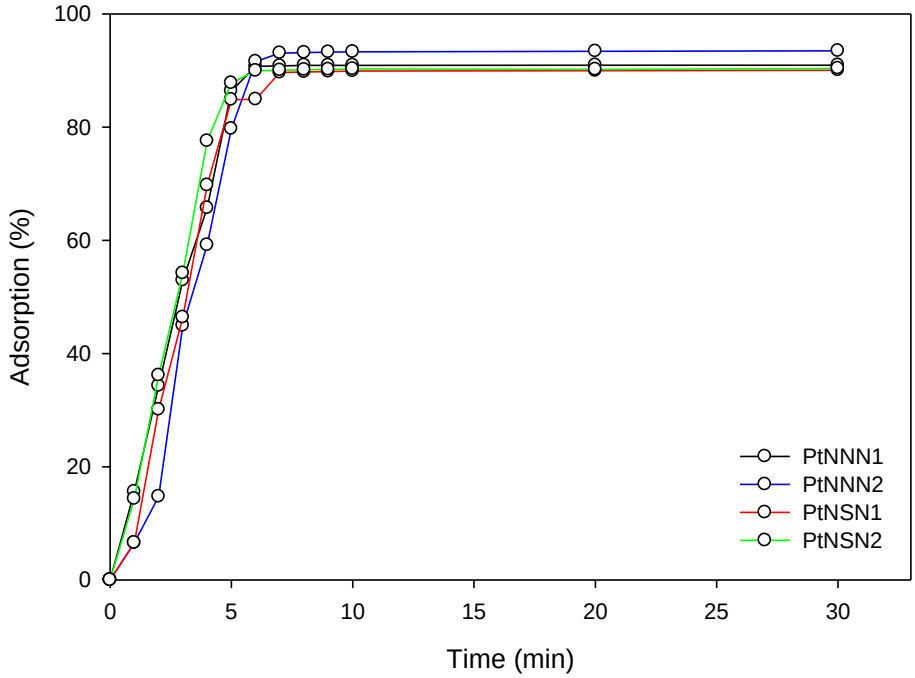

Figure 3.39: Percentage adsorption of platinum(II) in presence of *bis*-benzimidazole derivatives hosted on nanofibers.

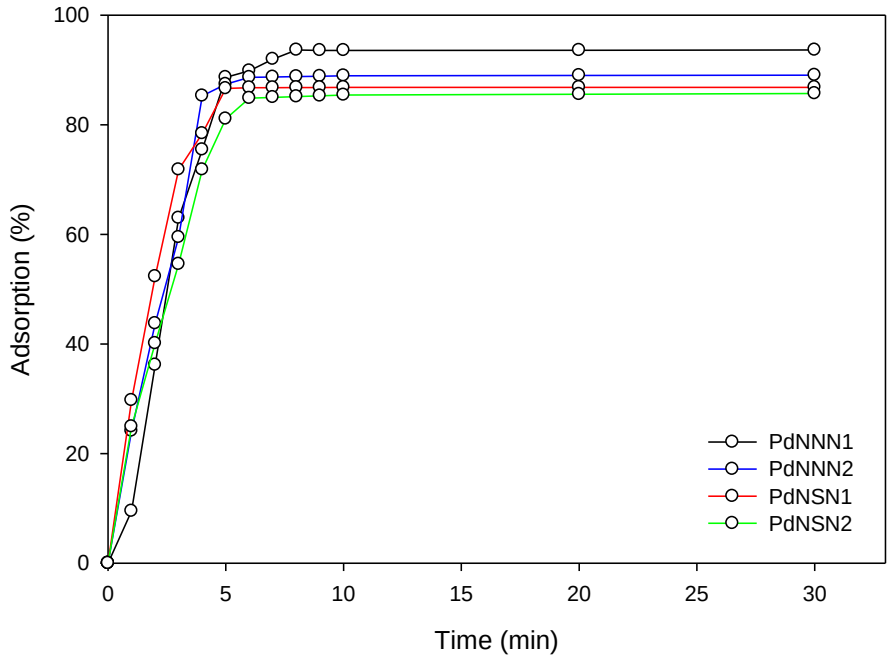

Figure 3.40: Percentage adsorption of palladium(II) in presence of *bis*-benzimidazole derivatives hosted on nanofibers.

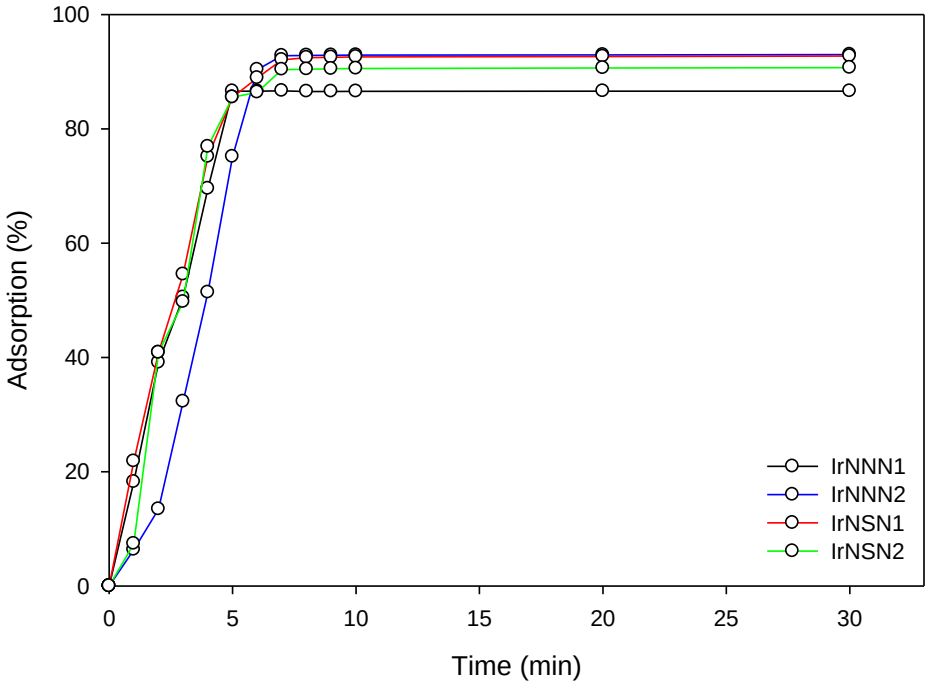

Figure 3.41: Percentage adsorption of iridium(III) in presence of *bis*-benzimidazole derivatives hosted on nanofibers.

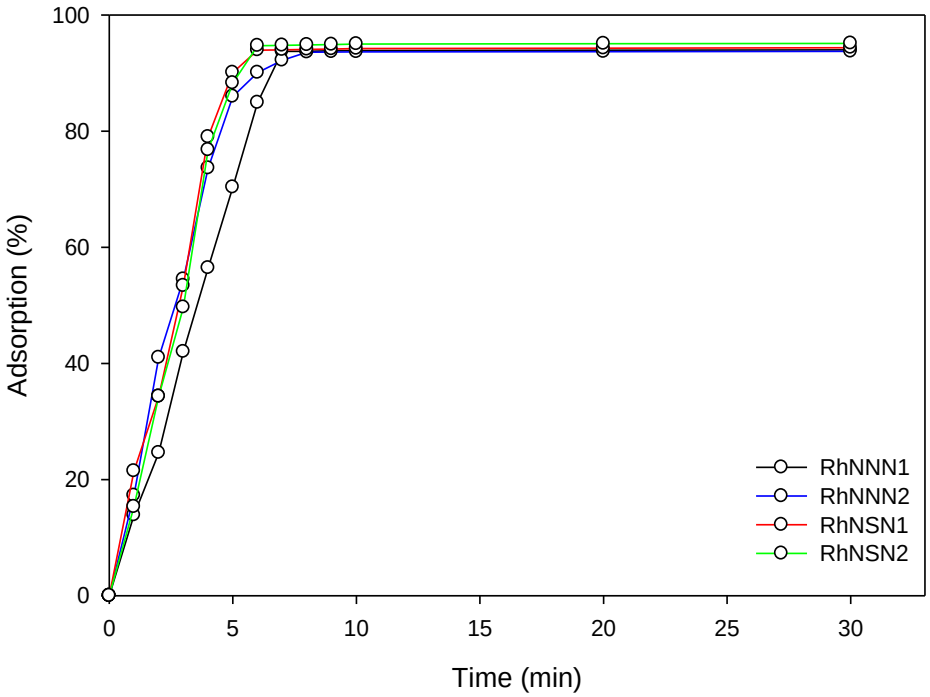

Figure 3.42: Percentage adsorption of rhodium(III) in presence of *bis*-benzimidazole derivatives hosted on nanofibers.

3.3.7.1 Adsorption kinetics

The kinetic mechanism that controls the adsorption process under batch study was followed by the pseudo-first-order model and pseudo-second-order model. In the pseudo-first-order model, it is assumed that adsorption takes place *via* a physical process, while the pseudo-second-order assumes that adsorption takes place *via* a chemical process [75, 151, 198, 199]. The plot of log q_e-q_t vs time (t) gave a straight line with R^2 values close to 1 for all adsorbents (NNN1, NNN2, NSN1 and NSN2) compared to the pseudo-second-order kinetics Figures 3.43-3.50. Tables 3.9-3.12 presents the R^2 coefficient as well as the kinetic constants for all sorbents.

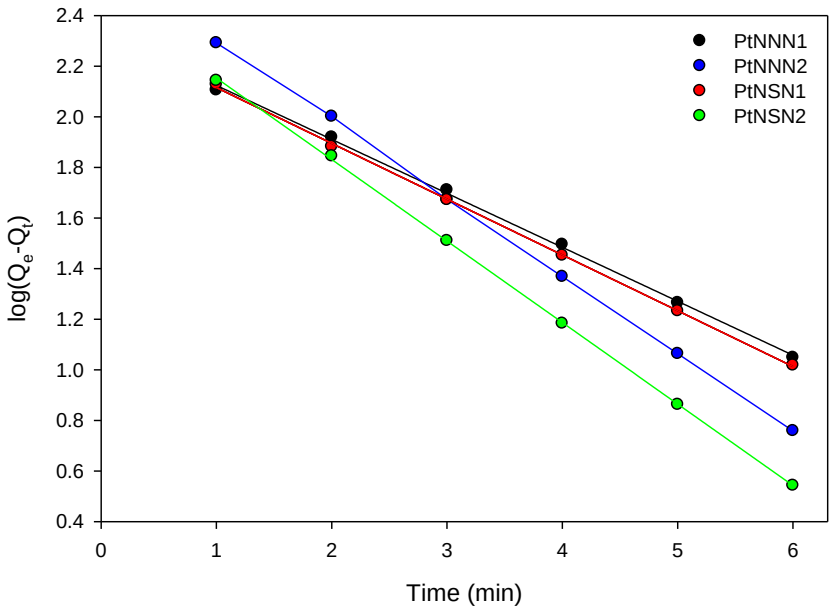

Figure 3.43: Pseudo-first-order plot for adsorption of platinum(II) using *bis*-benzimidazole derivatives hosted on nanofibers.

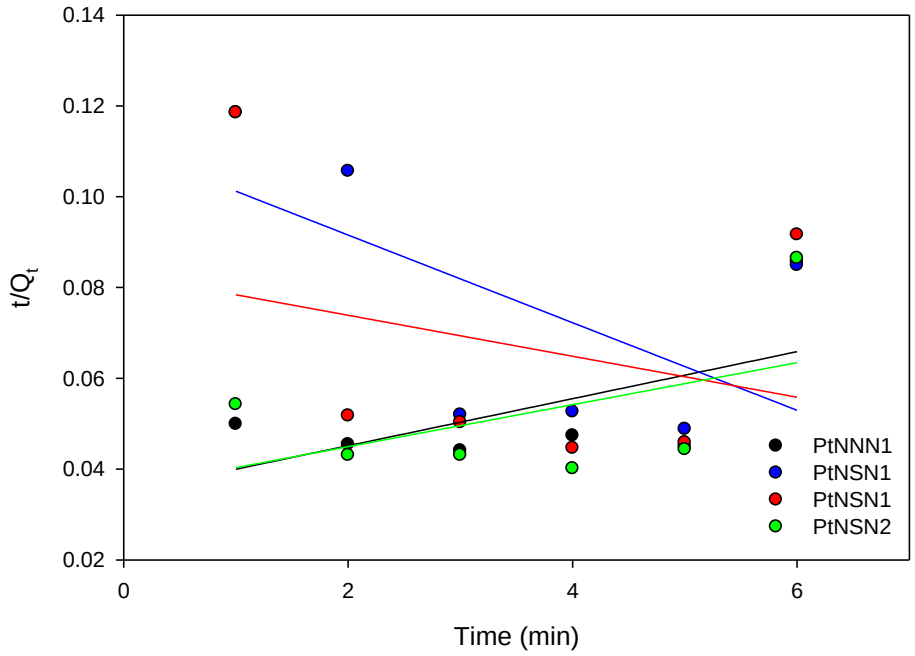

Figure 3.44: Pseudo-second-order plot for adsorption of platinum(II) using *bis*-benzimidazole hosted on nanofibers.

Table 3.9: Parameters of the pseudo-first-order and pseudo-second-order rate law for the adsorption of Pt(II) on nanofibers.

Resin	**Pseudo 1st order kinetics**			**Pseudo 2nd order kinetics**		
	Q_e (mg/g)	K_1 (min^{-1})	R^2	Q_e (mg/g)	K_2 ($g.mg^{-1}.min^{-1}$)	R^2
PVB-NNN1	216.3217	0.4926	0.9990	192.3077	0.0008	0.3574
PVB-NNN2	394.7299	0.7081	0.9998	103.093	0.0008	0.3525
PVB-NSN1	298.4695	0.5516	0.9996	222.222	0.0002	0.0755
PVB-NSN2	230.1442	0.7427	0.9998	217.3913	0.0006	0.2414

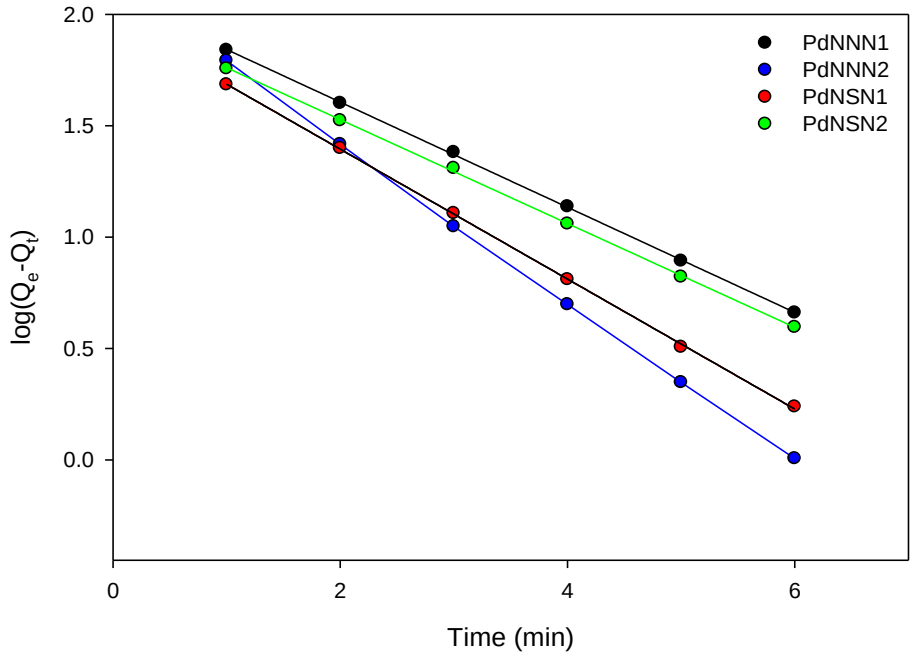

Figure 3.45: Pseudo-first-order plot for adsorption of palladium(II) using *bis*-benzimidazole hosted on nanofibers.

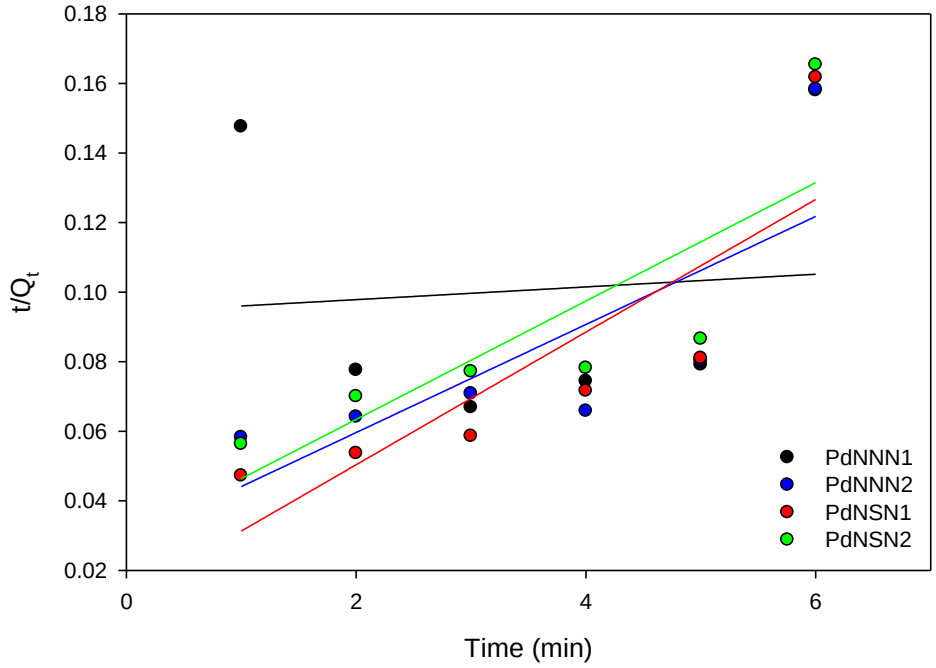

Figure 3.46: Pseudo-second-order plot for adsorption of palladium(II) using *bis*-benzimidazole hosted on nanofibers.

Table 3.10: Parameters of the pseudo-first-order and pseudo-second-order rate law for the adsorption of Pd(II) on nanofibers.

Resin	**Pseudo 1st order kinetics**			**Pseudo 2nd order kinetics**		
	Q_e (mg/g)	K_1 (min^{-1})	R^2	Q_e (mg/g)	K_2 ($g.mg^{-1}.min^{-1}$)	R^2
PVB-NNN1	145.2112	0.5412	0.9998	55.5555	0.0034	0.0070
PVB-NNN2	118.0321	0.8652	0.9997	64.5161	0.0084	0.5958
PVB-NSN1	99.1060	0.6634	0.9998	52.3560	0.0299	0.7097
PVB-NSN2	90.9913	0.5426	0.9999	58.8235	0.0099	0.6741

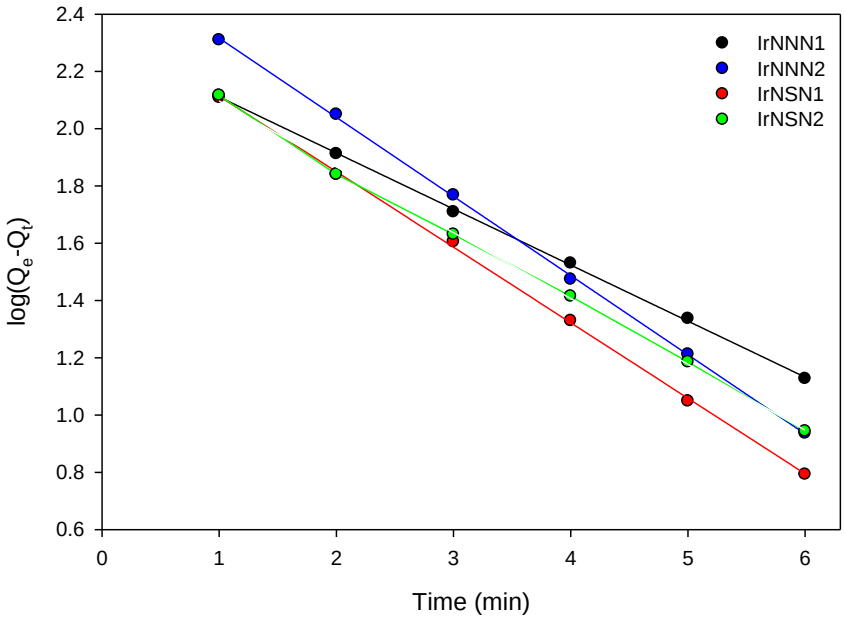

Figure 3.47: Pseudo-first-order plot for adsorption of iridium(III) using *bis*-benzimidazole hosted on nanofibers.

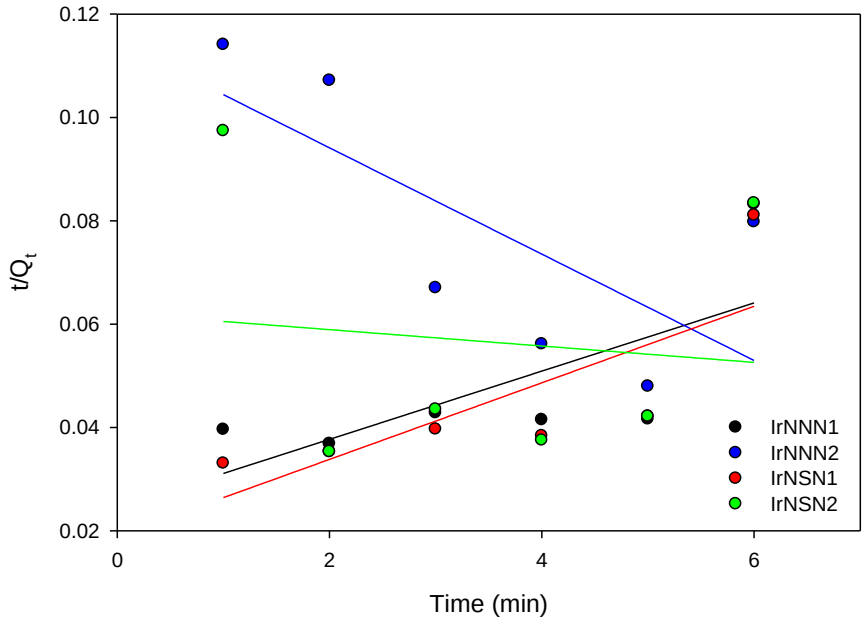

Figure 3.48: Pseudo-second-order plot for adsorption of iridium(III) using *bis*-benzimidazole hosted on nanofibers.

Table 3.11: Parameters of the pseudo-first-order and pseudo-second-order rate law for the adsorption of Ir(III) on nanofibers.

Resin	**Pseudo 1st order kinetics**			**Pseudo 2nd order kinetics**		
	Q_e (mg/g)	K_1 (min^{-1})	R^2	Q_e (mg/g)	K_2 ($g.mg^{-1}.min^{-1}$)	R^2
PVB-NNN1	181.8737	0.4454	0.9996	151.5152	0.0018	0.4939
PVB-NNN2	230.0539	0.5086	0.9997	97.0874	0.0009	0.5069
PVB-NSN1	196.0478	0.6384	0.9995	135.1351	0.0029	0.5936
PVB-NSN2	236.0478	0.5079	0.9986	86.2069	0.0022	0.0123

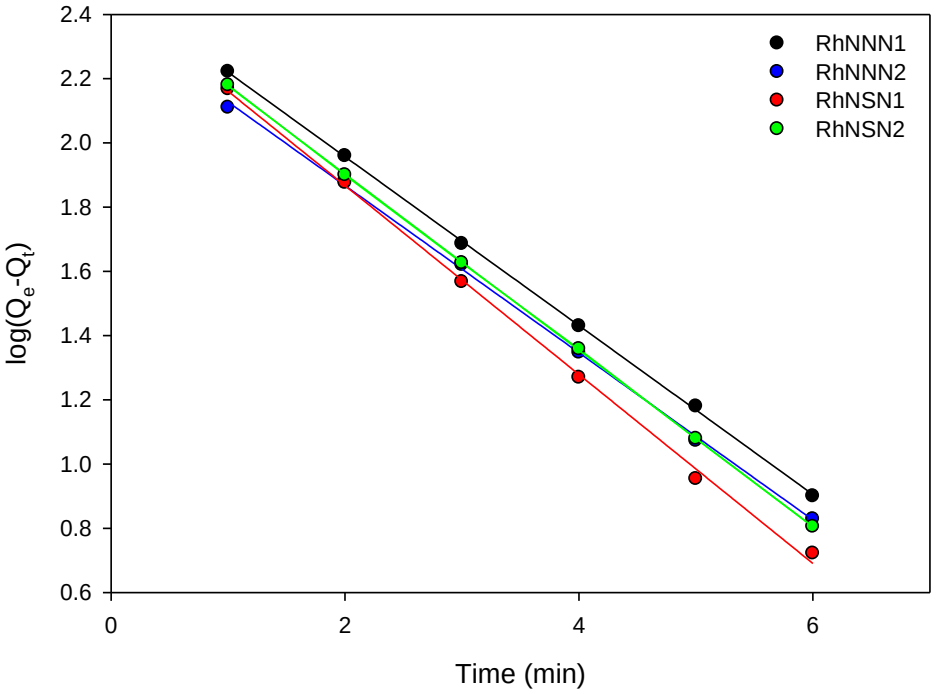

Figure 3.49: Pseudo-first-order plot for adsorption of rhodium(III) using *bis*-benzimidazole hosted on nanofibers.

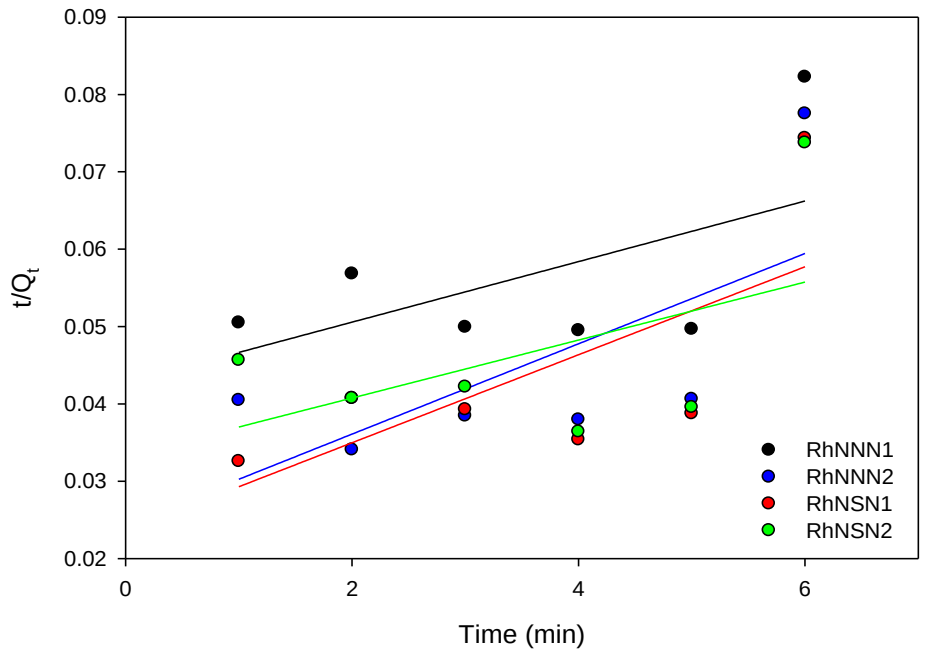

Figure 3.50: Pseudo-second-order plot for adsorption of rhodium(III) using *bis*-benzimidazole hosted on nanofibers.

Table 3.12: Parameters of the pseudo-first-order and pseudo-second-order rate law for the adsorption of Rh(III) on nanofibers.

Resin	**Pseudo 1st order kinetics**			**Pseudo 2nd order kinetics**		
	Q_e (mg/g)	K_1 (min^{-1})	R^2	Q_e (mg/g)	K_2 ($g.mg^{-1}.min^{-1}$)	R^2
PVB-NNN1	285.4960	0.6121	0.9998	172.4138	0.0004	0.3195
PVB-NNN2	264.1192	0.6188	0.9992	172.4138	0.0014	0.4558
PVB-NSN1	308.4608	0.7045	0.9986	256.4103	0.0014	0.4777
PVB-NSN2	307.3265	0.6361	1.0000	175.4386	0.0014	0.2601

Platinum(II) with *bis*-benzimidazoles functionalized nanofibers (NNN1, NNN2, NSN1 and NSN2) fitted the pseudo-first-order model (Figure 3.43). Q_e (mg/g) is the amount of metal ions adsorbed on the sorbent at equilibrium and it showed that the adsorption of Pt(II) using *bis*-benzimidazoles functionalized nanofibers increased in the order of NNN2 (394.73 mg/g) > NSN1 (298.47 mg/g) > NSN2 (230.14 mg/g) > NNN1 (216.32 mg/g) as shown in Table 3.9. This order was found in agreement with the multi-element column study loading capacity findings where the Pt(II) adsorption increased in the order NNN2 (33.96 mg/g) > NSN1 (30.95 mg/g) > NSN2 (23.89 mg/g) > NNN1 (14.92 mg/g) as shown in Figure 3.31. This implies that NNN2 on the surface of the nanofibers complexes better with Pt(II) than the other ligands. Pt(II) is known to be a soft metal and this showed that Pt(II) has a high affinity for soft ligands that contain N donor atoms.

Palladium(II) adsorption kinetics study was observed to fit the pseudo-first-order model for all the nanofibers functionalized with NNN1, NNN2, NSN1 and NSN2 (Figure 3.45).

The plot log q_e-q_t vs time(t) gave a straight line with R^2 values that were greater than 0.99 for all adsorbents (Table 3.10). The adsorption of Pd(II) using *bis*-benzimidazoles functionalized nanofibers increased in the order of NNN1 (145.21 mg/g) > NNN2 (118.03 mg/g) > NSN1 (99.11 mg/g) > NSN2 (90.99 mg/g). This order was to be found in agreement with the multi-element column study loading capacity findings where the Pt(II) adsorption increased in the order NNN1 (47.94 mg/g) > NNN2 (28.9 mg/g) > NSN1 (16.22 mg/g) > NSN2 (15.83 mg/g) as shown in Figure 3.31. This implies that NNN1 on the surface of the nanofibers complexes better with Pd(II) and that formation of five-membered ring chelates is preferred even between NSN1 and NSN2. Pd(II) is known to be a soft metal and it seems to have a higher affinity for the nitrogenous ligands than the sulfur-containing derivatives.

Iridium(III) adsorption kinetics study was observed to fit the pseudo-first-order model with resins NNN1, NNN2, NSN1 and NSN2 (Figure 3.47). The plot log q_e-q_t vs time (t) gave a straight line with R^2 values that were greater than 0.99 for all adsorbents (Table 3.11). The adsorption of Ir(III) using *bis*-benzimidazoles functionalized nanofibers increased in the order of NSN2 (236.05 mg/g) > NNN2 (236.05 mg/g) > NSN1 (196.02 mg/g) > NNN1 (181.87 mg/g). This order was found to be in agreement with the multi-element column study loading capacity findings where the Ir(III) adsorption increased in the order NSN2 (10.64 mg/g) > NNN2 (6.84 mg/g) > NSN1 (5.74 mg/g) > NNN1 (5.02 mg/g) as shown in Figure 3.31.

Rhodium(III) adsorption kinetics study was observed to fit the pseudo-first-order model with resins NNN1, NNN2, NSN1 and NSN2 (Figure 3.49). The plot log q_e-q_t vs time (t) gave a straight line with R^2 values that were greater than 0.99 for all adsorbents (Table

3.12). The adsorption of Rh(III) using *bis*-benzimidazoles functionalized nanofibers increased in the order of NSN1 (308.5 mg/g) > NSN2 (307.33 mg/g) > NNN1 (285.496 mg/g) > NNN2 (264.12 mg/g). This order was found to be in agreement with loading capacities from single element and the multi-element column study where the Rh(III) adsorption increased in the order NSN1 (47.28 mg/g) > NSN2 (19.95 mg/g) > NNN1 (17.47 mg/g) > NNN2 (14.91 mg/g) as shown in Figure 3.31. This implies that NSN1 on the surface of the nanofibers complexes better with Rh(III) to form an octahedral geometry, and five-membered ring chelates were preferred. Rh(III) is shown to have a higher affinity for the NSN ligands compared with NNN ligands. According to the DFT calculations in Table 3.1, the *bis*-benzimidazole ligands hardness increased in the order NSN2 (2.687 eV) > NSN1 (2.570 eV) > NNN1 (1.910 eV) > NNN2 (1.188 eV).

Adsorption kinetic studies showed an approximate adsorption rate per minute for pseudo-first-order model in the following order; NSN2 (0.7427 min^{-1}) > NNN2 (0.7081 min^{-1}) > NSN1 (0.5516 min^{-1}) > NNN1 (0.4926 min^{-1}) for Pt(II); NNN2 (0.8652 min^{-1}) > NSN1 (0.6634 min^{-1}) >NSN2 (0.5426 min^{-1}) > NNN1 (0.5412 min^{-1}) Pd(II); NSN1 (0.6384 min^{-1}) > NNN2 (0.6089 min^{-1}) > NSN2 (0.5079 min^{-1}) > NNN1 (0.4454 min^{-1}) Ir(III); NSN1 (0.7045 min^{-1}) > NSN2 > (0.6361 min^{-1}) > NNN2 (0.6188 min^{-1}) > NNN1 (0.6121 min^{-1}) Rh(III).

In conclusion adsorption kinetic studies using various *bis*-benzimidazoles functionalized nanofibers show that Pd, Pt, Ir and Rh adsorption was fast due to the availability of surface functional groups. Based on the obtained correlation coefficients (R^2), Pt(II), Pd(II), Ir(III) and Rh(III) fitted the pseudo-first-order model. The comparison

of metal ions to respective ligands adsorption kinetics done under batch adsorption conditions are in agreement with the multi-element column study.

3.3.7.2 Adsorption isotherms

The equilibrium adsorption isotherm has the importance in the design of adsorption systems [203]. The equilibrium data were analysed by Langmuir and Freundlich isotherms [150, 201, 203]. The Langmuir equation, which is effective for monolayer adsorption onto a completely homogeneous surface with a finite number of identical sites and with negligible interaction between adsorbed molecules, is represented in the linear form as shown in Chapter 2 (Section 2.3.2, equation 2.4) [207]. The parameters of the Langmuir and Freundlich isothermal models are presented in Figures 3.51-3.57 and Tables 3.13-3.16.

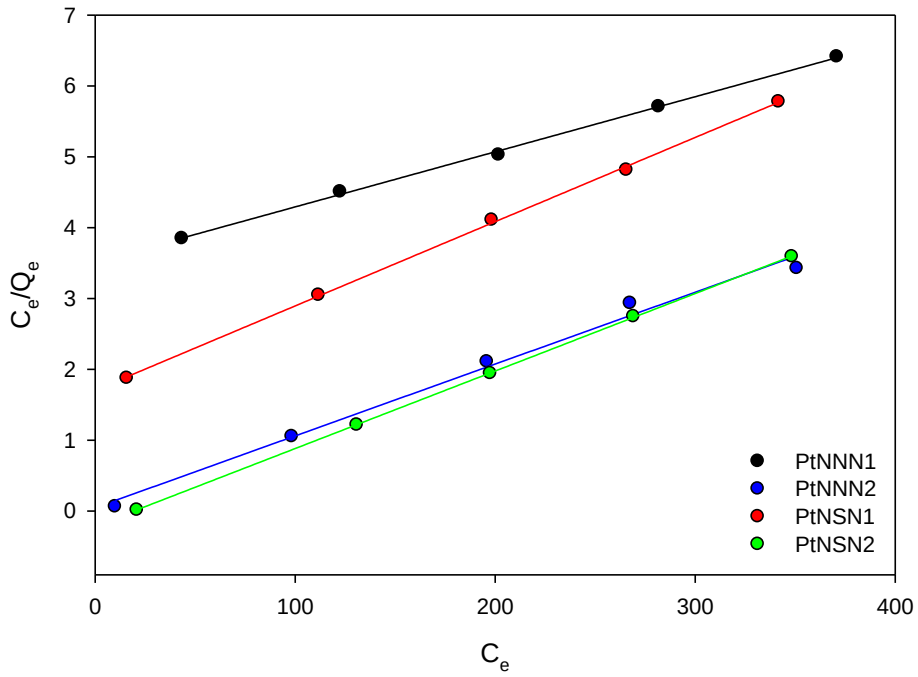

Figure 3.51: Plots of Langmuir isotherms for sorption of platinum(II) with NNN1, NNN2, NSN1 and NSN2 functionalized nanofibers.

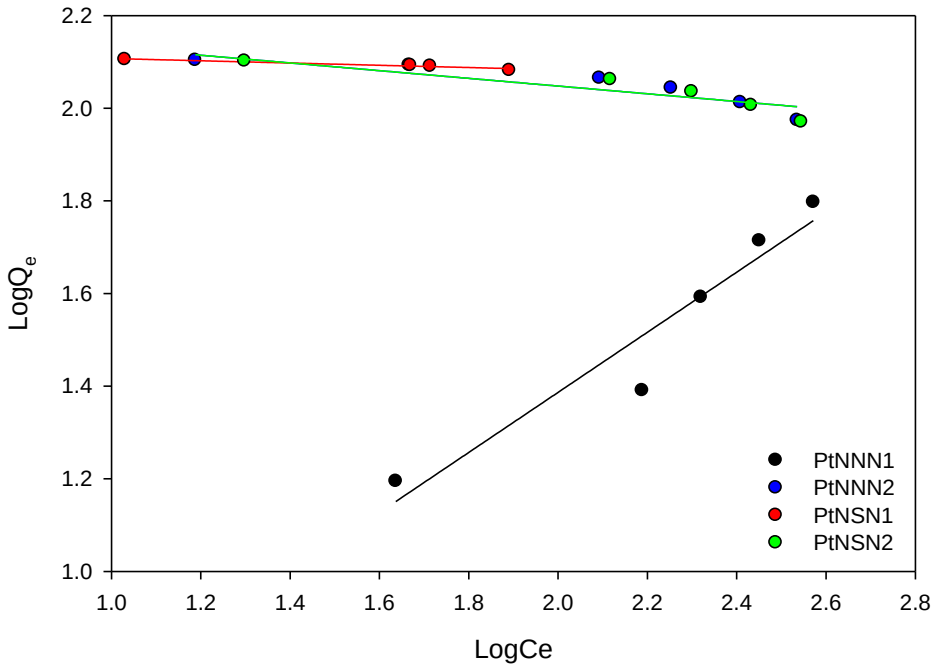

Figure 3.52: Plots of Freundlich isotherms for sorption of platinum(II) with NNN1, NNN2, NSN1 and NSN2 functionalized nanofibers.

Table 3.13: Langmuir and Freundlich isothermal parameters for adsorption of Pt(II) on functionalized nanofibers.

Resins	**Langmuir parameters**				**Freundlich parameters**		
	Q_o (mg/g)	R_L	b	R^2	K_f (mg/g)	N	R^2
PVB-NNN1	84.0336	0.2948	0.0022	0.998	1.2283	128.2051	0.9221
PVB-NNN2	128.2051	0.5473	0.0070	0.999	163.7948	84.0336	0.8064
PVB-NSN1	99.0099	0.0561	0.2162	0.990	135.4254	99.0099	0.9128
PVB-NSN2	91.7431	0.0526	0.05139	1.000	138.9953	91.7431	0.8064

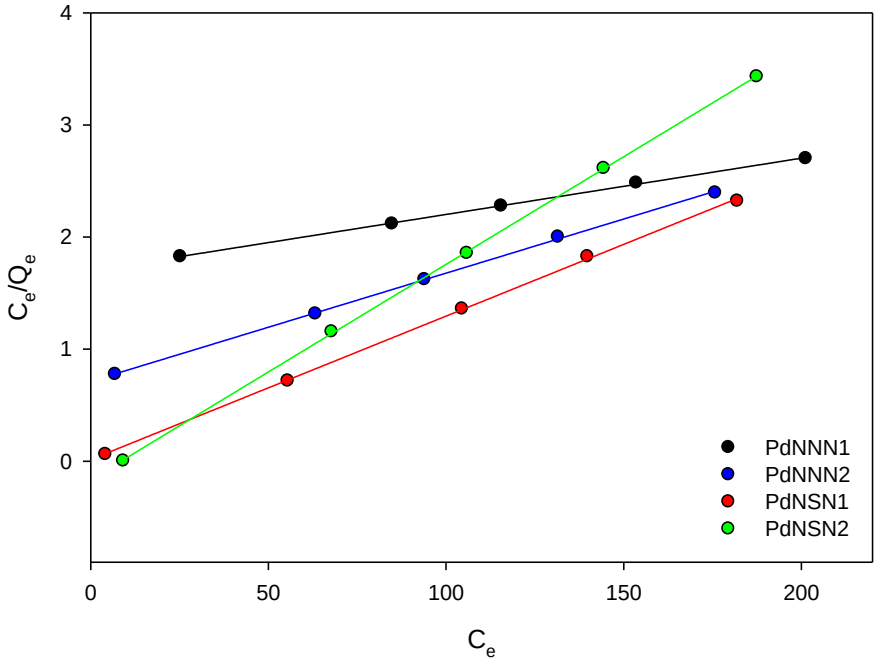

Figure 3.53: Plots of Langmuir isotherms for sorption of palladium(II) with NNN1, NNN2, NSN1 and NSN2 functionalized nanofibers.

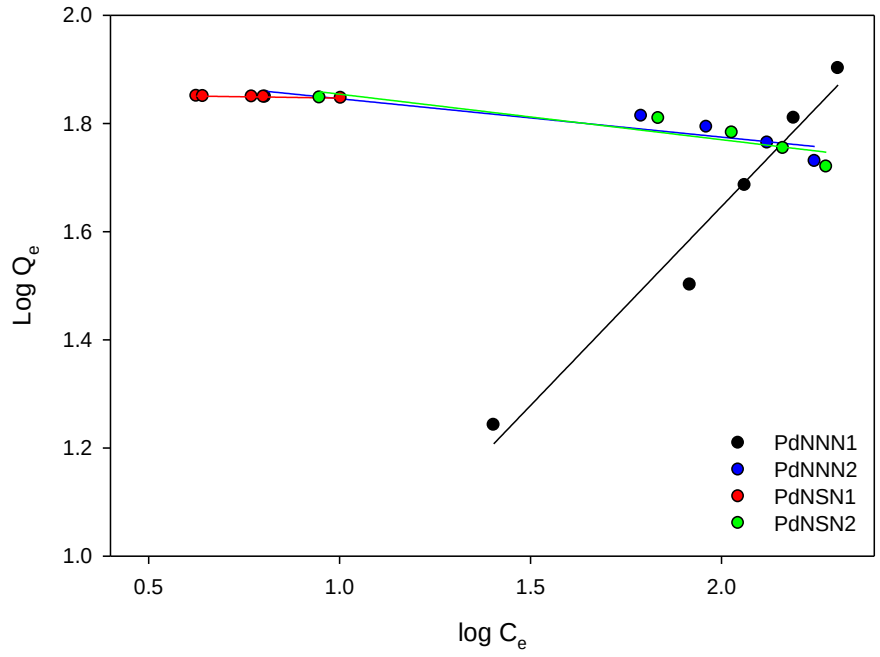

Figure 3.54: Plots of Freundlich isotherms for sorption of palladium(II) with NNN1, NNN2, NSN1 and NSN2 functionalized nanofibers.

Table 3.14: Langmuir and Freundlich isothermal parameters for adsorption of Pd(II) on functionalized nanofibers.

Resins	Langmuir parameters				Freundlich parameters		
	Q_o (mg/g)	R_L	b	R^2	K_f (mg/g)	N	R^2
PVB-NNN1	66.2251	0.1855	1	0.9999	1.4955	1.3591	0.9645
PVB-NNN2	5.8858	0.0053	1	0.9996	82.5468	14.0845	0.7974
PVB-NSN1	1.4027	0.0057	1	0.9997	71.8456	105.2632	0.9823
PVB-NSN2	0.5883	0.0049	1	0.9999	86.7561	11.8906	0.8219

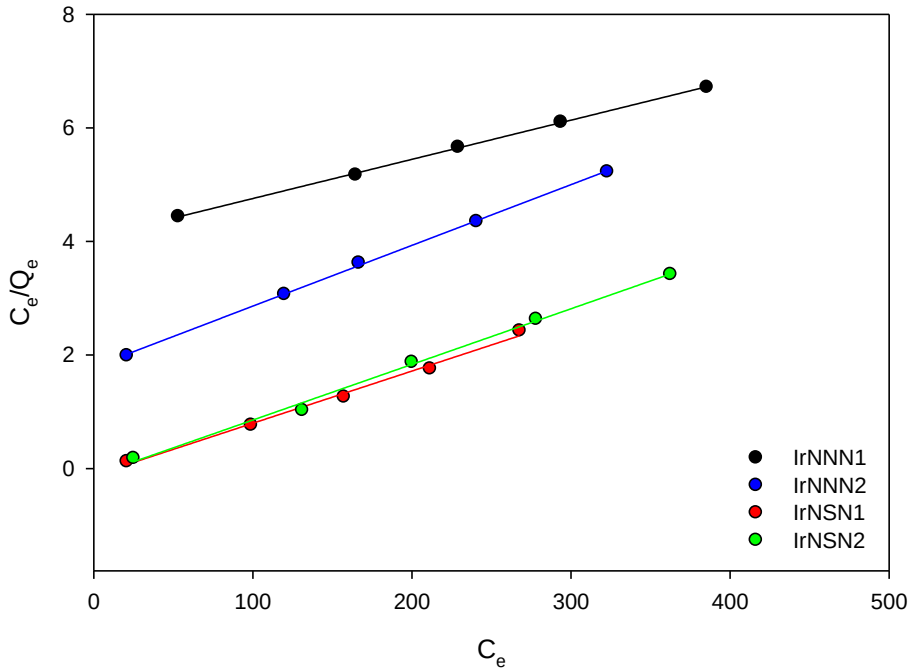

Figure 3.55: Plots of Langmuir isotherms for sorption of iridium(III) with NNN1, NNN2, NSN1 and NSN2 functionalized nanofibers.

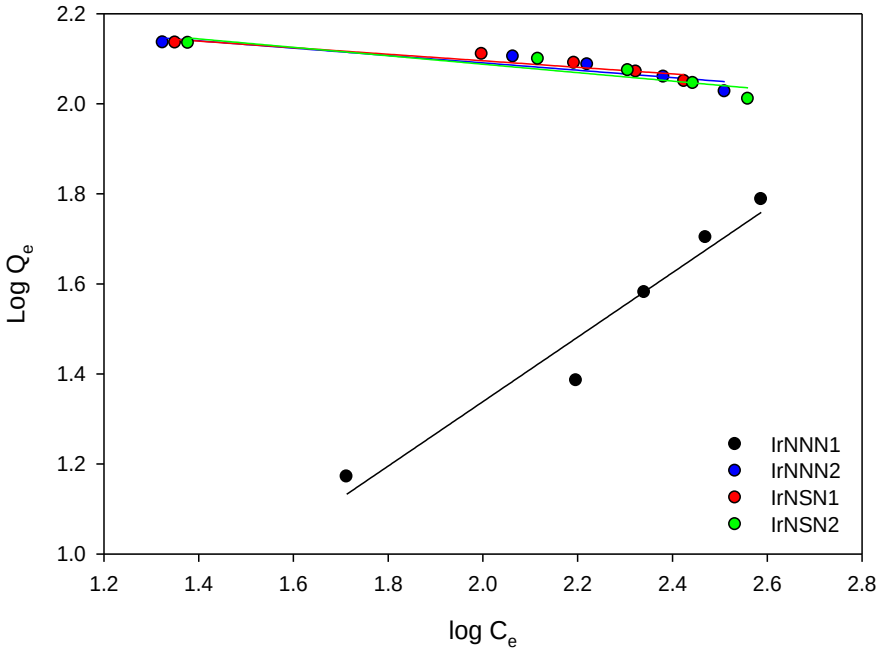

Figure 3.56: Plots of Freundlich isotherms for sorption of iridium(III) with NNN1, NNN2, NSN1 and NSN2 functionalized nanofibers.

Table 3.15: Langmuir and Freundlich isothermal parameters for adsorption of Ir(III) on functionalized nanofibers.

Resins	Langmuir parameters				Freundlich parameters		
	Q_o (mg/g)	R_L	b	R^2	K_f (mg/g)	N	R^2
PVB-NNN1	0.2459	0.0026	1	0.9996	0.8072	1.3972	0.9518
PVB-NNN2	7.9968	0.0026	1	0.9994	179.6387	12.2249	0.8334
PVB-NSN1	0.5581	0.0031	1	0.9939	174.1807	13.7363	0.8726
PVB-NSN2	8.2988	0.0037	1.0378	0.9963	188.5385	10.6610	0.8407

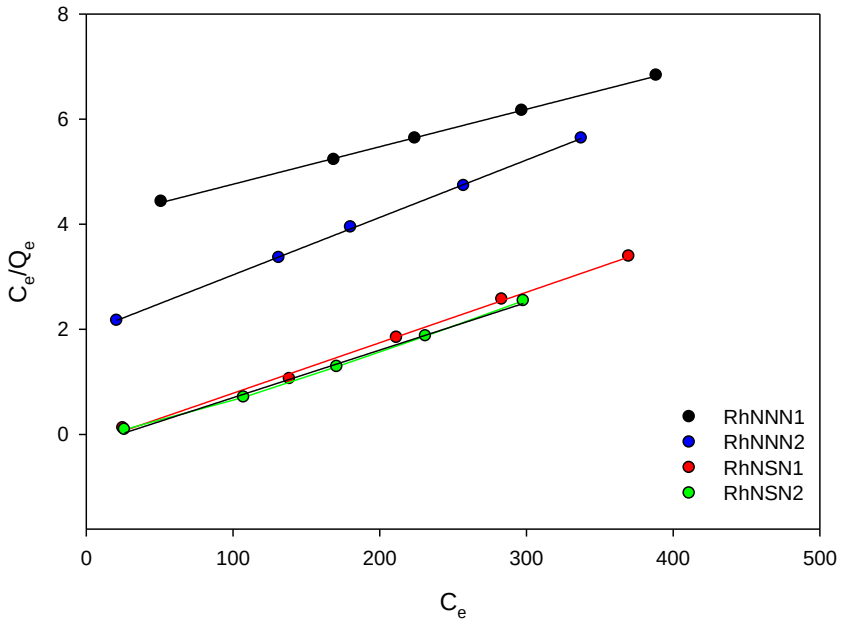

Figure 3.57: Plots of Langmuir isotherms for sorption of rhodium(III) with NNN1, NNN2, NSN1 and NSN2 functionalized nanofibers.

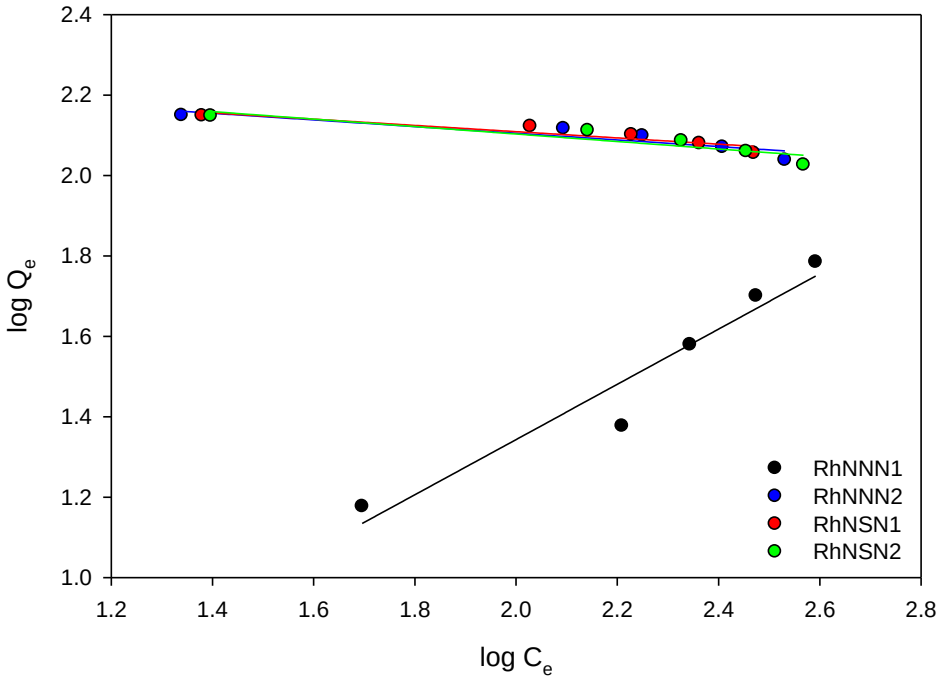

Figure 3.58: Plots of Freundlich isotherms for sorption of rhodium(III) with NNN1, NNN2, NSN1 and NSN2 functionalized nanofibers.

Table 3.16: Langmuir and Freundlich isothermal parameters for adsorption of Rh(III) on functionalized nanofibers.

Resins	Langmuir parameters				Freundlich parameters		
	Q_o (mg/g)	R_L	b	R^2	K_f (mg/g)	N	R^2
PVB-NNN1	91.7431	0.3440	0.0018	0.9996	0.9330	0.9330	0.9339
PVB-NNN2	104.1667	0.0589	0.0056	0.9997	186.5091	186.5091	0.8346
PVB-NSN1	140.8451	0.5934	0.0541	0.9979	183.8654	183.8654	0.8663
PVB-NSN2	109.8901	0.0578	0.0440	0.9964	194.4912	194.4912	0.8457

The plots of specific adsorption (C_e/Q_e) against the equilibrium concentration (C_e) show that the adsorption obeys the Langmuir model. The adsorption data for each sorbent and metal ion were consistent with a Langmuir adsorption model ($R^2 > 0.99$), strongly suggesting monolayer adsorption on the surface of adsorbents. The Langmuir constant Q_o (mg/g) is determined from the slope of the plot. One of the essential characteristics of the Langmuir isotherm can be expressed in terms of a dimensionless constant separation factor R_L that is given in Chapter 2 (Section 2.3.2, equation 2.5). The R_L values between 0 and 1 indicate favourable adsorption. The values of R_L in the present study were found to be between 0 and 1 indicating that the adsorption of Pt, Pd, Ir and Rh on *bis*-benzimidazoles derivatives sorbents are favourable. The Freundlich isotherm, on the other hand, assumes a heterogeneous sorption surface with sites that have different energies of sorption. From the plots, the Freundlich adsorption equation did not fit better as the correlation coefficient (R^2) was below 0.99. The Freundlich parameter, n, indicates the favourability of the adsorption. If the

adsorption intensity, n must be between 1 and 10. All adsorbents showed n values more than ten indicating that the adsorption intensity is not favourable.

The Langmuir constant for Pt(II) using *bis*-benzimidazoles functionalized nanofibers increased in the order of NNN2 (128.21 mg/g) > NSN1 (99.01 mg/g) > NSN2 (91.74 mg/g) > NNN1 (84.03 mg/g) as shown in Table 3.13. The column study multi-element loading capacity findings were in the following order; NNN2 (33.96 mg/g) > NSN1 (30.95 mg/g) > NSN2 (23.89 mg/g) > NNN1 (14.92 mg/g) for Pt(II) as shown in Figure 3.31. NNN1 (66.23 mg/g) > NNN2 (5.89 mg/g) > NSN1 (1.40 mg/g) > NSN2 (0.59 mg/g) for Pd(II) as shown in Table 3.14. This order was found in agreement with the column study multi-element loading capacity findings for Pd(II) adsorption increased in the order of NNN1 (47.94 mg/g) > NNN2 (28.9 mg/g) > NSN1 (16.22 mg/g) > NSN2 (15.83 mg/g) as shown in Figure 3.31. Ir(III) adsorption increased in the order of NSN2 (8.30 mg/g) > NNN2 (8.00 mg/g) > NSN1 (0.56 mg/g) > NNN1 (0.25 mg/g) as shown in Table 3.15. This order was found to be in agreement with the loading capacity findings in the multi-element column study where Ir(III) adsorption increased in the order of NSN2 (10.64 mg/g) > NNN2 (6.84 mg/g) > NSN1 (5.74 mg/g) > NNN1 (5.02 mg/g) as shown in Figure 3.31. Rh(III) adsorption increased in the order of NSN1 (140.85 mg/g) > NSN2 (109.89 mg/g) > NNN1 (104.17 mg/g) > NNN2 (91.74 mg/g) as shown in Table 3.16. This order was found to be in agreement with the multi-element column study loading capacity findings where Rh(III) adsorption increased in the order of NSN1 (47.28 mg/g) > NSN2 (19.95 mg/g) > NNN1 (17.47 mg/g) > NNN2 (14.91 mg/g) as shown in Figure 3.31. The observed order is also in agreement with kinetics data.

Adsorption kinetic studies were further compared for each ligand against the metals. NNN1 resin showed the Langmuir constant to increase in the order of Pd(II) (104.17 mg/g) > Rh(III) (84.03 mg/g) > Pt(II) (66.23 mg/g) > Ir(III) (0.25 mg/g). This order is in agreement with the column study multi-element loading capacity in the following order; Pd(II) (47.94 mg/g) > Rh(III) (17.47 mg/g) > Pt(II) (14.92 mg/g) > Ir(III) (5.02 mg/g). NNN2 resin showed the Langmuir constant to increase in the order of Pt(II) (128.21 mg/g) > Pd(II) (91.74 mg/g) > Rh(III) (8.00 mg/g) > Ir(III) (5.89 mg/g). This order is in agreement with the column study multi-element loading capacity increased in the order of Pt(II) (33.96 mg/g) > Pd(II) (28.9 mg/g) > Rh(III) (14.91 mg/g) > Ir(III) (6.84 mg/g). NSN1 resin showed the Langmuir constant to increase in the order of Rh(III) (140.85 mg/g) > Pt(II) 99.01 mg/g) > Pd(II) (1.40 mg/g) > Ir(III) (0.56 mg/g). This order is in agreement with the column study multi-element loading capacity increased in the order of Rh(III) (47.28 mg/g) > Pt(II) (30.95 mg/g) > Pd(II) (16.22 mg/g) > Ir(III) (5.74 mg/g). NSN2 resin showed the Langmuir constant to increase in the order of Rh(III) (109.89 mg/g) > Pt(II) (91.74 mg/g) > Pd(II) (8.30 mg/g) > Ir(III) (0.59 mg/g). This order is in agreement with the column study multi-element loading capacity in the following order; Rh(III) (23.89 mg/g) > Pt(II) (19.95 mg/g) > Pd(II) (15.83 mg/g) > Ir(III) (10.64 mg/g) as shown in Figure 3.31.

The experimental adsorption studies were also compared with theoretical calculated thermodynamics data. The theoretical calculated thermodynamics values are shown in Section 3.3.1.4 in Table 3.2 for *bis*-benzimidazole derivatives (NNN1, NNN2, NSN1 and NSN2). The theoretical calculated thermodynamics values show that negative ΔΔG values were observed for NSN1 and NSN2 interactions with $[RhCl_3(H_2O)_3]$

indicating the feasibility and spontaneity of the adsorption process. The negative ΔΔH values observed for NSN1 and NSN2 confirmed the exothermic nature of the overall sorption process for Rh(III). The experimental data support the suitability of NSN1 and NSN2 for rhodium(III) sorption, with NSN1 being were preferred due to the formation of five-membered ring chelates, However, NNN1 and NNN2 also have a capacity to extract Rh(III), albeit in low quantities compared with NSN ligands.

3.4 Conclusions

The ligands were successfully synthesized, and PVBC nanofibers were fabricated and functionalized with tridentate *bis*-benzimidazole ligands (NNN1, NNN2, NSN1 and NSN2). Ligands, unfunctionalized PVBC nanofibers and functionalized PVBC nanofibers formation were confirmed by FT-IR and elemental analysis. EDS studies were conducted to confirm the presence of nitrogen and other atoms on the materials. BET experiments were conducted to confirm the surface area of the nanofibers. The SEM images of the nanofibers showed well defined morphology of the materials.

In column studies, it was observed that $RhCl_3(H_2O)_3$ shows preference for the *bis*-benzimidazole ligands in 0.5 M HCl medium. The loading capacities for Rh(III) increased in the order NSN1 > NSN2 > NNN2 > NNN1. This order is in agreement with theoretical thermodynamics data. In the multi-element column study, a metal solution containing Rh(III), Pt(II), Pd(II), Ir(III) and Ni(II), it was observed that the *bis*-benzimidazole derivatives showed preference for Rh(III), Pt(II), Pd(II) and Ir(II) and no preference was shown for Ni(II). The loading capacities of NNN1, NNN2, NSN1 and NSN2 for rhodium were 0.17, 0.14, 0.46 and 0.19 mmol/g respectively. For palladium,

loading capacities were 0.45, 0.27, 0.15, 0.15 mmol/g for NNN1, NNN2, NSN1 and NSN2, respectively. For platinum, loading capacities were 0.08 mmol/g, 0.17 mmol/g, 0.16 mmol/g, 0.12 mmol/g for NNN1, NNN2, NSN1 and NSN2, respectively. For iridium, loading capacities were 0.03 mmol/g, 0.04 mmol/g, 0.03 mmol/g, 0.06 mmol/g for NNN1, NNN2, NSN1 and NSN2, respectively. The rhodium loading capacities on the sorbents were in the order NSN1> NSN2 > NNN2 > NNN1 that is in agreement with single element column study order, which showed the effect of sulfur in the uptake of rhodium(III). The NSN1 sorbent is ideal for uptake of Rh(III), Pt(II), Pd(II) from solutions of catalytic converters. The uptake of nickel(II) in the presence of PGMs is a promising result but more base metals that are present in the catalyst brick must also be tested.

Adsorption kinetics and isotherms studies confirmed the uptake of Pt(II), Pd(II), Ir(III) and Rh(III), where pseudo-first-order kinetics and Langmuir isotherm models were obeyed. The observed order in all studies was as follows (ligand for metals); NNN1: Pd > Rh > Pt > Ir; NNN2: Pt > Pd > Rh > Ir; NSN1: Rh > Pt > Pd > Ir; NSN2: Rh > Pt > Pd > Ir. Metal ions for ligands order was as follows; Pt: NNN2 > NSN1 > NSN2 > NNN1; Pd: NNN2 > NNN1 > NSN1 > NSN2; Ir: NSN2 > NNN2 > NSN1 > NNN1 and Rh: NSN1 > NSN2 > NNN2 > NNN1. Theoretical studies also suggested the order of rhodium uptake for the different functional groups. The best sorbent, PVB-NSN1 is not selective to rhodium(III) but has high affinity. It would be ideal for the separation of PGMs from secondary solutions of catalytic converters for recovery Rh(III), Pt(II) and Pd(II).

Chapter 4: Separation of iridium(IV) from rhodium(III) using quaternary diammonium cations hosted on polymer nanofibers

4.1 Introduction

The behaviour of the quaternary diammonium cations will be explored with respect to their effectiveness of separation of iridium(IV) ($[IrCl_6]^{2-}$) species from rhodium(III) ($[RhCl_5(H_2O)]^{2-}$) species in 6 M HCl. These cationic derivatives are expected to function *via* ion exchange. The focus of this study is on the uptake of iridium(IV) over rhodium(III) thereby improving the loading capacity. This is achieved by functionalization of diammonium derivatives with electron donating and electron withdrawing benzyl groups as quaternizing agents (Figure 4.1). The diamine backbone used is 1,10-diaminodecane (DMDA) based on precious studies [150, 152]. The quaternary diammonium cations designed are namely, tetramethylbenzyl-1,10-diammonium chloride (QuatDMDAMeBnz), tetrabenzyl-1,10-diammonium chloride (QuatDMDABnz), tetratrifluoromethylbenzyl-1,10-diammonium chloride (QuatDMDACF3Bnz) and tetranitrobenzyl-1,10-diammonium chloride (QuatDMDANO2Bnz).

However, the properties and behaviour of quaternary diammonium cations were previously investigated by Avela Majavu in our research group [150]. In this study, the diammonium cations studied were quaternized with a methyl group. These cations were derived from ethylenediamine (EDA), tetramethylenediamine (TMDA), hexamethylenediamine (HMDA), 1,8-diaminooctane (OMDA), 1,10-diaminodecane

(DMDA) and 1,12-diaminododecane (DDMDA) (Figure 4.2) [150]. The increase of the loading capacity of the quaternary diammonium cations was shown to increase as the methylene spacer increased from two to ten (Figure 4.3) [150]. The 1,10- diammonium cation showed a higher loading capacity, hence this study focused on improving DMDA by quaternizing with electron-donating and electron-withdrawing benzyl groups. However, in this study, the investigation of the quaternary diammonium cations (Figure 4.1) seeks to find the cation with the highest capacity for uptake of $[IrCl_6]^{2-}$. This has been carried out both experimentally (using a binary column study and adsorption studies) and theoretically (by DFT calculations).

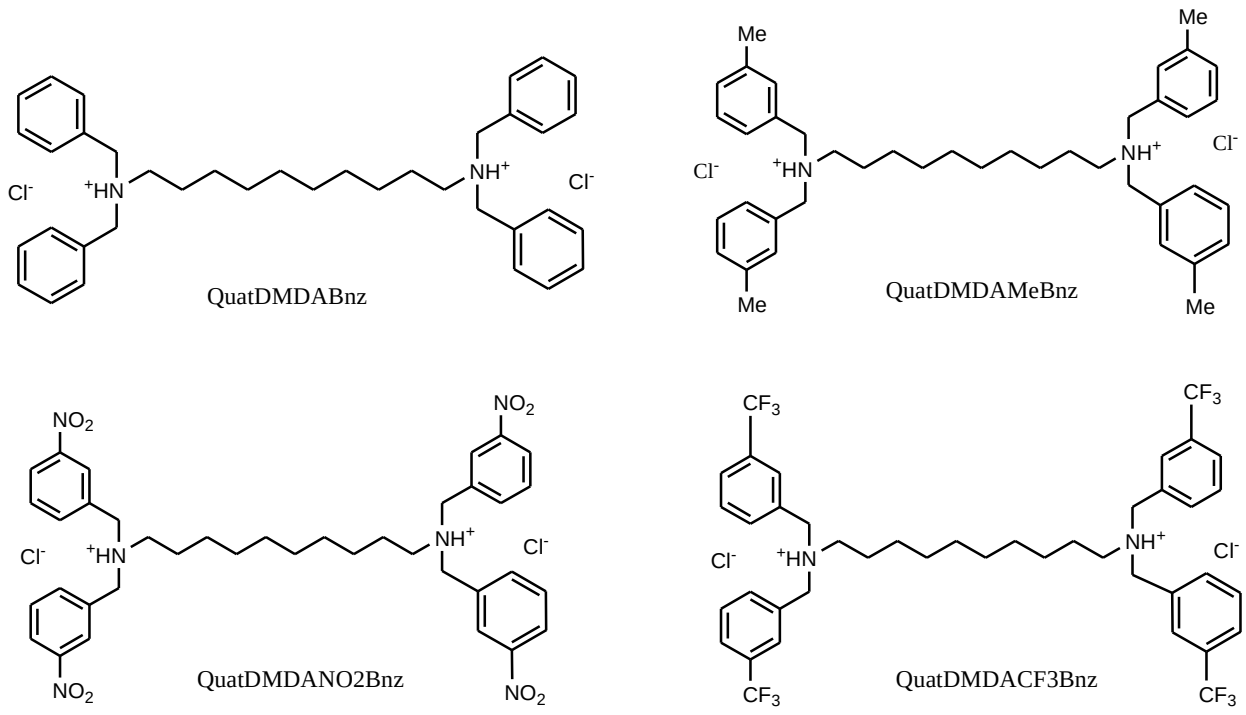

Figure 4.1: Chemical structure of the substituted quaternary diammonium cations used in this study

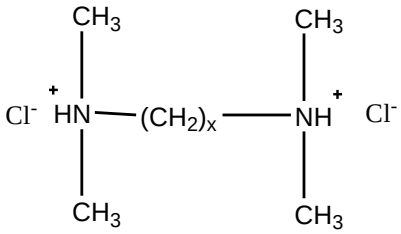

x = 2 (EDA), 4 (TMDA), 6 (HMDA), 8 (OMDA), 10 (DMDA), 12 (DDMDA)

Figure 4.2: Chemical structure of the quaternary diammonium cations quaternized with methyl groups.

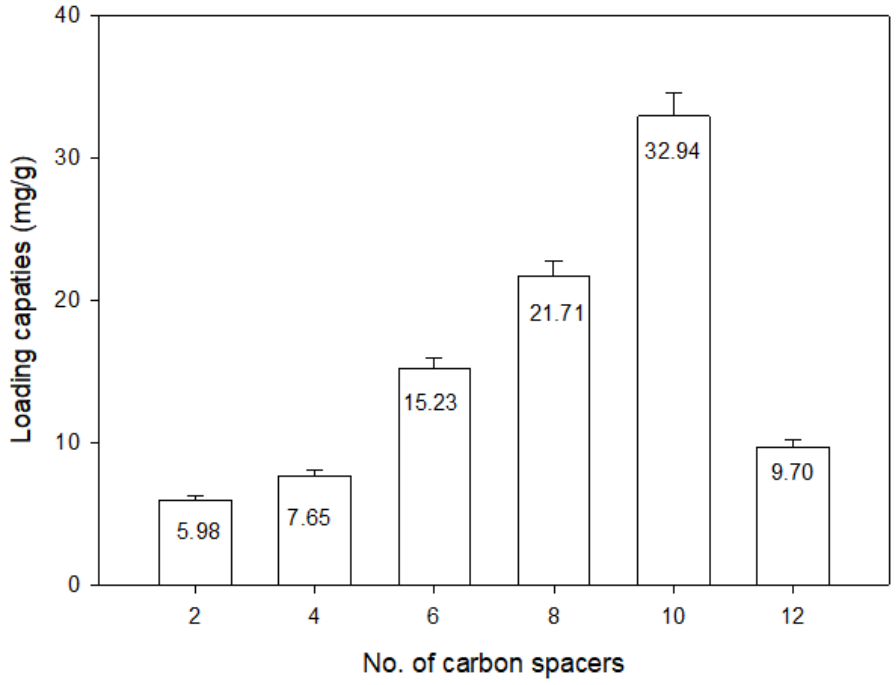

Figure 4.3: Loading capacities for $[IrCl_6]^{2-}$ extracted using quaternary diammonium cations (quaternized using a methyl group) hosted on nanofibers

A dominant force in the extraction of chlorido complexes of PGMs is the electrostatic attraction between the cation and the anion. However, it is suggested that hydrogen

bonding interactions also play a significant role in hosting the anion [208]. This study exploits the characteristics of the anion-cation interactions to derive specificity for the $[IrCl_6]^{2-}$ [209]. This chapter presents the fundamental chemistry involved in the anion-cation interaction which may be valuable in uncovering factors that can lead to successful separation of $[IrCl_6]^{2-}$ from $[RhCl_5(H_2O)]^{2-}$.

4.2 Experimental

4.2.1 Preparation of quaternary diammonium cations

The quaternary diammonium cations with prepared as follows: catalytic amounts of sodium iodide were added to either benzyl bromide, 4-methylbenzyl chloride, 3-trifluoromethylbenzyl chloride or 4-nitrobenzyl chloride in acetone. The resulting sodium bromide or sodium chloride precipitated out from the reaction mixture and was filtered out. The acetone was removed from the benzyl iodide derivatives. Seven moles of each benzyl iodide derivative was reacted with one mole of 1,10-diaminodecane and four moles of 2,6-lutidine in dry ethanol and the mixture was heated under reflux at 70°C for seven days. The resulting reaction mixture was concentrated, and the crude product was dissolved in chloroform and any hydroiodide present was extracted with a 3 M sodium hydroxide solution. The organic phase was then dried using sodium sulfate anhydrous for approximately 45 minutes. The iodide counterions were replaced with chlorides by stirring the salts in ethanolic silver chloride. The salts were filtered and stirred again with the ethanolic solution with the excess solid silver chloride for 24 hours. Silver iodide and excess silver chloride were

filtered off and THF was added to form a precipitate which was filtered, washed several times with 10 M HCl and dried The general procedure for the preparation of the quaternary ammonium salts is given in Scheme 4.1 [149, 151].

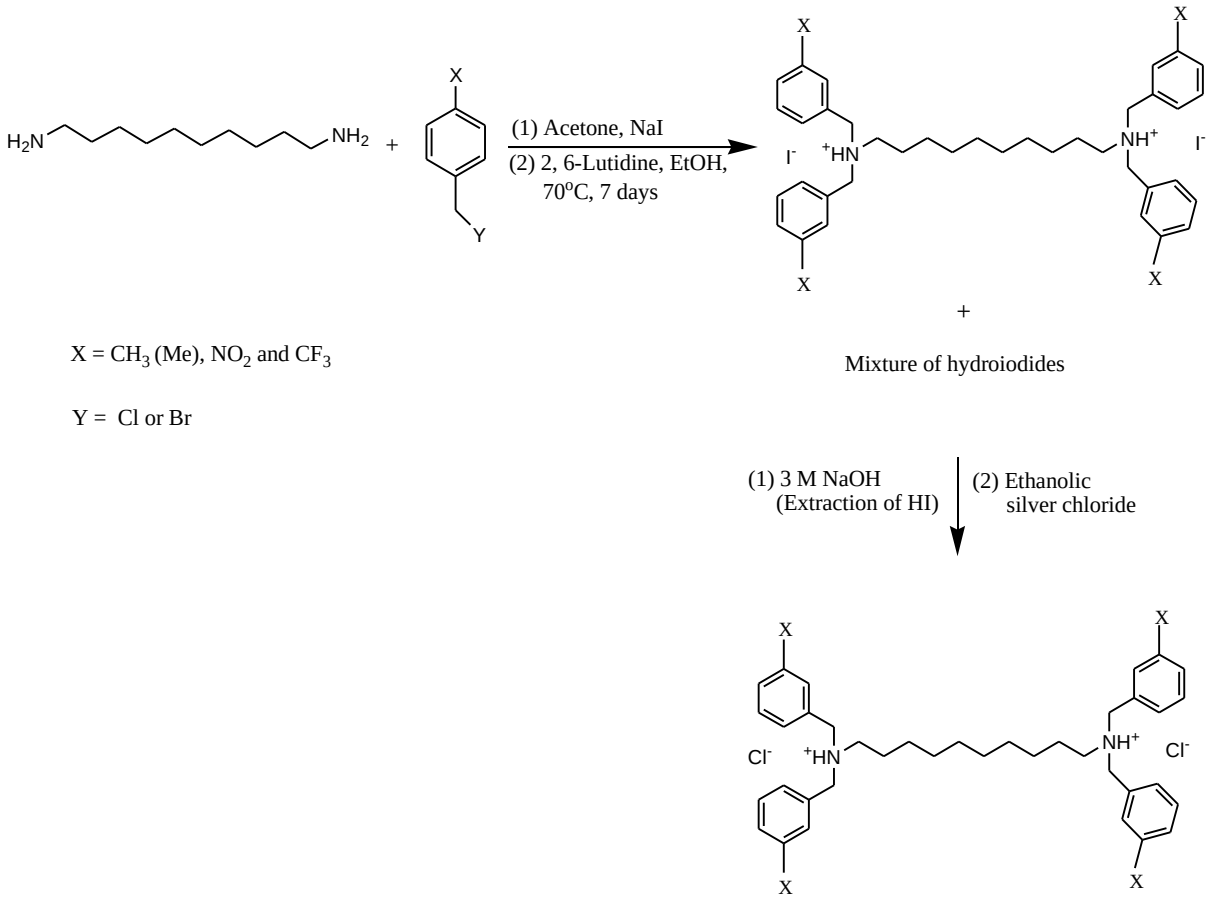

Scheme 4.1: Synthesis of diammonium salts quaternized with electron withdrawing and electron donating benzyl groups.

4.2.2 Fabrication of nanofibers

4.2.2.1 Preparation of polyvinylbenzylchloride (PVBC)

PVBC preparation was discussed in Chapter 3, Section 3.2.2.1.

4.2.2.2 Electrospinning

Electrospinning process was discussed in Chapter 3, Section 3.2.2.2.

4.2.2.3 Functionalization of PVBC nanofiber and quaternization of the diamine

The PVBC nanofibers were functionalized with 1,10-diaminodecane (DMDA) in dry ethanol (as a solvent) while being shaken for 7 days at 120 rpm on the shaker. The amine-functionalized PVBC nanofibers were quaternized with benzyl derivatives. The quaternization step was carried out as described by du Preez and Naidoo (2005) (Scheme 4.2), followed by Soxhlet extraction using ethanol for 24 hours [101, 102]. The fibers were then collected, washed with ethanol and dried in air. The nitrogen content (%) was determined by microanalysis.

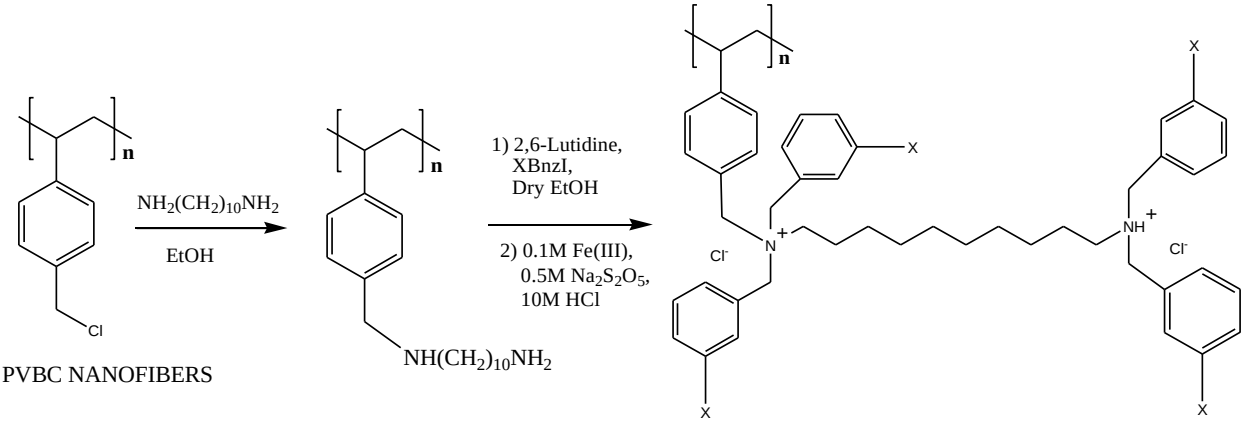

Scheme 4.2: Scheme for functionalization of PVBC nanofibers with quaternary diammonium cations.

4.2.3 Preparation of metal stock solutions

0.045 M rhodium and 0.015 M iridium solutions were prepared to give a molarity ratio of 3:1 rhodium to iridium solution in 6 M HCl. This synthetic mixture corresponds well with the real industrial feed solution [101].

4.2.3.1 Iridium solution

The iridium starting material was obtained as black solid iridium(III) chloride hydrate salt ($IrCl_3 \cdot xH_2O$). 0.22 g of the salt was weighed, and 50 mL of 6 M HCl was added. The solution was heated to reflux at 70°C for an hour and a brown solution was formed. The solution was allowed to cool, and then 4.36 g of sodium chlorate ($NaClO_3$) was added to oxidise Ir(III) to Ir(IV) during which a dark brown solution was obtained [104].

4.2.3.2 Rhodium solution

The rhodium starting material was obtained as black solid rhodium(III) chloride salt ($RhCl_3$). 0.47 g of the salt was weighed, and 50 mL of 6 M HCl was added. The solution was heated to reflux for an hour at 70°C and a dark red solution was obtained [196].

4.2.4 Column studies

4.2.4.1 Single element study

0.1 g of Quaternized nanofibers (F-QuatDMDABnz, F-QuatDMDAMeBnz, F-QuatDMDACF3Bnz and F-QuatDMDANO2Bnz) were respectively packed into a

custom-made glass column. A small amount of glass-wool was placed at both ends to retain the sorbent in the column. MilliQ water (5 mL) followed by 6 M HCl (5 mL) was successively passed through the packed column bed for conditioning the sorbent materials. 2 mL of a single metal solution was loaded onto the column. The solution was then allowed to flow using a previously optimized flow rate of 0.5 ml/hr [152]. 10 mL of 6 M HCl was used to wash off the un-adsorbed metal complex. 0.05 M (5 mL) solution of aqueous sodium metabisulfite was used as a stripping agent, and in the process, it reduced Ir(IV) to Ir(III). Thereafter, an elution step was carried out with 10 mL of 20% aqueous HCl solution. 0.5 mL fractions were collected throughout the process and finally diluted for ICP-OES analysis.

4.2.4.2 Binary mixture study

1 mL of $[RhCl_5(H_2O)]^{2-}$ solution was added to 1 mL of $[IrCl_6]^{2-}$ solution and the resulting mixture (2 mL) was loaded onto a conditioned column as mentioned in Section 4.2.4.1. Thereafter, the un-adsorbed metal complex species were washed off the column using 6 M HCl, followed by stripping with 0.05 M sodium metabisulfite solution and then elution with 10 mL 20% HCl. The collected 0.5 mL fractions were diluted appropriately and analysed for the metal content by ICP-OES.

4.2.5 Adsorption studies

4.2.5.1 Adsorption kinetics

The binding kinetics were carried out in the range of 1-30 minutes of equilibration. A 0.1 g of quaternized functionalized nanofibers were weighed and added into a beaker, and 10 mL of 6 M HCl solution was added. The mixture was shaken a mechanical shaker for 1 minute intervals up to 10 minutes thereafter 20 minutes and 30 minutes. 2 mL of the metal solution containing 1 mL 0.045 M Rh and 1 mL 0.015 M Ir was added, respectively. The mixture was placed on a rotary shaker at an agitation speed of 120 rpm. 50 µL amount of aliquots were sampled at fixed time intervals from 1 to 30 minutes. Samples were diluted appropriately, filtered through a 0.45 µm pore size filter and analyzed by ICP-OES. Two simplified kinetic models, pseudo-first order and pseudo-second-order, were investigated to test adsorption kinetics of the sorbents.

4.2.5.2 Adsorption isotherms

The studies were carried out at 25°C using 0.1 g of quaternized nanofibers with shaking in a mechanical shaker for 5 minutes using the concentration range of 923-2447 ppm for $[IrCl_6]^{2-}$ and 1408-4193 ppm for $[RhCl_5(H_2O)]^{2-}$. An adsorption isothermal study was carried out on two well know isotherms, namely Langmuir adsorption isotherm and Freundlich adsorption isotherm. These are, represented by equations in Chapter 2 (Section 2.4)

4.2.6 DFT Calculations

DFT calculation protocols are presented in Chapter 2, Sections 2.6.

4.3 Results and Discussion

4.3.1 DFT calculations

Theoretical investigations utilizing density functional theory (DFT) were carried out to explore the chemical behaviour of quaternary diammonium cations with respect to their interaction with $[IrCl_6]^{2-}$ and $[RhCl_5(H_2O)]^{2-}$. The chemical properties and behaviour of quaternary diammonium cations were investigated before and after interaction with $[IrCl_6]^{2-}$ and $[RhCl_5(H_2O)]^{2-}$. Four quaternary diammonium cations namely, QuatDMDABnz, QuatDMDAMeBnz, QuatDMDANO2Bnz and QuatDMDACF3Bnz were investigated mainly for the effectiveness of quaternizing groups based on their electron donating and electron withdrawing nature (Figure 4.1 and 4.5).

The calculated results of the modelled structures were mainly based on the thermodynamic data and chemical parameters such as highest occupied molecular orbital energy (HOMO (E_H)) and lowest unoccupied molecular orbital energy (LUMO (E_L)), band gap energy (HOMO-LUMO (E_G)), hardness (η), softness (σ) and electronegativity (χ). The energies of HOMO, LUMO, HOMO-LUMO gap were converted from a.u. to eV using the conversion factor 27.2114. However, the study was only concerned with the interactions of these quaternary diammonium cations

with $[IrCl_6]^{2-}$ and $[RhCl_5(H_2O)]^{2-}$. The results obtained have highlighted that density functional theory (DFT) is a reliable tool for explaining the properties of these cations. This approach is, therefore, a very useful means to predict, evaluate and investigate the chemical parameters as well as to gain insights into the cation-anion interaction.

4.3.1.1 HOMO and LUMO

The adduct formed on the metal ion species ($[IrCl_6]^{2-}$ and $[RhCl_5(H_2O)]^{2-}$) indicated that the HOMO positions originated around the metal ions and chlorides while the LUMO positions originated around the metal ions, chlorides for $[IrCl_6]^{2-}$ and $[RhCl_5(H_2O)]$ around the chlorides (Figure 4.4). The adduct formed on the quaternary diammonium cations indicated that the HOMO positions originated around two benzyl groups for QuatDMDABnz, QuatDMDAMeBnz and QuatDMDACF3Bnz, but for QuatDMDANO2Bnz around four benzyl groups (Figure 4.5).

Adducts formed between quaternary diammonium cations (QuatDMDABnz, QuatDMDAMeBnz, QuatDMDANO2Bnz, QuatDMDACF3Bnz) and $(IrCl_6)^{2-}$ which indicate that the HOMO positions originated around the benzyl for [QuatDMDABnz]($IrCl_6$), [QuatDMDAMeBnz]($IrCl_6$) and [QuatDMDACF3Bnz]($IrCl_6$) except for [QuatDMDANO2Bnz]($IrCl_6$) which indicated to be around $[IrCl_6]^{2-}$ while LUMO positions originated around $[IrCl_6]^{2-}$ anion (Figure 4.6). This shows that the interaction between quaternary diammonium cations and $[IrCl_6]^{2-}$ is possible and occurs through electron transfer. However, adduct formed between the quaternary diammonium cations and $[RhCl_5(H_2O)]^{2-}$ anion showed that the HOMO and LUMO

positions originated around the $[RhCl_5(H_2O)]^{2-}$ anion. Except for QuatDMDANO2Bnz cation, the LUMO position originated on the benzene rings (Figure 4.7). This confirmed that the quaternary diammonium cations have a preference for $[IrCl_6]^{2-}$, as this shows a transfer of electrons from HOMO to LUMO.

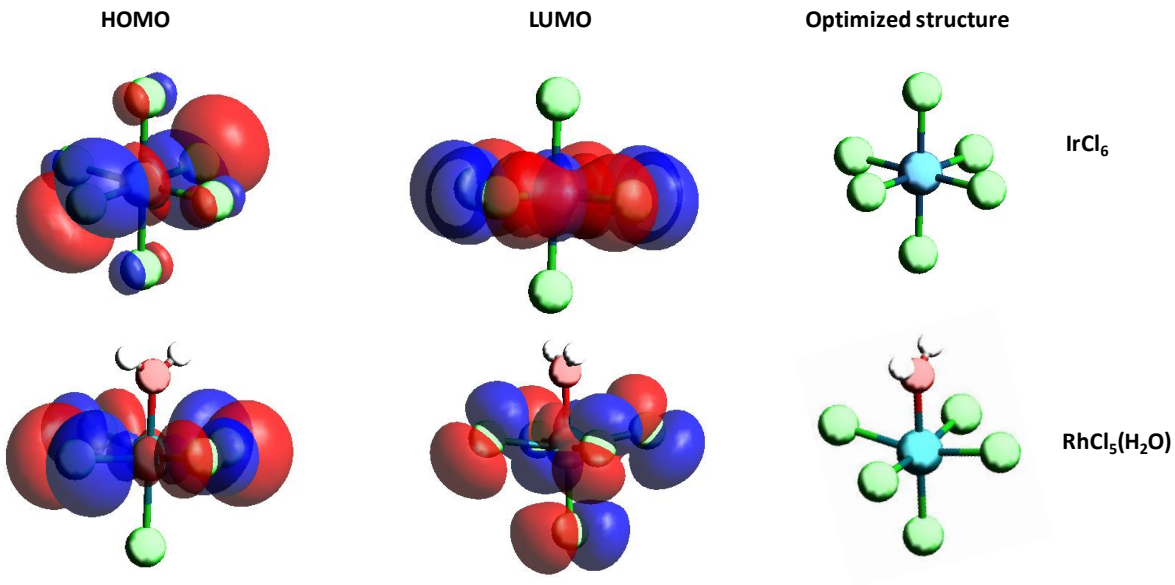

Figure 4.4: HOMO-LUMO of $[IrCl_6]^{2-}$ and $[RhCl_5(H_2O)]^{2-}$.

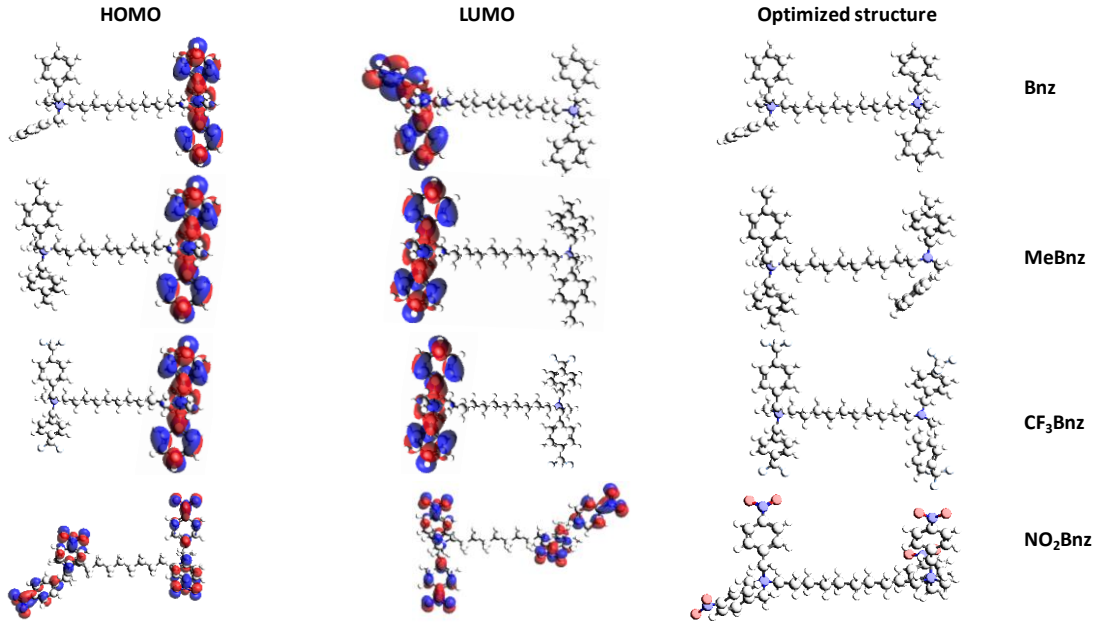

Figure 4.5: HOMO-LUMO of quaternary diammonium cations (QuatDMDABnz, QuatDMDAMeBnz, QuatDMDACF3Bnz and QuatDMDANO2Bnz).

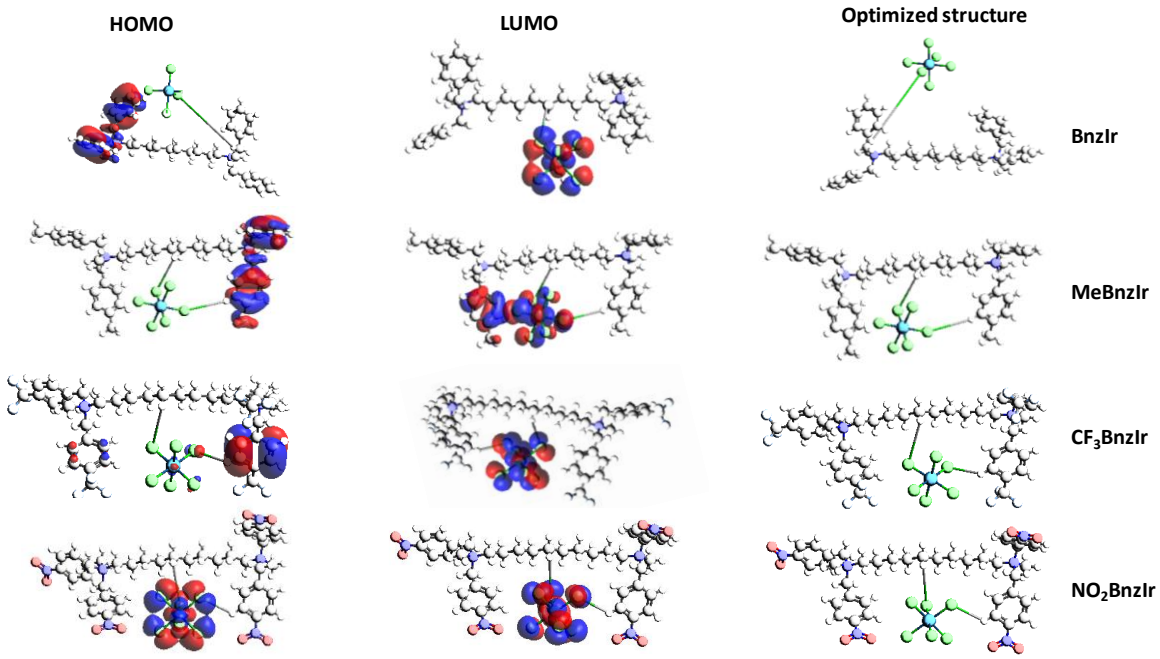

Figure 4.6: HOMO-LUMO of $[IrCl_6]^{2-}$ complexes with quaternary diammonium cations.

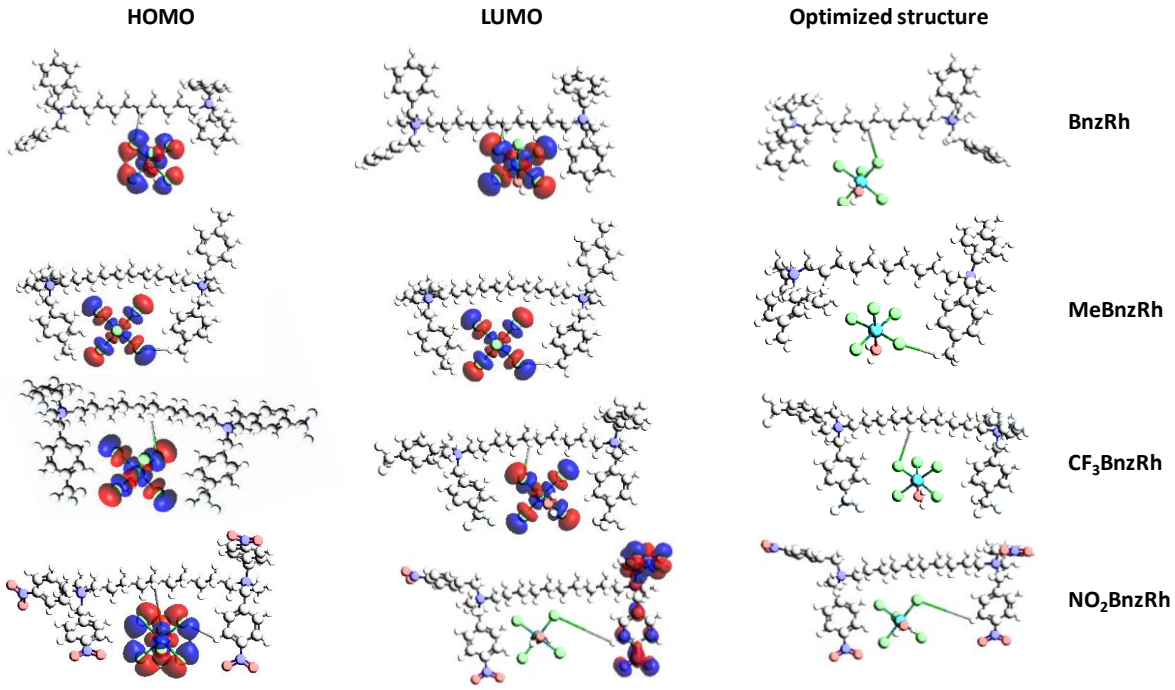

Figure 4.7: HOMO-LUMO of $[RhCl_5(H_2O)]^{2-}$ complexes with quaternary diammonium cations.

4.3.1.2 Band gap energy

The energy gap is an important parameter as a function of reactivity of the cation towards the interaction with the metal ion. As the energy gap decreases the reactivity of the cation increases leading to a better cation efficiency [154, 214]. The quaternary diammonium cations resulted in a decrease in the HOMO-LUMO energy gap in the following order QuatDMDABnz > QuatDMDAMeBnz > QuatDMDACF3Bnz > QuatDMDANO2Bnz. The sequence of reactivity of the cations concludes that QuatDMDANO2Bnz is the more reactive compared to QuatDMDACF3Bnz, QuatDMDAMeBnz and QuatDMDABnz. The metal ion species, $[IrCl_6]^{2-}$, is indicated to

have a lower energy gap compared to $[RhCl_5(H_2O)]^{2-}$. This Indicates that $[IrCl_6]^{2-}$ would be the preferred anion for complexing with quaternary diammonium cations.

Molecular interactions between the quaternary diammonium cations (QuatDMDABnz, QuatDMDAMeBnz, QuatDMDACF3Bnz and QuatDMDANO2Bnz) and $[IrCl_6]^{2-}$ resulted in a decrease in HOMO-LUMO energy gap when compared to the HOMO-LUMO gap of the quaternary diammonium cations, thus further indicating that interactions would form more stable adducts (Table 4.1). The band gap energy of the iridium complexes decreased in the order of [QuatDMDANO2Bnz]($IrCl_6$) (1.097) > [QuatDMDACF3Bnz]($IrCl_6$) (1.020 eV) > [QuatDMDAMeBnz]($IrCl_6$) (0.874 eV) > [QuatDMDABnz]($IrCl_6$) (0.757). Most stable complexes will be formed with iridium complexes due to the lower band energy gap compared that of rhodium complexes. The rhodium complexes energy gap decrease in the order of [QuatDMDAMeBnz]($RhCl_5(H_2O)$) (3.923 eV) > [QuatDMDABnz]($RhCl_5(H_2O)$) (3.904 eV) > [QuatDMDACF3Bnz]($RhCl_5(H_2O)$) (3.612 eV) > [QuatDMDANO2Bnz]($RhCl_5(H_2O)$) (2.613 eV).

4.3.1.2 Chemical hardness and softness

HOMO and LUMO were used to predict the interaction or ion pairing centres of the cations. For the simplest transfer of electrons, interaction should occur at the part of the molecule where the softness (σ) has the highest value, according to Koopman's theorem [182]. Absolute hardness and softness are important properties to measure molecular stability and reactivity. The quaternary diammonium cations and metal ions

hardness/ softness were investigated and calculated as shown in Chapter 2 equations 2.11 and 2.12.

The softness of quaternary diammonium cations increased in the order of QuatDMDANO2Bnz (12.189) > QuatDMDACF3Bnz (1.960) > QuatDMDAMeBnz (0.495) > QuatDMDABnz (0.333). The metal ions softness increased in the order of $[IrCl_6]^{2-}$ (2.273 eV) > $[RhCl_5(H_2O)]^{2-}$ (0.899). Normally, the cation with the least value of absolute hardness (hence, the highest value of absolute softness) is expected to have the highest cation efficiency [155, 214, 215]. This means QuatDMDANO2Bnz should have the highest cation efficiency according to the DFT calculations.

According to the complexation theory (Table 4.1), the [Cation]($IrCl_6$) complexes shows that the highest softness value in the following order; [QuatDMDANO2Bnz]($IrCl_6$) (1.823 eV) < [QuatDMDACF3Bnz]($IrCl_6$) (1.961 eV) [QuatDMDAMeBnz]($IrCl_6$) (2.643 eV) < [QuatDMDABnz]($IrCl_6$) (2.742 eV). [Cation]($RhCl_5(H_2O)$) complexes showed the lowest softness values in the following order; [QuatDMDAMeBnz]($RhCl_5(H_2O)$) (0.510 eV) < [QuatDMDACF3Bnz]($RhCl_5(H_2O)$) (0.511 eV) < [QuatDMDABnz]($RhCl_5(H_2O)$) (0.512 eV) < [QuatDMDANO2Bnz]($RhCl_5(H_2O)$) (0.756 eV). Hence, the iridium complexes are the most stable complexes and that is in agreement with the order of theoretical complexes energy gaps.

4.3.1.3 Electronegativity

The electronegativity (χ), indicates the tendency of a cation to attract electrons (or electron density) towards itself when interacting with a metal ion. The higher the

electronegativity of a cation the stronger its adsorption capacity. As displayed in Table 4.1, the electron-accepting ability of the cations were in the following order; QuatDMDAMeBnz < QuatDMDABnz < QuatDMDACF3Bnz < QuatDMDANO2Bnz. The QuatDMDANO2Bnz showed to be the most electronegative compared with QuatDMDACF3Bnz, QuatDMDAMeBnz and QuatDMDABnz. This showed QuatDMDANO2Bnz will interact strongly or bind more strongly with $[IrCl_2]^{2-}$. The electrostatic potential (ESP) also confirmed the electronegativity of the cations and observed two benzyl groups in all quaternary diammonium cations are electron rich, meaning only two benzyl groups interacting strongly with the metal ion (Figure 4.8).

The [Cation]($IrCl_6$) complexes show large electronegativity observed in the following order; [QuatDMDANO2Bnz]($IrCl_6$) (7.441 eV) > [QuatDMDACF3Bnz]($IrCl_6$) (7.409 eV) > [QuatDMDABnz]($IrCl_6$) (6.842 eV) > [QuatDMDAMeBnz]($IrCl_6$) (6.616 eV). The [Cation]($RhCl_5(H_2O)$) complexes showed lower electronegativity in the following order; [QuatDMDABnz]($RhCl_5(H_2O)$) (4.308 eV) < [QuatDMDAMeBnz]($RhCl_5(H_2O)$) (4.362 eV) < [QuatDMDACF3Bnz]($RhCl_5(H_2O)$) (4.392 eV) < [QuatDMDANO2Bnz]($RhCl_5(H_2O)$) (5.015 eV). The iridium complexes sequence agreed with the experimental findings in a binary column study. According to the electronegativity theory, QuatDMDANO2Bnz is the most preferred cation and form stable complexes with $[IrCl_6]^{2-}$.

Table 4.1: Chemical parameters, HOMO (E_H), LUMO (E_L), Band gap energies (E_G), Hardness (η), Softness (σ) and electronegativity(χ).

	E_H (eV)	E_L (eV)	E_G (eV)	η	σ	χ
Diammonium cations						
F-QuatDMDABnz	-4.402	-1.387	3.015	3.007	0.333	2.394
F-QuatDMDAMeBnz	-5.485	-1.443	4.042	2.021	0.495	2.464
F-QuatDMDACF3Bnz	-4.121	-2.037	2.084	1.042	1.960	3.079
F-QuatDMDANO2Bnz	-3.454	-3.290	0.164	0.082	12.189	3.372
Metal complex anions						
$[IrCl_6]^{2-}$	-9.860	-7.635	2.225	0.440	2.273	8.747
$[RhCl_5(H_2O)]^{2-}$	-8.427	-5.547	2.880	1.112	0.899	7.987
[Cation]($IrCl_6$) ion pairs						
[QuatDMDABnz]($IrCl_6$)	-6.887	-6.013	0.874	0.382	2.742	6.842
[QuatDMDAMeBnz]($IrCl_6$)	-6.994	-6.237	0.757	0.378	2.643	6.616
[QuatDMDACF3Bnz]($IrCl_6$)	-7.919	-6.899	1.020	0.510	1.961	7.409
[QuatDMDANO2Bnz]($IrCl_6$)	-7.989	-6.892	1.097	0.548	1.823	7.441
[Cation]($RhCl_5(H_2O)$) ion pairs						
[QuatDMDABnz]($RhCl_5(H_2O)$)	-6.271	-2.346	3.904	1.962	0.510	4.308
[QuatDMDAMeBnz]($RhCl_5(H_2O)$)	-6.314	-2.411	3.923	1.952	0.512	4.362
[QuatDMDACF3Bnz]($RhCl_5(H_2O)$)	-6.348	-2.436	3.612	1.956	0.511	4.392
[QuatDMDANO2Bnz]($RhCl_5(H_2O)$)	-6.321	-3.708	2.613	1.307	0.765	5.015

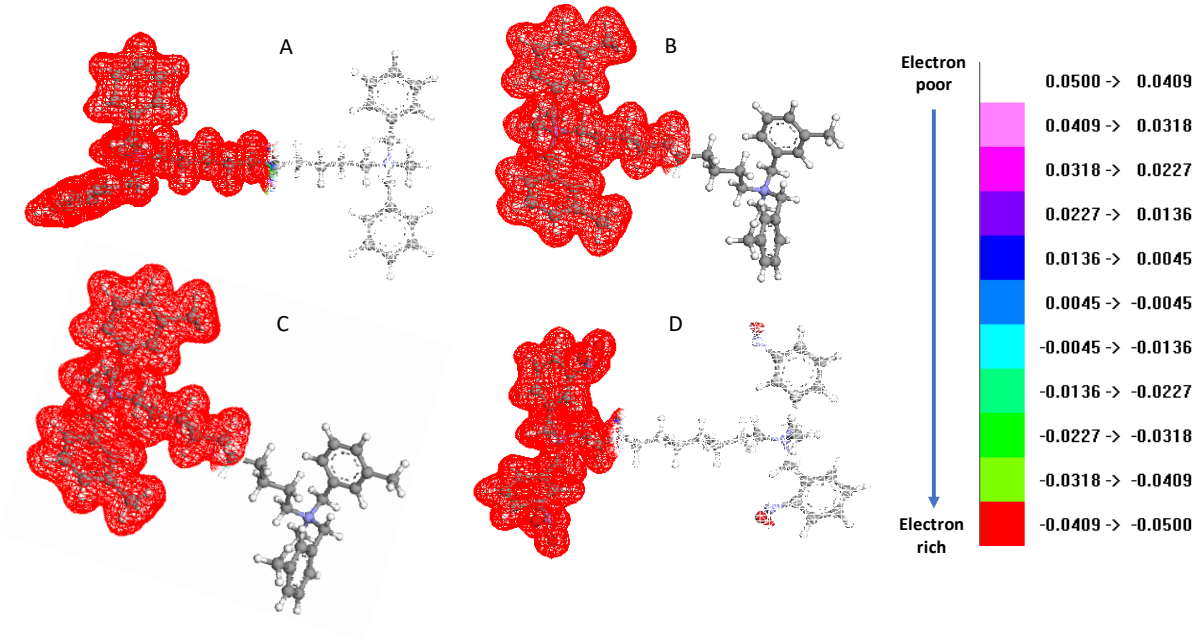

Figure 4.8: ESP of quaternary diammonium cations; (A)QuatDMDABnz, (B) QuatDMDAMeBnz (C) QuatDMDACF3Bnz and (D) QuatDMDANO2Bnz.

4.3.1.4 Thermodynamic data

Thermodynamic parameters such as free Gibbs energies (ΔΔG), enthalpy (ΔΔH) and entropy (ΔΔS) resulting from adduct formation are presented in Table 4.2. A decrease in free Gibbs energy of the system ($\Delta G_b < 0$) confirmed that the adsorption process was spontaneous or favoured. A decrease in the randomness of the interacting molecules gives rise to negative entropies ($\Delta S_b < 0$). Negative enthalpy (ΔH_b) value resulting from strong interaction between molecules contributed to an exothermic process.

The optimized structures of the metal ions, $[IrCl_6]^{2-}$ and $[RhCl_5(H_2O)]^{2-}$, cations (QuatDMDAMeBnz, QuatDMDABnz, QuatDMDACF3Bnz and QuatDMDANO2Bnz) and complexes ([QuatDMDANO2Bnz]($IrCl_6$), [QuatDMDACF3Bnz]($IrCl_6$), [QuatDMDABnz]($IrCl_6$), [QuatDMDAMeBnz]($IrCl_6$), [QuatDMDABnz]($RhCl_5(H_2O)$), [QuatDMDAMeBnz]($RhCl_5(H_2O)$), [QuatDMDACF3Bnz]($RhCl_5(H_2O)$) and [QuatDMDANO2Bnz]($RhCl_5(H_2O)$)) are shown in Figures 4.4-4.7 and Table 4.2. The thermodynamic data studies showed that the interactions between $[IrCl_6]^{2-}$ with quaternary diammonium cations were favourable, spontaneous and exothermic in nature. The order of favourability between the $[IrCl_6]^{2-}$ and quaternary diammonium cations increased in the order of [QuatDMDANO2Bnz]($IrCl_6$) (-244.913 kcal.mol^{-1}) > [QuatDMDACF3Bnz]($IrCl_6$) (-234.570 kcal.mol^{-1}) > $[IrCl_6$(F-QuatDMDABnz$)]^{2-}$ (-229.618 kcal.mol^{-1}) > [QuatDMDAMeBnz]($IrCl_6$) (-171.457 kcal.mol^{-1}). The thermodynamic values for [QuatDMDANO2Bnz]($IrCl_6$) were greater than that for $[IrCl_6$(F-QuatDMDACF3Bnz$)]^{2-}$, [QuatDMDABnz]($IrCl_6$), [QuatDMDAMeBnz]($IrCl_6$). The $[RhCl_5(H_2O)]^{2-}$ interaction with quaternary diammonium cations were least favoured. In the binary experimental (Rh and Ir) column study, the order of favourability towards $[IrCl_6]_{2-}$ agreed with the thermodynamic data, where QuatDMDANO2Bnz had the highest loading capacity. This shows in the column study the electron withdrawing cations are more preferred than the electron donating cations. This showed that the cations with electron withdrawing groups are the benzyl group were more favoured compared to those with electron donating groups on the benzyl groups.

Table 4.2: DFT molecular modelling thermodynamic data (ΔΔH, ΔΔG and ΔΔS) on the formation of an adduct between metal ions ($[IrCl_6]^{2-}$ and $[RhCl_5(H_2O)]^{2-}$) and Cations (QuatDMDABnz, QuatDMDAMeBnz, QuatDMDACF3Bnz and QuatDMDANO2Bnz).

[Cation](Anion)	**ΔΔG (Kcal.mol^{-1})**	**ΔΔH (kcal.mol^{-1})**	**ΔΔS (kcal.mol^{-1})**
[QuatDMDAMeBnz]($IrCl_6$)	-171.457	-185.933	-185.378
[QuatDMDABnz]($IrCl_6$)	-229.618	-195.013	-189.436
[QuatDMDACF3Bnz]($IrCl_6$)	-234.57	-245.275	-245.924
[QuatDMDANO2Bnz]($IrCl_6$)	-244.913	-250.155	-290.252
[QuatDMDAMeBnz]($RhCl_5(H_2O)$)	-135.8112	-145.8137	-145.7178
[QuatDMDABnz]($RhCl_5(H_2O)$)	-136.2065	-110.883	-109.329
[QuatDMDACF3Bnz]($RhCl_5(H_2O)$)	-139.3265	-138.623	-135.345
[QuatDMDANO2Bnz]($RhCl_5(H_2O)$)	-140.3480	-141.846	-140.391

4.3.2 Synthesis and characterization of quaternary diammonium chloride cations

The quaternary diammonium cations (tetramethylbenzyl-1,10-diammonium chloride (QuatDMDAMeBnz), tetrabenzyl-1,10-diammonium chloride (QuatDMDABnz), tetratrifluoromethylbenzyl-1,10-diammonium chloride (QuatDMDACF3Bnz), and tetranitrobenzyl-1,10-diammonium chloride (QuatDMDANO2Bnz)) were synthesized. Quaternary diammonium cations synthesis initially starts with a halide exchange reaction by converting benzyl chloride groups to benzyl iodide groups using catalytic

amounts of sodium iodide in acetone. This was followed by quaternization through substitution of the iodide by an amine for benzyl iodide or 4-methylbenzyl iodide or 3-triflouromethylbenzyl iodide or 4-nitrobenzyl iodide with 1,10-diamminodecane. 2,6-Lutidine was added to the reaction as a base to abstract the protons on the amine groups. A sodium hydroxide solution (3 M) was used to extract the hydroiodides. The iodide counterions were replaced with chlorides by stirring the salts in ethanolic silver chloride. The solution was filtered to remove silver iodide (and excess silver chloride), and then THF was added to form a precipitate which was filtered, washed several times with 10 M HCl and dried. The general procedure for the preparation of the quaternary ammonium salts is given in Scheme 4.1.

The purity of the cations was confirmed by elemental analyses and ^{1}H NMR characterization. The formation of the quaternary diammonium cations was confirmed by the appearance of the peaks in the region 6.89 to 8.00 ppm in the ^{1}H NMR spectra of these cations which signified the presence of benzene rings. The region between 3.21 to 3.85 ppm confirmed the presence of the methylene groups that connect the benzene ring and 1,10-diaminodecane, and while the region between 1.23 to 1.83 ppm confirmed the presence of the alkyl chain (methylene groups). The purity of the cations was further assured by elemental micro-analysis.

4.3.2.1 Tetrabenzyl-1,10-diammonium chloride (QuatDMDABnz)

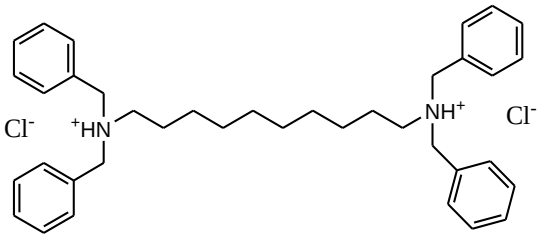

Yield = 32%. Anal. Calcd for $C_{38}H_{50}Cl_2N_2$ (%): C, 78.27; H, 8.58; N, 3.73. Found: C, 78.01; H, 8.33; N, 3.15. ^{1}H NMR (400 MHz, DMSO) σ(ppm): 7.06 (8H, d, CH), 7.14 (8H, d, CH), 7.07 (4H, s, CH), 3.85 (8H, t, CH_2), 1.63 (4H, m, CH_2), 1.23 (12H, m, CH_2) IR (V_{max}/cm^{-1}): 3162 ν(N-H), 3028 ν(C-H), 1683 ν(N-H), 1472 ν(C-H).

4.3.2.2 Tetramethylbenzyl 1,10-diammonium chloride (QuatDMDAMeBnz)

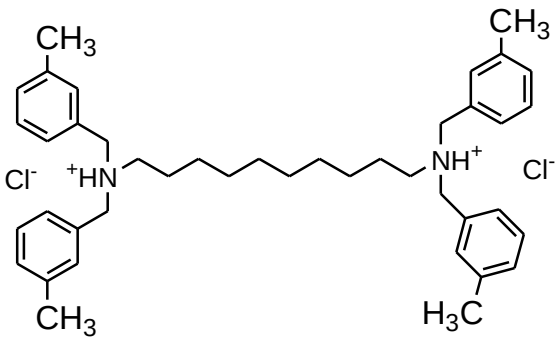

Yield = 36%. Anal. Calcd for $C_{42}H_{58}Cl_2N_2$ (%):C, 78.78; H, 8.98; N, 3.47. Found: C, 78.56; H, 8.56; N, 3.53. ^{1}H NMR (400 MHz, DMSO) σ(ppm): 6.86 (8H, d, CH), 7.00 (8H, d, CH), 3.21 (8H, t, CH_2), 1.57 (4H, m, CH_2), 1.19 (12H, m, CH_2). IR (V_{max}/cm^{-1}): 3112 ν(N-H), 3098 ν(C-H), 1695 ν(N-H), 1422 ν(C-H).

4.3.2.3 Tetranitrobenzyl-1,10-diammonium chloride (QuatDMDANO2Bnz)

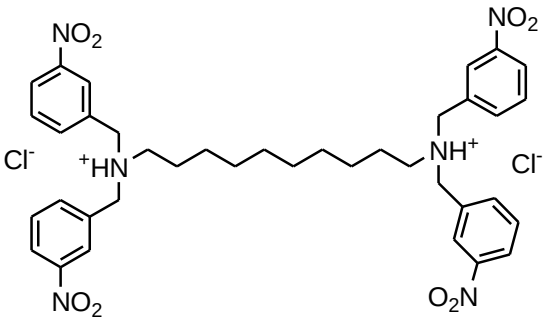

Yield = 31%. Anal. Calcd for $C_{38}H_{46}Cl_2N_6O_8$ (%): C, 63.15; H, 6.49; N, 9.02. Found: C, 63.03; H, 6.34; N, 8.99. ^{1}H NMR (400 MHz, DMSO) σ(ppm): 8.00 (8H, d, CH), 7.42 (8H, d,

CH), 3.45 (8H, t, CH_2), 1.83 (4H, m, CH_2), 1.32 (12H, m, CH_2). IR (V_{max}/cm^{-1}): 3222 ν(N-H), 3142 ν(C-H), 1629 ν(N-H), 1419 ν(C-H).

4.3.2.4 Tetratrifluoromethylbenzyl-1,10-diammonium chloride (QuatDMDACF3Bnz)

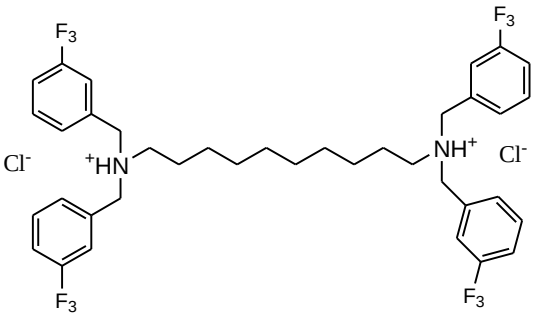

Yield = 22%. Anal. Calcd for $C_{38}H_{46}Cl_2N_2F_{12}$ (%): C, 62.17; H, 5.29; N, 2.74. Found: C, 62.05; H, 5.02; N, 2.64. ^{1}H NMR (400 MHz, DMSO) σ(ppm): 6.89 (8H, d, CH), 7.03 (8H, d, CH), 3.62 (8H, t, CH_2), 1.79 (4H, m, CH_2), 1.28 (12H, m, CH_2). IR (V_{max}/cm^{-1}): 3162 ν(N-H), 3129 ν(C-H), 1668 ν(N-H), 1489 ν(C-H).

4.3.3 Synthesis, functionalization and characterization of nanofibers

Synthesis and functionalization of PVBC nanofibers are presented in Chapter 3, Section 3.3.4. The PVBC nanofibers were functionalized with 1,10-diaminodecane (DMDA) in dry ethanol while being shaken for 7 days at 120 rpm on the shaker. The functionalized PVBC nanofibers were quaternized with benzyl derivatives in presence of a base, 2,6-lutidine. The quaternized PVBC nanofiber was further washed with 0.1 M Fe(III) followed but a hot solution of 0.5M $Na_2S_2O_5$ to converted iodine to iodide. 10 M HCl was used for conversion of iodide into chloride groups to form cationic quaternized PVBC nanofibers.

4.3.3.1 FT-IR spectroscopy

The infrared spectra of the quaternary diammonium cations ((tetramethylbenzyl-1,10-diammonium chloride (QuatDMDAMeBnz), tetrabenzyl-1,10-diammonium chloride (QuatDMDABnz), tetratrifluoromethylbenzyl-1,10-diammonium chloride (QuatDMDACF3Bnz), tetranitrobenzyl-1,10-diammonium chloride (QuatDMDANO2Bnz)), unfunctionalized and functionalized PVBC nanofibers with-1,10-diamminodecane were confirmed by FTIR. FTIR spectra of PVBC before and after functionalization with 1,10-diamminodecane are shown in Figure 4.9 (a & b). In all spectra adsorption band between 3205-3388 cm^{-1} was present revealing the stretching vibration of the v(N-H) and the band at 1578-1591 cm^{-1} for the v(N-H) stretching confirmed the presence of the diamine. Unfunctionalized nanofibers showed a strong peak at 669-673 cm^{-1} due to the ν(C-Cl) and a strong peak at 1262-1271 cm^{-1} which can be assigned to the (CH_2-Cl) bending. These peaks disappeared or got reduced after functionalization. This indicates that all sorbent materials contained cations after functionalization and quaternized.

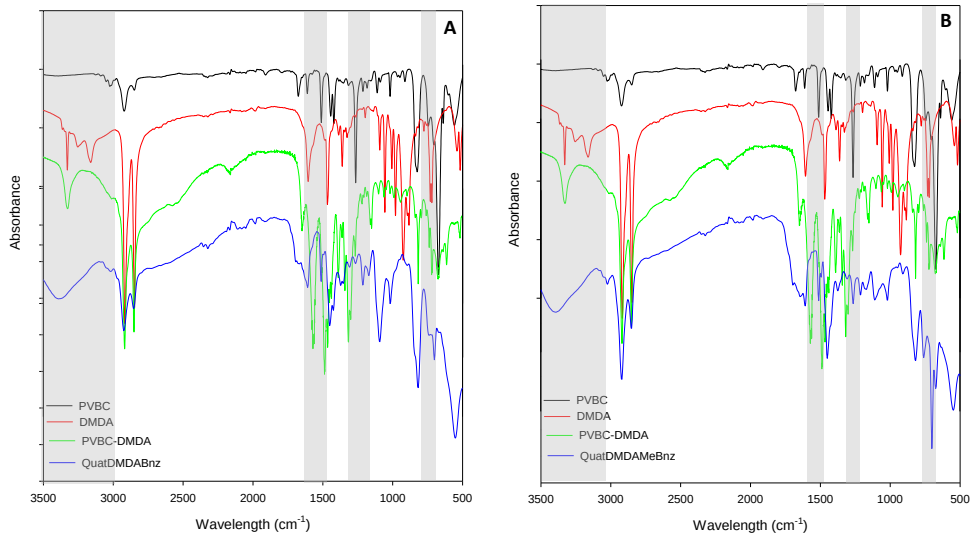

Figure 4.9(a): FTIR spectra for unfunctionalized PVBC (Black), DMDA (Red), functionalized PVBC with DMDA (green) and quaternized PVBC with (A) F-QuatDMDABnz and (B) F-QuatDMDAMeBnz (blue).

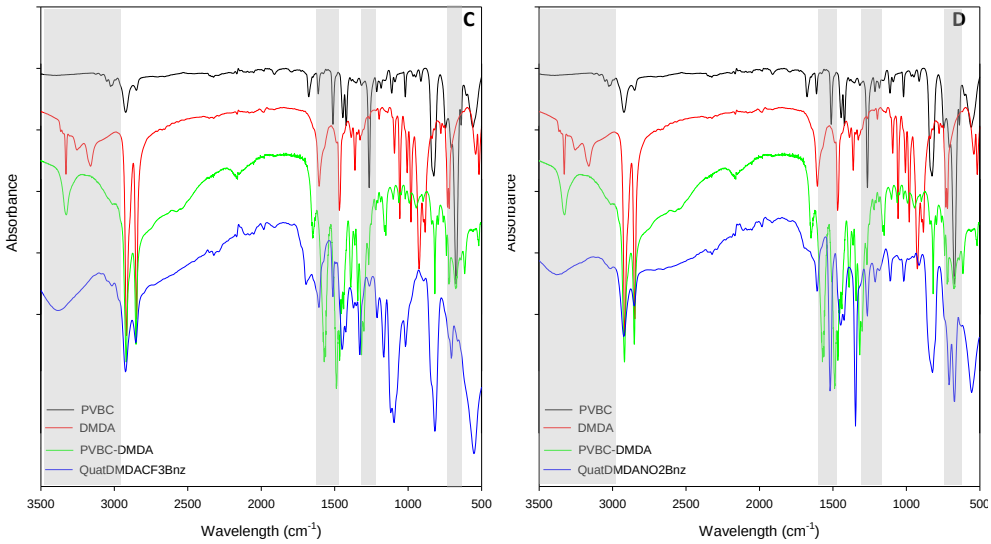

Figure 4.9(b): FTIR spectra for unfunctionalized PVBC (Black), DMDA (Red), functionalized PVBC with DMDA (green) and quaternized PVBC with (A) F-QuatDMDACF3Bnz and (B) F-QuatDMDANO2Bnz (blue).

4.3.3.2 Microanalysis of na nofibers

The purity of unfunctionalized PVBC nanofibers and functionalized PVBC nanofibers, with quaternary diammonium cations (F-QuatDMDAMeBnz, F-QuatDMDABnz, F-QuatDMDACF3Bnz and F-QuatDMDANO2Bnz), were done to confirm the composition of the nanofibers, results are presented in Table 4.3. Functionalized PVBC nanofibers were confirmed by the presence of hydrogen (%), nitrogen (%) and carbon (%). A decrease in the nitrogen content after functionalization was observed and this was evidence of the success of the functionalization reaction. It is not clear how the functionalization on the amine was achieved, i.e. whether on one or both amines.

Table 4.3: The microanalyses data (%) for the nanofibers before and after functionalization and quaternization with F-QuatDMDAMeBnz, F-QuatDMDABnz, F-QuatDMDACF3Bnz and F-QuatDMDANO2Bnz.

Sorbent materials*	**C (%)**	**H (%)**	**N (%)**	**C:N**	**Monomer: Cation**
PVBC	72.86	5.41	-	-	-
PVB-DMDA	78.45	11.12	7.42	6.54:0.53	2:1
F-QuatDMDAMeBnz	86.19	9.33	3.58	7.18:0.26	2:1
F-QuatDMDABnz	86.27	9.70	4.02	7.19:0.29	2:1
F-QuatDMDACF3Bnz	66.28	6.22	2.79	5.52:0.19	2:1
F-QuatDMDANO2Bnz	68.05	6.66	9.84	5.67:0.70	2:1

4.3.3.3 SEM images of nanofibers

The morphology of the unfunctionalized and functionalized nanofibers was observed using a scanning electron microscope (SEM) and the images are shown in Figure 4.10. The nanofibers showed no morphological changes or damage after the functionalization step. There were some changes in the diameter of the nanofibers after the functionalizing with different cations. The nanofiber sizes of the unfunctionalized ranges from 93-108 nm, while the size increased upon functionalization with F-QuatDMDAMeBnz (233-253 nm), F-QuatDMDABnz (251-274 nm), F-QuatDMDACF3Bnz (262-298 nm) and F-QuatDMDANO2Bnz (280-316 nm). These nanofibers diameters seem to be influenced by the size of the quaternary diammonium cations, the larger the cation the bigger the diameter.

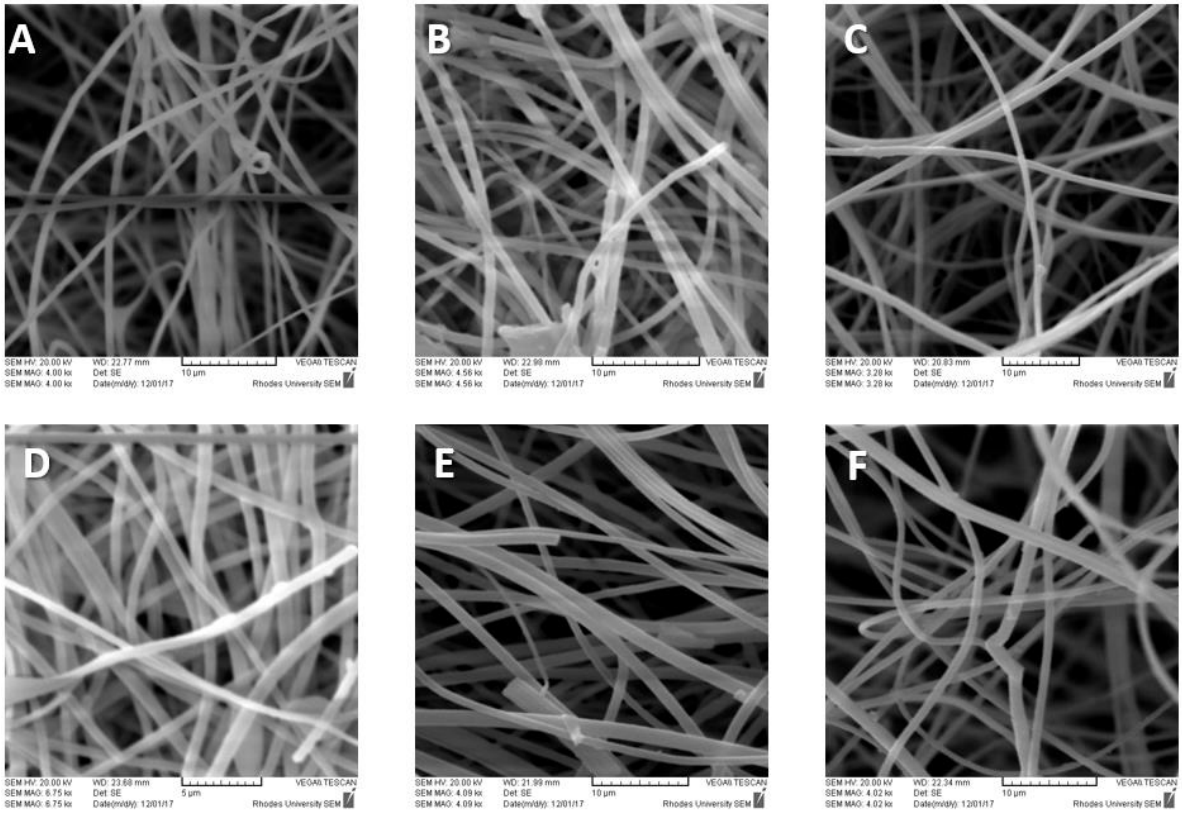

Figure 4.10: SEM images of nanofibers (A) Unfunctionalized PVBC nanofibers, (B) Functionalized with DMDA and (C) Quaternized with Benzyl (F-QuatDMDABnz), (D) Quaternized with 4-Methylbenzyl (F-QuatDMDAMeBnz), (E) Quaternized with 4-Nitrobenzyl (F-QuatDMDANO2Bnz) and (F) Quaternized with 3-triflouromethylbenzyl (F-QuatDMDACF3Bnz).

4.3.3.4 Energy dispersive spectroscopic analysis

Chemical characterization of the PVBC nanofiber before and after functionalization with QuatDMDAMeBnz, QuatDMDABnz, QuatDMDACF3Bnz and QuatDMDANO2Bnz were investigated with energy dispersive spectroscopic analysis

(EDS). The peaks showing the elements present on the sorbent materials are presented in Figure 4.11.

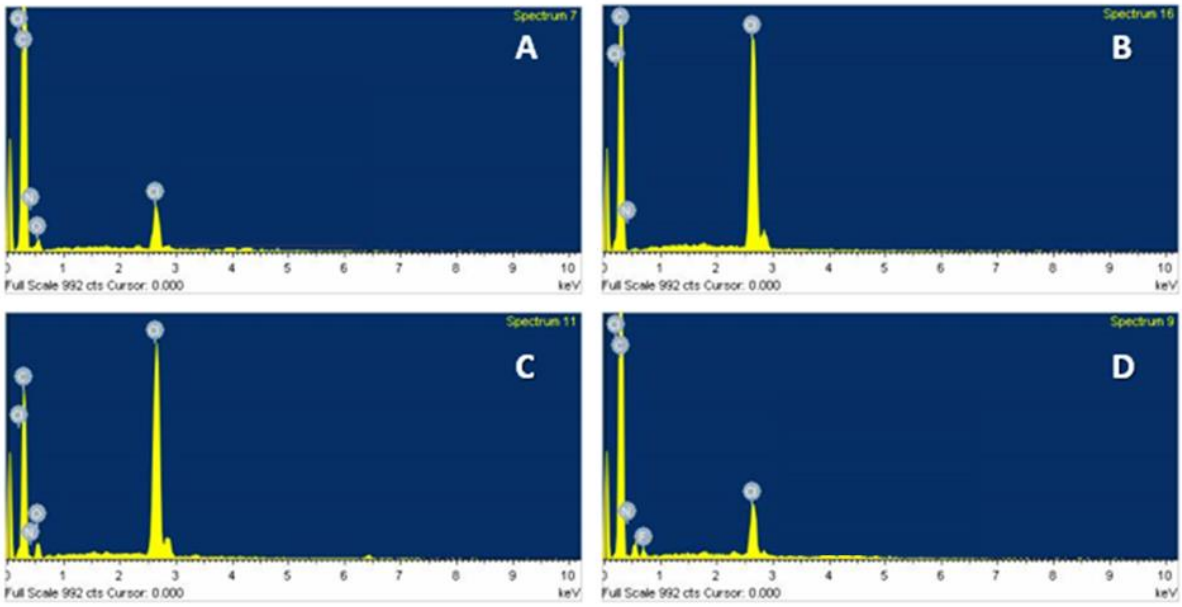

Figure 4.11: EDS images of nanofibers; (A) Quaternized with Benzyl (F-QuatDMDABnz), (B) Quaternized with 4-Methylbenzyl (F-QuatDMDAMeBnz), (C) Quaternized with 4-Nitrobenzyl (F-QuatDMDANO2Bnz) and (D) Quaternized with 3-triflouromethylbenzyl (F-QuatDMDACF3Bnz).

The unfunctionalized PVBC nanofiber reveals C and Cl atom which is expected for the nanofiber material. The two chlorides peaks one from ion-pairing anion while the peak at 2.9 eV is due to bended Cl- (CH_2-Cl) that was unreacted. The functionalization of the PVBC nanofiber material with cations QuatDMDAMeBnz, QuatDMDABnz, QuatDMDACF3Bnz and QuatDMDANO2Bnz were confirmed by the presence of N peaks in the spectra. N peak in the F-QuatDMDAMeBnz, F-QuatDMDABnz, F-

QuatDMDACF3Bnz and F-QuatDMDANO2Bnz material also confirmed the quaternization of DMDA with benzyl groups onto the nanofibers was successful. Traces of Cl were observed on the spectra of the functionalized materials, which could be due to the unfunctionalized parts of the PVBC nanofiber.

4.3.3.5 BET surface area of nanofibers

A Brunauer–Emmett–Teller (BET) model was used to calculate the specific surface area and a Barrett–Joyner–Halenda (BJH) model was used to calculate the pore volume distribution and the average pore size of the unfunctionalized nanofibers (A) PVBC nanofibers, and functionalized nanofibers (B) PVBC-DMDA, (C) F-QuatDMDAMeBnz, (D) F-QuatDMDACF3Bnz and (E) F-QuatDMDANO2Bnz as shown in Figure 4.12. Specific pore sizes and surface areas of unfunctionalized nanofibers (PVBC) and functionalized nanofibers are shown in Table 4.4.

The cavities created in unfunctionalized nanofiber (PVBC) and functionalized nanofibers (PVB-DMDA, F-QuatDMDABnz, F-QuatDMDAMeBnz, F-QuatDMDACF3Bnz and F-QuatDMDANO2Bnz) showed well defined pore openings with pore diameters of 51.33 Å (5.13 nm), 51.64 Å (5.16 nm), 51.81 Å (5.18 nm), 51.95 Å (5.20 nm), 52.27 Å (5.23 nm) and 52.61 Å (5.26 nm), respectively, and fall within the mesopore region (2 nm < pore diameter < 50 nm) [189–191]. Functionalized nanofibers exhibited a higher surface area than the unfunctionalized nanofibers due to the addition of cation upon functionalization. The changes in an increase in surface area of the functionalized nanofibers were attributed to the presence of a hysteresis

loop in the adsorption-desorption isotherms of the functionalized nanofibers (Figure 3.18). Hysteresis effects are similar to type III were observed (Figure 4.12). F-QuatDMDABnz, F-QuatDMDAMeBnz, F-QuatDMDACF3Bnz and PVB-F-QuatDMDANO2Bnz were observed to follow type-1 hysteresis loop that is found in materials which exhibit a narrow range of uniform mesopores. The functionalization effect of nanofibers may have influenced the observed pore diameter and surface area of the functionalized nanofibers [194-198].

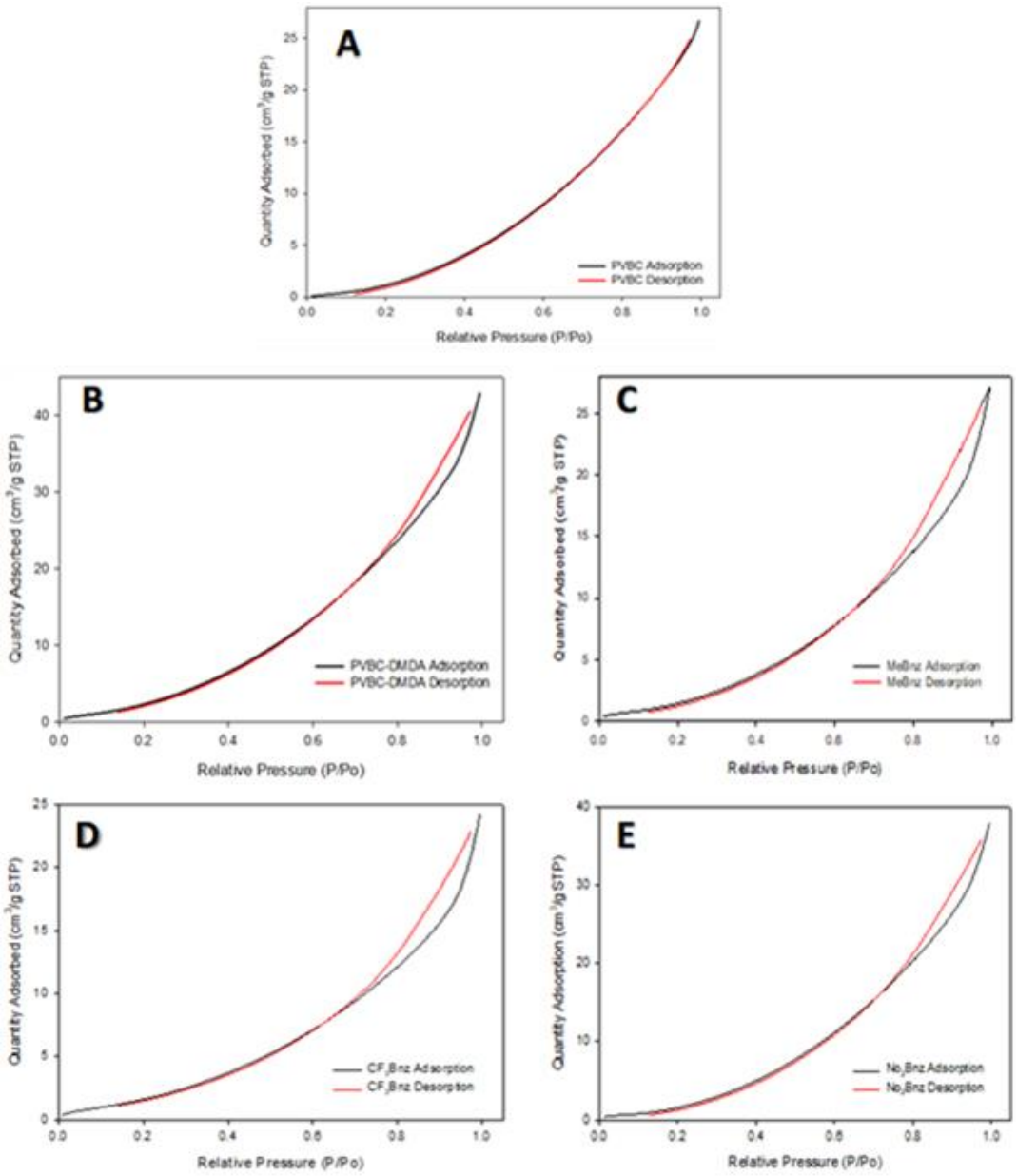

Figure 4.12: N_2 adsorption isotherms for unfunctionalized and functionalized nanofibers (with quaternary diammonium cations), (A) unfunctionalized PVBC nanofiber, (B) PVB-DMDA, (C) F-QuatDMDAMeBnz, (D) F-QuatDMDACF3Bnz and (E) F-QuatDMDANO2Bnz.

Table 4.4: BET surface area of functionalized nanofibers with quaternary diammonium cations.

Resins	BET-surface area (m^2/g)	Pore Size (Å) (Adsorption)	Pore Size (Å) (Desorption)
PVBC	7.54	51.33	51.52
PVB-DMDA	12.79	51.64	50.13
F-QuatDMDABnz	14.84	51.81	52.34
F-QuatDMDAMeBnz	15.61	51.95	52.65
F-QuatDMDACF3Bnz	17.40	52.27	52.87
F-QuatDMDANO2Bnz	19.31	52.61	52.62

4.3.3.6 Thermogravimetric analysis (TGA) of nanofibers

Thermogravimetric analysis of functionalized nanofibers with F-QuatDMDAMeBnz, F-QuatDMDABnz, F-QuatDMDACF3Bnz and F-QuatDMDANO2Bnz were conducted under a nitrogen atmosphere (Figure 4.13). Samples were heated from room temperature to 600°C at a heating rate of 10°C/min. The TGA curves for the functionalized nanofibers showed an initial weight loss of ~ 5% which occurred up to 100°C and was attributed to the intramolecular solvents. The TGA curves of functionalized nanofibers all gave similar decomposition patterns with three distinct step degradation process was observed at around 200-300°C, 300-400°C and between 400-450°C. The first weight loss was assigned to the decomposition of the functionalized nanofibers (quaternary diammonium cation) backbone which occurred at a temperature of about 200-300°C, hence, confirming the functionalized nanofiber's thermal stability. The second weight loss resulted in a breakdown of the polymer

nanofiber backbone between 300-400°C, where a small broad endothermic process was observed for PVB-DMDA, F-QuatDMDAMeBnz, F-QuatDMDABnz, F-QuatDMDACF3Bnz and F-QuatDMDANO2Bnz. The decomposition of the functional groups and the collapse of the polymer was observed from 400-450°C, show a sharp endothermic process for PVBC, PVB-DMDA, F-QuatDMDAMeBnz, F-QuatDMDACF3Bnz and F-QuatDMDANO2Bnz and thereafter residual amount has been completely decomposed by continuous heating until the end of the measurement at 600°C**.**

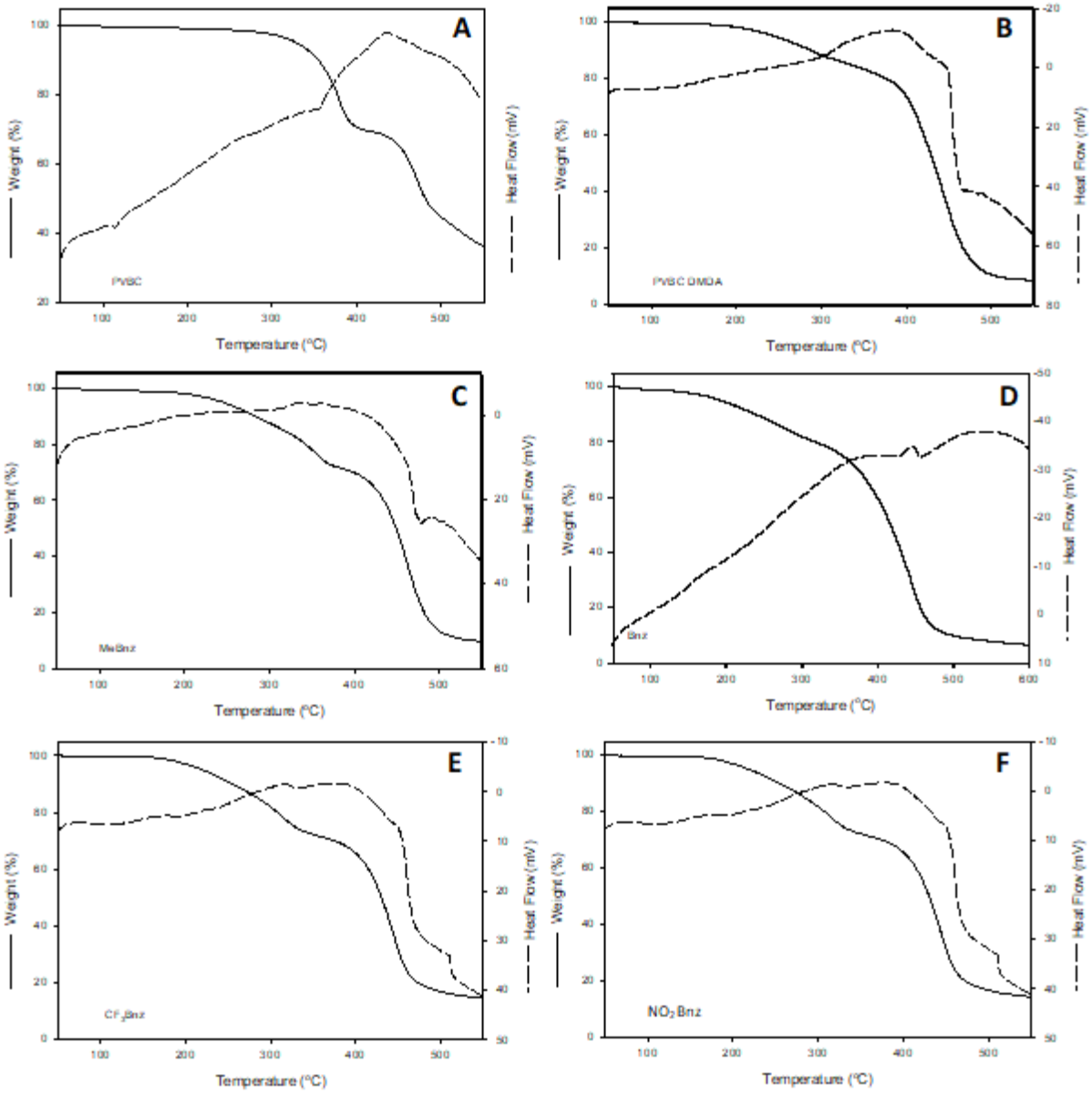

Figure 4.13: TGA diagrams of nanofibers; (A) PVBC, (B) PVBC-DMDA, (C) F-QuatDMDAMeBnz, (D) F-QuatDMDABnz, (E) F-QuatDMDACF3Bnz and (F) F-QuatDMDANO2Bnz.

4.3.4 UV-VIS spectroscopic characterization of the metal solution

4.3.4.1 Metal stock solution

The synthesis of the chloride species was carried out as outlined in the literature. The iridium and rhodium complex species were confirmed spectroscopically [150, 152]. A peak corresponding to $[IrCl_6]^{2-}$ was observed at 488 nm and $[RhCl_5(H_2O)]^{2-}$ peak was observed at 516 nm using a UV-Vis Spectrophotometer (Figure 4.14).

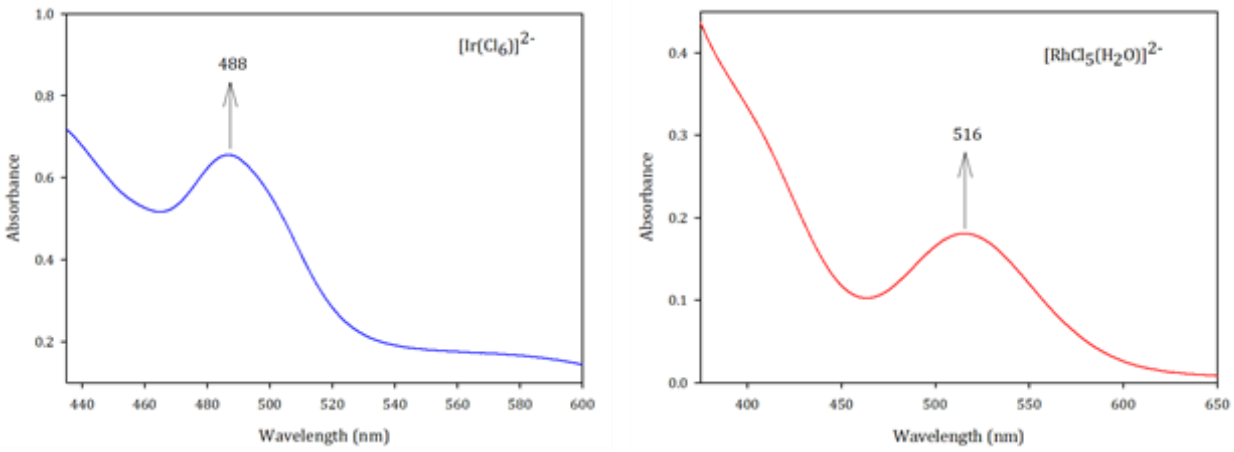

Figure 4.14: Uv-Vis spectra of $[IrCl_6]^{2-}$ and $[RhCl_5(H_2O)]^{2-}$ in 6 M HCl.

4.3.5 Crystal structure of $[IrCl_6]^{2-}$

$[IrCl_6]^{2-}$ complex was obtained in 6 M HCl solution as an ammonium salt. The geometry of the complex is suggested to be distorted octahedral and was isolated in a monoclinic crystal system and $C_{2/m}$ space group, selected crystal data, bond angles and distances are shown in Figure 4.15 and Tables 4.5 and 4.6. The monoclinic crystal described by vectors of unequal lengths, as in the orthorhombic system and the angles between these vectors must all be different [213]. The crystal data shows that the

complex is distorted octahedral due to the fact that the bond angles are not exactly 90°C to give a perfect octahedral geometry. The $[IrCl_6]^{2-}$ complex was compared with modelling bond distance; Cl_1-Ir-Cl_2 (90.0008), Cl_1ii-Ir-Cl_2i (89.9992) and Cl_2i-Ir-Cl_2 (180). The crystal data gives a confirmation of the iridium species that is being used in this study.

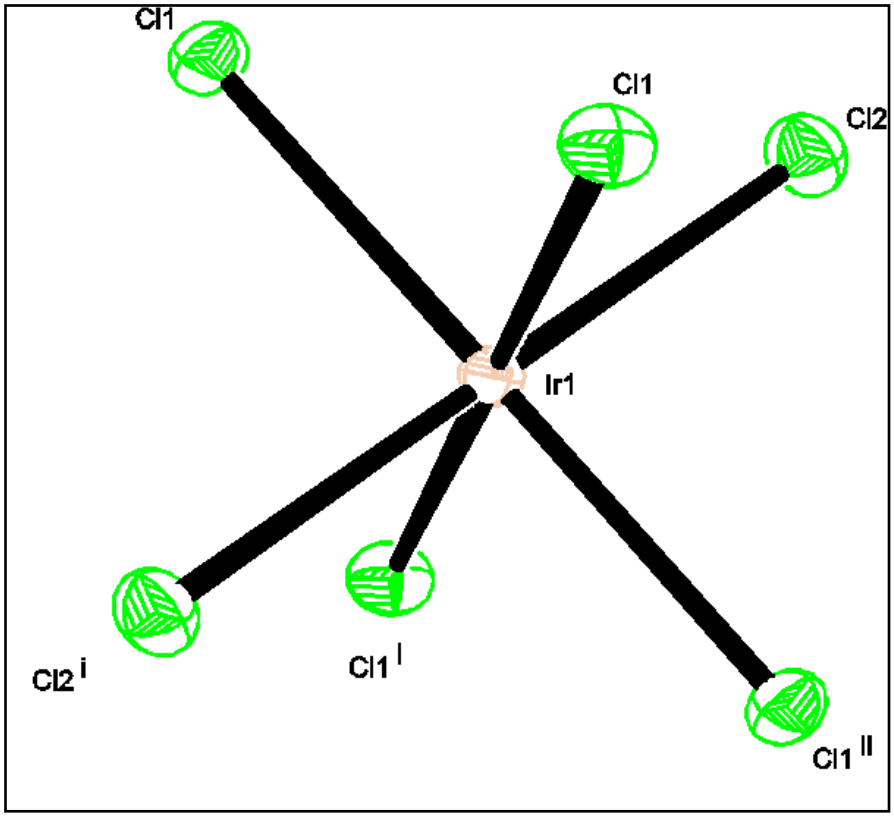

Figure 4.15: ORTEP diagram $[IrCl_6]^{2-}$ showing the atom-labelling scheme.

Table 4.5: Selected crystallographic data for $[IrCl_6]^{2-}$.

Compound	**$[IrCl_6]^{2-}$**
Chemical formula	$C_{16}Ir$
Formula weight	404.94
Crystal colour	Beige
Crystal system	monoclinic
Space group	$C_{2/m}$
Temperature (K)	200
Crystal size (mm^{-3})	0.10x 0.11x 0.22
α (Å)	15.1773(18)
b (Å)	7.1314(9)
c (Å)	6.7789(9)
α (˚)	90
β (˚)	100.479(5)
ɣ (˚)	90
V (Å)	721.48(16)
Z	2
D_{calc} ($g\ cm^3$)	2.288
μ/mm^{-1}	10.330
F (000)	466
Theta min-max (˚)	3.1, 28.3
S	1.09
Tot.uniq.data, r(int)	3487, 959, 0.031
Observed data [I>2.0σ(I)]	954
R	0.0898
R_w	0.2212

Table 4.6: Selected bond distances (Å) and angles (°) for $[IrCl_6]^{2-}$.

$[IrCl_6]^{2-}$	
Bond distances (Å)	
Ir_1-Cl_1	2.364(3)
Ir_1-Cl_2	2.374(5)
Ir1-Cl_1_(i)	2.364(3)
Ir_1-Cl_1_a(i)	2.374(5)
Ir_1-Cl_1_b	2.364(3)
Ir_1-Cl_1_c	2.364(3)
Bond angles (°)	
Cl_1-Ir_1-Cl_2	88.96(11)
Cl_1-Ir_1-Cl_2	89.00(12)
Cl_1-Ir_1-Cl_2	91.04
Cl_1-Ir_1-Cl_2	180.00
Cl_1-Ir_1-Cl_2	91.00
Cl_1-Ir_1-Cl_2	91.04

4.3.6 Column Studies

4.3.6.1 Column Study of the binary element elution profile

The performance of the sorbents with regards to $[IrCl_6]^{2-}$ selectivity over $[RhCl_5(H_2O)]^{2-}$ was studied under dynamic flow adsorption conditions. The adsorption/elution profiles of the sorbent materials are presented in Figure 4.16-4.19 below. The binary element elution profile study was carried out to essentially understand the activity of the

quaternary diammonium cations hosted on nanofibers towards the $[IrCl_6]^{2-}$ in 6 M HCl medium. The binary column study was carried out using quaternary diammonium cations (F-QuatDMDAMeBnz, F-QuatDMDABnz, F-QuatDMDACF3Bnz and F-QuatDMDANO2Bnz) with binary element solution containing 0.45 M of $[RhCl_5(H_2O)]^{2-}$ and 0.15 M of $[IrCl_6]^{2-}$ hosted on nanofibers. The binary column study elution profile was observed the quaternary diammonium cations show a preference for $[IrCl_6]^{2-}$ over $[RhCl_5(H_2O)]^{2-}$. However, the complexation of Ir(IV) was observed in fractions 30-50 after elution with 10 M HCl. The loading capacity for $[IrCl_6]^{2-}$ was shown in the following; F-QuatDMDAMeBnz (60.29 mg/g) < F-QuatDMDABnz (67.61 mg/g) < F-QuatDMDACF3Bnz (107.59 mg/g) < F-QuatDMDANO2Bnz (140.47 mg/g). F-QuaDMDANO2Bnz resin show a high preference for Ir(IV), due to kinetics and the thermodynamics of substitution will be different with metal ions to cations. This order is in agreement with the theoretical thermodynamic order where F-QuatDMDANO2Bnz was the most preferred for $[IrCl_6]^{2-}$. This was also confirmed by the energy dispersive spectroscopic analysis (EDS) of adsorbents after eluting with 20% (10 M) HCl shown in Figure 4.22. The traces amount of adsorbed $[IrCl_6]^{2-}$ were, however, observed on the spectrum, which suggests the strong coordination of the $[IrCl_6]^{2-}$ with the quaternary diammonium cationic sorbent materials.

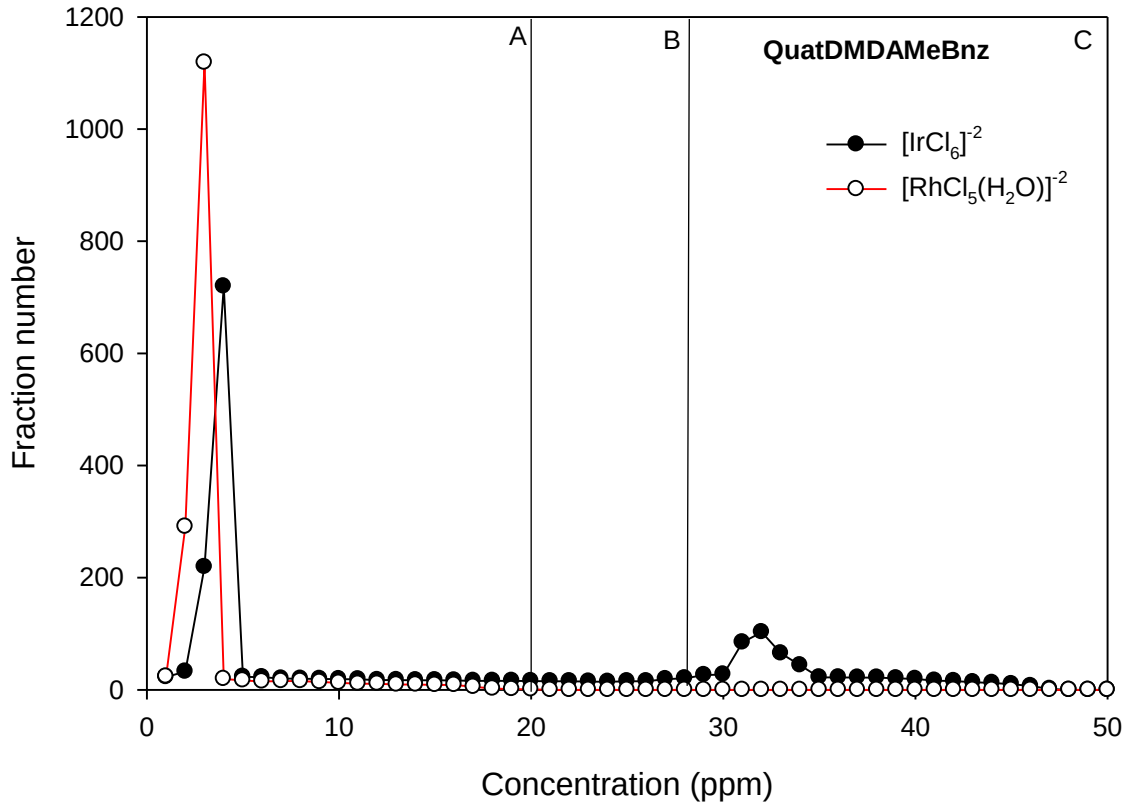

Figure 4.16: Binary column elution profile of $[IrCl_6]^{2-}$ and $[RhCl_5(H_2O)]^{2-}$ in 6 M HCl for F-QuatDMDAMeBnz on 0.1g of nanofiber, Loaded 2ml of binary solution where: (A) washing step with 10 ml of 6 M HCl, (B) stripping step with 5 ml of 0.05 M sodium metabisulfite solution and (C) elution step with 10 ml of 20% HCl (10 M).

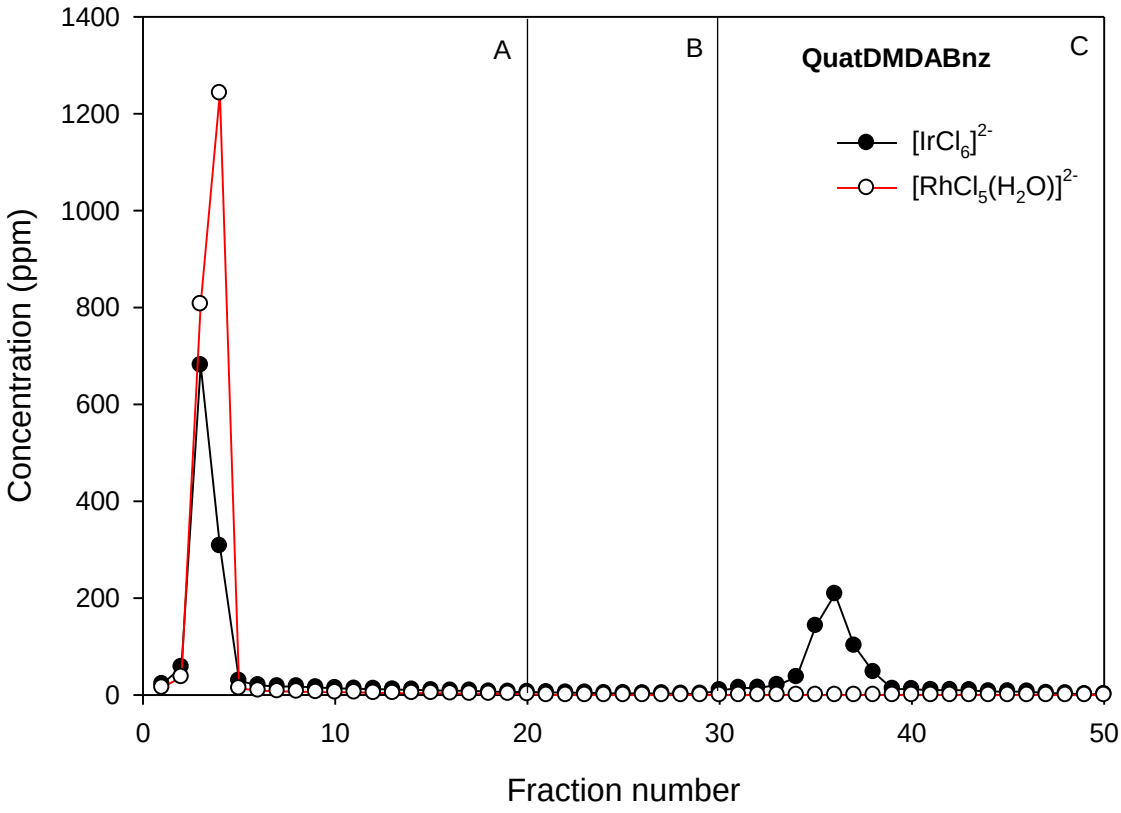

Figure 4.17: Binary column elution profile of $[IrCl_6]^{2-}$ and $[RhCl_5(H_2O)]^{2-}$ in 6 M HCl for F-QuatDMDABnz on 0.1g of nanofiber, Loaded 2ml of binary solution where: (A) washing step with 10 ml of 6 M HCl, (B) stripping step with 5 ml of 0.05 M sodium metabisulfite solution and (C) elution step with 10 ml of 20% HCl (10 M).

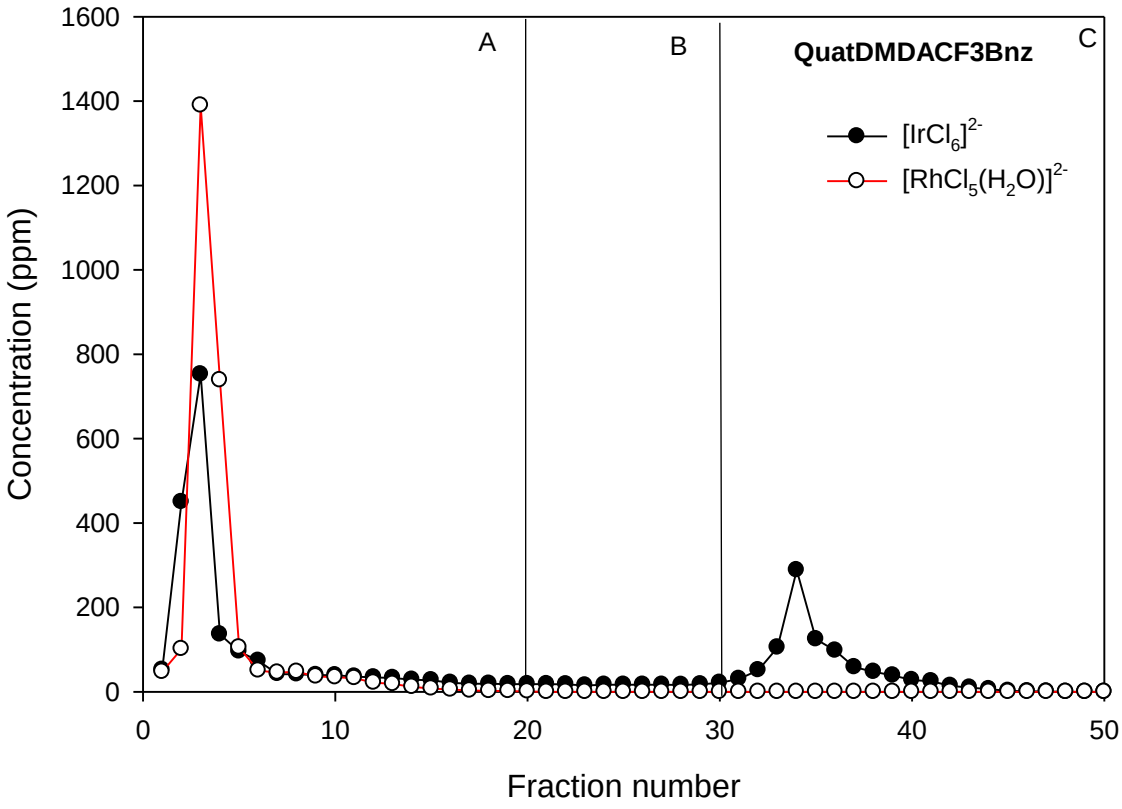

Figure 4.18: Binary column elution profile of $[IrCl_6]^{2-}$ and $[RhCl_5(H_2O)]^{2-}$ in 6 M HCl for F-QuatDMDACF3Bnz on 0.1g of nanofiber, Loaded 2ml of binary solution where: (A) washing step with 10 ml of 6 M HCl, (B) stripping step with 5 ml of 0.05 M sodium metabisulfite solution and (C) elution step with 10 ml of 20% HCl (10 M).

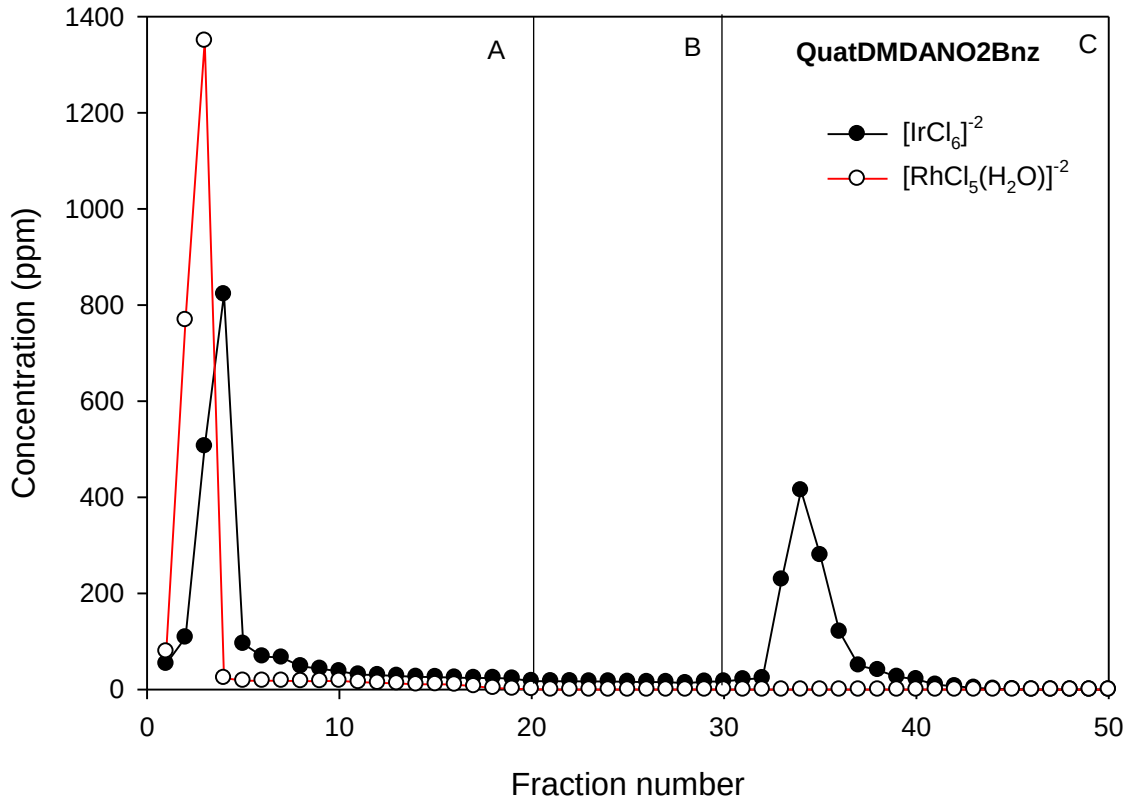

Figure 4.19: Binary column elution profile of $[IrCl_6]^{2-}$ and $[RhCl_5(H_2O)]^{2-}$ in 6 M HCl for F-QuatDMDANO2Bnz on 0.1g of nanofiber, Loaded 2ml of binary solution where: (A) washing step with 10 ml of 6 M HCl, (B) stripping step with 5 ml of 0.05 M sodium metabisulfite solution and (C) elution step with 10 ml of 20% HCl (10 M).

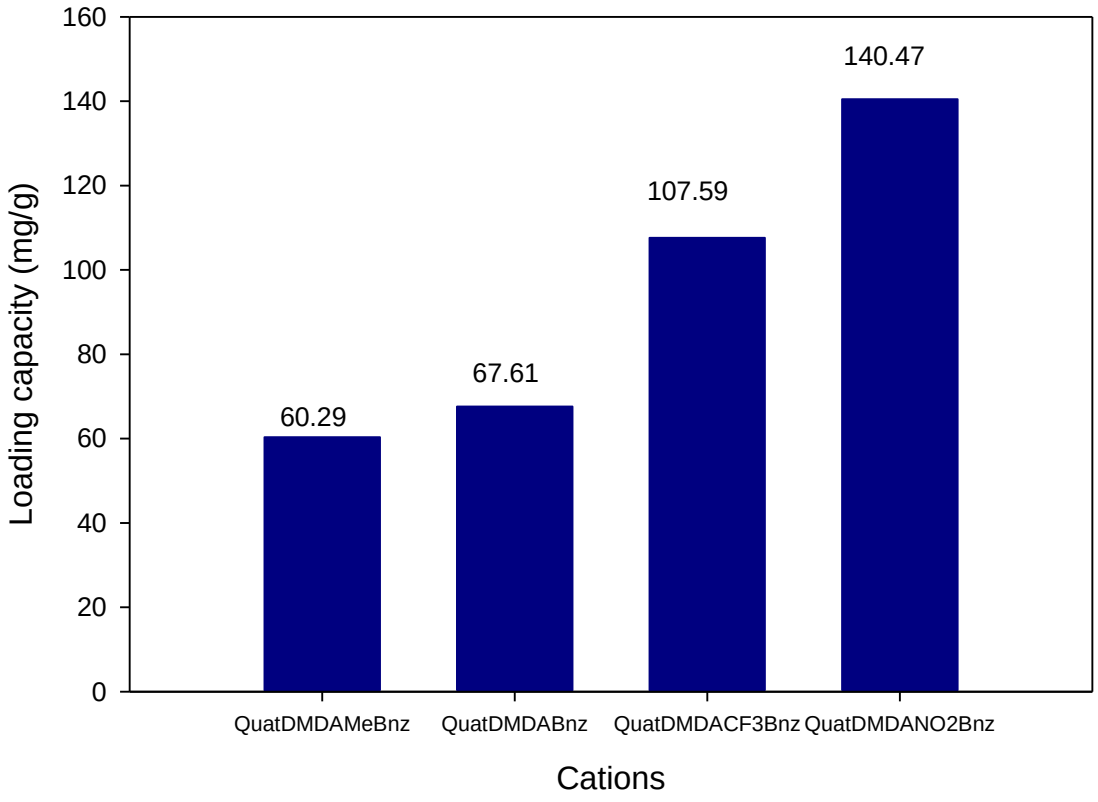

Figure 4.20: Loading capacities of $[IrCl_6]^{2-}$ in 6 M HCl extracted using quaternary diammonium cations (F-QuatDMDAMeBnz, F-QuatDMDABnz, F-QuatDMDACF3Bnz and F-QuatDMDANO2Bnz) hosted on nanofibers.

4.3.6.2 Scanning electron microscope (SEM) of the used sorbent material

The morphology of the sorbent materials F-QuatDMDAMeBnz and F-QuatDMDANO2Bnz were observed using a scanning electron microscope (SEM) and the images are shown in Figure 4.21. The morphology of the used nanofibers after eluting with 20% HCl solution was observed/analysed. The nanofibers showed no

morphological changes after the column study. The SEM images do not show any significant changes in the size or shape of the sorbent materials, indicating possible reusability of the sorbent materials with minimum loss in functionality.

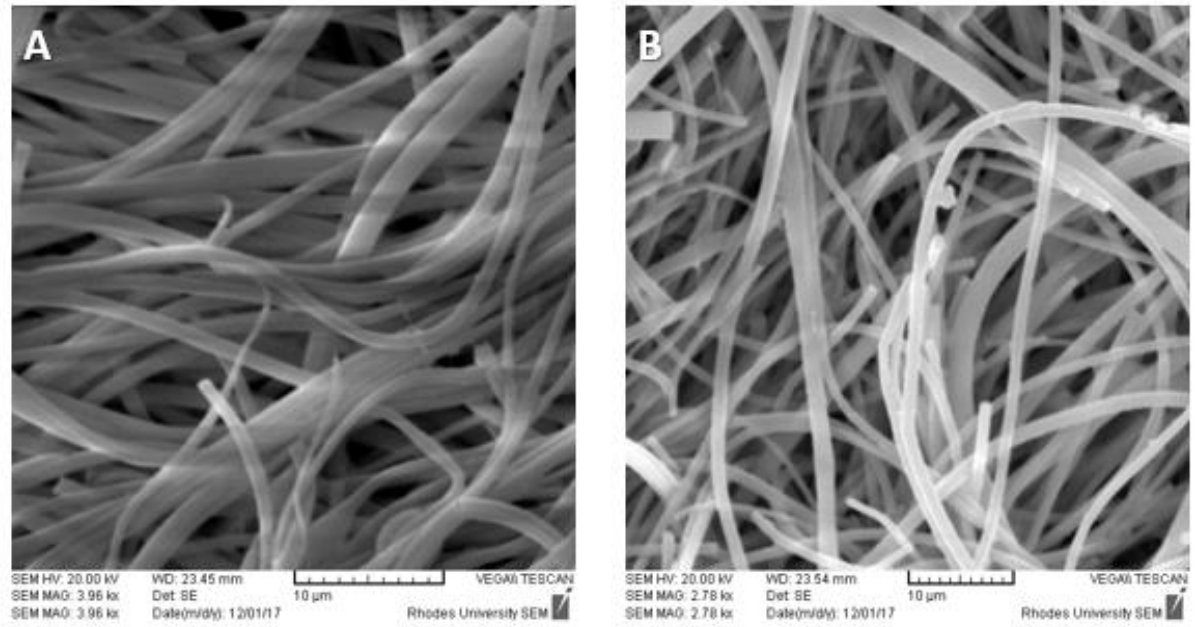

Figure 4.21: SEM images of used binary elements (Rh and Ir) nanofibers after eluting with 20% HCl solution; (A) F-QuatDMDAMeBnz and (B) F-QuatDMDANO2Bnz.

4.3.6.3 Energy dispersive spectroscopy (EDS) analysis of used sorbent material

The recovery of $[IrCl_6]^{2-}$ ions from the sorbent materials was investigated by the analysis of the EDS of materials (Figure 4.22) after elution with 20% HCl solution. Presence of Ir peaks in the spectra of the F-QuatDMDANO2Bnz and F-QuatDMDAMeBnz sorbent materials confirms the retention of $[IrCl_6]^{2-}$ on the sorbent materials after use. The spectra suggest that the elution agent was effective in

removing the adsorbed Ir on the F-QuatDMDAMeBnz and F-QuatDMDANO2Bnz sorbent materials. While there were traces amounts of adsorbed Ir were observed on the spectrum, which suggests the strong coordination of the Ir with the quaternary diammonium cationic sorbent materials.

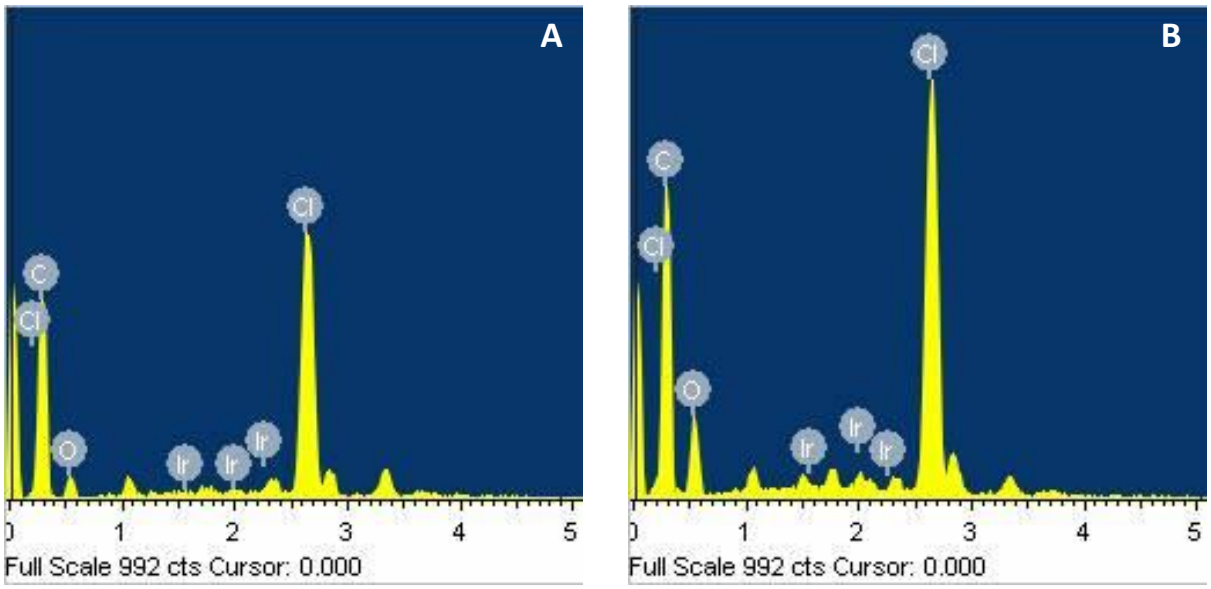

Figure 4.22: EDS spectra of binary (Ir and Rh) sorbent materials after elution with 20% HCl 3% (A) F-QuatDMDAMeBnz and (B) F-QuatDMDANO2Bnz.

4.3.7 Adsorption studies

Adsorption studies of quaternary diammonium cations were performed by a batch process for a better understanding of the adsorption kinetics and isotherms. In the adsorption studies, the effect of time on the adsorption of $[IrCl_6]^{2-}$ onto the nanofibers functionalized with quaternary diammonium cations (F-QuatDMDAMeBnz, F-QuatDMDABnz, F-QuatDMDACF3Bnz and F-QuatDMDANO2Bnz) were studied,

respectively (Figures 4.23-4.26). Adsorption studies show that the adsorption with quaternary diammonium cations was initially fast due to the availability of active sites on the surface of the sorbents. Adsorption equilibrium was reached within 6-8 minutes due to the adsorption rate slowed as the surface of the sorbent saturation is reached. Figures 4.23 and 4.24 shows the fraction adsorption of metal ions as the function of time. Figures 4.25 and 4.26 shows the percentage adsorption as the function of time.

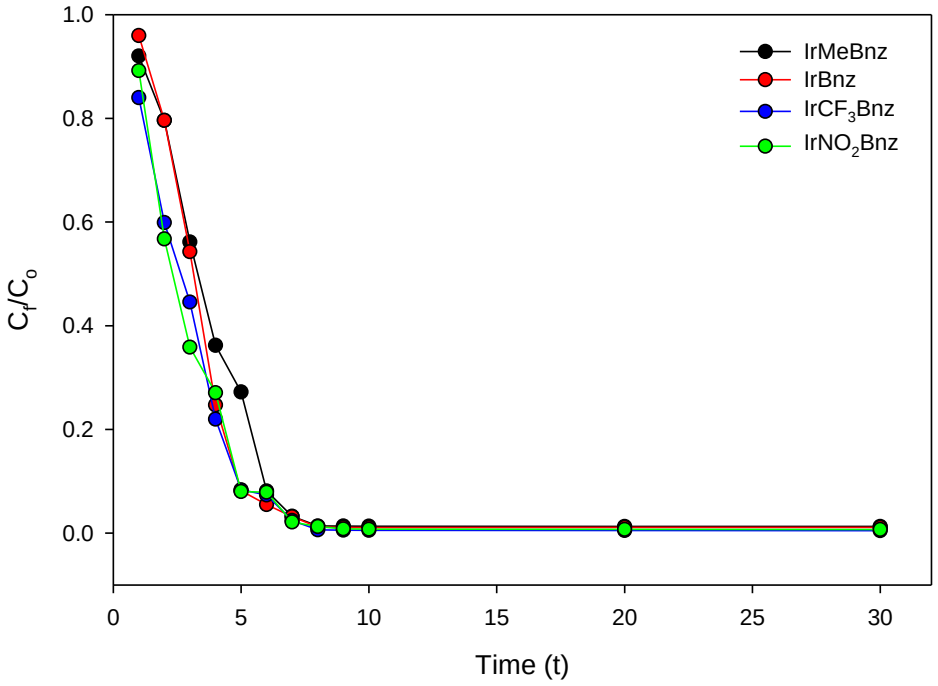

Figure 4.23: Fraction adsorption of $[IrCl_6]^{2-}$ in presence of quaternary diammonium cations hosted on nanofibers.

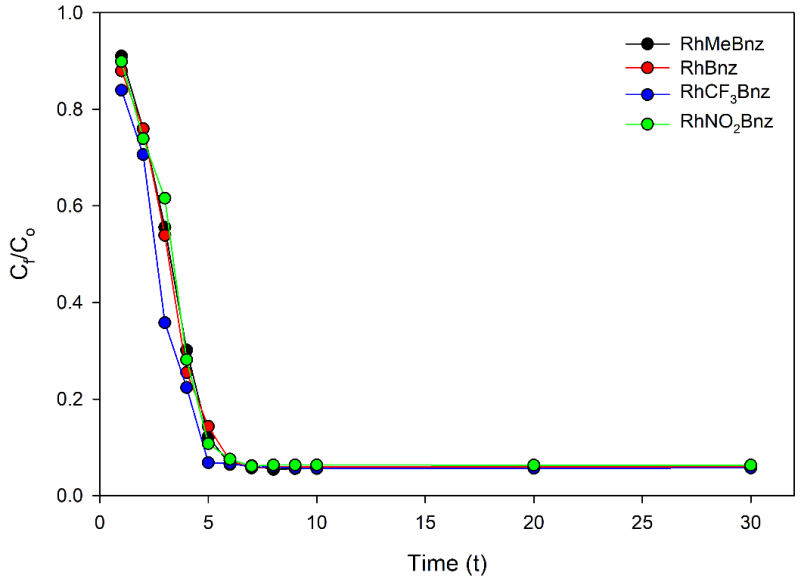

Figure 4.24: Fraction adsorption of $[RhCl_5(H_2O)]^{2-}$ in presence of quaternary diammonium cations hosted on nanofibers.

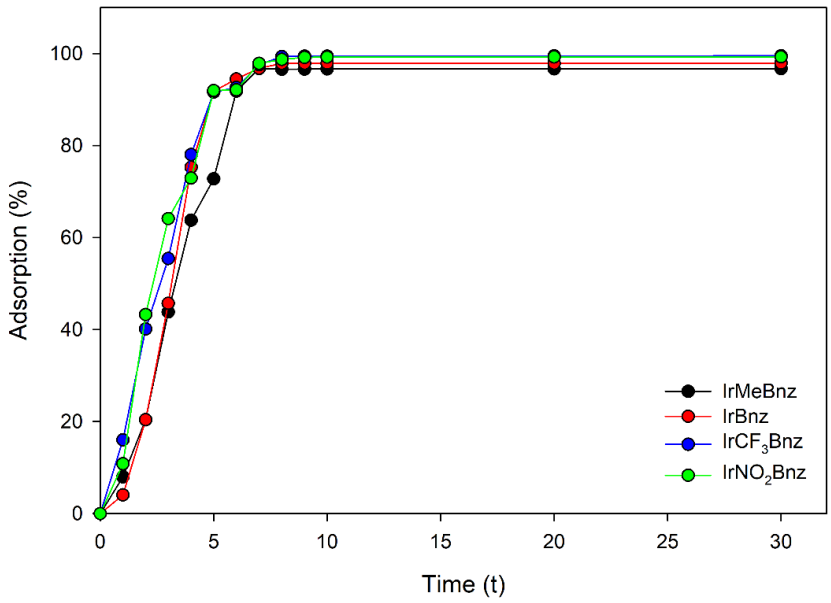

Figure 4.25: Adsorption percentage of $[IrCl_6]^{2-}$ in presence of quaternary diammonium cations hosted on nanofibers.

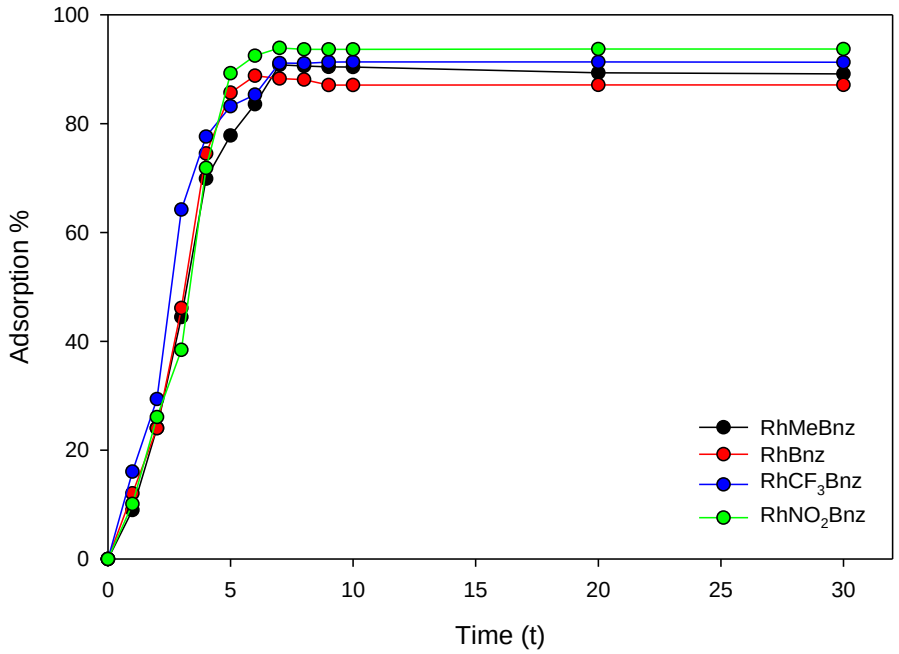

Figure 4.26: Adsorption percentage of $[RhCl_5(H_2O)]^{2-}$ in presence of quaternary diammonium cations hosted on nanofibers.

4.3.7.1 Adsorption Kinetics

The kinetic mechanism that controls the adsorption process under batch study was followed by the pseudo-first-order model and pseudo-second-order model. In the pseudo-first-order model, assumes that adsorption takes place *via* a physical process, while the pseudo-second-order assumes that adsorption takes place *via* a chemical process [75, 151, 198, 199]. The plot of t/Q_t vs time (t) gave a straight line for both metal ion with better R^2 for all adsorbents (F-QuatDMDAMeBnz, F-QuatDMDABnz, F-QuatDMDACF3Bnz and F-QuatDMDANO2Bnz) compared to the pseudo-first-order kinetics. Tables 4.7 and 4.8 presents the R^2 coefficient as well as the kinetic constants

for all sorbents. Hence the adsorption kinetics were confirmed to follow the pseudo-second-order.

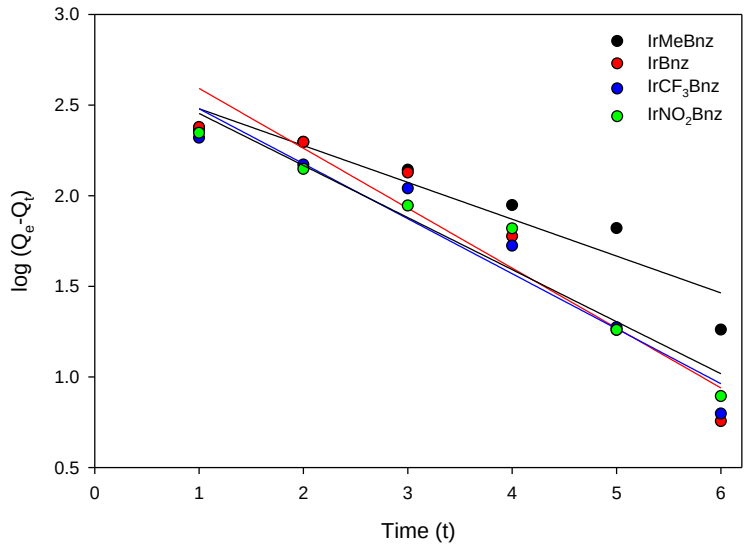

Figure 4.27: Pseudo-first-order plot of $[IrCl_6]^{2-}$ in presence of quaternary diammonium cations hosted on nanofibers.

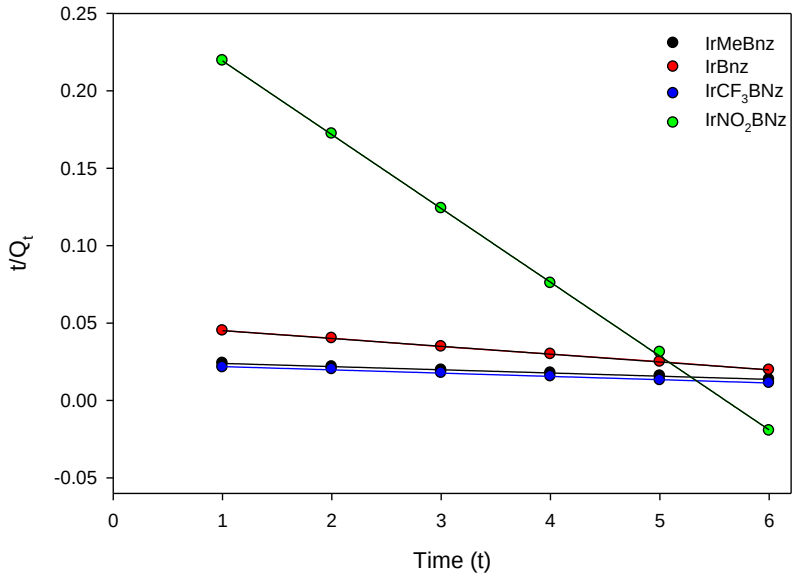

Figure 4.28: Pseudo-second-order plot of $[IrCl_6]^{2-}$ derivatives in presence of quaternary diammonium cations hosted on nanofibers.

Table 4.7: Parameters of the pseudo-first-order and pseudo-second-order rate law for the adsorption of on $[IrCl_6]^{2-}$ nanofibers.

Resin	**Pseudo 1st order kinetics**			**Pseudo 2nd order kinetics**		
	Q_e (mg/g)	K_1 (min^{-1})	R^2	Qe (mg/g)	K_2 ($g.mg^{-1}.min^{-1}$)	R^2
F-QuatDMDAMeBnz	481.948	0.468	0.889	155.015	$8.14x10^{-6}$	0.999
F-QuatDMDABnz	550.808	0.699	0.927	181.455	$4.800x10^{-4}$	0.999
F-QuatDMDACF3Bnz	606.7363	0.661	0.944	183.655	$8.32x10^{-4}$	0.993
F-QuatDMDANO2Bnz	837.529	0.761	0.939	233.590	$9.350x10^{-4}$	1

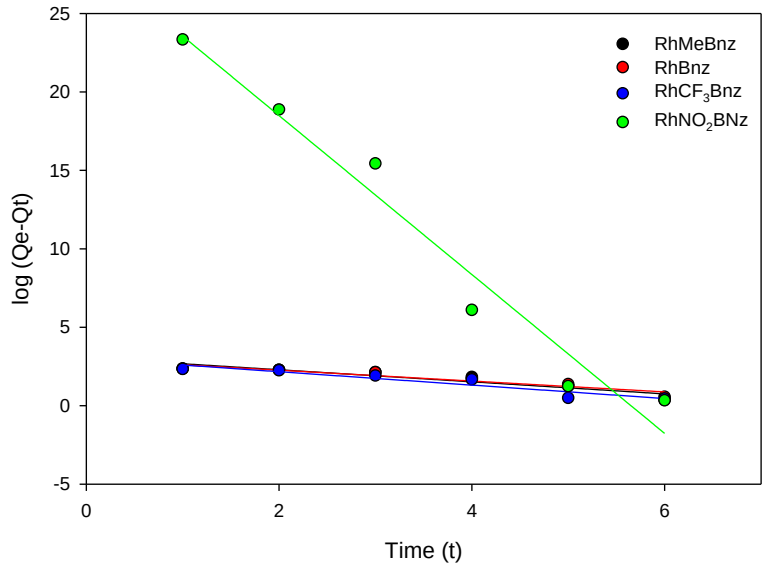

Figure 4.29: Pseudo-first-order plot of $[RhCl_5(H_2O)]^{2-}$ in presence of quaternary diammonium cations hosted on nanofibers.

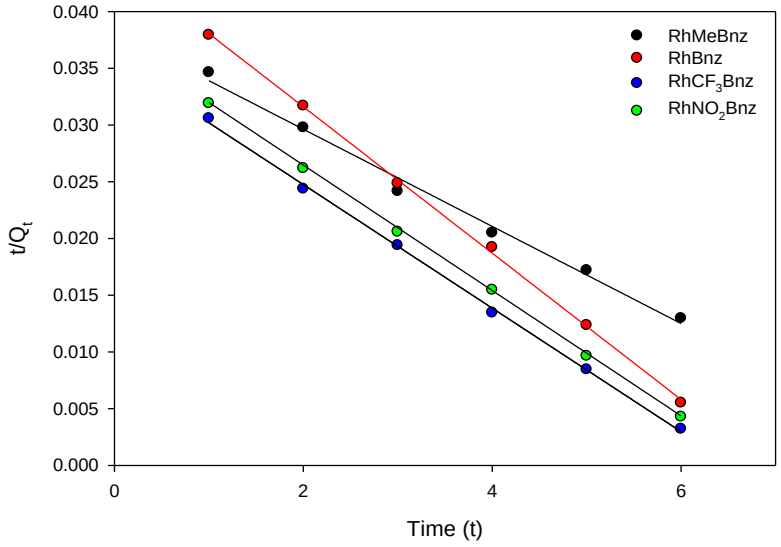

Figure 4.30: Pseudo-second-order plot of $[RhCl_5(H_2O)]^{2-}$ derivatives in presence of quaternary diammonium cations hosted on nanofibers.

Table 4.8: Parameters of the pseudo-first-order and pseudo-second-order rate law for the adsorption of on $[RhCl_5(H_2O)]^{2-}$ nanofibers.

Resin	**Pseudo 1st order kinetics**			**Pseudo 2nd order kinetics**		
	Q_e (mg/g)	K_1 (min^{-1})	R^2	Qe (mg/g)	K_2 ($g.mg^{-1}.min^{-1}$)	R^2
F-QuatDMDAMeBnz	104.472	0.885	0.864	125.435	$6.14x10^{-6}$	0.992
F-QuatDMDABnz	89.949	0.797	0.892	133.990	$1.800x10^{-4}$	0.999
F-QuatDMDACF3Bnz	114.288	0.983	0.893	141.425	$5.350x10^{-4}$	0.999
F-QuatDMDANO2Bnz	979.490	1.632	0.955	143.685	$6.32x10^{-4}$	0.999

$[IrCl_6]^{2-}$ with quaternary diammonium functionalized nanofibers (F-QuatDMDAMeBnz, F-QuatDMDABnz, F-QuatDMDACF3Bnz and F-QuatDMDANO2Bnz) show to fit the pseudo-second-order model (Figure 4.28). The plot t/Qt vs time(t) gave a straight line

with R^2 values that were greater than 0.99 for all adsorbents F-QuatDMDAMeBnz, F-QuatDMDABnz, F-QuatDMDACF3Bnz and F-QuatDMDANO2Bnz, respectively (Table 4.7). Where Qe (mg/g) is the amount of metal ions adsorbed on the sorbent at equilibrium, at time t (minutes). Adsorption kinetic studies show an approximate adsorption rate (K_2) for pseudo-second-order model in the following order; F-QuatDMDAMeBnz ($8.14x10^{-6}$ $g.mg^{-1}.min^{-1}$) < F-QuatDMDABnz ($4.800x10^{-4}$ $g.mg^{-1}.min^{-1}$) < F-QuatDMDACF3Bnz ($8.32x10^{-4}$ $g.mg^{-1}.min^{-1}$) < F-QuatDMDANO2Bnz ($9.350x10^{-4}$ $g.mg^{-1}.min^{-1}$) for Ir(IV). Adsorption kinetic loading capacity (q_e) using quaternized nanofibers was shown in the order following order; F-QuatDMDAMeBnz (155.02 mg/g) < F-QuatDMDABnz (181.46 mg/g) < F-QuatDMDACF3Bnz (183.66 mg/g) < F-QuatDMDANO2Bnz (233.59 mg/g) for Ir(IV). This order was found in agreement with the multi-element column study loading capacity findings where the Ir(IV) adsorption was observed in the following order; F-QuatDMDAMeBnz (60.29 mg/g) < F-QuatDMDABnz (67.61 mg/g) < F-QuatDMDACF3Bnz (107.59 mg/g) < F-QuatDMDANO2Bnz (140.47 mg/g). Rh(III) adsorption kinetic capacity was lower compared to Ir(IV); (F-QuatDMDAMeBnz (125.44 mg/g) < F-QuatDMDABnz (133.99 mg/g) < F-QuatDMDACF3Bnz (141.43 mg/g) < F-QuatDMDANO2Bnz (143.69 mg/g)). This implies that F-QuatDMDANO2Bnz on the surface of the nanofibers complexes better with $[IrCl_6]^{2-}$ proposing to form ion pairing. This may be due to Ir(IV) metal ions kinetics and thermodynamics of substitution prefer F-QuatDMDANO2Bnz compared to F-QuatDMDAMeBnz, F-QuatDMDABnz and F-QuatDMDACF3Bnz.

4.3.7.2 Adsorption Isotherms

The equilibrium adsorption isotherm has the importance in the design of adsorption systems [202]. The equilibrium data were analysed by Langmuir and Freundlich isotherms [150, 208, 215]. The Langmuir equation, which is effective for monolayer adsorption onto a completely homogeneous surface with a finite number of identical sites and with negligible interaction between adsorbed molecules, is represented in the linear form as shown in Chapter 2 Section 2.3.2, Equation 2.4 [208, 211]. The Freundlich isotherm, on the other hand, assumes a heterogeneous sorption surface with sites that have different energies of sorption. Freundlich isotherm indicates multiple layered adsorptions on adsorbents.

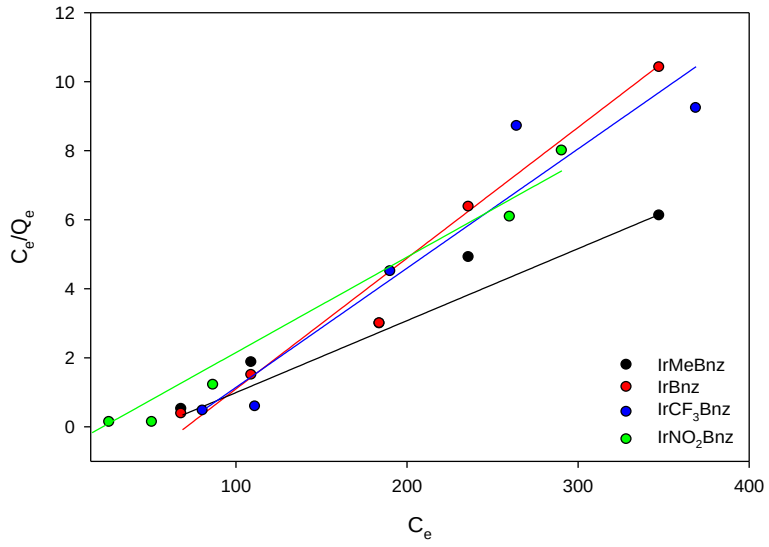

Figure 4.31: Plots of Langmuir isotherms of $[IrCl_6]^{2-}$ in presence of quaternary diammonium cations adsorption on nanofibers.

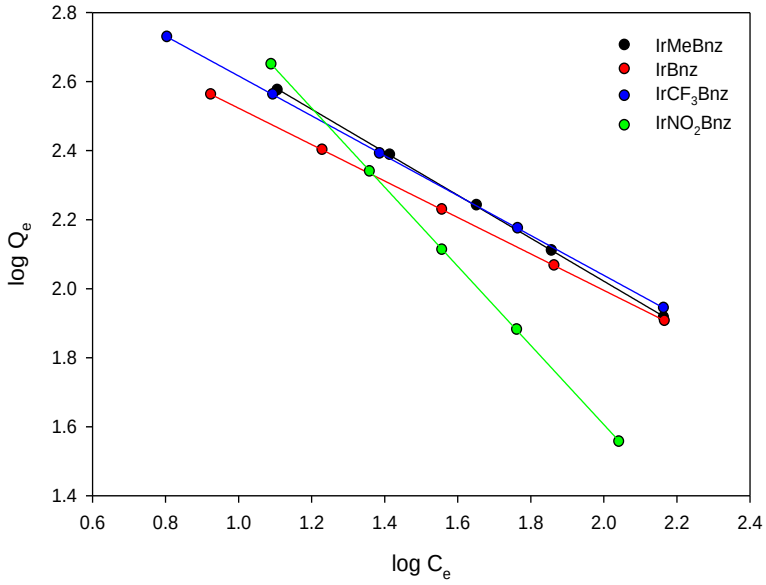

Figure 4.32: Plots of Freundlich isotherms of $[IrCl_6]^{2-}$ in presence of quaternary diammonium cations adsorption on nanofibers.

Table 4.9: Langmuir and Freundlich isothermal parameters for adsorption of $[IrCl_6]^{2-}$ on nanofibers.

Resins	**Langmuir parameters**			**Freundlich parameters**		
	Q_o (mg/g)	R_L	R^2	K_f (mg/g)	N	R^2
F-QuatDMDAMeBnz	26.399	0.156	0.895	112.461	1.605	0.999
F-QuatDMDABnz	48.0769	0.354	0.947	156.315	1.894	0.999
F-QuatDMDACF3Bnz	2.894	0.0429	0.916	185.353	1.731	0.999
F-QuatDMDANO2Bnz	3.618	0.0531	0.981	794.328	0.872	0.999

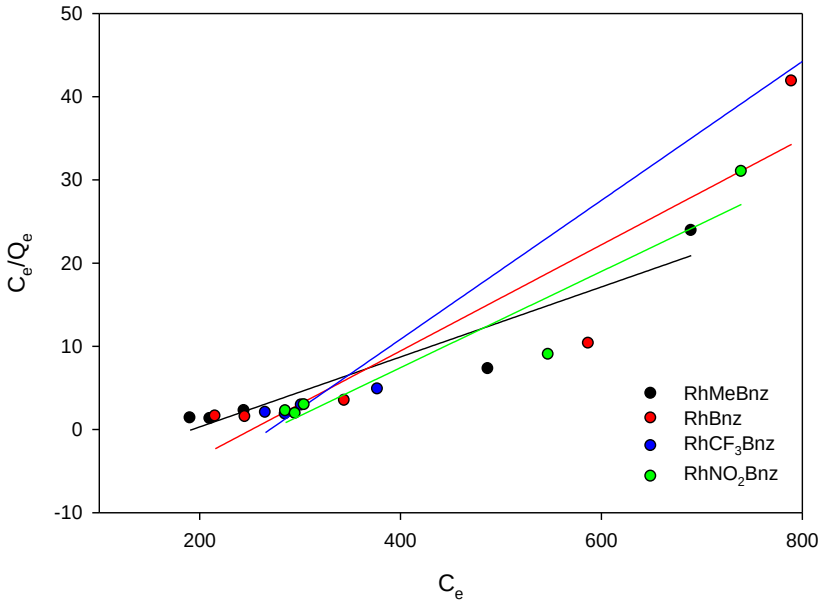

Figure 4.33: Plots of Langmuir of $[RhCl_5(H_2O)]^{2-}$ in presence of quaternary diammonium cations adsorption on nanofibers.

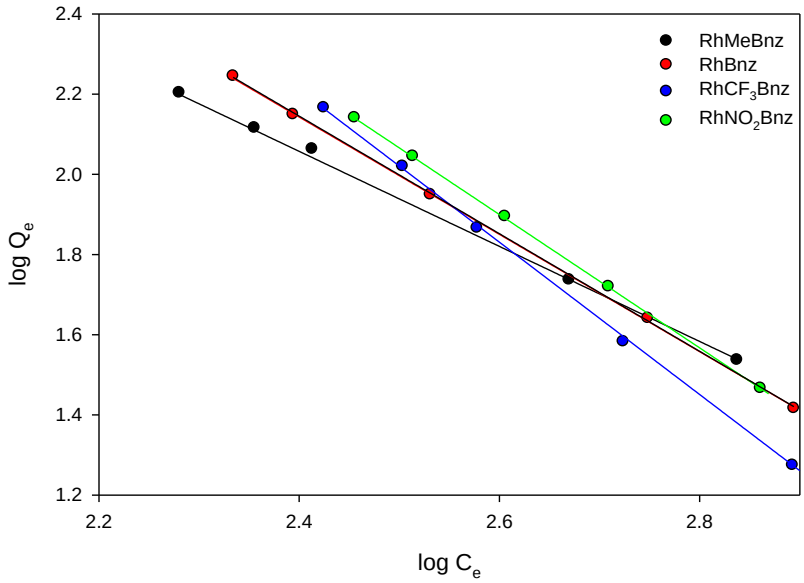

Figure 4.34: Plots of Freundlich isotherms of $[RhCl_5(H_2O)]^{2-}$ in presence of quaternary diammonium cations adsorption on nanofibers.

Table 4.10: Langmuir and Freundlich isothermal parameters for adsorption of $[RhCl_5(H_2O)]^{2-}$ on nanofibers.

Resins	**Langmuir parameters**			**Freundlich parameters**		
	Q_o (mg/g)	R_L	R^2	K_f (mg/g)	N	R^2
F-QuatDMDAMeBnz	8.285	0.00521	0.899	12.706	2.378	0.999
F-QuatDMDABnz	6.821	0.00532	0.828	36.983	1.568	0.999
F-QuatDMDACF3Bnz	5.219	0.00412	0.983	40.365	1.198	0.999
F-QuatDMDANO2Bnz	6.006	0.00654	0.891	177.828	1.730	0.999

The adsorption behaviour of quaternary diammonium cations (F-QuatDMDAMeBnz, F-QuatDMDABnz, F-QuatDMDACF3Bnz and F-QuatDMDANO2Bnz) functionalized on nanofibers were followed using the Langmuir and Freundlich isotherms. The parameters of the Langmuir and Freundlich isothermal models are presented in Figures 4.31-4.34 and Tables 4.9-4.10. The plots of specific adsorption log q_e against the equilibrium concentration log C_e shows that the adsorption obeys the Freundlich model. The adsorption data for each sorbent and metal ion were consistent with a Freundlich adsorption model where $R^2 > 0.99$, strongly suggesting multiple-layered adsorption on the surface of adsorbents. The Freundlich constants k_f and n are determined from the slope of the plot and are presented. Where n (adsorption intensity) indicates the favourability of the adsorption, n must be between 1 and 10. All adsorbents showed n values less than ten indicating that the adsorption intensity is favourable.

Adsorption isotherms for $[IrCl_6]^{2-}$ with quaternary diammonium cationic resins (F-QuatDMDAMeBnz, F-QuatDMDABnz, F-QuatDMDACF3Bnz and F-QuatDMDANO2Bnz) hosted on nanofibers show to fit the Freundlich adsorption isotherm model. The plots of specific adsorption log q_e against the equilibrium concentration log C_e gave a straight line with R^2 values that were greater than 0.99 for all adsorbents F-QuatDMDAMeBnz, F-QuatDMDABnz, F-QuatDMDACF3Bnz and F-QuatDMDANO2Bnz, respectively. The adsorption isotherms for Ir(IV) using quaternary diammonium cationic resins was observed in the order following order; F-QuatDMDANO2Bnz (749.33 mg/g) > F-QuatDMDACF3Bnz (185.35 mg/g) > F-QuatDMDABnz (156.32 mg/g) > F-QuatDMDAMeBnz (112.46 mg/g) as shown in Table 4.9. Adsorption isotherms for F-QuatDMDANO2Bnz were greater than that of F-QuatDMDAMeBnz, F-QuatDMDABnz, F-QuatDMDACF3Bnz. This order was found in agreement with the multi-element column study loading capacity findings in the following order F-QuatDMDAMeBnz (60.29 mg/g) < F-QuatDMDABnz (67.61 mg/g) < F-QuatDMDACF3Bnz (107.59 mg/g) < F-QuatDMDANO2Bnz (140.47 mg/g) for Ir(IV) as shown in Figure 4.20. While for Rh(III) adsorption loading capacity was lower compared to Ir(IV) in the following order; (F-QuatDMDAMeBnz (12.71 mg/g) < F-QuatDMDABnz (36.98 mg/g) < F-QuatDMDACF3Bnz (40.37 mg/g) < F-QuatDMDANO2Bnz (177.83 mg/g)) as shown in Table 4.10 . This implies that F-QuatDMDANO2Bnz on the surface of the nanofibers complexes better with Ir(IV) proposing to form ion pairing. Hence, quaternary diammonium cations show higher adsorption with $[IrCl_6]^{2-}$ compared to $[RhCl_5(H_2O)]^{2-}$.

The adsorption kinetics and isotherms were in agreement when compared with the experimental adsorption studies and calculated theoretically thermodynamics values. This concludes theoretically that all the quaternary diammonium cations are greatly favoured for $[IrCl_6]^{2-}$ and that is in agreement with the experimental adsorption study and column study. Hence the modelled theoretical study is chemically driven interactions same as the experimental adsorption study being driven by chemical interactions. The experimental adsorption studies show that all the quaternary diammonium cations with $[IrCl_6]^{2-}$ are feasible for the adsorption process, hence this follows the chemisorption process.

4.4 Conclusions

The PVBC nanofibers were successfully synthesized and functionalized with quaternary diammonium cations (F-QuatDMDAMeBnz, F-QuatDMDABnz, F-QuatDMDACF3Bnz and F-QuatDMDANO2Bnz). The formation and functionalities on the materials were clearly confirmed by FT-IR spectroscopy and elemental analysis. The loading capacities for metal ions ($[IrCl_6]^{2-}$ and $[RhCl_5(H_2O)]^{2-}$) were investigated using four quaternary diammonium cations (F-QuatDMDAMeBnz, F-QuatDMDABnz, F-QuatDMDACF3Bnz and F-QuatDMDANO2Bnz). EDS studies were conducted to confirm the presence of nitrogen and other atoms on the materials. BET experiments were conducted to confirm the surface area of the nanofibers. The SEM images of the nanofibers showed well defined morphology of the materials.

In column studies, it was observed that binary element metal solution containing iridium and rhodium in the form of $[IrCl_6]^{2-}$ and $[RhCl_5(H_2O)]^{2-}$. Preference was shown for $[IrCl_6]^{2-}$ with quaternary diammonium cations (F-QuatDMDAMeBnz, F-QuatDMDABnz, F-QuatDMDACF3Bnz and F-QuatDMDANO2Bnz) in 6 M HCl medium. Therefore, the column studies proved to be satisfactory since $[IrCl_6]^{2-}$ was preferred and order of loading capacities was observed as follows; F-QuatDMDANO2Bnz (140.47 mg/g) > F-QuatDMDACF3Bnz (107.59 mg/g) > F-QuatDMDABnz (67.61 mg/g) > F-QuatDMDAMeBnz (60.29 mg/g) as shown in Figure 4.20 . This order is in agreement with theoretical studies of thermodynamic values, adsorption kinetics and isotherms studies confirmed the uptake of $[IrCl_6]^{2-}$ where pseudo-second-order kinetics and Freundlich isotherm model.

Chapter 5: Conclusions and Future work

5.1 Conclusions

This study focuses mainly on two parts; Part 1 (Chapter 3) focused on the design of reagents that are selective for platinum group metals over Ni(II) in 0.5 M solution sing tridentate *bis*-benzimidazole ligands hosted on nanofibers and Part 2 (Chapter 4) focused on the separation of $[IrCl_6]^{2-}$ from $[RhCl_5(H_2O)]^{2-}$ from 6 M HCl solution using quaternary diammonium functionalised polymer nanofibers. These experiments were carried out in order to understand the adsorption capacities and the selectivity of the functionalized polymer nanofibers towards the PGMs. The basic chemistry of the design of the reagents was exploited using both experimental and theoretical studies.

5.1.1 Theoretical studies

5.1.1.1 Interaction of *bis*-benzimidazole ligands with $[RhCl_3(H_2O)_3]$

Theoretical investigations utilizing density functional theory (DFT) has been carried out in this study to explore the structural behaviour of *bis*-benzimidazole derivatives (NNN1, NNN2, NSN1 and NSN2) with respect to their effectiveness for the selectivity of rhodium(III) through coordination chemistry. The rhodium species of interest are *mer*-$[RhCl_3(H_2O)_3]$ and *fac*-$[RhCl_3(H_2O)_3]$ hence the experimental study was carried out in 0.5 M HCl in order to obtain the neutral rhodium(III) species. The chemical properties and behaviour of *bis*-benzimidazoles were investigated before and after interaction with the rhodium(III) species. The HOMO-LUMO studies showed that *bis*-

benzimidazole ligands containing sulfur (NSN1 and NSN2) have a lower energy gap, higher softness and higher electronegativity. This indicated that NSN1 and NSN2 ligands will be the most reactive and would have a higher binding affinity towards rhodium(III) compared to NNN1 and NNN2 ligands.

The thermodynamic data studies showed that the interaction between *mer*-$[RhCl_3(H_2O)_3]$ with NSN1 and NSN2 and *fac*-$[RhCl_3(H_2O)_3]$ with NSN1 and NSN2 were favourable, spontaneous and exothermic in nature. The order of favourability between the metal ions complex species and *bis*-benzimidazole ligands was as follows; *mer*-$[RhCl_3(NSN2)]$ > *mer*-$[RhCl_3(NSN1)]$ > *fac*-$[RhCl_3(NSN1)]$ > *fac*-$[RhCl_3(NSN2)]$, where the *mer* geometry was more favoured with NSN1 and NSN2, while *fac* geometry was the least favoured as shown in Table 3.2. The interaction between *mer*-$[RhCl_3(H_2O)_3]$ with NNN1 and NNN2 and *fac*-$[RhCl_3(H_2O)_3]$ with NNN1 and NNN2 were not favourable. It was observed that the tridentate *bis*-benzimidazole ligands containing sulfur were the most preferred for interaction with rhodium(III). This was in agreement with the loading capacities obtained in the single element column study for Rh(III) in the following order; NSN1 (181.06 mg/g) > NSN2 (148.55 mg/g) > NNN2 (131.88 mg/g) > NNN1 (75.87 mg/g) as shown in Figure 3.31.

5.1.1.2 Interaction of quaternary diammonium cations with $[IrCl_6]^{2-}$ and $[RhCl_5(H_2O)]^{2-}$

Theoretical studies were explored to understand the chemical behaviour of diammonium cations with respect to their effectiveness for separation of iridium(IV)

from rhodium(III). The chemical properties and behaviour of diammonium cations were investigated before and after interaction with $[IrCl_6]^{2-}$ and $[RhCl_5(H_2O)]^{2-}$. Four quaternary diammonium cations where investigated, namely; tetramethylbenzyl-1,10-diammonium chloride (QuatDMDAMeBnz), tetrabenzyl-1,10-diammonium chloride (QuatDMDABnz), tetratrifluoromethylbenzyl-1,10-diammonium chloride (QuatDMDACF3Bnz) and tetranitrobenzyl-1,10-diammonium chloride (QuatDMDANO2Bnz). HOMO-LUMO studies have shown that the cations with electron withdrawing groups on the benzyl substituent (QuatDMDACF3Bnz and QuatDMDANO2Bnz) have a lower energy gap, higher softness and higher electronegativity. Hence, these have shown potential to interact strongly with the QuatDMDANO2Bnz compared to the cations with electron donating groups on the benzyl substituent (QuatDMDAMeBnz and QuatDMDABnz). The thermodynamic data studies showed that the interaction between $[IrCl_6]^{2-}$ with quaternary diammonium cations was favourable, spontaneous and exothermic in nature. The order of favourability of ion-pairing between the $[IrCl_6]^{2-}$ and quaternary diammonium cations was as follows; [QuatDMDANO2Bnz]($IrCl_6$) > [QuatDMDACF3Bnz]($IrCl_6$) > [QuatDMDABnz]($IrCl_6$) > [QuatDMDAMeBnz]($IrCl_6$) as shown in Table 4.7, where the cations with electron withdrawing substituents were more favoured. The interaction between $[RhCl_5(H_2O)]^{2-}$ with quaternary diammonium cations were not strongly favoured compared with $[IrCl_6]^{2-}$. The loading capacity for $[IrCl_6]^{2-}$ was shown in the following; F-QuatDMDAMeBnz (60.29 mg/g) < F-QuatDMDABnz (67.61 mg/g) < F-QuatDMDACF3Bnz (107.59 mg/g) < F-QuatDMDANO2Bnz (140.47 mg/g) as shown in Figure 4.20.

5.1.2 Experimental

5.1.2.1 Fabrication, characterization of materials and column studies

The PVBC was synthesized and electrospun into nanofibers. PVBC nanofibers were successfully functionalized with *bis*-benzimidazole derivative and quaternary diammonium groups, respectively. The functional groups on the materials were confirmed by spectral analysis (FTIR and NMR), elemental analysis and EDS analysis. The studies were conducted to confirm the presence of the ligand atoms on the materials. The SEM images of the polymer nanofibers showed the morphology of the sorbent materials before and after use, thereby confirming the re-usability of the materials. BET experiments confirmed the surface area of the nanofibers. There was no direct relationship between the surface area and performance of the materials, and the only advantage would have been surface chemistry taking place due to the nature of the materials. The level of functionalization of PVBC also does not relate to performance as PVB-NSN1 and PVB-NSN2 which have a 6:1 (monomer:L) ratio perform better than PVB-NNN1 and PVB-NNN2 which have a lower monomer:L ratio of 5:1 (suggesting better functionalization). This points to other factors being important for the chemical reaction involved such as thermodynamics and kinetics. The same applies for the functional cations for $[IrCl_6]^{2-}$, the surface area is not readily related to the performance of the materials.

(a) Extraction of PGMs using *bis*-benzimidazole ligands

The single element column study, in 0.5 M HCl medium, confirmed that the *bis*-benzimidazole derivatives show uptake of $RhCl_3(H_2O)_3$. The order of the *bis*-benzimidazoles for coordination with rhodium(III) was observed as follows; NSN1 > NSN2 > NNN2 > NNN1. The interactions between Rh(III) and *bis*-benzimidazoles was further confirmed by the loading capacities of NSN1, NSN2, NNN1 and NNN2 which were 181.06 mg/g, 148.55 mg/g, 131.88 mg/g and 75.87 mg/g, respectively as shown in Figure 3.31. The multi-element column elution profile containing Rh(III), Ir(III), Pd(II), Pt(II) and Ni(II) metal solution in 0.5 M HCl medium was carried using the *bis*-benzimidazole resins. All bis-benzimidazoles resins have shown a preference for all metal ions except the nickel(II) metal ion. NNN1 resin has shown more uptake of palladium(II) over rhodium(III), platinum(III) and iridium(III). NNN2 sorbent material has shown the following order of extraction Pd > Pt > Rh > Ir. NSN1 sorbent material has shown the following order of extraction; Rh > Pt > Pd > Ir. NSN2 sorbent material has shown the following order of extraction; Rh > Pt > Pd > Ir. It has been observed that NNN2 followed by NNN1 have shown more uptake of palladium, and NSN1 has shown more uptake of rhodium followed by NSN2. With respect to *bis*-benzimidazole resins (NNN1, NNN2, NSN1 and NSN2) with metal ions (Pd(II), Pt(II), Ir(III) and Rh(III)) their loading capacities are given as follows: Pt (14.92 mg/g), Pd (47.94 mg/g), Ir (5.02 mg/g) and Rh (17.47 mg/g) for NNN1; Pt (33.96 mg/g), Pd (28.9 mg/g), Ir (6.84 mg/g) and Rh (14.91 mg/g), for NNN2; Pt (33.96 mg/g), Pd (28.9 mg/g), Ir (6.84 mg/g) and Rh (14.91 mg/g) for NSN1; Pt (23.89 mg/g), Pd (15.83 mg/g), Ir (10.64 mg/g) and Rh

(19.95 mg/g) for NSN2. The loading capacities of the ligands with metal ions represented in mmol/g are given as follow: Pd(II) (0.45 mmol/g) > Rh(III) (0.17 mmol/g) > Pt(II) (0.08 mmol/g) > Ir(III) (0.03 mmol/g) for NNN1; Pd(II) (0.27 mmol/g) > Pt(II) (0.17 mmol/g) > Rh(III) (0.14 mmol/g) > Ir(III) (0.04 mmol/g) for NNN2; Rh(III) (0.46 mmol/g) > Pt(II) (0.16 mmol/g) > Pd(II) (0.15 mmol/g) > Ir(III) (0.03 mmol/g) for NSN 1; Rh(III) (0.19 mmol/g) > Pd(II) (0.15 mmol/g) > Pt(II) (0.12 mmol/g) > Ir(III) (0.06 mmol/g) for NSN2. Therefore, the *bis*-benzimidazole resins were found not to be selective for rhodium(III) only as proposed but to be selective for the four (Rh(III), Ir(III), Pd(II) and Pt(II)). Hence, these *bis*-benzimidazole resins can be used in cases that need to extract all four PGMs or a combination of any of the four from solutions containing base metals. In this context, NSN1 is the best ligand for this application.

(b) Extraction of $[IrCl_6]^{2-}$ with quaternary diammonium cations

The binary (Ir/Rh) column study was carried out to investigate the performance of quaternary diammonium cationic resins (F-QuatDMDAMeBnz, F-QuatDMDABnz, F-QuatDMDACF3Bnz and F-QuatDMDANO2Bnz) using a solution containing 0.45 M of Rh and 0.15 M of Ir in 6 M HCl. The column elution profile of the quaternary diammonium cationic resins for the two anions was shown to have a preference for $[IrCl_6]^{2-}$ over $[RhCl_5(H_2O)]^{2-}$. Interactions of the quaternary diammonium cations with $[IrCl_6]^{2-}$ were greater with F-QuatDMDANO2Bnz resin, relative to F-QuatDMDAMeBnz, F-QuatDMDABnz and F-QuatDMDACF3Bnz resins. All quaternary diammonium cationic sorbent materials have shown selectivity for $[IrCl_6]^{2-}$ with different metal uptake/ loading capacity depending on the cation and no metal uptake was observed

for $[RhCl_5(H_2O)]^{2-}$ as the anion was washed out during the washing step. The order of the extraction of $[IrCl_6]^{2-}$ with the quaternary diammonium cations was observed as follows; F-QuatDMDANO2Bnz > F-QuatDMDACF3Bnz > F-QuatDMDABnz > F-QuatDMDAMeBnz as shown in Figure 4.20. The loading capacities, respectively, were 140.47 mg/g, 107.59 mg/g, 67.61 mg/g and 60.29 mg/g. These results are in agreement with theoretical studies and conclude that the electron-withdrawing substituents on the cationic resins result in selective interaction of $[IrCl_6]^{2-}$ with the materials.

5.1.3 Adsorption kinetics and isotherms

5.1.3.1 *Bis*-benzimidazoles

The adsorption behaviour of materials with *bis*-benzimidazole ligands for platinum group metals ions in 0.5 M HCl aqueous solution has been investigated as a function of equilibrium time and concentration. Studies showed that the adsorption equilibrium time for *bis*-benzimidazole ligands was reached with 6-7 minutes. The adsorption was fast due to the availability of active sites on the surface of the sorbents and adsorption rate slowed as surface saturation was reached.

The kinetics of the sorption were analysed by using the pseudo-first-order and pseudo-second-order kinetic models. Kinetic parameters and related correlation coefficients for each kinetic model of metal ion (Pt(II), Pd(II), Ir(III) and Rh(III)) with bis-benzimidazole ligands (NNN1, NNN2, NSN1 and NSN2) have shown that the adsorption for all metal ions could be described by the pseudo-first-order equation.

Adsorption kinetic studies showed an approximate adsorption rate per minute (K_1) for pseudo-first-order model in the following order; NSN2 (0.7427 min^{-1}) > NNN2 (0.7081 min^{-1}) > NSN1 (0.5516 min^{-1}) > NNN1 (0.4926) for Pt(II) as shown in Table 3.9; NNN2 (0.8652 min^{-1}) > NSN1 (0.6634 min^{-1}) > NSN2 (0.5426 min^{-1}) > NNN1 (0.5412 min^{-1}) for Pd(II) as shown in Table 3.10; NSN1 (0.6384 min^{-1}) > NNN2 (0.6089 min^{-1}) > NSN2 (0.5079 min^{-1}) > NNN1 (0.4454 min^{-1}) for Ir(III) as shown in Table 3.11; and NSN1 (0.7045 min^{-1}) > NSN2 > (0.6361 min^{-1}) > NNN2 (0.6188 min^{-1}) > NNN1 (0.6121 min^{-1}) for Rh(III) as shown in Table 3.12. This proved that the kinetics play a role in adsorption and separation of rhodium(III).

The plots of specific adsorption (C_e/Q_e) against the equilibrium concentration (C_e) showed that the adsorption obeys the Langmuir model. The adsorption data for each sorbent and metal ion were consistent with a Langmuir adsorption model where R^2 > 0.99, strongly suggesting monolayer adsorption on the surface of adsorbents.

The *bis*-benzimidazole ligands investigated in this study showed good potential for the removal of rhodium, iridium, platinum and palladium.

5.1.3.2 Quaternary diammonium cations

In the adsorption studies the effect of time on the adsorption of $[IrCl_6]^{2-}$ onto the nanofibers functionalized with quaternary diammonium cations (F-QuatDMDAMeBnz, F-QuatDMDABnz, F-QuatDMDACF3Bnz and F-QuatDMDANO2Bnz) was studied, respectively (Figures 4.23 to 4.26). Adsorption studies showed that the adsorption with

quaternary diammonium cations was initially fast due to the availability of active sites on the surface of the sorbents. Adsorption equilibrium was reached within 6-8 minutes.

The kinetic mechanism that controls the adsorption process was followed by the pseudo-first-order model and pseudo-second-order model. The plot of t/Q_t vs time (t) gave a straight line with better R^2 above 0.99 for all adsorbents (F-QuatDMDAMeBnz, F-QuatDMDABnz, F-QuatDMDACF3Bnz and F-QuatDMDANO2Bnz) which shows the adsorption followed a pseudo-second-order. This suggested that the adsorption process is presumably *via* chemisorption. Adsorption kinetic studies showed the following order; F-QuatDMDAMeBnz ($8.14x10^{-6}$ $g.mg^{-1}.min^{-1}$) < F-QuatDMDABnz ($4.800x10^{-4}$ $g.mg^{-1}.min^{-1}$) < F-QuatDMDACF3Bnz ($8.32x10^{-4}$ $g.mg^{-1}.min^{-1}$) < F-QuatDMDANO2Bnz ($9.350x10^{-4}$ $g.\ mg^{-1}.min^{-1}$) for Ir(IV) as shown in Table 4.7. The kinetics data correlates well with the performance of the materials which showed the following order of loading capacities; F-QuatDMDAMeBnz (60.29 mg/g) < F-QuatDMDABnz (67.61 mg/g) < F-QuatDMDACF3Bnz (107.59 mg/g) < F-QuatDMDANO2Bnz (140.47 mg/g) as shown in Figure 4.20.

The plots of specific adsorption log Q_e against the equilibrium concentration log C_e showed that the adsorption obeys the Freundlich model. The adsorption data for each sorbent and metal ion were consistent with a Freundlich adsorption model where $R^2 >$ 0.99, strongly suggesting multiple-layered adsorption on the surface of adsorbents.

The quaternary diammonium cations investigated in this study showed great prospect for separation of iridium from rhodium in 6 M HCl medium.

5.2 Future work

The methods that has been developed in this thesis for the separation of platinum group metals, using *bis*-benzimidazoles for Rh(III), Ir(III), Pd(II) and Pt(II), and quaternary diammonium cations for Ir(IV) extraction, will be applied on spent secondary resources that contain platinum group metals, i.e. catalytic converter. Silica will be used as a support material due to the robust nature of this support material and its economic viability (compared to production of nanofibers). Silica is readily produced on a large scale.

PGMs (Pd, Pt and Rh) are extensively used in automobile industry manufacturing catalytic converters owing to their specific physical and chemical properties. Since ores containing PGMs are rare and the processes for the production of PGMs with high purity from these ores are very complicated, recovery of PGMs from secondary sources such as spent catalyst can be viewed to become very popular in the near future. The role of the PGMs in the catalytic converter is; (i) rhodium is used as a reduction catalyst, (ii) palladium as an oxidation catalyst and (iii) platinum for both reduction and oxidation in automobile catalytic converters to lower the emission level from the exhaust gas (such as CO, NO_x and HC conversion to CO_2, N_2, and CO_2 and H_2O respectively) [168, 215–218].

The chemistry that has been developed will be applied in real systems, in an attempt to recover PGMs from urban secondary sources. The most common car catalytic converters are the honeycomb monolith type cordierite skeleton ($2MgO{\cdot}2Al_2O_3{\cdot}5SiO_2$). They are fixed in the wash-coat surface by coating from a solution of

hexachloroplatinic(IV) acid ($H_2PtCl_6 \cdot 6H_2O$), palladium(II) chloride ($PdCl_2$) and rhodium(III) chloride ($RhCl_3$). PGMs will be recovered after dismantling, pre-processing (making smaller particles) and leaching of spent honeycomb type automotive catalytic converters used in vehicle exhaust systems (Figure 5.1). Other metals that might be present in the leach solutions of catalytic converters are Ru, Os, Se, Cu, Fe, Ni, Ce, Zr, La, Pb, Al and alkaline-earths. These metals are known to improve the stability of catalytic converters hence their presence cannot be avoided in the leach solutions of catalytic converters [163, 170, 219, 220]. In this study, only the effect of Ni(II) against the PGMs was investigated and proved to be non-interfering in the separation of Rh(III), Pd(II) and Pt(II). The rest of the base metal ions need to be investigated for their effect in the application of the NSN1 resin.

Figure 5.1: Recovery of precious metals (Pd(II), Pt(II) and Rh(III)) from the spent catalytic converter.

Economically, the precious metals have been historically important as currency, and remain important as investment commodities. Naturally, selective extraction and separation of PGMs from associate metals become a problem in subsequent hydrometallurgical processing of these complex solutions [221–223]. Hence an

initiative was taken to find better ways to solve the problem by developing extraction methods for the platinum group metal ions.

The iridium(IV)-specific materials developed in this study could be useful for industrial feed solutions (OPM streams) and this avenue will be explored with the SA mining industry. The material containing QuatDMDANO2Bnz will be useful due to its better properties. The design of materials, especially anion exchange solid phase materials, to improve the loading capacity and separation factors for the PGMs remains an interesting area of research.

References

[1] D. A. Holwell and I. Mcdonald, “A review of the behaviour of platinum group elements within natural magmatic sulfide ore systems,” *Platinum Metals Review*, vol. 54, pp. 26–36, 2010.

[2] T. H. Nguyen, C. H. Sonu, and M. S. Lee, “Separation of Pt(IV), Pd(II), Rh(III) and Ir(IV) from concentrated hydrochloric acid solutions by solvent extraction,” *Hydrometallurgy*, vol. 164, pp. 71–77, 2016.

[3] International Platinum Group Metals Association, “The Primary production of platinum group metals (PGMs),” pp. 1-7, 2013.

[4] R. Masetlana, N. Dlambulo, L. Themba, and P. Mwape, “Mineral Economics South Africa’s mineral industry,” *Department: Mineral and energy republic of South Africa*, pp. 1–276, 2015.

[5] L. B. Hunt, “History of Iridium,” *Platinum Metals Review*, vol. 31, pp. 32–41, 1987.

[6] M. B. Smith, “Cobalt, rhodium and iridium,” vol. 109, pp. 153-167, 2013.

[7] *Chapter 26 - Cobalt, Rhodium and Iridium*, vol. 1, pp. 1113-1143, 1997.

[8] A. Fornalczyk and M. Saternus, “Removal of platinum group Metals from the used auto catalytic converter,” *Metalurgija Metabk*, vol. 56, pp. 133–136, 2009.

[9] E. Molotova, J. Pandya, and J. Klein, “Catalysts and metal recycling: Expectations are too high,” *Chemicals,* pp. 1-168, 2013.

[10] J. Matthey, “JM PGM market report,” pp. 1-48, 2018.

[11] H. E. Hilliard, "Platinum-group metals" *Geological survey minerals year book,* 58.1-58.12, 2002.

[12] D. Kraemer, M. Junge, and M. Bau, “Oxidized Ores as Future Resource for Platinum Group Metals: Current State of Research,” *Chemie Ingenieur Technik*, vol. 89, pp. 53–63, 2017.

[13] B. Harrison, B. J. Cooper, and A. J. J. Wilkins, “Control of Nitrogen Oxide Emissions from Automobile Engines,” *Platinum Metals Review*, vol. 25, pp. 14–22, 1981.

[14] Platinum 2002 Interim Review, “Other Platinum Group Metals,” pp. 18-19, 2002.

[15] E. Hark, R. Jager, and P. E. Kasatkin, “The platinum-group metal based catalysts for oxygen electroreduction reaction,” *Baltic electrochemistry conference*, 2016.

[16] K. Sun, B. H. Fan, and J. Y. Ouyang, “Nanostructured Platinum Films Deposited by Polyol Reduction of a Platinum Precursor and Their Application as Counter Electrode of Dye-Sensitized Solar Cells,” *Journal of physical chemistry C*, vol. 114, pp. 4237–4244, 2010.

[17] R. Gaita and S. J. Al-Bazi, “An ion-exchange method for selective separation of palladium, platinum and rhodium from solutions obtained by leaching automotive catalytic converters,” *Talanta*, vol. 42, pp. 249-255, 1995.

[18] F. L. Bernardis, R. A. Grant, and D. C. Sherrington, “A review of methods of separation of the platinum-group metals through their chloro-complexes,” *Reactive and Functional Polymers*, vol. 65, pp. 205–217, 2005.

[19] W. J. Gerber, “Rhodium(III) speciation-A chromatographic study with ICP-MS,” *PhD Thesis, Nelson Mandela University*, 2006.

[20] S. J. Al-Bazi and A. Chow, “Platinum metals-solution chemistry and separation methods (ion-exchange and solvent extraction),” *Talanta*, vol. 31, pp. 815–836, 1984.

[21] A. I. Busev and V. K. Akomov, “Some antipyrine derivatives in the analytical chemistry of the platinum metals,” *Talanta*, vol. 11, pp. 1657, 1964.

[22] J. Rajput, “The separation of rhodium and iridium in an hydrochloric acid medium,” *MSc Dissertation, University of Port Elizabeth*, 1998.

[23] Gindin L.M., “Extraction of Elements of Platinum Group,” *Izvestiya Sibirskogo Otdeleniya Akademii Nauk SSSR*, vol. 15, pp. 395, 1970.

[24] K. M. Ali and D. F. C. Morrism, “Application of solvent extraction to the refining of precious metals. I. Purification of Rhodium” *Journal of the Less Common Metals*, vol. 13, pp. 53-61, 1970.

[25] W. R. Inman, "Precious metals: A historical review of methods for their determination" *The Journal of The Minerals, Metals & Materials Society*, Vol. 20, 12, pp 18–25, 1968.

[26] P. P. Sun and M. S. Lee "Separation of Pt(IV) and Pd(II) from the loaded Alamine 336 by stripping" *Hydrometallurgy*, Vol. 109, 1–2, pp. 181-184, 2011.

[27] G. A. Kanert and A. Chow, “Solvent extraction separation of Rhodium from Iridium with Tri-n-Octylamine as a liquid anion-exchanger” *Analytical Chemistry*, vol. 69, pp. 253-491, 1974.

[28] J. Li, M. S. Safarzadeh, M. S. Moats, J. D. Miller,. K. MarcLeVier, M. Dietrich and R. YuWan, "Thiocyanate hydrometallurgy for the recovery of gold. Part IV: Solvent extraction of gold with Alamine 336" *Hydrometallurgy*, Vol. 113-114, pp. 24-30, 2012.

[29] F. E. Beamish, “The analytical chemistry of the noble metals,” *Pergamon Press, Oxford*, 1st edition, 1966.

[30] F. E. Beamish and J. C. Van Loon, "Recent Advances in the Analytical Chemistry of the Noble Metals" *Pergamon Press, Oxford*, 1st edition. 1972.

[31] S. N. Ivanova, L. M. Gindin, and L. Y. Mironova, “Studying the Mechanism of Rhodium Extraction by Tetraoctyl Ammonium Chloride,” *Zhurnal Neorganicheskoi Khimii*, vol. 12, pp. 1638, 1967.

[32] L. M. Gindin, “Extraction of Elements of Platinum Group,” *Zhurnal Vsesoyuznogo Khimicheskogo Obshchestva im. D. I. Mendeleeva.*, vol. 15, pp. 395, 1970.

[33] B. Gupta and I. Singh "Extraction and separation of platinum, palladium and rhodium using Cyanex 923 and their recovery from real samples" Hydrometallurgy, Vol. 134–135, pp. 11-18, 2013.

[34] Ivanova, S.N., Selezneva, and I. Krapivnitskaya, “Effect of Diluents on the Reversibility of Extraction of Platinum Metals in Systems with Salts of Amines and Quaternary Ammonium Bases,” *Materialy VI vsesoyuzn.konf. po khimii ekstraktsii (Proc. of the VI Vses. Conf. on the Chemistry of Extraction)*, vol. 2, pp. 200, 1980.

[35] M. A. Khattak and R. J. Magee, "Extraction of platinum metals by high-molecular-weight amines. rhodium(III) systems" *Analytica Chimica Acta*, vol. 45, , pp. 297-304, 1969.

[36] B. R. Reddy, B.Raju, J. Y. Lee, and H. K. Park "Process for the separation and recovery of palladium and platinum from spent automobile catalyst leach liquor using LIX 84I and Alamine 336" *Journal of Hazardous Materials*, Vol. 180, 1–3, pp. 253-258, 2010.

[37] C. Pohlandt, "The extraction of noble metals withn-octylaniline" *Talanta,* vol. 26, pp. 199-206*,* no. 3. Mar. 1979*.*

[38] P. P.Sun and M. S. Lee "Separation of Ir(IV) and Rh(III) from mixed chloride solutions by solvent extraction" Hydrometallurgy, Vol. 105, 3–4, pp. 334-340, 2011.

[39] E. Benguerel, G. P. Demopoulos, G. Cote and D. Bauer, "An investigation on

the extraction of rhodium from aqueous chloride solutions with 7 substituted 8 hydroxyquinolines" *Solvent Extraction and Ion Exchange*, Vol. 12, 3, pp. 497–516, 1994.

[40] M. Mojski, “Extraction of platinum metals from hydrochloric acid medium with triphenylphosphine solution in 1,2-dichloroethane,” *Talanta*, vol. 27, pp. 7–10, 1980.

[41] G. H. Faye and W. R. Inman, “A scheme for the separation of platinum, palladium, rhodium, and iridium by solvent extraction,” *Analytical Chemistry*, vol. 35, pp. 985–988, 1963.

[42] E. Benguerel, G. P. Demopoulos and G.B. Harris "Speciation and separation of rhodium(III) from chloride solutions: a critical review" Hydrometallurgy Vol. 40, pp. 135–152, 1996.c

[43] D. V. Chavan and P. M. Dhadke, "Extraction separation of Ir(III) and Rh(III) withCyanex 923 from chloride media: a possible recovery from spent catalyst" *Journal of Chemical Technology and Biotechnology,* Vol. 8, pp. 925–932, 2002.

[44] C. S. Kedari, M. T. Coll, A. Fortuny, E. Goralska and A. M. Sastre, "Liquid-liquidextraction of Ir, Ru and Rh from chloride solutions and their separation usingdifferent commercially available solvent extraction reagents" *Separation Science and Technology,* Vol. 40, pp. 1927–1946, 2005.

[45] G. Levitin and G. Schmuckler, "Solvent extraction of rhodium chloride from aqueoussolutions and its separation from palladium and platinum" *Reactive and Functional Polymers,* Vol. 54, pp.149–154, 2003.

[46] A. A. Mhaske and P. M. Dhadke, "Extraction separation studies of Rh, Pt and Pd using Cyanex 921 in toluene-a possible application to recovery from spent catalysts" *Hydrometallurgy,* Vol. 61, pp.143–150, 2001.

[47] J. S. Preston, and A. C. du Preez, "Solvent extraction of platinum-group metals

fromhydrochloric acid solutions by dialkyl sulphoxides" *Solvent Extraction and Ion Exchange,* Vol. 20, 3, pp. 359–374, 2002.

[48] L. H. Zou, J. Chen, Y. Huang, "An alternative way to separating Ir(IV) and Rh(III) ions from a mixed chloride solution with added stannous chloride" *Hydrometallurgy*, Vol. 72, pp. 31–37, 2004.

[49] A. Mhaske, P. Dhadke, "Extraction studies of platinum group metals with Cyanex 925 in toluene-role of tin(II) chloride in their separation" *Separation Science and Technology*, Vol. 37, pp. 1861–1875, 2002.

[50] S. J. Al-Bazi, and A. Chow, "Platinum metals—solution chemistry and separation methods (ion exchange and solvent extraction)", *Talanta,* Vol. 31, pp. 815–836, 1984.

[51] E. R. Els, L. Lorenzen and C. Aldrich, "The adsorption of precious metals and basemetals on a quaternary ammonium group ion exchange resin" *Minerals Engineering*, Vol. 13, pp. 401–414, 2000.

[52] S. Aktas "Rhodium recovery from rhodium-containing waste rinsing water via cementation using zinc powder" *Hydrometallurgy*, Vol. 106, 1–2, pp. 71-75, 2011.

[53] J. C. Park, "Purification and recovery of rhodium metal by the formation of intermetallic compounds" *Bulletin of the Korean Chemical Society*, Vol. 29 pp. 1787-1789, 2008.

[54] G. G. Tertipis and F. E. Beamish, “Solvent extraction separation and spectrophotometric determina- tion of rhodium and iridium,” *Analytical Chemistry*, vol. 34, pp. 623–625, 1962.

[55] R. Stella and M. Di Casa, " Radioanalytical investigation on rhodium extraction behaviour with tri-n-butylphosphate from iodide solutions" *Journal of Radioanalytical and Nuclear Chemistry*, vol. 16, pp. 183-190, 1973.

[56] Z. Hubicki, M. Wawrzkiewicz, G. Wójcik, D. Kołodyńska and A. Wołowicz, " Ion Exchange Method for Removal and Separation of Noble Metal Ions" *Intech Open - Open Science Open Minds*, pp. 1-35, 2015.

[57] E. W. Berg and W. L. Senn, "Separation of rhodium and iridium by multiple fractional extraction" *Analytica Chimica Acta*, vol. 19, pp. 109–113, 1958.

[58] Z. Hubickin, M. Leszczynska, B. Lodyga, and A. Lodyga, “Recovery of palladium (II) from chloride-nitrate solutions using ion-exchange resins with S-donor atoms,” *Desalination*, vol. 207, pp. 80–86, 2007.

[59] F. G. Helfferich, “Theories of ion-exchange column performance: A critical study,” *Angewandte Chemie International Edition in English*, vol. 1, pp. 440–453, 1962.

[60] M. A. Congost, D. Salvatierra, G. Marques, J. L. Bourdelande, J. Font, and M. Valiente, “A novel phosphine sulphide functionalized polymer for the selective separation of Pd(II) and Au(III) from base metals,” *Reactive and Functional Polymers*, vol. 28, pp. 191–200, 1996.

[61] F. A. Settle, "Ion chromatography, Handbook of instrumental techniques for Analytical chemistry*" Journal of Liquid Chromatography & Related Technologies*, vol. 21, pp. 3072-3076, 1998.

[62] P. K. Jal, S. Mishra, and B. K. Patel, “Chemical modification of silica surface by immobilization of functional groups for extractive concentration of metal ions,” *Talanta*, vol. 62, pp. 1005–1028, 2004.

[63] B. Shah and U. Chudasama, “Synthesis and characterization of a novel hybrid material as amphoteric ion exchanger for simultaneous removal of cations and anions,” *Journal of Hazardous Materials*, vol. 276, pp. 138–148, 2014.

[64] J. Kramer, A. Scholten, W. L. Driessen, and J. Reedijk, “The recovery of a

rhodium-containing catalyst by various new silica based amine ion exchangers," *European Journal of Inorganic Chemistry*, vol. 6, pp. 1488–1494, 2002.

[65] C. Colombo, C. J. Oates, A. J. Monhemius, and J. A. Plant, "Complexation of platinum , palladium and rhodium with inorganic ligands in the environment," *Geochem: Exploaration, Environment, Analysis*, vol. 8, pp. 91–101, 2008.

[66] A. A. Mhaske and P. M. Dhadke, "Extraction separation studies of Rh, Pt and Pd using Cyanex 921 in toluene a possible application to recovery from spent catalysts" Hydrometallurgy, Vol. 61, pp. 143–150, 2001.

[67] F.A. Cotton and G. Wilkinson, "Advanced Inorganic Chemistry" A Comprehensive Text. Wiley and Sons, New York. pp. 410, 1969.

[68] E. R. Els, L. Lorenzen and C. Aldrich, "The adsorption of precious metals and base metals on a quaternary ammonium group ion exchange resin" Minerals Engineering, Vol.13, pp. 401–414, 2000.

[69] C. R. M. Rao and C. S. Reddi, "Platinum group metals (PGM): occurrence, use and recent trends in their determination" Trend in Analytical Chemistry, Vol 19, pp. 565–586, 2000.

[70] P. A. Tasker, R. G. Plieger, and L. C. West, "Metal complexes for hydrometallurgy and extraction" Comprehensive Coordination Chemistry II, Vol. 9, pp. 759–808, 2004.

[71] K. J. Bell, A. N. Westra, R. J. Warr, J. Chartres, R. Ellis, C. C. Tong, A. J. Blake, P. A. Tasker and M. Schröder, "Outer-sphere coordination chemistry. Selective extraction and transport of the [PtCl6]2− ion" Angewandte Chemie. International Edition, Vol. 47, 9, pp. 1745–1748, 2008.

[72] F. G. Seeley and S. J. Crouse, "Extraction of metals from chloride solutions with amines," Journal of Chemical & Engineering Data, vol. 11, pp. 424–429, 1966.

[73] F. L. Bernardis, R. A. Grant and D. C. Sherrington, "A review of methods of separation of the platinum-group metals through their chlorocomplexes" Reactive and Functional Polymers, Vol. 65, pp. 205–217, 2005.

[74] C. Fontas, E. Antico, V. Salvado, M. Valiente and M. Hidalgo, "Chemical pumping of rhodium by a supported liquid membrane containing Aliquat 336 as carrier" *Analytica Chimica Acta* vol. 346 pp.199-206, 1997.

[75] A. N. Nikoloski, K. L. Ang, and D. Li, “Recovery of platinum, palladium and rhodium from acidic chloride leach solution using ion exchange resins,” *Hydrometallurgy*, vol. 152, pp. 20–32, 2015.

[76] A. N. Nikoloski and K. L. Ang, “Review of the application of ion exchange resins for the recovery of platinum-group metals from hydrochloric acid solutions,” *Mineral Processing and Extractive Metallurgy Review*, vol. 35, pp. 369–389, 2014.

[77] D. O. Moumakwa, “an overview of current platinum group metal exploration projects and new mine developments in South Africa" *, Mineral economics*, Report R51,” pp. 1-12, 2013.

[78] A. R. Porcari, “N-hydroxyphthalimide/ cobalt acetate, a new catalytic oxidative system for the synthesis of benzimidazoles,” *Synthetic Communications*, vol. 2, pp. 1–8, 2011.

[79] A. Baghai and H. J. M. Bowen, “Separation of rhodium and iridium using silicone rubber foam treated with tri-n-octylamine,” *Analyst*, vol. 101, pp. 661–165, 1976.

[80] I. Omae, “Intramolecular five-membered ring compounds and their applications,” *Coordination Chemistry Reviews*, vol. 248, pp. 995–1023, 2004.

[81] F. Basolo and R. C. Johnso, “Coordination Chemistry,” *Journal of chemical education*, vol. 64, pp. 130, 1994.

[82] A. K. Prokof'ev, "Intramolecular Coordination in Organic Derivatives of Non-transition Elements," *Uspekhi Khimii*, vol. 45, pp. 1028, 1976.

[83] A. K. Prokof'ev, "Intramolecular Coordination in Organic Derivatives of Non-transition Elements," *Russian Chemical Reviews*, vol. 45, pp. 519–543, 1976.

[84] I. Omae, "Organometallic intramolecular-coordination compounds containing a π-allyl donor ligand," *Coordination Chemistry Reviews*, vol. 53, pp. 261–291, 1984.

[85] I. Omae. "Organometallic intramolecular-coordination compounds. Recent aspects in the study of sulfur donor ligands" Coordination Chemistry Reviews vol. 28 (2-3), pp. 97-115, 1979.

[86] I. Omae, "Organotin Chemistry," *Journal of Organometallic Chemistry*, vol. 21, pp. 355, 1989.

[87] S. J. S. Flora and V. Pachauri, "Chelation in metal intoxication," *International Journal of Environmental Research and Public Health*, vol. 7, pp. 2745–2788, 2010.

[88] L. Fitjer, C. Seeneck, S. Gaini-Rahimi, U. Schröder, K. Justus, P. Puder, M. Dittmer, C. Hassler, J. Weiser, M. Noltemeyer and M. Teichert, " A new rotane family: Synthesis, structure, conformation, and dynamics of [3.4]-, [4.4]-, [5.4]-, and [6.4] rotane" *Journal of the American Chemical Society*, vol. 120, pp. 317-328, 1998.

[89] K. Declercq, L. Párkányi, J. P. Sasvári, and G. Germain, "The crystal and molecular structure of decaphenylcyclopentasilane, $C_{60}H_{50}Si_5$," *Acta Crystallographica Section*, vol. B34, pp. 3678–3682, 1978.

[90] L. Ross and M. Z. Dräger, " Phases of Decaphenylcyclopentagermane $(Ph_2Ge)_s$ "*Zeitschrift für Naturforschung*, vol. 38b, pp. 665, 1983.

[91] S. Matsuda, S. Kikkawa, and M. Nomura, " Direct reaction of β-halopropionate with tin" *Kogyo Kagaku Zasshi*, vol. 69, pp. 649-653, 1966.

[92] N. J. Williams, N. E. Dean, D. G. Van Derveer, R. C. Luckay, and R. D. Hancock, “Strong metal ion size based selectivity of the highly preorganized ligand PDA (1,10-phenanthroline-2.9-dicarboxylic acid) with trivalent metal ions. A crystallographic, fluorometric, and thermodynamic study,” *Inorganic Chemistry*, vol. 48, pp. 7853–7863, 2009.

[93] D. J. Cram and J. M. Cram, “Design of complexes between synthetic hosts and organic guests,” *Accounts of Chemical Research*, vol. 11, pp. 8–14, 1978.

[94] D. L. Melton, G. D. Van Derveer, and R. D. Hancock, “Complexes of greatly enhanced thermodynamic stability and metal ion size-based selectivity, formed by the highly preorganized non-macrocyclic ligand 1,10-phenanthroline-2,9-dicarboxylic acid. A thermodynamic and crystallographic study,” *Inorganic Chemistry*, vol. 45, pp. 9306–9314, 2006.

[95] R. D. Shannon, “Revised Effective Ionic Radii and Systematic Studies of Interatomie Distances in Halides and Chaleogenides,” *Acta Crystallographica Section A*, vol. A32, pp. 751–757, 1976.

[96] R. D. Hancock, “The pyridyl group in ligand design for selective metal ion complexation and sensing,” *Chemical Society Reviews*, vol. 42, pp. 1500–1524, 2013.

[97] R. D. Hancock and L. J. Bartolotti, “A DFT analysis of the effect of chelate ring size on metal ion selectivity in complexes of polyamine ligands,” *Polyhedron*, vol. 52, pp. 284–293, 2013.

[98] R. D. Hancock, “Molecular mechanics, calculations and metal ion recognition,” *Accounts of Chemical Research*, vol. 23, pp. 253–257, 1990.

[99] C. J. Pederson, “Cyclic polyethers and their complexes with metal salts,” *Journal of the American Chemical Society*, vol. 89, pp. 36, 1967.

[100] A. E. Martell and R. M. Smith, “Critical Stability Constant Database, 46,”

National Institute of Science and Technology, 2003.

[101] J. G. H. Du Preez and U. Naidoo, “Separation of rhodium and iridium. Part V. Application and further development of a new diquaternary ammonium resin,” *Solvent Extraction and Ion Exchange*, vol. 23, pp. 439–447, 2005.

[102] J. G. H. du Preez and U. Naidoo, “The separation of rhodium and iridium. Part IV. The synthesis and application of a new diquaternary ammonium resin,” *Solvent Extraction and Ion Exchange*, vol. 23, pp. 101–112, 2005.

[103] U. Naidoo, “ The separation of iridium and rhodium,” *Doctoral PhD thesis, Univeristy of Port Elizabeth*, 2002.

[104] J. G. H. du Preez, C. Viviers, T. Louw, E. Hosten, and H. Jonck, “The separation of rhodium and iridium. II. Chloridation and chlorination of iridium(III) and (IV),” *Solvent Extraction and Ion Exchange*, vol. 22, pp. 175–188, 2004.

[105] J. G. H. du Preez and C. Viviers, “The separation of rhodium and iridium. I. Active centra and the HCl effect,” *Solvent Extraction and Ion Exchange*, vol. 21, pp. 815–826, 2003.

[106] E. Goralska, M. T. Coll, A. Fortuny, C. S. Kedari, and A. M. Sastre, “Studies on the selective separation of Ir(IV), Ru(III) and Rh(III) from chloride solutions using alamine 336 in kerosene,” *Solvent Extraction and Ion Exchange*, vol. 25, pp. 65–77, 2007.

[107] N. J. K. Simpson, “Solid Phase Extraction, Principles Techniques and Application,” 1st edition, CPC Press, USA, 2000.

[108] D. J. Walsh, P. Crosby, and R. F. Dalton, “Polymer II exhibited improved chelation characteristics toward lanthanide metal ions,” *Polymer*, vol. 24, pp. 423–456, 1983.

[109] G. Schmuckler, “Chelating resins—their analytical properties and applications,” *Talanta*, vol. 12, pp. 281–290, 1965.

[110] B. S. Garg, R. K. Sharma, N. Bhojak, and S. Mittal, “Chelating Resins and Their Applications in the Analysis of Trace Metal Ions,” *Microchemical Journal*, vol. 61, pp. 94–114, 1999.

[111] S. K. Sahni and J. Reedijk, “Coordination chemistry of chelating resins and ion exchangers,” *Coordination Chemistry Reviews*, vol. 59, pp. 1–139, 1984.

[112] J. Reedijk, “Metal-ligand exchange kinetics in platinum and ruthenium complexes: Significance for effectiveness as anticancer drugs,” *Platinum Metals Review*, vol. 52, pp. 2–11, 2008.

[113] M. Chanda and G. L. Rempel, “Polyethyleneimine gel-coat on silica. High uranium capacity and fast kinetics of gel-coated resin,” *Reactive Polymer*, vol. 25, pp. 25–36, 1995.

[114] J.Y. Lee, R.J. Kumar, J.S. Kim and H.K. Park, “Liquid-liquid extraction/separation of platinum(IV) and rhodium(III) from acidic chloride solutions using tri-iso-octylamine,” *Journal of Hazardous Materials*, vol. 168, pp. 424–429, 2009.

[115] J. Kramer, W. L. Driessen, K. R. Koch, and J. Reedijk, “Highly selective extraction of platinum group metals with silica-based (poly)amine ion exchangers applied to industrial metal refinery efluents,” *Hydrometallurgy*, vol. 64, pp. 59–68, 2002.

[116] S. Mane, S. Ponrathnam, and N. Chavan, “Synthesis and characterization of hypercrosslinked hydroxylfunctionalized co-polymer beads,” *European Polymer Journal*, vol. 59, pp. 46–58, 2014.

[117] J.J. Allen, “Surface characteristics of silica polyamine composites,” *Doctoral Thesis, The University of Montana*, 2011.

[118] O.E. Fayemi, A.S. Ogunlaja, E. Antunes, P. Kempgens, T. Nyokong, N. Torto, and Z.R. Tshentu, “Adsorption and separation of platinum and palladium using polyamine functionalised styrene-based beads and nanofibers,” *Minerals Engineering*, vol. 53, pp. 256–265, 2013.

[119] A. Greiner and J. H. Wendorff, “Electrospinning: A fascinating method for the preparation of ultrathin fibers,” *Angewewandte Chemie International Edition*, vol. 46, pp. 5670–5703, 2007.

[120] G. F. McLean, T. Niet, S. Prince-Richard, and N. Djilali, “An assessment of alkaline fuel cell technology,” *International Journal of Hydrogen Energy*, vol. 27, pp. 507–526, 2002.

[121] S. Lu, J. Pan, A. Huang, L. Zhuang, and J. Lu, “Alkaline polymer electrolyte fuel cells completely free from noble metal catalysts,” *Proceeding of the National Academy of Science of the United Sates of America*, vol. 105, pp. 20611–20614, 2008.

[122] J. R. Varcoe, R. C. T. Slade, and E. L. H. Yee, “An alkaline polymer electrochemical interface: a breakthrough in application of alkaline anion-exchange membranes in fuel cells,” *Chemical Communications*, vol. 13, pp. 1428–1429, 2006.

[123] D. H. Reneker and I. Chun, “Nanometre diameter fibres of polymer, produced by electrospinning,” *Nanotechnology*, vol. 7, pp. 216–223, 1996.

[124] T. Ondarcuhu and C. Joachim, “Drawing a single nanofibre over hundreds of microns,” *Europhysics Letters*, vol. 42, pp. 215–225, 1998.

[125] C. R. Martin, “Membrane-Based Synthesis of Nanomaterials,” *Chemistry of materials*, vol. 8, pp. 1739–1746, 1996.

[126] J. H. He, Y. Liu, L. F. Mo, Y. Q. Wan, and L. Xu, *Electrospun Nanofibers and Their Applications*. 2008.

[127] D. Li and Y. Xia, “Electrospinning of Nanofibers: Reinventing the Wheel?,” *Advanced Materials*, vol. 16, pp. 1151–1169, 2004.

[128] W. E. Teo and S. Ramakrishna, “A review on electrospinning design and nanofibre assemblies,” *Nanotechnology*, vol. 17, pp. R89–R106, 2006.

[129] Y. J. Ryu, H. Y. Kim, K. H. Lee, H. C. Park, and D. R. Lee, “Transport properties of electrospun nylon 6 nonwoven mats,” *European Polymer Journal*, vol. 39, pp. 1883–1896, 2003.

[130] A. Frenot and I. S. Chronakis, “Polymer Nanofibers Assembled by Electrospinning,” *Current Opinion in Colloid and Interface Science*, vol. 8, pp. 64–75, 2003.

[131] Z. M. Huang, Y. Z. Zhang, M. Kotaki, and S. Ramakrishna, “A review on polymer nanofibers by electro-spinning applications in nanocomposites,” *Composites Science and Technology*, vol. 63, pp. 2223–2253, 2003.

[132] D. H. Reneker, A. L. Yarin, H. Fong, and S. Koombhongse, “Bending Instability of Electrically Charged Liquid Jets of Polymer Solutions in Electrospinning,” *Journal of applied chemistry*, vol. 87, pp. 4531–4544, 2000.

[133] W. Hai-Sheng, F. Guo-Dong, and L. Xin-Song, “Functional polymer nanofibers from electrospinning,” *Resent Patents on Nanotechnology*, vol. 3, pp. 21–31, 2009.

[134] Y. Dzenis, “Spinning continuous fibers for nanotechnology,” *Science*, vol. 304, pp. 1917–1988, 2004.

[135] A. Kumar, "Nanofibers"*, IntechOpen,* pp. 234-245, 2010.

[136] Q. P. Pham, U. Sharma, and A. G. Mikos, “Electrospinning of polymeric nanofibers for tissue engineering applications: A review.,” *Tissue Engineering*, vol. 12, pp. 1197–1211, 2006.

[137] L. Persano, A. Camposeo, C. Tekmen, and D. Pisignano, “Industrial upscaling of electrospinning and applications of polymer nanofibers: A review.,” *Macromolecular Materials and Engineering*, vol. 298, pp. 504–520, 2013.

[138] S. Kidoaki, I. K. Kwon, and T. Matsuda, “Mesoscopic spatial designs of nano- and micron-fiber meshes for tissue-engineering matrix and scaffold based on newly devised multilayering and mixing electrospinning techniques.,” *Biomaterials*, vol. 26, pp. 37–46, 2005.

[139] L. I. Anderson, “Selective solid phase extraction of bio and environmental samples using molecularly imprinted polymers,” *Bioseperation*, vol. 10, pp. 353–364, 2001.

[140] D. L. Pavia, G. M. Lampman, and G. S. Kriz, “Introduction to spectroscopy,” *Thomson Learning, Inc*, vol. 14, pp. 353–358, 2001.

[141] A. I. Okewole, “Application of bidentate N,N’-donor extractants in the hydrometallurgical separation of base metals from an acidic sulfate medium,” *PhD Thesis, Rhodes University*, 2012.

[142] L.J. Farrugia, “ORTEP-3 for Windows - a Version of ORTEP-III with a Graphical User Interface (GUI),” *Journal of Applied Crystallography*, vol. 30, pp. 565, 1997.

[143] S. Sivrikaya, H. Altundag, and M. Zengin, “Separation, preconcentration and recovert of Pd(II) ions using newly modified silica gel with Bis(3-aminopropyl)amine,” *Separation Science and Technology*, vol. 46, pp. 2032–2040, 2011.

[144] T. Akkaya, M. Gulfen, and U. Olgun, “Adsorption of rhodium(III) ions onto ploy(1,8-diaminonaphtalene) chelating polymer: Equilibrium, kinetics and thermodynamic study, Reactive and Functional Polymers,” *Reactive and Functional Polymers*, vol. 73, pp. 1589–1596, 2013.

[145] J. Goel, K. Kadirvelu, C. Rajagopal, and V. K. Garg, “Removal of lead(II) by

adsorption using treated granular activated carbon: Batch and column studies," *Journal of Hazardous Materials*, vol. B125, pp. 211–220, 2005.

[146] M. Hasan, A. L. Ahmad, and B. H. Hameed, "Adsorption of reactive dye onto cross-linked chitosal/oil palm ash composite beads," *Chemical Engineering Journal*, vol. 136, pp. 164–172, 2008.

[147] M. Min *et al.*, "Micro-nano structure poly(ether sulfones)/poly(ethyleneimine) nanofibrous affinity membranes for adsorption of anionic dye and heavy metal ions in aqueous solution," *Chemical Engineering Journal*, vol. 197, pp. 88–100, 2012.

[148] G. C. Ania, A. M. F. Patricia, E. V. M. Suárez-Iha, and R. P. R. Rocha, Fábio, "Adsorption of 1-(2-thiazolylazo)-2-naphthol on amberlite XAD-7 and silica gel: isotherms and kinetic studies," *Journal of the Brazilian Chemical Society*, vol. 25, pp. 648–657, 2014.

[149] T. Akkaya, M. Gulfen, and U. Olgun, "Adsorption of rhodium(III) ions onto ploy(1,8-diaminonaphtalene) chelating polymer: Equilibrium, kinetics and thermodynamic study," *Reactive and Functional Polymers*, vol. 73, pp. 1589–1596, 2013.

[150] A. Majavu, A. S. Ogunlaja, and Z. R. Tshentu, "Separation of rhodium(III) and iridium(IV) chlorido complexes using polymer microspheres functionalized with quaternary diammonium groups," *Separation Science and Technology (Philadelphia)*, vol. 52, pp. 71–80, 2017.

[151] T. M. Elmorsi, Z. H. Mohamed, W. Shopak, and A. M. Ismaiel, "Kinetic and Equilibrium Isotherms Studies of Adsorption of Pb(II) from Water onto Natural Adsorbent," *Journal of Environmental Protection*, vol. 5, pp. 1667–1681, 2014.

[152] A. Majavu, A. S. Ogunlaja, E. C. Hosten, and Z. R. Tshentu, "Functional nanofibers for separation of rhodium(III) and iridium(IV) chlorido species," *Minerals Engineering*, vol. 87, pp. 32–44, 2016.

[153] M. J. Frisch, G. W. Trucks, H. B. Schlegel, G. E. Scuseria, M. Robb, J. R. Cheeseman, J. Montgomery, T. Vreven, K. N. Kudin, J. C. Burant, J. M. Millam, S. S. Iyengar, J. Tomasi, V. Barone, B. Mennucci, M. Cossi, G. Scalmani, N. Rega, G. Petersson, H. Nakatsuji, M. Hada, M. Ehara, K. Toyota, R. Fukuda, J. Hasegawa, H. Ishida, T. Nakajima, Y. Honda, O. Kitao, H. Nakai, M. Klene, X. Li, J. E. Knox, H. P. Hratchian, J. B. Cross, C. Adamo, J. Jaramillo, R. Gomperts, R. E. Stratmann, O. Yazyev, A. J. Austin, R. Cammi, C. Pomelli, J. Ochterski, P. Y. Ayala, K. Morokuma, G. Voth, P. Salvador, J.J. Dannenberg, V. G. Zakrzewski, S. Dapprich, A. D. Daniels, M. C. Strain, O. Farkas, D. K. Malick, A. D. Rabuck, K. Raghavachari, J. B. Foresman, J. V. Ortiz, Q. Cui, A. G. Baboul, S. Clifford, J. Cioslowski, B. B. Stefanov, G. Liu, A. Liashenko, P. Piskorz, I. Komaromi, R. L. Martin, D. J. Fox, T. Keith, M. Al-Laham, C. Y. Peng, A. Nanayakkara, M. Challacombe, P. M. W. Gill, B. Johnson, W. Chen, M. W. Wong, C. Gonzalez, J. Pople, “Gaussian 09W Tutorial: An Introduction To Computational Chemistry Using G09W and Avogadro Software” pp. 1-34, 2009.

[154] S. Erkan kariper, K. Sayin, and D. Karakaş, “Theoretical study on the antitumor properties of Ru(II) complexes containing 2-pyridyl, 2-pyridine-4-carboxylic acid ligands,” *Journal of Molecular Structure*, vol. 1149, pp. 473–486, 2017.

[155] F. C. Hagemeister, C. J. Gruenloh, and T. S. Zwier, “Density functional theory calculations of the structures, binding energies, and infrared spectra of methanol clusters,” *Journal of Physical Chemistry A*, vol. 102, pp. 82–94, 1998.

[156] P. J. Stephens, F. J. Devlin, C. F. Chabalowski, and M. J. Frisch, “Ab Initio Calculation of Vibrational Absorption and Circular Dichroism Spectra Using Density Functional Force Fields,” *Journal of Physical Chemistry*, vol. 98, pp. 11623–11627, 1994.

[157] K. Kim and K. D. Jordan, “Comparison of Density Functional and MP2 Calculations on the Water Monomer and Dimer,” *Journal Physical Chemistry*, vol. 98, pp. 10089–10094, 1994.

[158] R. G. Pearson, “Chemical hardness: Applications from molecules to solids,” *Journal of Chemical Education*, vol. 64, pp. 561–570, 1997.

[159] H. Chermette, “Chemical reactivity indexes in density functional theory,” *Journal of computational chemistry*, vol. 20, pp. 129–154, 1999.

[160] R. G. Parr and R. G. Pearson, “Absolute Hardness: Companion Parameter to Absolute Electronegativity,” *Journal of the American Chemical Society*, pp. 105–7512, 1983.

[161] W. Yang and R. G. Parr, “Hardness, Softness, and the Fukui Function in the Electronic Theory of Metals and Catalysis,” *Proceedings of the National Academy of Sciences*, vol. 82, pp. 6723–6726, 1985.

[162] A. S. Ogunlaja and O. S. Alade, “Catalysed oxidation of quinoline in model fuel and the selective extraction of quinoline-N-oxide with imidazoline-based ionic liquids,” *Egyptian Journal of Petroleum*, vol. 27, pp. 159–168, 2018.

[163] D. J. De Aberasturi, R. Pinedo, I. R. Ruiz De Larramendi, J. I. R. Ruiz De Larramendi, and T. Rojo, “Recovery by hydrometallurgical extraction of the platinum-group metals from car catalytic converters,” *Minerals Engineering*, vol. 24, pp. 505–513, 2011.

[164] H. Dong, J. Zhao, J. Chen, Y. Wu, and B. Li, “Recovery of platinum group metals from spent catalysts: A review,” *International Journal of Mineral Processing*, vol. 145, pp. 108–113, 2015.

[165] U.S. Geological Survey, “Mineral Commodity Summaries - Platinum Group Metals,” *U.S. Geological Survey*, pp. 126–127, 2017.

[166] C. Kim, S. I. Woo, and S. H. Jeon, “Recovering of platinum-group metals from recycled automobile catalytic converters by carbochlorination,” *Industrial & Engineering Chemistry Research*, vol. 39, pp. 1185–1192, 2000.

[167] K. Dewar, “The Catalytic Converter Industry in South Africa,” *Platinum 2012*, pp. 893–904, 2012.

[168] C. H. Kim, S. I. Woo, and S. H. Jeon, “Recovery of platinum-group metals from recycled automotive catalytic converters by carbochlorination,” *Industrial and Engineering Chemistry Research*, 2000.

[169] J. Willner and A. Fornalczyk, “Dissolution of ceramic monolith of spent catalytic converters by using hydrometallurgical methods,” *Archives of Metallurgy and Materials*, vol. 60, pp. 2945–2948, 2015.

[170] R. Rumpold and J. Antrekowitsch, “Recycling of Platinum Group Metals From Automotive Catalysts By an Acidic Leaching Process,” *Southern African Institute of Mining and Metallurgy - Platinum*, pp. 695–714, 2012.

[171] T. Bossi and J. Gediga, “The Environmental Profile of Platinum Group Metals,” *Johnson Matthey Technology Review*, vol. 61, pp. 111–121, 2017.

[172] J. Matthey, “The environmental profile of Platinum Group Metals (PGMs),” *Johnson Matthey Technology Review*, vol. 61, pp. 111, 2017.

[173] H. T. Truong and M. S. Lee, “Separation of Pd (II) and Pt (IV) from hydrochloric acid solutions by solvent extraction with Cyanex 301 and LIX 63,” *Minerals Engineering*, vol. 115, pp. 13–20, 2018.

[174] H. E. Hilliard, “Platinum-Group Metals,” *U.S. Geology Survey Minerals Yearbook*, pp. 58.1-58.12, 2002.

[175] P. J. Loferski, “Platinum-Group Metals,” *2014 Minerals Yearbook*, pp. 119, 2016.

[176] J. B. Wright, “The chemistry of the benzimidazoles,” *Chemical Reviews*, vol. 48, pp. 397–541, 1951.

[177] C. J. Matthews, T. A. Leese, W. Clegg, M. R. J. Elsegood, L. Horsburgh, and J. C. Lockhart, “A route to bis(benzimidazole) ligands with built-in asymmetry: Potential models of protein binding sites having histidines of different basicity,” *Inorganic Chemistry*, vol. 35, pp. 7563–7571, 1996.

[178] P. R. Martínez-Alanis, M. L. Ortiz, I. Regla, and I. Castillo, “Synthesis of N -Boc-Protected Bis(2-benzimidazolylmethyl)amines,” *Synlett*, pp. 423–426, 2010.

[179] M. Bouchouit, M.E. Said, M. Kara Ali, S. Bouacida, H. Merazig, N. Kacem Chaouche, A. Chibani, B. Zouchoune, A. Belfaitah, and A. Bouraiou, “Synthesis, X-ray structure, theoretical investigation, corrosion inhibition and antimicrobial activity of benzimidazole thioether and theirs metal complexes,” *Polyhedron*, vol. 119, pp. 248–259, 2016.

[180] A. I. Okewole, E. Antunes, T. Nyokong, and Z. R. Tshentu, “The development of novel nickel selective amine extractants: 2,20′-pyridylimidazole functionalised chelating resin,” *Minerals Engineering*, vol. 54, pp. 88–93, 2013.

[181] D. A. Palmer and G. M. Harris, “Kinetics, Mechanism, and Stereochemistry of the Aquation and Chloride Anation Reactions of fac- and mer-Trichlorotriaquorhodium(III) Complexes in Acidic Aqueous Solution. A complete Reaction Scheme for Complex Ions of the General Formula $[RhCl_n(OH_2)_{6-n}]^3$,” *Inorganic Chemistry*, vol. 14, pp. 1316–1321, 1975.

[182] I. Piyanzina, B. Minisini, D. Tayurskii, and J. F. Bardeau, “Density functional theory calculations on azobenzene derivatives: a comparative study of functional group effect,” *Journal of Molecular Modeling*, vol. 21, pp. 2–5, 2015.

[183] D. Q. Dao, T. D. Hieu, T. Le Minh Pham, D. Tuan, P. C. Nam, and I. B. Obot, “DFT study of the interactions between thiophene-based corrosion inhibitors and an Fe_4 cluster,” *Journal of Molecular Modeling*, vol. 23, pp. 260, 2017.

[184] M. V. Putz, N. Russo, and E. Sicilia, “About the Mulliken electronegativity in

DFT," *Theoretical Chemistry Accounts*, vol. 114, pp. 38–45, 2005.

[185] Z. F. Ebrahimi and D. J. D. Wilson, "DFT investigation of the electronic structure of amphetamines: effect of substituent on O and N chemical shielding and electric field gradient tensors," *International Journal of Computational Biology and Drug Design*, vol. 8, pp. 311, 2015.

[186] N.P. Magwa, Nomampondo. E. Hosten, G.M. Watkins and Z.R. Tshentu, "An Exploratory Study of Tridentate Amine Extractants: Solvent Extraction and Coordination Chemistry of Base Metals with Bis((1R-benzimidazol-2-yl)methyl)amine," *International Journal of Nonferrous Metallurgy*, vol. 1, pp. 49–58, 2012.

[187] L. Dobrzańska and G. O. Lloyd, "2,2'-(Butane-1,4-diyl)dibenzimidazolium dichloride dehydrate," *Acta crystallographica Section E*, vol. E62, pp. o1205–o1207, 2006.

[188] M. S. Abdul-Quadir, R. Van Der Westhuizen, W. Welthagen, E. E. Ferg, Z. R. Tshentu, and A. S. Ogunlaja, "Adsorptive denitrogenation of fuel over molecularly imprinted poly-2-(1*H* -imidazol-2-yl)-4-phenol microspheres," *New Journal of Chemistry*, vol. 42, pp. 13135–13146, 2018.

[189] M. Thommes, K. Kaneko, A. V. Neimark, J. P. Olivier, F. Rodriguez-Reinoso, J. Rouquerol and K. S. W. "Physisorption of gases, with special reference to the evaluation of surface area and pore size distribution (IUPAC Technical Report)," *Pure and Applied Chemistry*, vol. 87, pp. 1051–1069, 2015.

[190] S. A. Nabavi, G. T. Vladisavljevic, Y. Zhu, and M. Vasilije, "Synthesis of size-tuneable CO_2 -philic imprinted polymeric particles (MIPs) for low-pressure CO_2 capture using oil-in-oil suspension polymerisation," *Environmental Science & Technology*, vol. 51, pp. 11476–11483, 2017.

[191] S. Lowell, J. Shields, M. A. Thomas, and M. Thommes, "Characterization of

Porous Solids and Powders: Surface Area, Pore size and Density", 2004.

[192] J. Rouquerol, F. Rouquerol, K. S. W. Sing, P. Llewellyn, and G. Maurin, “Adsorption by Powders and Porous Solids: Principles, Methodology and Applications,” 2nd edition, Academic press, 2014.

[193] E. R. Cohen, T. Cvitas, J. G. Frey, B. Holmström, K. Kuchitsu, R. Marquardt, I. Mills, F. Pavese, M. Quack, J. Stohner, H. L. Strauss, M. Takami and A. J. Thor, "Quantities, Units and Symbols in Physical Chemistry", 3rd edition, 2007.

[194] P. A. Monson, “Understanding adsorption/desorption hysteresis for fluids in mesoporous materials using simple molecular models and classical density functional theory,” *Microporous Mesoporous Mater*, vol. 160, pp. 47–66, 2012.

[195] J. Landers, G. Y. Gor, and A. V. Neimark, “Density functional theory methods for characterization of porous materials,” *Colloid and Surfaces A: Physicochemical and Engineering Aspects*, vol. 437, pp. 3–32, 2013.

[196] W. J. Gerber, K. R. Koch, H. E. Rohwer, E. C. Hosten, and T. E. Geswindt, “Separation and quantification of $[RhCl_n(H_2O)_{6-n}]_{3-n}$(n = 0-6) complexes, including stereoisomers, by means of ion-pair HPLC-ICP-MS,” *Talanta*, vol. 82, pp. 348–358, 2010.

[197] P. Ricci, L. Pfeifer, T. Khotavivattana, V. Gouverneur, M. Médebielle, and J. R. Morphy, “The dual role of thiourea in the thiotrifluoromethylation of alkenes,” *Chemical Science*, vol. 8, pp. 1195–1199, 2016.

[198] S. Kedari, M. T. Coll, A. Fortuny, E. Goralska, and A. M. Sastre, “Liquid-liquid extraction of Ir, Ru, and Rh from chloride solutions and their separation using different commercially available solvent extraction reagents,” *Separation Science and Technology*, vol. 40, pp. 1927–1946, 2005.

[199] J. M. Sánchez, M. Hidalgo, J. Havel, and V. Salvadó, “The speciation of

rhodium(III) in hydrochloric acid media by capillary zone electrophoresis," *Talanta*, vol. 56, pp. 1061–1071, 2002.

[200] E. Benguerel, G. P. Demopoulos, and G. B. Harris, "Speciation and separation of rhodium (III) from chloride solutions: A critical review," *Hydrometallurgy*, vol. 40, pp. 135–152, 1996.

[201] P. S. Kumar, K. Ramakrishnan, S. D. Kirupha, and S. Sivanesan, "Thermodynamic and kinetic studies of cadmium adsorption from aqueous solution onto rice husk," *Brazilian Journal of Chemical Engineering*, vol. 27, pp. 347–355, 2010.

[202] Z. Abdeen and S. G. Mohammad, "Study of the Adsorption Efficiency of an Eco-Friendly Carbohydrate Polymer for Contaminated Aqueous Solution by Organophosphorus Pesticide," *Open Journal of Organic Polymer Materials*, vol. 04, pp. 16–28, 2014.

[203] M. Mahmoodi, R. Salehi, and M. Arami, "Binary System Dye Removal from Colored Textile Wastewater Using Activated Carbon: Kinetic and Isotherm Studies," *Desalination*, vol. 272, pp. 187–195, 2011.

[204] I. Langmuir, "The Adsorption of Gases on Plane Surfaces of Glass, Mica and Platinum," *Journal of the American Chemical Society*, vol. 40, pp. 1361–1403, 1918.

[205] H. Freundlich, "Over the adsorption in the Solution," *Journal of Physical Chemistry*, vol. 57, pp. 385–470, 1906.

[206] M. M. Dubinin and L. V. Radushkevich, "Equation of the Characteristic Curve of Activated Charcoal," *Proceedings of the Academy of Sciences USSR,* vol. 55, pp. 331–333, 1947.

[207] I. Langmuir, "The Constitution and Fundamental Properties of Solids and Liquids," *Journal of the American Chemical Society*, vol. 38, pp. 2221–2295, 1916.

[208] W. Kathrin, A. Bianca, T. Sohnel, M. Wenzel, K. Gloe, J. R. Price, L. F. Lindoy, A. J. Blake and M. Scroder, “Polymanime-based anion receptors: Extraction and structural studies,” *Coordination chemistry Reviews*, vol. 250, pp. 287–3003, 2006.

[209] A. Bianchi, E. Garcia-Espana, S. Mangani, M. Micheloni, P. Oriol, and P. Paoletti, “Anion co-ordination chemistry and crystal structure of the super complex $[H_8L][Co(CN)_6]_2Cl_2.10H_2O$ (L= 1, 4, 7, 10, 13, 16, 19, 22, 25, 28-Deca-azacyclotriacontane),” *Journal of Chemical Society, Chemical Communications*, pp. 729–731, 1987.

[210] A. Altun, E. Kuliyev, and N. M. Aghatabay, “Tautomeric conversion, vibrational spectra, and density functional studies on peripheral sulfur derivatives of benzothiazole and benzothiazoline isomers,” *Spectrochimica Acta - Part A: Molecular and Biomolecular Spectroscopy*, vol. 152, pp. 181–191, 2016.

[211] G. P. Soares and S. Guerini, “Structural and Electronic Properties of Impurities on Boron Nitride Nanotube,” *Journal of Modern Physics*, vol. 02, pp. 857–863, 2011.

[212] K. Thirumala Prasad, G. Gupta, A. K. Chandra, M. Phani Pavan, and K. Mohan Rao, “Spectral, structural and DFT studies of platinum group metal 3,6-bis(2-pyridyl)-4-phenylpyridazine complexes and their ligand bonding modes,” *Journal of Organometallic Chemistry*, vol. 695, pp. 707–716, 2010.

[213] A. Abbasi, M. Y. Skripkin, L. Eriksson, and N. Torapava, “Ambidentate coordination of dimethyl sulfoxide in rhodium(iii) complexes,” *Dalton Transactions*, vol. 40, pp. 1111–1118, 2011.

[214] A. Ramesh, H. Hasegawa, W. Sugimoto, T. Maki, and K. Ueda, “Adsorption of gold(III), platinum(IV) and palladium(II) onto glycine modified crosslinked chitosan resin,” *Bioresource Technology*, vol. 99, pp. 3801–3809, 2008.

[215] P. P. Sun and M. S. Lee, “Recovery of Platinum from Chloride Leaching Solution of Spent Catalysts by Solvent Extraction,” *Materials Transactions*, vol. 54, pp.

74–80, 2013.

[216] X. He, J. Sun, Y. Huan, J. Hu, and D. Yang, “Influence of Al_2O_3/CeZrAl composition on the catalytic behavior of Pd/Rh catalyst,” *Journal of Rare Earths*, vol. 28, pp. 59–63, 2010.

[217] P. Sun and M. Lee, “Separation of Rh(III) from the mixed chloride solutions containing Pt(IV) and Pd(II) by extraction with Alamine336 by stripping,” *Bulletin of the Korean Chemical Society*, vol. 31, pp. 1945–1950, 2010.

[218] B. Raju, J. R. Kumar, J. Lee, H. Kwonc, M. L. Kantam, and B. R. Reddy, “Separation of platinum and rhodium from chloride solutions containing aluminum , magnesium and iron using solvent extraction and precipitation methods,” *Journal of Hazardous Materials*, vol. 227–228, pp. 142–147, 2012.

[219] R. Gaita and S. J. Al-Bazi, “An ion-exchange method for selective separation of palladium, platinum and rhodium from solutions obtained by leaching automotive catalytic converters,” *Talanta*, vol. 42, pp. 249–255, 1995.

[220] S. Steinlechner and J. Antrekowitsch, “Potential of a Hydrometallurgical Recycling Process for Catalysts to Cover the Demand for Critical Metals, Like PGMs and Cerium,” *Journal of The Minerals, Metals & Materials Society*, vol. 67, pp. 406–411, 2015.

[221] A. Cieszynska and M. Wisniewski, “Selective extraction of palladium(II) from hydrochloric acid solutions with phosphonium extractants,” *Separation and Purification Technology*, vol. 80, pp. 385-389, 2011.

[222] C. Nowottny, W. Halwachs, and K. Schügerl, “Recovery of platinum, palladium and rhodium from industrial process leaching solutions by reactive extraction,” *Separation and Purification Technology*, vol. 12, pp. 135–144, 1997.

[223] A. P. Paiva, G. I. Carvalho, M. C. Costa, A. M. R. Costa, and C. A. Nogueira,

"Recovery of Palladium From a Spent Automobile Catalyst Leaching Solution By a Thiodiglycolamide Derivative," *wastes: Solutions, Treatments and Opportunities*, pp. 1-5, 2015.